


May 2019

The Effective Use of Portland Cement in Reactive Powder Hybrid Asphalt Concrete

Clayton Cloutier

University of Wisconsin-Milwaukee

Follow this and additional works at: <https://dc.uwm.edu/etd>

 Part of the [Civil Engineering Commons](#), and the [Materials Science and Engineering Commons](#)

Recommended Citation

Cloutier, Clayton, "The Effective Use of Portland Cement in Reactive Powder Hybrid Asphalt Concrete" (2019). *Theses and Dissertations*. 2054.

<https://dc.uwm.edu/etd/2054>

This Dissertation is brought to you for free and open access by UWM Digital Commons. It has been accepted for inclusion in Theses and Dissertations by an authorized administrator of UWM Digital Commons. For more information, please contact open-access@uwm.edu.

THE EFFECTIVE USE OF PORTLAND CEMENT IN REACTIVE
POWDER HYBRID ASPHALT CONCRETE

by

Clayton J. Cloutier

A Dissertation Submitted in
Partial Fulfillment of the
Requirements for the Degree of

Doctor of Philosophy
in Engineering

at

The University of Wisconsin-Milwaukee

May 2019

ABSTRACT
THE EFFECTIVE USE OF PORTLAND CEMENT IN REACTIVE POWDER HYBRID
ASPHALT CONCRETE

by

Clayton J. Cloutier

The University of Wisconsin-Milwaukee, 2019
Under the Supervision of Professor Konstantin Sobolev

Today, building a durable and cost-efficient infrastructure while minimizing future repair needs is a challenging task, and innovative technological breakthroughs are needed. Limited research has been conducted to investigate the use of portland cement (PC) to improve the performance of asphalt pavements. Portland cement in bitumen materials is attractive as it can improve the performance and reduce costs. Warm Mix Asphalt (WMA) is also an attractive alternative to Hot Mix Asphalt (HMA) as this material produces tremendous energy savings by lowering the production temperatures and enhances certain performance characteristics. It can be envisioned that the use of portland cement incorporated into an asphalt matrix can result in a hybrid product with enhanced long-term performance (especially in wet environments) characterized by better salt-scaling, freeze-thaw resistance, and self-healing properties (thermally-induced and moisture-induced). This study explores the interactions and compatibility of different types of portland cements with bitumen binders and identifies the potential improvement of performance in WMA portland cement hybrid systems.

The objectives of this research were to identify and characterize 5 portland cements used as reactive powders compounds: Lafarge Type I (LF), St. Mary Type I (SM), Buzzi Unicem

CSA (CSA), Lafarge Oil Well (OW), and Kerneos High Alumina (HA), 1 Weston spray dryer absorber (SDA), and 1 Payne & Dolan control limestone filler (LS) and determine how these materials were compatible with asphalt binders. The effect of the chemical properties, physical properties, and mineralogical composition of all powders performance of mastics based on different asphalt binders is discussed. The powders were mixed with asphalt binders (PG58-28 and PG52-34) at 0, 5, 15, 25% concentration by volume with a variable blade speed mixer and these mixtures were modified with a Warm Mix Asphalt (WMA) additive (Evothem by Ingevity®).

Rheological properties were investigated using a Dynamic Shear Rheometer (DSR). Complex Shear Modulus (G^*) and Phase Angle (δ) parameters were obtained for the mastics (binders with fillers). It was demonstrated that the addition of powders at 15% and higher dosages significantly affected the stiffness. Performance related indicators were determined for viscosity using the Brookfield Rotational Viscometer and rutting ($G^*/\sin(\delta)$), Multiple Stress Creep and Recovery (J_{nr} and % Recovery), fatigue ($G^*\sin(\delta)$), and aging resistance (aging index) using the DSR. Thermal cracking ($S(t)$ and m -value) was evaluated at low temperatures with the Bending Beam Rheometer. All reactive powder (cement based) and SDA mastics were compared to control limestone mastics. LF mastics were comparable to the control for rutting resistance but enhanced the low-temperature performance. SM mastics were also comparable for rutting resistance and comparable for low-temperature evaluations. CSA mastics enhanced the rutting resistance, aging resistance, and low-temperature thermal cracking resistance and at the same time did not hinder the fatigue resistance. OW mastics resembled similarities for workability, rutting resistance, and low-temperature testing. HA mastics demonstrated improvements for rutting resistance and did not hinder thermal cracking resistance. SDA

mastics improved the rutting resistance and demonstrated comparable results for fatigue resistance, aging resistance, and thermal cracking resistance.

A subset of 2 reactive powders (LF and CSA) were used at an optimized dosage of 25% concentration by volume binder replacement with WMA PG58-28 and WMA PG52-34 binders to evaluate and analyze the effect on typical Superpave® mixture testing such as mixture workability (% G_{mm}) and aging resistance (aging index) using a Superpave® Gyrotory Compactor, moisture damage resistance (IDT) using an Indirect Tensile Machine, and fatigue (E^*) and thermal cracking ($S(t)$) using a MTS environmental chamber. Durability testing was performed to evaluate freeze-thaw (mass change) and salt-scaling (mass loss). The results demonstrated that CSA mixtures enhanced the freeze-thaw performance, however, the results from the salt-scaling testing were inconclusive. Overall, the results of the mixture performance testing overwhelmingly supported the observations from the mastic stage testing.

Statistical analysis was evaluated to correlate the physical and chemical properties with rheological performance. It was observed that Rigden voids, specific gravity, Na_2O , and P_2O_5 had the best correlation to rheology, viscosity, and rutting resistance. As Rigden voids, Na_2O , and P_2O_5 increased in concentration the stiffness of the mastics increased, and as specific gravity increased in concentration the stiffness of the mastic decreased.

The results of this research puts significant confidence in utilization of portland cement reactive powders in asphaltic pavements. The next steps are crucial to build on these findings and encourage the paving industry to adopt portland cement powders. The mechanism of the physio-chemical interaction between the reactive powders and the asphalt binder must be evaluated using further testing to quantify the effects of portland cement and promote it as a binder enhancer for commercial use.

© Copyright by Clayton J. Cloutier, 2019
All Rights Reserved

DEDICATION

I dedicate this research to my friends and family who have given me unconditional love and support along the way.

TABLE OF CONTENTS

ABSTRACT	ii
TABLE OF CONTENTS	vii
LIST OF FIGURES	xiii
LIST OF TABLES.....	xx
LIST OF ABBREVIATIONS	xxiv
ACKNOWLEDGEMENTS	xxv
1. INTRODUCTION	1
1.1 BACKGROUND AND PROBLEM STATEMENT	1
1.2 HYPOTHESIS	5
1.3 OBJECTIVES	5
1.4 RESEARCH METHODOLOGY	6
2. LITERATURE REVIEW	7
2.1 ASPHALT BINDER	7
2.1.1 Chemical Composition	7
2.1.2 Oxidation and Age Hardening	9
2.1.3 Performance Grading System	12
2.1.4 Temperature Susceptibility	13
2.1.4.1 High-Temperature Behavior	13
2.1.4.2 Intermediate-Temperature Behavior	14
2.1.4.3 Low-Temperature Behavior	14
2.2 MINERAL AGGREGATES.....	15
2.2.1 Aggregates in Engineering Applications	15
2.2.2 Physical Properties of Aggregates	16
2.2.3 Aggregate Gradation	19
2.3 SUPERPAVE® ASPHALT MASTICS	22
2.3.1 Mastic Behavior	22
2.3.2 Effect of Fillers on Asphalt Mastic Stiffness	26

2.3.3 Effect of Fillers on Asphalt Mastic Aging Resistance	31
2.4 SUPERPAVE® ASPHALT MIXTURES	33
2.4.1 Mixture Behavior	33
2.4.2 Asphalt Workability	34
2.4.3 Age-Hardening Resistance	35
2.4.4 High-Temperature Permanent Deformation (Rutting)	36
2.4.5 Intermediate-Temperature Fatigue Cracking	37
2.4.6 Low-Temperature Thermal Cracking	39
2.4.7 Moisture Susceptibility	40
2.5 COAL COMBUSTION PRODUCTS (CCPs)	41
2.5.1 Coal Combustion Products	41
2.5.2 Chemical and Physical Properties	42
2.5.3 Spray Dryer Absorber (SDA)	42
2.5.4 Using Spray Dryer Absorber Products	43
2.5.5 Effect of Coal Combustion Products (CCPs) in Asphalt Mixtures.....	43
2.6 PORTLAND CEMENT	46
2.6.1 Portland Cement Products	46
2.6.2 Chemical and Physical Properties	46
2.6.3 Effect of Portland Cement Products in Asphalt Mixtures	50
3. MATERIALS AND TESTING METHODS	53
3.1 CHARACTERIZATION OF REACTIVE POWDERS	53
3.1.1 Chemical Properties	54
3.1.1.1 Chemical Composition	54
3.1.1.2 Loss on Ignition (LOI)	54
3.1.1.3 Crystallography	55
3.1.2 Physical Properties	56
3.1.2.1 Specific Gravity	56
3.1.2.2 Particle Size Distribution (PSD)	56
3.1.2.3 Shape	57

3.1.2.4 Rigden Voids	57
3.2 SUPERPAVE® ASPHALT MASTIC TESTING PROTOCOL	57
3.2.1 Mastic Preparation	59
3.2.1.1 Mixing Procedure	59
3.2.2 Aging Procedures	60
3.2.2.1 Rolling Thin Film Oven (RTFO)	60
3.2.2.2 Pressure Aging Vessel (PAV)	61
3.2.3 Brookfield Rotational Viscometer (RV)	62
3.2.4 Dynamic Shear Rheometer (DSR)	63
3.2.4.1 Time Sweep	63
3.2.4.2 Multiple Stress Creep and Recovery (MSCR)	68
3.2.5 Bending Beam Rheometer (BBR)	70
3.3 SUPERPAVE® ASPHALT MIXTURE TESTING PROTOCOL	72
3.3.1 Mixture Preparation	73
3.3.1.1 Mixing Procedure	74
3.3.2 Aging Procedures	75
3.3.2.1 Short-Term Aging	75
3.3.2.2 Long-Term Aging	75
3.3.3 Asphalt Mixture Volumetrics	76
3.3.3.1 Aggregate Volumetrics	76
3.3.3.2 Determination of G_{mm} and G_{mb}	77
3.3.3.3 Volumetric Calculations of Asphalt Mixture	78
3.3.3.3.1 Bulk Specific Gravity of Aggregates	79
3.3.3.3.2 Effective Specific Gravity of Aggregates	79
3.3.3.3.3 Asphalt Absorption	80
3.3.3.3.4 Effective Asphalt Content	80
3.3.3.3.5 Voids in Mineral Aggregate (VMA).....	81
3.3.3.3.6 Percent Air Voids	81
3.3.3.3.7 Voids in the Mineral Aggregate Filled with Asphalt (VFA)	81

3.3.3.3.8 Powder Proportion (Powder-to-Binder Ratio)	82
3.3.4 Workability	83
3.3.5 Aggregate Coating	88
3.3.6 Aging Resistance	91
3.3.7 Moisture Damage	92
3.3.7.1 Specimen Conditioning	92
3.3.7.2 Indirect Tensile Test (IDT)	94
3.3.8 Fatigue-Cracking Resistance	97
3.3.9 Thermal-Cracking Resistance	101
3.4 DURABILITY TESTING	104
3.4.1 Self-Healing	105
3.4.2 Mixture Durability Testing	106
3.4.2.1 Freeze-Thaw	106
3.4.2.1.1 Standard Freeze-Thaw	106
3.4.2.1.2 IDT Freeze-Thaw	107
3.4.2.2 Salt-Scaling	107
3.5 FIELD IMPLEMENTATION TESTING	109
4. RESULTS AND DISCUSSION	111
4.1 REACTIVE POWDER CHARACTERIZATION	111
4.1.1 Chemical Properties	111
4.1.1.1 Chemical Oxide Composition	112
4.1.1.2 Loss on Ignition (LOI)	117
4.1.1.3 Crystallography	118
4.1.2 Physical Properties.....	120
4.1.2.1 Specific Gravity	121
4.1.2.2 Particle Size Distribution (PSD)	121
4.1.2.3 Particle Shape	125
4.1.2.4 Rigden Voids	126
4.2 MASTIC TESTING (NON-PERFORMANCE RELATED INDICATORS)	127

4.2.1 Complex Shear Modulus (G^*).....	128
4.2.1.1 Relative Complex Shear Modulus (G^*_r)	132
4.2.1.2 Relative Phase Angle (δ_r)	133
4.3 MASTIC TESTING (PERFORMANCE RELATED INDICATORS)	135
4.3.1 Constructability.....	135
4.3.2 Rutting Resistance	138
4.3.2.1 Superpave® Rutting Factor ($G^*/\sin(\delta)$)	139
4.3.2.2 Non-Recoverable Compliance (J_{nr})	143
4.3.2.3 % Recovery	146
4.3.3 Fatigue Resistance	148
4.3.4 Aging Resistance	150
4.3.5 Thermal-Cracking Resistance.....	153
4.3.5.1 Creep Stiffness (S_t)	154
4.3.5.2 m-value	157
4.4 SUMMARY OF MASTIC RESULTS	159
4.5 MIXTURE TESTING.....	160
4.5.1 Asphalt Mixtures.....	161
4.5.2 Aggregate Blends.....	161
4.5.3 Aggregate Coating	164
4.5.4 Constructability.....	167
4.5.5 Aging Resistance	172
4.5.6 Moisture Damage.....	175
4.5.7 Fatigue Resistance	182
4.5.8 Thermal-Cracking Resistance.....	186
4.6 DURABILITY TESTING	190
4.6.1 Self-Healing	190
4.6.2 Mixture Durability Testing	192
4.6.2.1 Freeze-Thaw	193
4.6.2.1.1 Standard Freeze-Thaw	193

4.6.2.1.2 IDT Freeze-Thaw	195
4.6.2.2 Salt-Scaling	199
5. STATISTICAL MODELING OF THE REACTIVE POWDER EFFECTS ON ASPHALT MASTICS	203
5.1 THE EFFECT OF REACTIVE POWDER PROPERTIES ON TESTING PARAMETERS	203
5.2 MULTIPLE LINEAR REGRESSION MODELS	213
6. FIELD IMPLEMENTATION STUDY	221
6.1 LABORATORY RESEARCH STUDY.....	222
6.1.1 Experimental Design	222
6.1.2 Asphalt Mixtures.....	223
6.1.3 Aggregate Blends.....	224
6.1.4 Aggregate Coating	226
6.1.5 Constructability.....	230
6.1.6 Aging Resistance	236
6.1.7 Moisture Damage.....	241
6.1.8 Fatigue Resistance	251
6.1.9 Thermal-Cracking Resistance.....	256
6.2 COST ANALYSIS	261
7. CONCLUSIONS	265
7.1 MASTIC STUDY	265
7.2 MIXTURE STUDY	268
7.3 DURABILITY STUDY	271
7.4 STATISTICAL MODELING STUDY	272
8. REFERENCES	275
9. CURRICULUM VITAE	281

LIST OF FIGURES

Figure 2.1: Chemical Composition of Asphalt Binder (Bentur et al., 1998)	9
Figure 2.2: Spring-Dashpot Model of Viscoelastic Asphalt Behavior	14
Figure 2.3: Visual Assessment of Particle Shape	17
Figure 2.4: Moisture States of Aggregates	19
Figure 2.5: Aggregate Gradation Curves (Domone, P., & Illston, J., 2010)	21
Figure 2.6: Schematic Showing the Hypothesis of Asphalt-Filler Interaction (Tunnicliff, 1960).....	25
Figure 2.7: Conceptual Model Parameters of the Increase of Stiffness in Terms of Filler Influence	25
Figure 2.8: Progression of G^* Ratio with Respect to Filler Concentration	30
Figure 2.9: Tack Factor (Mastic Integrity) at Different Filler Concentrations	31
Figure 2.10: Aging Master Curves for (a) Complex Modulus and (b) Phase Angle	32
Figure 2.11: Rutting Characteristic of Asphalt Pavement due to Vehicle Loads	36
Figure 2.12: Rutting Damage Caused by Traffic Loads	37
Figure 2.13: Asphalt Fatigue (Alligator) Cracking	38
Figure 2.14: Low-Temperature Thermal Cracking	40
Figure 2.15: Typical Particle Size Distribution Curve for Portland Cement	47
Figure 2.16: Hydration Process of Portland Cement	48
Figure 2.17: Degree of Reaction of Portland Cement Compounds During Hydration	49
Figure 2.18: The Amount of Cementitious Particles that Hydrate after 28 Days	52
Figure 3.1: Rolling Thin Film Oven (RTFO)	60
Figure 3.2: Pressure Aging Vessel (PAV)	61
Figure 3.3: Rotational Viscometer (RV) (Pavement Interactive, 2015)	63
Figure 3.4: Stress-Strain Response of Viscoelastic Materials (after the Asphalt Institute 2003)	64
Figure 3.5: Complex Shear Modulus Representation	66
Figure 3.6: Multiple Stress Creep and Recovery Test Principle	69

Figure 3.7: The Determination of J_{nr} (after D'Angelo, 2009).....	69
Figure 3.8: The Determination of % Recovery (after D'Angelo, 2009).....	70
Figure 3.9: Creep and Recovery Stress (σ) and Strain (ϵ) Versus Time (t).....	71
Figure 3.10: Bending Beam Rheometer	72
Figure 3.11: Component Diagram of Compacted HMA Specimen	76
Figure 3.12: Superpave® Gyratory Compactor	84
Figure 3.13: Superpave® Gyratory Compactor Mold	85
Figure 3.14: Maximum Theoretical Specific Gravity vs. Number of Gyration (Faheem et al. 2008).....	87
Figure 3.15: Indirect Tension Test at Failure	95
Figure 3.16: Typical Fatigue Curve	98
Figure 3.17: 10 Hz Sine Wave Representation of Fatigue Test	100
Figure 3.18: MTS Environmental Chamber with IDT Testing Frame	101
Figure 3.19: Low-Temperature Load vs. Load-Line Displacement Representation	103
Figure 3.20: Stiffness (S) Determination of Low-Temperature Testing	103
Figure 4.1: SiO ₂ Content for Investigate Powders	113
Figure 4.2: Al ₂ O ₃ Content for Investigated Powders.....	113
Figure 4.3: Fe ₂ O ₃ Content for Investigated Powders	114
Figure 4.4: CaO Content for Investigated Powders	115
Figure 4.5: SO ₃ Content for Investigated Powders	115
Figure 4.6: Ternary Diagram for Investigated Powders	116
Figure 4.7: Loss on Ignition (LOI) for Investigated Powders	118
Figure 4.8: XRD for Control Limestone	119
Figure 4.9: XRD for Spray Dryer Absorber (SDA).....	119
Figure 4.10: XRD for Reactive Powders	120
Figure 4.11: Specific Gravity of Investigated Powders.....	121
Figure 4.12: Particle Size Distribution (PSD) of Investigated Powders	122
Figure 4.13: D ₁₀ Values of Investigated Powders	123
Figure 4.14: D ₅₀ Values of Investigated Powders	124

Figure 4.15: D ₉₀ Values of Investigated Powders	125
Figure 4.16: SEM Images of (a) Control Limestone (b) Spray Dryer Absorber (SDA) (c) Portland Cement Reactive Powder	126
Figure 4.17: Rigden Voids (RV) of Investigated Powders	127
Figure 4.18: Complex Modulus (G*) for Unaged PG58-28 WMA (Evothem) Mastics at 58°C	131
Figure 4.19: Complex Modulus (G*) for Unaged PG52-34 WMA (Evothem) Mastics at 52°C	131
Figure 4.20: Relative Complex Modulus (G*) for Unaged PG58-28 WMA (Evothem) Mastics at 58°C	133
Figure 4.21: Relative Complex Modulus (G*) for Unaged PG52-34 WMA (Evothem) Mastics at 52°C	133
Figure 4.22: Viscosity for Unaged PG58-28 WMA (Evothem) Mastics at 58°C	137
Figure 4.23: Viscosity for Unaged PG52-34 WMA (Evothem) Mastics at 52°C	138
Figure 4.24: G*/sin(δ) for RTFO Aged PG58-28 WMA (Evothem) Mastics at 58°C	142
Figure 4.25: G*/sin(δ) for RTFO Aged PG52-34 WMA (Evothem) Mastics at 52°C	142
Figure 4.26: J _{nr} for RTFO Aged PG58-28 WMA (Evothem) Mastics at 58°C	145
Figure 4.27: J _{nr} for RTFO Aged PG52-34 WMA (Evothem) Mastics at 52°C	145
Figure 4.28: G* sin(δ) for PAV Aged PG58-28 WMA (Evothem) Mastics at 19°C	150
Figure 4.29: G* sin(δ) for PAV Aged PG52-34 WMA (Evothem) Mastics at 13°C	150
Figure 4.30: Aging Index for PG58-28 WMA (Evothem) Mastics at 19°C	152
Figure 4.31: Aging Index for PG52-34 WMA (Evothem) Mastics at 13°C	153
Figure 4.32: Stiffness S(t) for PAV Aged PG58-28 WMA (Evothem) Mastics at -18°C	156
Figure 4.33: Stiffness S(t) for PAV Aged PG52-34 WMA (Evothem) Mastics at -24°C	156
Figure 4.34: m-value for PAV Aged PG58-28 WMA (Evothem) Mastics at -18°C	158

Figure 4.35: m-value for PAV Aged PG52-34 WMA (Evotherm) Mastics at -24°C.....	158
Figure 4.36: Aggregate Particle Size Distribution Curves	162
Figure 4.37: JMF Particle Size Distribution Curves	163
Figure 4.38: Superpave® Gradation Limitations	164
Figure 4.39: Aggregate Coating (a) WMA PG58-28 LS Control (b) WMA PG58-28 LF (c) WMA PG58-28 CSA (d) WMA PG52-34 LS Control (e) WMA PG52-34 LF (f) WMA PG52-34 CSA	167
Figure 4.40: Densification Curve for 4-MT WMA PG58-28 Mixtures.....	168
Figure 4.41: Densification Curve for 4-MT WMA PG52-34 Mixtures	169
Figure 4.42: Percent Air at 8 Gyration for Short-Term and Long-Term Aged WMA PG58-28 Mixtures	173
Figure 4.43: Percent Air at 8 Gyration for Short-Term and Long-Term Aged WMA PG52-34 Mixtures	173
Figure 4.44: Aging Index for WMA PG58-28 Mixtures	174
Figure 4.45: Aging Index for WMA PG52-34 Mixtures	175
Figure 4.46: Horizontal Tensile Stress at Center of Specimen for WMA PG58-28 Mixtures	178
Figure 4.47: Horizontal Tensile Stress at Center of Specimen for WMA PG52-34 Mixtures	178
Figure 4.48: Vertical Compressive Stress at Center of Specimen for WMA PG58-28 Mixtures	179
Figure 4.49: Vertical Compressive Stress at Center of Specimen for WMA PG52-34 Mixtures	179
Figure 4.50: Tensile Strain at Failure for WMA PG58-28 Mixtures	180
Figure 4.51: Tensile Strain at Failure for WMA PG52-34 Mixtures	181
Figure 4.52: TSR for WMA PG58-28 Mixtures	182
Figure 4.53: TSR for WMA PG52-34 Mixtures	182
Figure 4.54: Vertical Deformation Fatigue Slope for WMA PG58-28 Mixtures	184
Figure 4.55: Vertical Deformation Fatigue Slope for WMA PG52-34 Mixtures	184

Figure 4.56: Number of Cycles Drop in E^* for WMA PG58-28 Mixtures	185
Figure 4.57: Number of Cycles Drop in E^* for WMA PG52-34 Mixtures	186
Figure 4.58: Fracture Energy (G_f) for WMA PG58-28 Mixtures.....	187
Figure 4.59: Fracture Energy (G_f) for WMA PG52-34 Mixtures	188
Figure 4.60: Stiffness $S(t)$ for WMA PG58-28 Mixtures	189
Figure 4.61: Stiffness $S(t)$ for WMA PG52-34 Mixtures	189
Figure 4.62: SEM Images of Control Limestone Mastic at (a) 50X (b) 100X (c) 500X	192
Figure 4.63: SEM Images of LF Mastic at (a) 50X (b) 100X (c) 500X	192
Figure 4.64: SEM Images of CSA Mastic at (a) 50X (b) 100X (c) 500X	192
Figure 4.65: Freeze-Thaw Mass Change (%) for WMA PG58-28 Mixtures	194
Figure 4.66: Freeze-Thaw Mass Change (%) for WMA PG52-34 Mixtures	195
Figure 4.67: Freeze-Thaw Horizontal Tensile Stress at Center of Specimen for WMA PG58-28 Mixtures	196
Figure 4.68: Freeze-Thaw Horizontal Tensile Stress at Center of Specimen for WMA PG52-34 Mixtures	196
Figure 4.69: Freeze-Thaw Vertical Compressive Stress at Center of Specimen for WMA PG58-28 Mixtures	197
Figure 4.70: Freeze-Thaw Vertical Compressive Stress at Center of Specimen for WMA PG58-28 Mixtures	198
Figure 4.71: Freeze-Thaw Tensile Strain at Failure for WMA PG58-28 Mixtures	199
Figure 4.72: Freeze-Thaw Tensile Strain at Failure for WMA PG52-34 Mixtures	199
Figure 4.73: Salt-Scaling Mass Loss (g/m^2) for WMA PG58-28 Mixtures	201
Figure 4.74: Salt-Scaling Mass Loss (g/m^2) for WMA PG52-34 Mixtures	201
Figure 5.1: Multiple Linear Regression Model for Determining Complex Modulus G^* for WMA PG58-28 Mastics at 25% Concentration by Volume	217
Figure 5.2: Multiple Linear Regression Model for Determining Viscosity for WMA PG58-28 Mastics at 25% Concentration by Volume	218

Figure 5.3: Multiple Linear Regression Model for Determining Rutting Factor $G^*/\sin(\delta)$ for WMA PG58-28 Mastics at 25% Concentration by Volume	218
Figure 5.4: Multiple Linear Regression Model for Determining Complex Modulus G^* for WMA PG52-34 Mastics at 25% Concentration by Volume	219
Figure 5.5: Multiple Linear Regression Model for Determining Viscosity for WMA PG52-34 Mastics at 25% Concentration by Volume	219
Figure 5.6: Multiple Linear Regression Model for Determining Rutting Factor $G^*/\sin(\delta)$ for WMA PG52-34 Mastics at 25% Concentration by Volume	220
Figure 6.1: Wausau, WI Road Paving Project	222
Figure 6.2: JMF Particle Size Distribution Curves	226
Figure 6.3: Aggregate Coating (a) 2-MT HMA Control (b) 2-MT HMA SDA (c) 4-MT HMA Control (d) 4-MT HMA SDA (e) 4-MT HMA SDA (PG52-34) (f) 4-MT WMA Control (g) 4-MT WMA SDA (h) 4-MT WMA SDA (PG52-34) (i) 6-MT WMA SDA	229
Figure 6.4: Densification Curves for 2-MT HMA Mixtures	231
Figure 6.5: Densification Curves for 4-MT HMA Mixtures	232
Figure 6.6: Densification Curves for 4-MT and 6-MT WMA Mixtures	233
Figure 6.7: Aging of 2-MT HMA (a) %Air at 8 Gyration (b) Aging Index	238
Figure 6.8: Aging of 4-MT HMA (a) %Air at 8 Gyration (b) Aging Index	239
Figure 6.9: Aging of 4-MT WMA and 6-MT WMA (a) %Air at 8 Gyration (b) Aging Index	240
Figure 6.10: Horizontal Tensile Stress (MPa) at the Center of the Specimen (a) 2-MT HMA (b) 4-MT HMA (c) 4-MT WMA and 6-MT WMA	245
Figure 6.11: Vertical Tensile Stress (MPa) at the Center of the Specimen (a) 2-MT HMA (b) 4-MT HMA (c) 4-MT WMA and 6-MT WMA	246
Figure 6.12: Horizontal Tensile Strain (mm/mm) at Failure (a) 2-MT HMA (b) 4-MT HMA (c) 4-MT WMA and 6-MT WMA	248

Figure 6.13: Tensile Strength Ratio (a) 2-MT HMA (b) 4-MT HMA (c) 4-MT WMA and 6-MT WMA	250
Figure 6.14: 2-MT HMA (a) Vertical Deformation Slope (b) Number of Cycles Drop in E^*	253
Figure 6.15: 4-MT HMA (a) Vertical Deformation Slope (b) Number of Cycles Drop in E^*	254
Figure 6.16: 4-MT WMA and 6-MT WMA (a) Vertical Deformation Slope (b) Number of Cycles Drop in E^*	256
Figure 6.17: Fracture Energy (G_f) for (a) 2-MT HMA (b) 4-MT HMA (c) 4-MT WMA and 6-MT WMA	259
Figure 6.18: Stiffness $S(t)$ for (a) 2-MT HMA (b) 4-MT HMA (c) 4-MT WMA and 6-MT WMA	261

LIST OF TABLES

Table 2.1: Types of Disperse Systems.	22
Table 2.2: Main Compounds of Portland Cement	47
Table 3.1: Testing Matrix for Characterization of Reactive Powders.	53
Table 3.2: Testing Matrix for Mastic Study.....	58
Table 3.3: Testing Matrix for Mixture Study.....	73
Table 3.4: Superpave® Volumetric Mixture Design Requirements.....	82
Table 3.5: Superpave® Gyrotory Compaction Parameters for Different Roadway Applications	87
Table 3.6: Surface Area Factors for Different Aggregate Sizes.	89
Table 3.7: Testing Matrix for Durability Testing.....	105
Table 3.8: Testing Matrix for Field Implementation Study.	109
Table 4.1: Filler Materials used in Mastic Testing.	111
Table 4.2: Chemical Oxide Contents for Investigated Powders.	117
Table 4.3: DSR Measured Indicators for Unaged PG58-28 HMA and Unaged PG58-28 WMA (Evotherm) at 58°C	129
Table 4.4: DSR Measured Indicators for Unaged PG58-28 HMA and Unaged PG58-28 WMA (Evotherm) at 52°C.....	129
Table 4.5: Relative Phase Angle (δ_r) for Unaged PG58-28 WMA (Evotherm) Mastics at 58°C.	134
Table 4.6: Relative Phase Angle (δ_r) for Unaged PG52-23 WMA (Evotherm) Mastics at 52°C.	134
Table 4.7: Viscosity for Unaged PG58-28 HMA and Unaged PG58-28 WMA (Evotherm) at 135°C.	136
Table 4.8: Viscosity for Unaged PG52-34 HMA and Unaged PG52-34 WMA (Evotherm) at 135°C	136
Table 4.9: $G^*/\sin(\delta)$ for Unaged PG58-28 HMA and Unaged PG58-28 WMA (Evotherm) at 58°C	140

Table 4.10: $G^*/\sin(\delta)$ for Unaged PG52-34 HMA and Unaged PG52-34 WMA (Evotherm) at 58°C	140
Table 4.11: $G^*/\sin(\delta)$ for RTFO Aged PG58-28 HMA and RTFO Aged PG58-28 WMA (Evotherm) at 58°C	140
Table 4.12: $G^*/\sin(\delta)$ for RTFO Aged PG52-34 HMA and RTFO Aged PG52-34 WMA (Evotherm) at 52°C	141
Table 4.13: J_{nr} for RTFO Aged PG58-28 HMA and RTFO Aged PG58-28 WMA (Evotherm) at 58°C	143
Table 4.14: J_{nr} for RTFO Aged PG52-34 HMA and RTFO Aged PG52-34 WMA (Evotherm) at 52°C	144
Table 4.15: % Recovery for RTFO Aged PG58-28 HMA and RTFO Aged PG58-28 WMA (Evotherm) at 58°C	146
Table 4.16: % Recovery for RTFO Aged PG52-34 HMA and RTFO Aged PG52-34 WMA (Evotherm) at 52°C	146
Table 4.17: % Recovery for RTFO Aged Binders and Mastics	147
Table 4.18: $G^*\sin(\delta)$ for PAV Aged PG58-28 HMA and PAV Aged PG58-28 WMA (Evotherm) at 19°C	149
Table 4.19: $G^*\sin(\delta)$ for PAV Aged PG52-34 HMA and PAV Aged PG52-34 WMA (Evotherm) at 13°C	149
Table 4.20: Aging Index for PG58-28 HMA and PG58-28 WMA (Evotherm) at 19°C	151
Table 4.21: Aging Index for PG52-34 HMA and PG52-34 WMA (Evotherm) at 13°C	151
Table 4.22: $S(t)$ for PAV Aged PG58-28 HMA and PAV Aged PG58-28 WMA (Evotherm) at -18°C	155
Table 4.23: $S(t)$ for PAV Aged PG52-34 HMA and PAV Aged PG52-34 WMA (Evotherm) at -24°C	155
Table 4.24: m-value for PAV Aged PG58-28 HMA and PAV Aged PG58-28 WMA (Evotherm) at -18°C	157

Table 4.25: m-value for PAV Aged PG52-34 HMA and PAV Aged PG5-34 WMA (Evotherm) at -24°C	157
Table 4.26: Performance Testing Summary of all Asphalt Mastics	159
Table 4.27: 4-MT JMF Aggregate Combinations	161
Table 4.28: Particle Size Distributions (PSD) for all Aggregate Types	162
Table 4.29: Calculated Surface Area of Aggregates	165
Table 4.30: Asphalt Film Thickness for Control and Reactive Powder Mixtures	166
Table 4.31: WMA PG58-28 Asphalt Mixture Volumetrics	170
Table 4.32: WMA PG52-34 Asphalt Mixture Volumetrics	171
Table 4.33: Moisture Damage Load and Flow Results for WMA PG58-28 Mixtures ..	176
Table 4.34: Moisture Damage Load and Flow Results for WMA PG52-34 Mixtures ..	177
Table 5.1: Complex Modulus (G^*) for Unaged WMA PG58-28 Mastics at 58°C and Unaged WMA PG52-34 Mastics at 52°C	204
Table 5.2: Viscosity for Unaged Mastics based on WMA PG58-28 and WMA PG52-34 Binders at 135°C.....	204
Table 5.3: $G^*/\sin(\delta)$ for RTFO Aged WMA PG58-28 at 58°C and RTFO Aged WMA PG52-34 Mastics at 52°C.....	204
Table 5.4: Correlation Matrix Between the Reactive Powder Properties and Complex Modulus (G^*) of Mastics	207
Table 5.5: Correlation Matrix Between the Reactive Powder Properties and Viscosity of Mastics	208
Table 5.6: Correlation Matrix Between the Reactive Powder Properties and Rutting Factor $G^*/\sin(\delta)$ of Mastics	209
Table 5.7: Correlation Matrix Between the Reactive Powder Properties Related to Complex Modulus (G^*) of Mastics	211
Table 5.8: Correlation Matrix Between the Reactive Powder Properties Related to Viscosity of Mastics	212
Table 5.9: Correlation Matrix Between the Reactive Powder Properties Related to Rutting Factor $G^*/\sin(\delta)$ of Mastics	213

Table 5.10: Input Parameters Used to Determine the Multiple Linear Regression	
Models for Complex Modulus (G^*)	215
Table 5.11: Input Parameters Used to Determine the Multiple Linear Regression	
Models for Viscosity	216
Table 5.12: Input Parameters Used to Determine the Multiple Linear Regression	
Models for Rutting Factor $G^*/\sin(\delta)$	216
Table 6.1: Experimental Research Testing Matrix	223
Table 6.2: 2-MT JMF Aggregate Combinations.....	224
Table 6.3: 4-MT JMF Aggregate Combinations.....	225
Table 6.4: 6-MT JMF Aggregate Combinations.....	225
Table 6.5: Calculated Surface Area of Aggregates	227
Table 6.6: Asphalt Film Thickness for Control and SDA Mixtures	228
Table 6.7: 2-MT HMA Mixture Volumetrics	235
Table 6.8: 4-MT HMA and WMA Mixture Volumetrics	235
Table 6.9: 6-MT WMA Mixture Volumetrics	236
Table 6.10: The Ultimate Load (kN) and Horizontal Deformation at Failure (mm)	
of all Mixtures Tested for IDT	243
Table 6.11: Pavement Quantities for Inbound Traffic Sections.....	263
Table 6.12: Pavement Quantities for Outbound Traffic Sections	263
Table 6.13: Material Cost Analysis for Different Asphalt Mixtures	264
Table 6.14: Total Cost Analysis for Inbound Traffic Sections	264
Table 6.15: Total Cost Analysis for Outbound Traffic Sections	264

LIST OF ABBREVIATIONS

AASHTO	American Society of State Highway and Transportation Officials
ASTM	American Society for Testing Materials
BBR	Bending Beam Rheometer
DSR	Dynamic Shear Rheometer
δ	Phase Angle
E^*	Complex Fatigue Modulus
G^*	Complex Shear Modulus
G_f	Fracture Energy
G_{mb}	Bulk Specific Gravity
G_{mm}	Maximum Specific Gravity
IDT	Indirect Tensile Test
MSCR	Multiple Stress Creep and Recovery
PAV	Pressure Aging Vessel
RTFO	Rolling Thin Film Oven
$S(t)$	Stiffness
SDA	Spray Drying Agent
SEM	Scanning Electron Microscope
SGC	Superpave® Gyrotory Compactor
VFA	Voids Filled with Asphalt
VMA	Voids in Mineral Aggregate

ACKNOWLEDGMENTS

I would like to express my sincere gratitude to Dr. Konstantin Sobolev for his knowledge and expertise during the project developmental stages. He has become one of the biggest influences in my life and his help and recommendations have been vital to this research. Without his guidance I would not be where I am today.

I would like to thank Portland Cement Association, Mathy Construction Co., American Asphalt of Wisconsin, Payne and Dolan Inc., WE Energies, Lafarge, St. Marys Cement Inc., Buzzi Unicem, and Kerneos Inc., and all other sponsors of this research who made this work possible. A special thanks to Steve Kosmatka, Carlton Travis, Gail Hoard, Tom Jansen, Andrew Hanz, Ervin Dukatz, and Ahmed Faheem for their continuous help and support.

CHAPTER 1

INTRODUCTION

1.1 BACKGROUND AND PROBLEM STATEMENT

Asphalt cement is one of the oldest materials used in construction. Asphalt was first used as a construction material in Sumeria (Mesopotamia), around 6,000 B.C., as a shipbuilding material. From there, asphalts were then used in Egypt around 2600 B.C. as a material for waterproofing, mummification, and building structures. In various parts of the world, asphalt continued to be used as mortar for buildings and paving blocks, caulking for ships, and numerous waterproofing applications. In the United States, the first known natural asphalt pavement was laid in 1876 on Pennsylvania Avenue in Washington, D.C. Before the mid-1850s asphalt came from natural pools at different locations in the world such as Trinidad Lake. With the discovery and refining of petroleum in Pennsylvania, asphalt became very well-known. By 1907, most of the asphalt came directly from the distillation process from petroleum refineries than from the natural deposits. Today, almost all asphalt materials come from refined petroleum (Roberts et al. 1996).

Asphalt concrete is composed of two different ingredients: asphalt cement and aggregates. Asphalt cement consists of approximately 5% of the total mixture mass whereas the aggregates consist of the remaining 95% mass. Asphalt cement, or binder, is a mixture of petroleum hydrocarbons with different chemical structures. The primary elements present in asphalt are carbon and hydrogen. Other elements present are sulfur, nitrogen, oxygen, vanadium, and nickel. Asphalt binder is a strong and durable material that has great adhesive and

waterproofing features. Asphalt binder can be very elastic and brittle at low temperatures and can be very fluid (viscous) at high temperatures. At intermediate temperatures, asphalt cement is considered a viscoelastic material since it demonstrates both elastic and viscous properties. Due to these variations in material behavior at different temperatures, asphalt cement is considered a thermoplastic material (Roberts et al., 1996).

Asphalts used in the construction industry are typically classified as asphalt cements, emulsified asphalts, and cutback asphalts. The most common type of asphalt material is Hot Mix Asphalt (HMA). Hot Mix Asphalt is widely used as a material in the construction of flexible pavements. The asphalt cement can be heated to make the material less viscous so that it can flow easier enabling the compaction. This allows the material to liquefy and then be mixed with aggregates to make asphalt concrete. Since the asphalt material is sticky, it adheres to the aggregate particles to produce HMA.

Aggregates are used in asphalt applications because they act as a stone framework which is important in terms of material strength. Aggregates in asphalt pavements range from coarse aggregates to fine aggregates. According to the American Society for Testing and Materials (ASTM) the No. 4 sieve size (4.75 mm) separates the coarse and fine aggregates (ASTM C136). Anything above the No. 10 sieve size (2.00 mm) is considered gravel, boulders, or cobbles, whereas anything below the No. 10 sieve size (2.00 mm) is considered either sand or mineral fillers. Mineral fillers are classified as the portion of the fine aggregates that pass the No. 200 sieve (0.075 mm). These mineral fillers usually take up less than 8% of Hot Mix Asphalt (HMA), by mass, but have a large effect on the HMA field performance. Properly classifying and grading aggregates to a specific particle size distribution is critical for asphalt mixtures.

Today, building a durable and cost-efficient infrastructure while minimizing future repair needs is a challenging task, and innovative technological breakthroughs are needed. Researchers have investigated the use of mineral fillers including portland cement (PC) and industrial by-products such as fly ash to improve the performance of asphalt pavements (Ali et al., 1996; Churchill et al., 1999; Asi et al., 2005; Tapkin, 2008; Faheem & Bahia, 2010). However, in all these studies cement and fly ash were viewed as fillers with the expectation of performance similar to mineral fillers. Sobolev et al. (2013) demonstrated that the incorporation of fly ash in asphalt mixtures (ASHphalt) improves the performance of asphalt at the levels compared to those achieved with polymer modification. This effect was attributed to the unique spherical shape, the beneficial size distribution, and the chemical composition of fly ash.

Overall, the use of cement, lime, and fly ash in bitumen materials is attractive as it improves the performance and reduces costs and environmental impacts associated with production and application of asphalt (Tapkin, 2008). The advantages of these reactive powder fillers in asphalt include improved mixing, placing and compaction, stability, resistance to water damage, rutting resistance, flexibility, and resistance to freeze-thaw damage (Carpenter, 1952; Warden et al., 1952; Zimmer, 1970; Sankaran & Rao, 1973; Henning, 1974; Tons et al., 1983; Suheibani, 1986; Cabrera & Zoorob, 1994; Tapkin, 2008).

In the past, there was a considerable effort to demonstrate the benefits of cementitious materials in mastics and Hot Mix Asphalt (HMA) (Sobolev et al., 2014), however, recent research based on Superpave® testing protocol related to cement application in HMA is very limited. The fatigue performance of dense graded asphalt-aggregate mixtures with portland cement used to replace a normal filler was reported by Tapkin (2008). It was demonstrated that

fatigue life of the specimens with portland cement is considerably higher than that of the specimens with natural filler. The effect of cement addition on the properties of asphalt binders using Superpave testing methods was reported for different cement-to-asphalt (C/A) ratios from 0.05 to 0.30 by volume of asphalt binder (Al-Khateeb & Al-Akhras, 2011). It was demonstrated that the C/A ratio of 0.15 was optimal resulting in a balanced increase in the rotational viscosity and the value of the DSR $G^*/\sin(\delta)$ rutting parameter of asphalt binders.

Warm Mix Asphalt (WMA) is an attractive alternative to Hot Mix Asphalt (HMA) as this material produces tremendous energy savings. World Bank (2009) estimated that for every 10°C decrease in production temperature, there was an average savings of nearly 1 L of fuel oil and approximately 1 kg of CO₂ emissions per ton of HMA mix produced. It was also reported from other field testing evaluations that the addition of WMA additives to conventional HMA resulted in a decrease in production temperature between 15°C and 40°C. The benefits of WMA additives also showed an increase in mixture durability, mat compactions, and use of Recycled Asphalt Pavements (RAP) in the mixtures (Federal Highway Administration, 2007).

It can be envisioned that the use of portland cement incorporated into an asphalt matrix can result in a hybrid product with enhanced long-term performance (especially in wet environments) such as better salt-scaling, freeze-thaw resistance, and self-healing properties. There is a need to look at cement modification and Superpave® testing methodology examining the performance of asphalt concrete containing different types of portland cement (optionally combined with fly ash). This study explores the interactions and compatibility of different types of portland cement with bitumen binders and will identify the potential improvement of performance in WMA-portland cement hybrid systems.

1.2 HYPOTHESIS

The use of portland cement can have beneficial interactions with asphalt binders and can result in enhanced performance of Warm Mix Asphalt (WMA) equally or over-performing the fillers which are conventionally used in asphalt mixtures. Such beneficial interactions can help to engineer the asphalt mastics and asphalt concrete with improved performance.

1.3 OBJECTIVES

- Conduct rheological testing and analyze the performance of 5 types of portland cements combined with 2 asphalt binders modified and used as a Warm Mix Asphalt (WMA) at 3 different dosages of cement, up to 50% bitumen replacement by weight (approximately, 25% by volume) and compare to a control limestone mineral filler as well as a spray dryer absorber (SDA) by-product.
- Conduct the fatigue and Multiple Stress Creep and Recovery (MSCR) tests and evaluate the low-temperature performance using Bending Beam Rheometer (BBR) on aged specimens with portland cement.
- Conduct testing on asphalt mixtures (WMA) with optimal portland cement content in terms of aggregate coating, workability, aging resistance, moisture damage resistance, fatigue cracking resistance, and low-temperature thermal cracking resistance.
- Conduct durability testing on optimal asphalt mixtures for self-healing, freeze-thaw, and salt scaling exposure.
- Conduct the correlation analysis on asphalt mastics to determine which chemical and physical properties with influence material performance.
- Conduct a field implementation study and test industrial-grade WMA according to industrial standards.

1.4 RESEARCH METHODOLOGY

The research objectives were met by completing the following tasks:

Task 1: Literature Review

- Conduct an extended review on asphalt mastic and mixture characteristics.
- Report on current research efforts on asphalt mastics with traditional fillers and investigate the limited research on asphalt mastics or mixtures that have been modified with portland cement.

Task 2: Experimental Design and Testing

- Determine the portland cement materials (reactive powders), asphalt binder types, and WMA additive to use in the mastic and mixture testing protocol.
- Evaluate the chemical and physical properties of the reactive powders.
- Access the Superpave® testing specifications and evaluate mastics and mixtures to understand the influence of reactive powders on material performance.
- Assess the influence of reactive powders on durability testing of asphalt specimens.

Task 3: Data Analysis

- Determine statistical correlations between the chemical and physical properties of reactive powders and the performance related indicators of the mastics determined from the Superpave® testing protocol.
- Develop multiple linear regression models to predict testing outputs from chemical and physical property independent variables.

Task 4: Field Implementation

- Implement laboratory research study to industrial pilot test and evaluate cost analysis.

CHAPTER 2

LITERATURE REVIEW

2.1 ASPHALT BINDER

2.1.1 Chemical Composition

Asphalt is defined by the American Society for Testing Materials (ASTM) as a “dark brown to black cementitious material in which the predominating constituents are bitumens which occur in nature or are obtained in petroleum processing” (Asphalt Institute, 2003). Asphalt is made from crude petroleum which is a product that can be found naturally in the world. About 90 to 95 percent by weight of asphalt bitumen is composed of hydrogen and carbon, which is why it is referred to as a hydrocarbon. The carbon atoms can arrange in different configurations which allows the asphalt to behave in different ways. There are three distinct arrangements that carbon can configure: straight or branched chains, simple or complex saturated rings, and one or more stable six-carbon condensed unsaturated ring structures. The remaining portion of asphalt contains both heteroatoms (hydrogen, nitrogen, and sulfur) and metals. The heteroatoms and metals provide asphalt with many unique characteristics because they are reactive with other molecules. The type, rather than quantity, of each element is more critical to the overall asphalt molecular composition. Since asphalt is derived from an organic petroleum product, the molecular structure is diverse and very dependent on the crude source. (Peterson, 1984).

The heteroatoms attach to the carbon atoms in different configurations. Within these molecular configurations, there is an imbalance of electrochemical forces. For this reason these asphalt molecules are considered to be polar. Each polar group, therefore, has an electropositive

charge and an electronegative charge. Since similar charges and opposite charges have different effects with each other, these characteristics influence asphalt properties and performance.

These polar groups can also vary depending on the source of the asphalt material and this can influence the performance of the asphalt material. Non-polar groups in asphalt act as solvents for the polar groups and this also affects the physical and aging properties of the asphalt cement (Roberts et al., 1996).

There are many different molecular structures comprising asphalt cements. Researchers have focused on categorizing these structures into major fractions (Figure 2.1). Asphalt cement consists of both asphaltenes and maltenes (petrolenes). Asphaltenes are dark brown friable solids that are chemically complex and have the highest polarity when compared to the other asphalt components. The asphaltenes are responsible for the adhesive properties of asphalt which is directly related to viscosity. When the asphaltene content is less than 10%, the compaction effort is very high and it is difficult to compact the asphalt concrete to the appropriate density. Maltenes, on the other hand, consist of both resins (highly polar hydrocarbons) and oils (aromatics and saturates). Resins are dark brown and semisolid or solid, and are temperature dependent which affects the viscosity of the overall asphalt material. When heated, these resins act as a fluid material, but at low temperatures these resins become brittle. The resins are responsible for dispersing asphaltenes in the oil, which is a clear or white liquid that, during oxidation, produces asphaltene and resin molecules. This compatible and balanced system is what makes asphalt suitable as a binder material in the construction industry (Domone & Illston, 2010; Mamlouk & Zaniewski, 2017; Roberts et al., 1996).

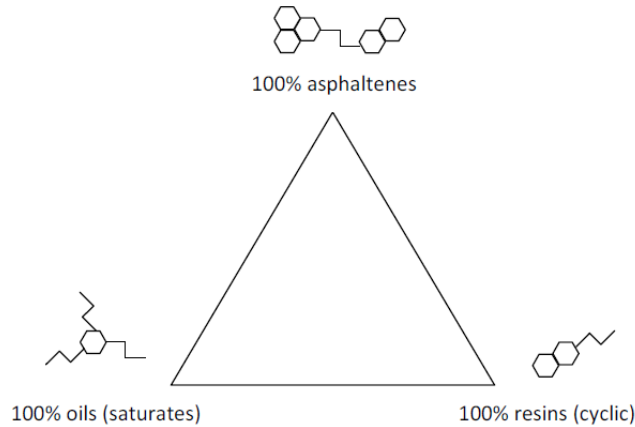


Figure 2.1: Chemical Composition of Asphalt Binder (Bentur et al., 1998)

2.1.2 Oxidation and Age Hardening

Asphalt cement is an organic material and thus reacts with atmospheric oxygen. Bituminous materials are exposed to the environment and therefore these materials can harden and age. However, the rate of oxidation and age hardening both depend on the natural conditions, such as temperature, as well as the chemical composition of the bituminous material. The oxidation process occurs more quickly at higher temperatures. Oxidation alters the structure and composition of the asphalt molecules and changes the rheological properties of asphalt cement so that it becomes more brittle, especially at lower temperatures. Since rheological properties are critical in asphalt development, oxidation and age hardening are important factors to consider (Asphalt Institute, 2001; Domone & Illston, 2010).

During the oxidation process, oxygen molecules from the atmosphere form asphaltenes by combining with resins and oils. The polarity and molecular weight fraction both increase while the molecular weight components decrease. Due to this result, the viscosity of the bituminous materials increases. The asphalt also becomes unstable because there are

discontinuities between the saturates and the other components. This instability within the material creates a lack of cohesion and this can lead to cracking. Volatiles are also lost in the oxidation process. If the bitumen is subjected to higher temperatures, and if there is a large portion of low molecular weight components, there will be a loss of volatiles and this will lead to a more rapid age hardening process (Domone & Illston, 2010).

A large amount of oxidation and age hardening occurs during the HMA process when the asphalt is heated for mixing and compacting. At the beginning of the mixing process, the asphalt binder is placed into the mixer and mixed with heated aggregates. During this mixing process the hot asphalt cement is exposed to air temperatures from 275 to 325°F (135 to 163°C). At this time, the asphalt cement also exists in thin films while it coats the aggregates, and this allows oxidative hardening to occur at a faster rate. High temperatures change the rheological properties of the asphalt cement by decreasing the penetration and increasing the viscosity. The reason this happens is because of oxidation and because of the loss of more volatile components (Roberts et al., 1996).

After the short-term oxidation during mixing, transportation, and placement, the asphalt then experiences a long-term form of oxidation, exposure during service life called age hardening. Once the asphalt pavement has been compacted and opened to vehicle traffic, the age hardening process continues, but at a slower rate. This process usually happens until the asphalt reaches its limiting density (compaction to percent air voids) under the traffic loads. During the construction process volatilization occurs which associated with the process of volatile components evaporating from the asphalt pavement. Physical hardening also occurs when asphalt has been exposed to low temperatures (typically less than 0°C) for long periods of time.

Also, if the HMA pavement has a higher air void content than designed, there is a larger amount of air, water, and light that can penetrate the pavement and cause the pavement to age faster. This is why asphalt compaction in the field is a critical parameter (Kandhal, Sandvig, Koehler, & Wenger, 1973).

Changes in asphalt cement properties, such as penetration at 25°C (77°F) and viscosity at 60°C (140°F), as well as changes in pavement properties, such as percent of air voids in the pavements, have been known to affect pavement performance with time and have been found to follow a hyperbolic model (Brown, 1957; Lee, 1973; Kandhal, 1975). Based on this theory, the changes in physical properties follow a hyperbolic function with time and approach a definite limit as time increases (Roberts et al., 1996). The following equation expresses the age hardening of asphalt in the field:

$$\frac{T}{\Delta Y} = a + bT \quad \text{Eq. 2.1}$$

where:

ΔY = change in test property with time T or the difference between the zero-life value and the value at any significant time;

T = time;

a = constant, the intercept of the line on the ordinate;

b = slope;

1/b = the ultimate change of the property at infinite time.

The degree of age hardening can be quantified in terms of penetration or viscosity. The percent retained penetration (Eq. 2.2) and the aging index (Eq. 2.3) have been used to assess the relative aging of asphalt cements of different grades and/or from different sources.

$$\% \text{Retained Penetration} = \frac{\text{Penetration of aged asphalt}}{\text{Penetration of original asphalt}} * 100 \quad \text{Eq. 2.2}$$

$$\text{Aging Index (Viscosity)} = \frac{\text{Viscosity of aged asphalt}}{\text{Viscosity of original asphalt}} \quad \text{Eq. 2.3}$$

2.1.3 Performance Grading System

In 1987, the Strategic Highway Research Program (SHRP) developed a new system for HMA characterization based on a pavement-temperature performance rather than an air-temperature performance. The final outcome from this SHRP effort resulted in what is known as Superpave® - *Superior Performance Asphalt Pavements*. The main reasons for developing Superpave® were to extend the pavement life, reduce the life-cycle costs, to reduce the maintenance costs, and to minimize premature failure (McGennis et al., 1994). With these ideas in mind, a new system of asphalt grading was also developed, as well as a detailed specification for mineral aggregates. The new system of asphalt selection is based on a temperature design to describe the viscoelastic and failure properties of asphalt binders which can more realistically relate to asphalt concrete properties and field performance (McGennis et al. 1995).

The new Superpave® grading system introduced a Performance Grading (PG) classification. This means that the asphalt binder is selected based on its performance in relation to temperature. The asphalt binder is selected based on maximum, minimum, and intermediate pavement design temperatures. This Performance Grade philosophy ensures that the selected binder will meet the performance requirements at the selected temperatures. The PG binders are defined by a term such as PG 58-28. The first number, 58, refers to the high-temperature grade which means that the binder is capable of physically performing at 58°C. This temperature is selected based on the seven-day average maximum pavement temperature. The second number,

-28, refers to the average seven-day low-temperature grade. This means that the binder possesses adequate physical properties in pavements down to at least -28°C. The intermediate temperature is the average of the maximum and minimum pavement design temperatures plus 4°C. When testing asphalt binders or mixtures, it is critical to conduct a thorough analysis at all three temperatures (McGennis et al., 1994).

2.1.4 Temperature Susceptibility

Asphalt cement is a material that undergoes extreme changes when temperature fluctuates. At low temperatures asphalt cement can be very elastic and brittle, at high temperatures it can be very fluid and viscous, and at intermediate temperatures it can be considered a viscoelastic material since it exhibits both elastic and viscous properties. Because of the variations in behavior (temperature dependent) asphalt cement is considered a thermoplastic material. Temperature susceptibility, therefore, is the rate at which the consistency of the asphalt binder changes with respect to the change in temperature. This temperature susceptibility demonstrates a linear inverse relationship between viscosity and temperature; as temperature increases, viscosity decreases. Since asphalt cement exhibits these extreme variations in material properties (with temperature), Superpave® methodology was developed to control high-temperature pavement rutting, intermediate-temperature fatigue, and low-temperature thermal cracking (Asphalt Institute, 2001, 2003; Roberts et al., 1996).

2.1.4.1 High-Temperature Behavior

At high temperatures, most asphalt cements act as a viscous, Newtonian material where the shear stress and shear strain are proportional. Viscosity is the material property that characterizes the resistance of liquids to flow. Therefore, for Newtonian fluids, the viscosity is independent of the shear rate. Also, at higher pavement temperatures, a high stiffness, which is

the relationship between stress and strain as a function of time of loading and temperature, is generally a desirable property because this allows for the pavement to resist rutting (Asphalt Institute, 2003; Finn, 1967; Kandhal et al., 1988; Kandhal, Sandvig, & Wenger, 1973).

2.1.4.2 Intermediate-Temperature Behavior

At intermediate temperatures, asphalt binders are considered a viscoelastic material because these demonstrate characteristics of both a viscous liquid and an elastic solid. For this reason, the response can be represented by a spring-dashpot model which is defined by the Burger's model (Figure 2.2). Forces that are exerted on the asphalt material cause the parallel reactions and also cause an immediate elastic response. Mostly all of this response is recoverable with time while some of the response is plastic and can't be recovered (Figure 2.2). The non-recoverable aspect can be related to repeated cyclic loading and unloading of the material and this can result in fatigue failure (Asphalt Institute, 2003).

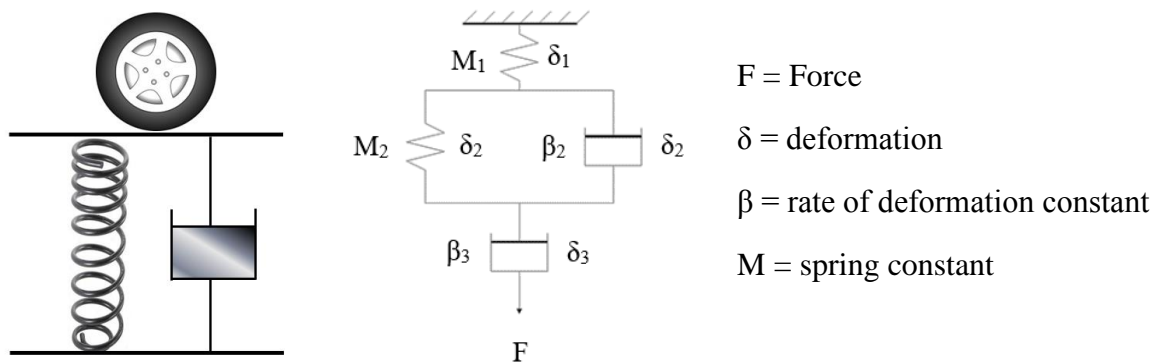


Figure 2.2: Spring-Dashpot Model of Viscoelastic Asphalt Behavior

2.1.4.3 Low-Temperature Behavior

At low temperatures, most asphalt cements act as an elastic material where the ratio of shear stress to shear strain is not proportional. At these lower temperatures the material behaves elastically like a rubber band in which it deforms under load but then returns to its

original shape once it is unloaded. Typically, at lower temperatures however, a low stiffness is generally desired because this allows the asphalt material to resist low-temperature cracking. If the material is stressed beyond the material capacity or strength, the brittle elastic solids can fracture and this results in thermal cracking (Asphalt Institute, 2003; Finn, 1967; Kandhal et al., 1988; Kandhal, Sandvig, & Wenger, 1973).

2.2 MINERAL AGGREGATES

2.2.1 Aggregates in Engineering Applications

Aggregate selection is critical in engineering applications. Determining the appropriate chemical and physical properties of aggregates is important for every construction project because these properties dictate the quality of the material. The characteristics of aggregates vary drastically, however, because most aggregates are produced in a quarry or gravel pit where there are significant differences between the aggregate sources. This makes it obvious that during any construction project the aggregates need to be monitored and tested so that they continuously meet the requirements of the mix design and the project. Specifications, especially in respect to grading requirements, need to be met to ensure the quality of the aggregates for every engineering project (Goetz & Wood, 1960; Meininger & Nichols, 1990).

During typical construction projects, such as subgrade developments or any paving applications, a large quantity of aggregates are used. Since there is a large amount of material quantity that is being consumed, there are high costs associated with these materials as well as availability concerns. Using locally available aggregates is very important, especially to control the transportation or delivery costs. Reducing the costs associated with transporting the aggregate from the quarry to the job site needs to be evaluated and this can be a challenge at

times. Pricing and availability are both criteria that are always evaluated during any project, but the main aggregate characteristics are what dictate the application of the material. These aggregates can be used as a base material, in portland cement or asphalt paving applications, or even in concrete building construction. Typically, in portland cement concrete, aggregates consist of approximately 79 to 85% by mass. In asphalt pavements, aggregates consist of about 92 to 96% of the total mass where the remaining percent is asphalt binder. Considering these large amounts of aggregates in these applications, it makes it clear that proper aggregate determination and proportioning is vital (Mamlouk & Zaniewski, 2006).

2.2.2 Physical Properties of Aggregates

Aggregates are used in asphalt applications because they act as a stone framework which is important in terms of material strength. Most aggregates that are selected for asphalt mixtures are typically from natural sources (sands, gravels, or crushed rocks). There are many different individual particle characteristics that are important when determining the type of aggregate to be used and when determining the aggregate application. The main importance of the aggregate in HMA applications is to provide both strength and stability. These properties are evaluated based on the particle shape, size texture, cleanliness, durability, toughness, and absorption (Mamlouk & Zaniewski, 2006; Roberts et al., 1996).

Aggregate size, shape, and texture are the key factors that dictate the packing density of HMA mixtures. These parameters determine how the particles will pack together into a dense configuration, and at the same time determine the movement of the aggregates in the mixture. In mixtures with small aggregates, the packing density is greater than those with large aggregates. Mid-size and small-size aggregates fill the void spaces between large aggregates which is why

an optimal combination of aggregates is necessary for HMA mixtures. For compacted HMA mixtures, angular-shaped and rough particles experience greater internal friction and interlock which means that there is greater stability and greater strength. Asphalt cement tends to form stronger mechanical bonds with angular-shaped and rough-textured particles which aids in higher overall strengths. The downfall with these types of particles is that they need larger amounts of added asphalt binder in order to increase the workability. On the other hand, round-shaped particles can be coated easier and also experience better workability which means that there is less compaction effort to obtain the appropriate density. Figure 2.3 illustrates the differences between round and angular-shaped aggregates. During construction, however, the ease of compaction is not sufficient as this can lead to rutting (Mamlouk & Zaniewski, 2006; Roberts et al., 1996).

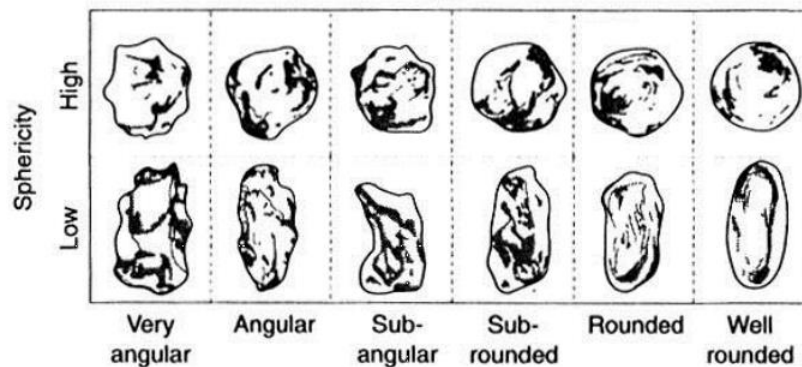


Figure 2.3: Visual Assessment of Particle Shape

Cleanliness is an important attribute when describing aggregates. Cleanliness is typically characterized by the absence of unwanted particles within aggregate mixtures. The more foreign materials in the HMA mixture, the more undesirable the mixture is. Some of the more typical unwanted materials are clay lumps, shale, wood, mica, vegetation, soft particles, and even

excess dust from the aggregate crushing operation. Different tests, such as the sand equivalent test and plasticity index, can be used to characterize the quantity of harmful materials.

Generally, there can be between 0.2 to 10 percent of deleterious particles in asphalt mixtures but the limiting value depends on the exact composition of the contaminant (Asphalt Institute, 2001; Roberts et al., 1996).

Durability is referred to as the ability for aggregates to resist weathering. Aggregates are exposed to extreme environmental conditions such as wetting, drying, freezing and thawing, and sulfate exposure. These aggregates need to be able to resist the disintegration after being exposed to these situations because strength is a big concern when dealing with HMA mixtures. Most of the aggregates are covered with asphalt binder which prevents moisture getting inside the particles. However, moisture absorption is a key factor that can lead to the deterioration, so it is important to control and reduce moisture intake. Not only is weathering a big concern but aging of the materials is also important. Over time, the aggregate particles experience large amounts of weathering, so it is critical to account for aggregate stability in order to provide a longer service life (Roberts et al., 1996).

Aggregate toughness is the ability to resist the damaging effects of loads. Through internal friction, aggregates must transmit, or transfer, the wheel loads from the vehicle traffic down to the underlying layers. These aggregates are exposed to crushing, degradation, and disintegration during the stockpiling procedure and must be tough to resist these processes. When mixed with asphalt binder, these aggregates also need to be tough to resist the HMA pavers, rollers, and heavy truck mechanical degradation throughout the life cycle of the material. External vehicle forces have a large effect on the aggregates in HMA mixtures so it is critical for

these materials to be able to resist such loads (Asphalt Institute, 2001; Mamlouk & Zaniewski, 2006; Roberts et al., 1996).

Absorption refers to ability for aggregates to capture and store water in the pores or surface voids. There are different moisture conditions of aggregates and these moisture conditions have a large effect on the aggregate properties. Aggregates can be completely dry (all pores empty), air dry (partially saturated but pores are partially filled), fully saturated surface dry (all pores full but no excess water), or wet (excess water), Figure 2.4. In HMA mixtures, the aggregate absorption is critical because with saturated aggregates the bitumen is unable to act as a binder. Aggregates with higher absorption capabilities are undesirable and uneconomical because of larger amounts of added asphalt cement in these mixtures to bind the aggregates together. However, there also needs to be some asphalt absorption because this allows for proper bonding between the aggregates and asphalt. Therefore, aggregates in asphalt mixtures should typically be low-absorbing aggregates (Domone & Illston, 2010; Mamlouk & Zaniewski, 2006).

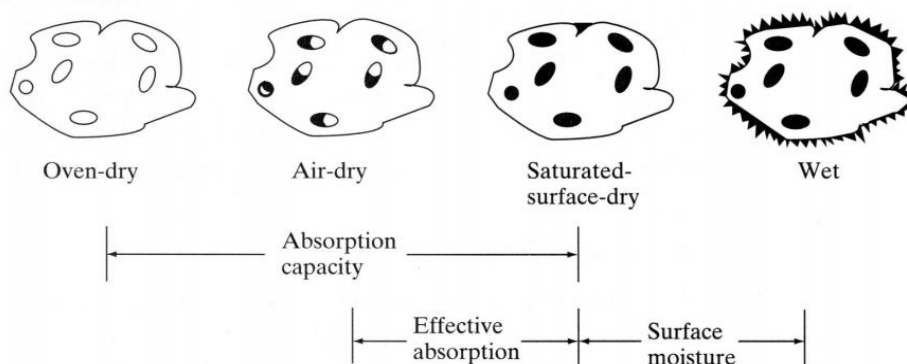


Figure 2.4: Moisture States of Aggregates

2.2.3 Aggregate Gradation

Gradation is referred to as the classification of aggregates based on different sizes. This classification scheme describes the particle size distribution of different aggregate blends. The

three main aggregate sizes that are used in asphalt mixture characterization are coarse, fine, and mineral filler materials. In HMA mixtures, large aggregates can be advantageous and more economical because they can provide a better packing orientation and also have less surface area which reduces the amount of binder to coat the aggregates. However, HMA mixtures with large aggregates tend to require more compaction effort which means that they are more difficult to work into place. Therefore, when evaluating the aggregate gradation, it is vital to also evaluate the construction considerations and equipment capabilities to ensure a proper design (Mamlouk & Zaniewski, 2006).

The American Society for Testing and Materials (ASTM) characterizes aggregates as coarse, fine, and mineral fillers. These particle sizes are categorized based on size requirements. Gradation is evaluated by passing the aggregates through different series of sieves and then assessing the aggregates that are either retained on or passed through the specific sieve size (ASTM C136). The sieve retains the aggregates that are larger than that defined by a sieve size, and at the same time passes the aggregates that are smaller than that of specific sieve size opening. According to ASTM, the No. 4 sieve size (4.75 mm) separates the coarse and fine aggregates. Anything above the No. 4 sieve size (4.75 mm) is considered gravel, boulders, or cobbles, whereas anything below the No. 4 sieve size (4.75 mm) is considered either sand or mineral fillers. Mineral fillers are classified as the portion of the fine aggregates that pass the No. 200 sieve (0.075 mm). Aggregate classification is very important when determining the aggregates that are intended to be used in HMA mixtures.

Particle size distributions are used to classify the aggregate mixtures. Different aggregate gradations that can be potentially used are gap-graded, continuously-graded, and uniformly-

graded (Figure 2.5). Gap-graded mixtures typically represent the aggregate blends that are missing one or more particle size fractions. Uniformly-graded mixtures are those that generally consist of one type of aggregate blend, therefore, these mixtures are composed of either small, medium, or large aggregates only. Lastly, continuously-graded aggregate blends have aggregates ranging from small to large in a consistent manner. Typically, continuous gradations produce the best densification arrangement of aggregates representing particulate systems because these gradations provide all aggregate types which results in relatively low compaction efforts. Using a gap-graded and uniformly-graded aggregate distribution can cause problems because the density and compaction requirements for asphalt mixtures can't be achieved.

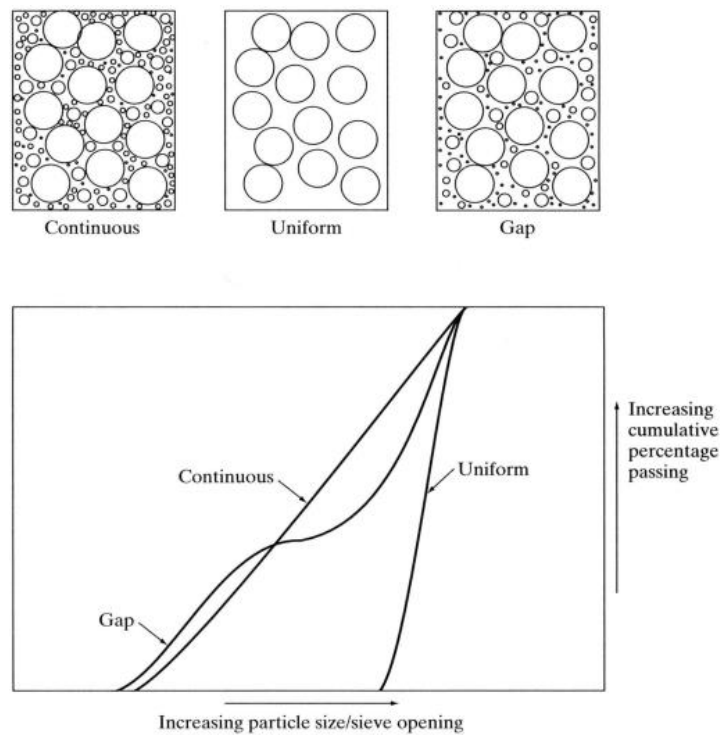


Figure 2.5: Aggregate Gradation Curves (Domone, P., & Illston, J., 2010)

Aggregate gradations in which the void space has a minimum (i.e. reaching a maximum packing density) are important and these blends are based on continuously-graded mixtures. These type of mixtures develop high strength due to excellent aggregate interlock. Superpave® has developed gradation requirements to ensure that aggregate mixtures meet the specifications. Superpave® uses a 0.45 Power Curve gradation which employs a graphical technique to show the cumulative particle size distribution of the aggregate blend. The vertical axis represents the percent passing of aggregates and the horizontal axis represents the sieve size. The most important feature of the 0.45 Power Curve is that this curve represents the maximum density gradation achieved by compaction methods (which are different from geometrical random packings). This curve represents a gradation in which the aggregate particles combine in their densest possible arrangement and this is important to develop interlock and strength in the aggregate mixture (Asphalt Institute, 2001).

2.3 SUPERPAVE® ASPHALT MASTICS

2.3.1 Mastic Behavior

When solid particles are distributed in a continuous matrix of different composition it is considered a dispersion. Different types of dispersed systems (Table 2.1) can be defined depending on the nature of the disperse phase and medium (Tadros, 2010).

Table 2.1: Types of Disperse Systems

Disperse Phase	Disperse Medium	Type
Solid	Liquid	Suspension
Liquid	Liquid	Emulsion
Liquid	Solid	Gel
Liquid	Gas	Aerosol
Gas	Liquid	Foam
Solid	Solid	Composite

Asphalt mastics are considered particulate composite materials where the asphalt binder is mixed with mineral filler particles. These filler particles are the dispersed phase within the matrix. Composite materials are made from two or more materials with significantly different physical or chemical properties, that when combined, produce a material with characteristics different from the individual components. In a complex multiphase system, such as asphalt mastics, it is necessary to control the rheology of the formulation during its preparation and during its application to maintain its long-term physical stability (Tadros, 2010). Rheology is the science that studies viscoelastic materials (i.e. the study of deformation and flow of matter).

The dimensions of the particles of the internal phase are of great importance. Depending on the dimensions of the particles, the systems can be identified as a colloidal systems or systems outside the colloidal range. In colloidal systems, particles sizes are within 1 nm to 1000 nm (1 μm). On the other hand, the system is considered outside of the colloidal range if the particles are larger than 1 μm . Fly ash sizes range between 10 and 100 μm , which makes the asphalt mastic a system that falls outside the colloidal range.

In both of these cases, colloidal range and outside the colloidal range, the property of the system is determined by the nature of the interface that separates the internal phase from the medium in which it is dispersed. The structure of the interfacial region determines the properties of the system, and in particular the tendency of the particles to form aggregate units or to remain as individual particles (Tadros, 2010).

Rigden (1947) studied filler characteristics that could be directly related to the characteristics of different filler-binder mixtures at low and high filler concentrations. By measuring the bulk volume of compacted dry samples and considering the asphalt filling the voids in the dry compacted bed as fixed asphalt, while the asphalt in excess of that fixed is

considered as free asphalt. In his research, Rigden called this concept the fractional voids concept and found that the value of the fractional volume voids in compacted dry filler, obtained by the test method developed by him and later modified by Anderson (1982), is most simply related to the filler-binder systems flow properties (viscosity) studied over a wide range of stress and at temperatures from 0°C to 45°C. Rigden used the conical viscometer and the constant load tensile test to study the viscosity of filler-binder systems at low and high concentrations, respectively and noticed that as the concentration of filler is increased, the viscosity increases rapidly until it reaches a maximum value in which measurement of viscosity becomes difficult. This maximum value occurs at a concentration of filler corresponding to the binder content, giving maximum resistance to deformation also known as the optimum binder content. After using the Rigden voids test on different fillers for which optimum binder content was known, Rigden showed that a simple relationship between the voids and optimum binder content exists that is independent of the type of filler. This leads to his most important finding, that the degree of packing of filler in a filler-binder system largely determines the flow properties of the system and that the chemical differences between various fillers are of lesser significance (Rigden, 1947).

Tunncliffe (1960) investigated the importance of size distribution, shape and surface texture results in the stiffening effect of asphalt mastics. He postulated that adding mineral fillers of the same size distribution, shape and surface texture but of different mineralogy or surface chemistry resulted in various stiffening effects. He theorized that this effect of mineral fillers on mastics and HMA could be very different because of a gradient of stiffening. He proposed that the gradient of stiffening effect is greatest at the surface and decreases with distance from the surface (Figure 2.6).

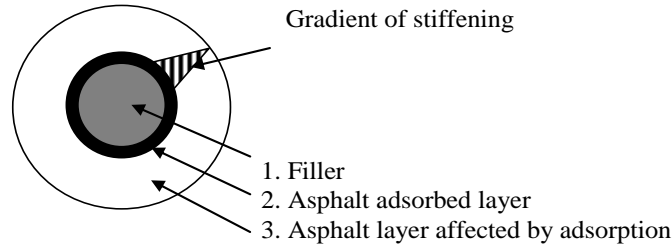


Figure 2.6: Schematic Showing the Hypothesis of Asphalt-Filler Interaction (Tunnicliff, 1960)

Faheem (2009) (based on Tunnicliff's (1960) theory) considered the fractional voids concept introduced by Rigden (1947) and proposed a conceptual model on the interaction of the fillers with the surrounding asphalt matrix that considers the asphalt mastics as particulate composite material. Figure 2.7 presents the increase of stiffness of the mastic due to the addition of mineral filler.

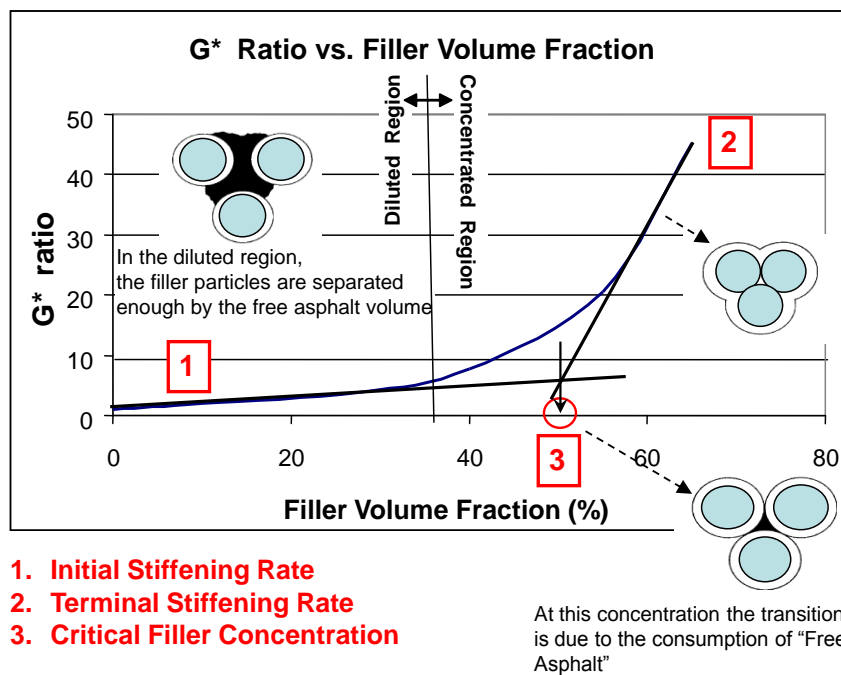


Figure 2.7: Conceptual Model Parameters of the Increase of Stiffness in Terms of Filler Influence

Two different regions can be clearly identified. On the left side of the plot of G^*_r vs. filler volume, the increase in the mastic stiffness is linear until a certain filler volume concentration. This region is called the diluted region. Within this region, the stiffness is highly dependent on the free asphalt content available that separates the filler particles. Faheem (2009) called the stiffening rate within the diluted region the Initial Stiffening Rate. The right side of the plot is identified as the concentrated region or jammed state, where the rate of increase becomes nonlinear and rapidly reaches an asymptotic linear trend. Faheem (2009) stated that as the volume of free asphalt starts to diminish toward the end of the diluted region, the stiffness of the mastic starts to increase rapidly, and he called this increase of stiffening rate the Terminal Stiffening Rate. Faheem (2009) also identified the Critical Filler Concentration as the transition between the diluted and concentrated regions.

2.3.2 Effect of Fillers on Asphalt Mastic Stiffness

The influence of fillers in asphalt binders has been the center of attention of researchers for many years starting from the early 1900's. Researchers found that the incorporation of filler particles, irrespective of their properties, increases the stiffness of the composite asphalt material. Richardson (1905) reported that the effect of fillers on stiffening asphalts varies depending on the geometric characteristics and the interaction with the asphalts. He theorized, based on experience of the time, that the study of the behavior of mineral aggregate surfaces and film thickness is the basis for the construction of a perfect asphalt. He also postulated that the more viscous the bitumen and the larger amount of filler that it contains, the thicker the film thickness, which translates to greater cementing power.

Heukelom and Wiga (1971) looked at the particle-particle interaction of the dispersion and differentiated two extreme cases. These two extreme cases are known as the flocculated

state, in which agglomeration of particles can occur, and the fully peptized state, in which the continuous phase separates all particles from one another. When the particles are in the flocculated state or not fully peptized, the particles can occupy a larger volume since they are agglomerated making the effective volume concentration larger, which results in a higher viscosity. This work resulted in developing a unique relationship to express the rheological characteristics of dispersions in terms of volume concentration and rate of shear. Their goal was to derive an equation that could be valid for dispersions (in general). This equation was based on their belief that the stiffness of the mastic at filler volume concentration approached infinity as this equation became equal to the maximum packing of the filler (Eq. 2.4).

$$\frac{1}{\sqrt{\eta_r}} = 1 - (1 + k)(1 + m,)C_v \quad \text{Eq. 2.4}$$

where:

η_r = relative viscosity;

k = shear rate factor;

m = peptization and shape factor;

C_v = volume concentration of the fillers.

This unique relationship uses two factors, one that takes into account the shape and state of peptization (1+m) and the other that takes into account the rate of shear (1+k).

Anderson and Goetz (1973) studied the mechanical behavior and reinforcement of asphalt-filler mixtures. The authors researched the stress-strain response of mastics and the potential for interaction between two mineral fillers and two asphalt binders. The mineral fillers that were used in this research were quartz and calcite, representing the range of materials between acidic and basic. These two mineral fillers were divided in three different ranges of sizes under the No. 200 sieve to study the interaction with different particle size of the fillers.

The two asphalt binders of this study were AC-20 viscosity grade but with different viscosities at 77°F (25°C), which indicated that one behaved as a Newtonian fluid and the other as a non-Newtonian fluid. Mineral fillers were added at a concentration of 40% by volume.

Anderson and Goetz applied sinusoidal and quasi-static shear stress to asphalt and asphalt-filler samples at three different temperatures and measured the resulting strains to characterize the dynamic and creep behavior. By comparing quasic-static, sinusoidal and viscosity results, the authors evaluated the potential for reinforcement of the mineral filler. They noticed that the viscosity of the Non-Newtonian behavior asphalt binder increased with decreasing particle size, which means that its behavior was dependent on particle size. On the other hand, the viscosity of asphalt binder with Newtonian behavior was independent of particle size. This indicates that the reinforcement potential of the mineral fillers is more pronounced for the non-Newtonian mixtures, which led the authors to suggest that the reinforcement might be due to the presence of some sort of physico-chemical interaction.

Anderson et al. (1983) studied the influence of baghouse fines on the design of asphalt mixtures. The authors determined the properties of seven baghouse dusts from typical plant operations and studied their effect on the design of asphalt concrete mixtures. The authors measured the penetration, viscosity at 275 and 140°F (135 and 60°C), and softening point of the asphalt-dust mixtures prepared with seven fillers at five filler-asphalt ratios. The penetration results indicated a decrease in the penetration with increased filler content. Viscosity and softening point increased with increased filler content. These results are a clear indication of the stiffening potential of fillers when added to asphalt binder. The authors also noticed that penetration, viscosity and softening point results are independent of filler size, which means that fineness alone is not a measure of the stiffening potential.

Faheem and Bahia (2008) studied the effect of mineral fillers on damage resistance of asphalt binders and mastics to permanent strain accumulation and fatigue. Two asphalt binders, PG58-28 and PG70-22, and two fillers of different mineralogy, limestone (basic) and granite (acidic) were mixed at 25% and 50% concentration by volume and tested on the DSR. The permanent strain was measured from creep and recovery test. Samples were loaded for 1 second at 100 Pa, followed by 9 seconds of rest period, and the accumulated permanent deformation at the end of 100 loading cycles was used to evaluate the rutting resistance of asphalt mastics. The test was conducted at 52°C, 58°C and 64°C. The fatigue test was conducted under repeated shear cyclic loading at 28°C, and the complex shear modulus (G^*) and phase angle (δ) were measured as a function of number of loading cycles. Fatigue resistance was characterized by the amount of loading cycles required for a 50% reduction of the complex shear modulus (G^*). The Superpave® fatigue factor, $G^* \sin \delta$, was also measured.

The results demonstrated that the presence of mineral fillers in asphalt significantly increased the complex shear modulus and fatigue life of asphalt mastics as compared with those of the asphalt binders. In terms of rutting resistance, it was found that the addition of fillers enhanced the resistance to rutting, in terms of total terminal strain and non-recoverable compliance. These effects were found to be highly independent of filler mineralogy. For the fatigue life, it was found that mastics cycles to failure were significantly larger than that of the asphalt binder with the limestone filler (basic) having more positive effects than the granite filler (acidic). This can be related to the mineralogical property of the filler. Faheem and Bahia (2008) also found that $G^* \sin(\delta)$ results increased consistently with the addition of fillers. However, the authors found that the $G^* \sin(\delta)$ appeared to not be sensitive to a filler type.

Faheem (2009) measured G^* ratio for fly ash and granite blends at different filler content. Figure 2.8 demonstrates the increase of the G^* ratio with the addition of fillers. The initial rate of increasing stiffness was comparable between the fillers. For the granite filler, around 35% by volume, the rate of stiffening started to increase rapidly until 50% by volume where no more filler could be added without introducing air voids. On the other hand, the transition of mastics with fly ash was more gradual.

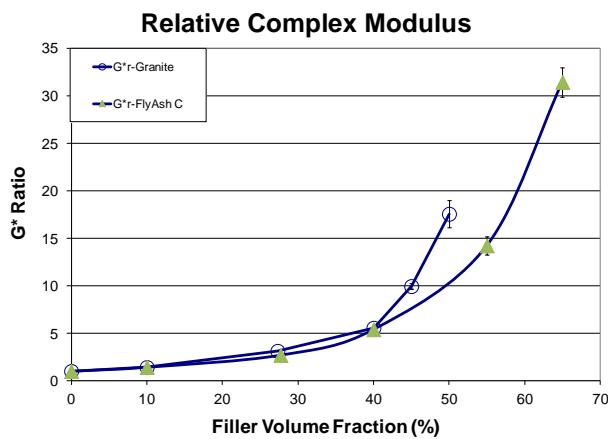


Figure 2.8: Progression of G^* Ratio with Respect to Filler Concentration

Faheem (2009) also investigated the mastic integrity at the same concentrations using the Tack test on the DSR. Figure 2.9 demonstrates that the maximum integrity of the mastic with granite was achieved at a 27% volume concentration, while for the fly ash mastics it was achieved at 45%. In general, at concentrations more than 10% by volume, fly ash mastics outperformed the granite filler mastics, indicating that fly ash enhanced the bonding strength and improved the tack factor when compared to the standard fillers used in the paving industry. It is important to note that this performance was duplicated when the same fillers were used with a different binder from a different crude source.

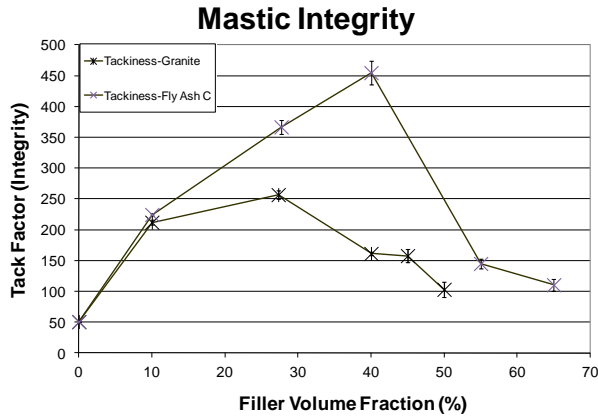


Figure 2.9: Tack Factor (Mastic Integrity) at Different Filler Concentrations

2.3.3 Effect of Fillers on Asphalt Mastic Aging Resistance

Miró et al. (2005) studied the effects of fillers on the aging of bitumen. The purpose of adding the fillers by volume in this research study (and not by weight) was to avoid ignoring the filling effect of the fillers. The researchers added two types of fillers, hydrated lime and calcium carbonate, to an 80 to 100 pen bitumen and prepared a mixture with granite aggregate. Asphalt mixtures were made with Marshall molds, aged in an oven at 80°C for 0, 2, 4 and 7 days, and then tested using the Barcelona Traccion Directa (BTD) test at 20°C and a standard deformation rate of 1 mm/min. After the hydrated lime specimens were tested on the BTD, the bitumen was extracted by the centrifuge method to assess the effect of this filler on the aging of the bitumen.

Miró et al. (2005) analyzed the penetration, softening point and dynamic viscosity of the recovered bitumen was analyzed at 135°C and observed that the addition of hydrated lime filler produced a slight decrease in the penetration and a slight increase in the softening point and dynamic viscosity. According to the researchers, these results indicated that the greater amount of filler used resulted in lower age hardening of the bitumen material.

Huang and Zheng (2007) studied the effect of filler surface on the rheological properties focusing on the long-term aging characteristics by measuring the rheological properties of unaged and aged asphalt-filler systems as a function of aging time. Two different types of fillers, limestone and granite, and two asphalt binders from different sources classified under the Superpave® binder testing protocol as PG58-28 and PG58-10 were used in this study. Asphalt-filler mixes were prepared by mixing 20% of filler (by the weight) of asphalt and aged in the Pressure Aging Vessel (PAV) at 60°C for 100, 400, 800 and 2000 hours. A frequency sweep test was conducted on the aged materials on a Dynamic Shear Rheometer at 25°C and 60°C using 8 and 25 mm plates.

The researchers reported that the properties of the asphalt binder were dependent on the duration of aging time, a phenomenon that can be considered similar to the temperature dependency of asphalt binder in terms of rheological properties. This means that as the aging time increased, the complex modulus increased and the phase angle decreased at a given frequency as shown in Figure 2.10.

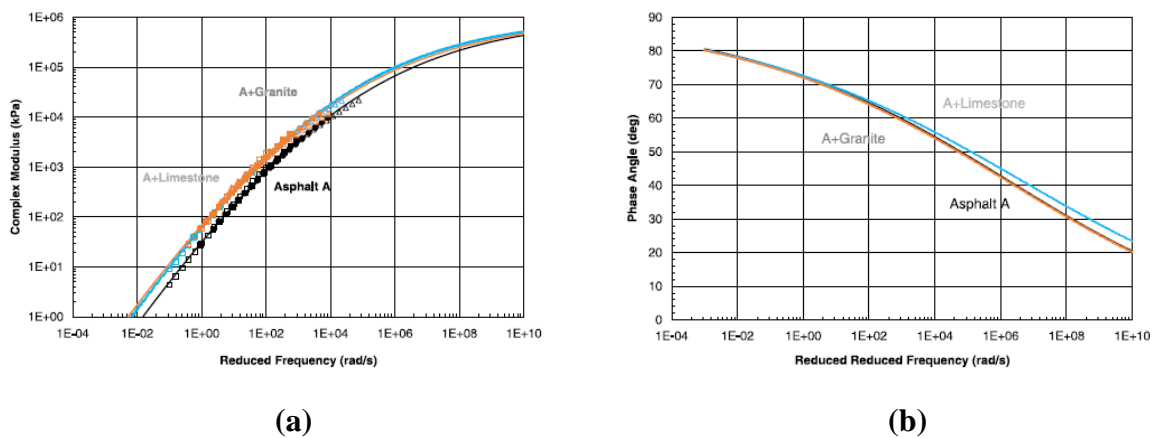


Figure 2.10: Aging Master Curves for (a) Complex Modulus and (b) Phase Angle

Wu and Airey (2011) investigated the influence of two fillers of different mineralogy, limestone (basic) and gritstone (acidic), on the aging properties of mastics and recovered binders. They used the DSR and Fourier Transform Infrared Spectroscopy (FTIR) tests to measure the asphalt mastic and binder properties at different stages of the Thin Film Oven Test (TFOT).

The authors found that the acidic and basic fillers affect bitumen aging in different ways due to their mineral structures, with the basic limestone filler possessing stronger adsorption capabilities than the acidic gritstone filler. It was concluded that the aging properties of mastics were highly mineral dependent and that the mineral filler could influence the aging properties through catalyzing the oxidation of bitumen components by absorbing oily components and adsorbing polar fractions.

2.4 SUPERPAVE® ASPHALT MIXTURES

2.4.1 Mixture Behavior

Asphalt pavements cover nearly 93% of the 2 million miles of paved roads in the United States. Asphalt mixtures consist primarily of asphalt binder and aggregates. These ingredients are mixed together at high temperatures and compacted while the material is still hot. The asphalt binder acts as a binding material that holds the aggregate particles together. The asphalt mixture glues the aggregate particles into a dense configuration and provides excellent waterproofing abilities. When the aggregates are combined with the asphalt binder, the aggregates act as a stone framework which provides strength and toughness to the structure. The overall asphalt concrete performance depends entirely on the pavement design which includes the types of aggregates used as well as the type of asphalt binder that is selected.

The objective of asphalt concrete is to provide the following properties (Roberts, 1996):

- Workability to reduce the effort of mixing, placing, and compacting;
- Resistance to hardening or aging;
- Stability and resistance to permanent deformation under traffic loads;
- Fatigue resistance to prevent fatigue cracking under cyclic (repeated) loads;
- Thermal-cracking resistance that can occur due to the contraction of the material;
- Resistance to moisture damage that can result from stripping of asphalt.

When wheel loads are applied to the pavement, the main stresses that act on the HMA pavement are vertical compressive stress and shear stress within the asphalt layer, as well as horizontal tensile stresses at the bottom of the asphalt layer. This means that the HMA material must be internally strong to resist the compressive and shear stresses to prevent the permanent deformation. The material must also be strong in tension to withstand the stresses at the bottom of the asphalt layer as well as resisting cracking and fatigue failures. For cold climates, the material must also be able to resist freeze-thaw cycles which means that the HMA pavement needs to resist rapid decreasing and increasing temperatures. The individual components of HMA are important, but mixtures of HMA need to be analyzed to ensure that both the asphalt binder and the mineral aggregates act together (Asphalt Institute, 2001).

2.4.2 Asphalt Workability

The HMA mixtures are generally hot (115°C-165°C) during the production process which means that the overall viscosity is significantly lower than when the material is at normal (operating) temperatures. When the asphalt binder is mixed with aggregates, the mixture will only be compactable when the asphalt viscosity is within an optimum range. Being able to handle the material is critical during the construction process. The material needs to be capable

of mixing, placing, and compacting without excessive compaction effort. In HMA asphalts, the amount of entrapped air in the material is a critical part of evaluating the performance of the material. The optimum asphalt content has been defined by Superpave® as the asphalt content that produces 4 percent air voids at the final design. In general, the target air void content is 8 percent which represents the density of the material at the completion of the construction of the asphalt layer. After the construction process, vehicle traffic generally continues to compact the material to some ultimate degree. Therefore, in terms of workability, it is critical to develop asphalt mixtures that are easy to mix, place, and compact, but at the same time can achieve appropriate values of air content over the service life (Roberts et al., 1996).

2.4.3 Age-Hardening Resistance

As previously mentioned, age-hardening resistance is a key factor when determining the quality of an HMA mixture. The asphalt material needs to be able to resist the effects of age-hardening which can be correlated to a longer service life. When evaluating the aging of an HMA material it is important to evaluate the mixture by examining both the asphalt binder, and the mineral aggregates acting together, since this is a more realistic approach to pavement analysis and design. The aggregates are capable of deteriorating throughout the production process, as well as during the life cycle of the HMA pavement. The asphalt binder also evolves during the service life by hardening due to oxidation. This process makes the material stiff and brittle, especially at low temperatures, so this results in crack formation and propagation. The hardening of the material also results in penetration reduction and an increase in the softening point. Reducing the rate at which the asphalt pavement ages also prevents unnecessary repair costs associated with cracking (Domone & Illston, 2010; Roberts et al., 1996).

2.4.4 High-Temperature Permanent Deformation (Rutting)

Rutting in HMA refers to the progressive movements of material under repeated loads which can occur from consolidation or through plastic flow. Rutting results from permanent distortion of the material due to wheel track loading, which is the most common form of permanent deformation. Permanent deformation is described by a surface cross section that is no longer in its original position or location. It is referred to as permanent deformation because this is an accumulation of small amounts of unrecoverable deformation that occur each time a load is applied (Roberts et al., 1996). Figure 2.11 (Asphalt Institute, 2001) and Figure 2.12 provide a visual representations of the effects of rutting due to wheel track loading.

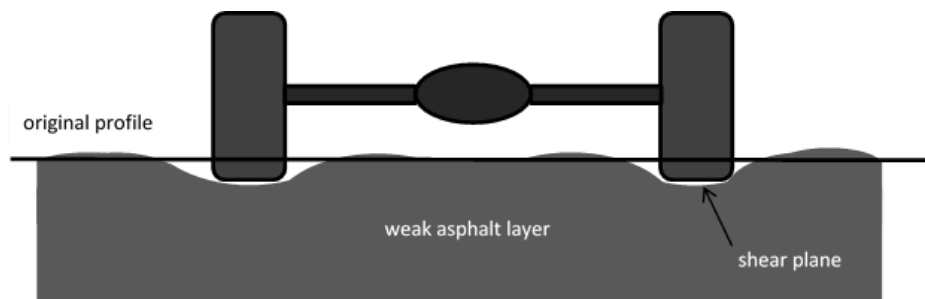


Figure 2.11: Rutting Characteristic of Asphalt Pavement due to Vehicle Loads

Generally, the deformation of the asphalt pavement is the type of rutting that is a major concern in mix design. Rutting in the HMA layer results from an asphalt mixture with low shear strength required to resist the applied traffic loads. This response can be caused by using high amounts of added asphalt binder as well as poor compaction of the mixture. Using excessive amounts of asphalt binder in a mixture causes the loss of the internal friction between the aggregate particles, and this allows the particles to move more freely. By not compacting the HMA mixture properly, this allows for more air voids to deform during the continuous traffic loads. At this point, the wheel loads are then carried by the asphalt binder rather than the strong

aggregate framework. This results in small amounts of permanent deformations that forms a rut characterized by a downward and lateral movement of the pavement (Asphalt Institute, 2001; Roberts et al., 1996).



Figure 2.12: Rutting Damage Caused by Traffic Loads

In HMA pavement analysis, it is always critical to develop asphalt mixtures that reduce the ability to deform in terms of rutting. Mixtures should not deform when exposed to traffic loading. Rutting can be reduced by using larger aggregate sizes, and more angular and rough texture aggregates to increase particle friction. Stiffer asphalt binders can also be used to resist rutting at higher temperatures. At higher temperatures, when the material becomes less viscous, the resistance to permanent deformation becomes difficult. At this point, the primary strength is provided by the aggregate structure which means that the stone framework needs to be strong. Therefore, selecting appropriate aggregates (types and grades) is vital to the overall strength when it comes to rutting resistance. Binder selection is also important because stiffer asphalt binders can resist permanent deformations (Asphalt Institute, 2001; Roberts et al., 1996).

2.4.5 Intermediate-Temperature Fatigue Cracking

Fatigue cracking refers to failure due to repeated loads at intermediate temperatures. Under repeated cyclic loading, the asphalt pavement fractures under a fluctuating stress which

is less than the maximum tensile strength of the material. Fatigue cracking occurs when the applied traffic loads overstress the asphalt material and then cracks form as a result. This damage associated with permanent deformation is typically due to shear distortion or volumetric changes (Perng, 1989). Intermediate longitudinal cracks in the wheel path are typically good indicators that fatigue cracking has occurred. Eventually, these cracks combine, forming alligator cracking, which weakens larger sections of the pavement (Finn, Nair, & Hilliard, 1978). Figure 2.13 illustrates how fatigue cracking has propagated through a large asphalt pavement section.



Figure 2.13: Asphalt Fatigue (Alligator) Cracking

Fatigue cracking can be caused by a number of reasons and different factors depending on the conditions. Some of the factors that can affect fatigue cracking are the asphalt content, air void content, aggregate characteristics, temperature, and traffic loading (Hartman, Gilchrist, & Walsh, 2001). Asphalt cements that become hard during the aging process also develop poor fatigue characteristics because these materials become brittle due to the excessive age-hardening. Thin pavement sections and pavement sections with weak underlying layers are vulnerable to fatigue cracking as well since these are exposed to higher deflections under heavy

loads. These high deflections cause horizontal stresses at the bottom of the asphalt layer and this can result in fatigue-type failures (Shu, Huang, and Vukosavljevic, 2007).

Typically, fatigue cracking means that the asphalt pavement has sustained the designed amount of traffic loads, and this means the HMA section needs repair which is common. The HMA mixtures should not crack when subjected to repeated, cyclic-type, loads over a long period of time but it is inevitable to prevent cracking forever. Fatigue cracking at the end of the pavement service life is expected, but fatigue cracking before the end of the pavement life means that the traffic loads were underestimated in the pavement design. In order to prevent fatigue cracking, designers should extensively evaluate the loading patterns during the design phase, use thicker pavements, keep the subsurface dry, use pavement materials not excessively weakened by moisture, and use HMA that is resilient enough to withstand normal deflections. In order to overcome fatigue cracking, the HMA should act as a soft elastic material when loaded and unloaded in tension (Asphalt Institute, 2001).

2.4.6 Low-Temperature Thermal Cracking

A big concern to asphalt pavement designers is low-temperature thermal cracking. Thermal cracking is especially important to evaluate in climates with cold temperatures because these are non-load associated cracks. Thermal cracks are intermittent transverse cracks that are formed when the asphalt material shrinks or contracts due to low temperatures. The tensile stresses within the layer exceed the tensile strength of the material and then the asphalt layer cracks. These thermal cracks can form from a single-cycle of low temperatures or can develop from repeated freezing and thawing cycles (Kandhal, 1978). Figure 2.14 demonstrates the intermittent transverse cracks that were developed from low-temperature cycles.



Figure 2.14: Low-Temperature Thermal Cracking

When performing an evaluation on low-temperature conditions, proper asphalt binder selection is the best way to resist thermal cracking. Researchers have recommended that limiting asphalt binder stiffness values in HMA mixtures will reduce the effects of thermal cracking (Fromm & Phang, 1971; Gaw, 1977; Kandhal, 1978, 1980). Asphalt binders that are harder tend to perform worse in low-temperature. Asphalt binders that are excessively aged also have poor performance at lower temperatures because these materials have developed age-hardening due to excessive oxidation. Therefore, mixtures should be designed with soft asphalt binders that are resistant to aging to minimize effects of low-temperature thermal cracking (Roberts et al., 1996).

2.4.7 Moisture Susceptibility

When exposed to moisture, some HMA mixtures lose the adhesion between the asphalt binder and the surface of the aggregate particles. Asphalt mixtures with high permeability tend to allow excessive air and water into the material. Once the water is within the asphalt pavement, it can deteriorate the structure by destroying the contact zone with asphalt binder,

aggregate particles, or both. Once the materials deteriorate, the bonding between the aggregate and the binder is compromised and the pavement starts to fail. After the bituminous material has been stripped from the aggregates, the overall strength is reduced, and this strength loss can lead to rapid distresses. In some cases, the asphalt binder can be stripped off the aggregate completely so that the only thing that remains is the bare aggregate particle. In most common cases, however, the strength progressively reduces over time and this strength reduction can lead to rutting and cracking in the wheel path (Domone & Illston, 2010; Mamlouk & Zaniewski, 2006).

There have been many different methods to reduce the moisture damage in asphalt pavements. Some of these methods include increasing the asphalt content, altering the aggregate gradation to reduce the void volumes, using clean aggregates, and also using asphalt cement with higher viscosity (Doyle, 1958; Mamlouk & Zaniewski, 2006). Increasing the asphalt content and altering the aggregate gradation can both reduce the void volume while providing more bituminous material that can bond to the aggregate particles. Additionally, cleaning the aggregates allows for better binding and higher viscosity asphalt resists the urge to strip from the aggregates. Moisture susceptibility is a significant variable when evaluating the overall life expectancy of the asphalt material and it is also essential in HMA design analysis.

2.5 COAL COMBUSTION PRODUCTS (CCPs)

2.5.1 Coal Combustion Products

Fly ash materials, or coal combustion products (CCPs) are the most commonly used pozzolans in civil engineering applications. Fly ash is a by-product of the coal combustion process. Carbon and most volatile materials are burned off by burning pulverized coal in electric power plants, however a significant amount of residual components pass through the

combustion chamber such as aluminosilicates, feldspar, and quartz, and. Upon coal combustion, these minerals fuse, and then the exhaust gases carry the fused materials (fly ash) out of the chamber. The fly ash material then cools down forming spherically shaped particles which can be either hollow or solid. Fly ash typically accounts for about 75 to 85% of the total coal ash, however the remainder of the material is collected as boiler slag or bottom ash. Fly ash can differ depending on the type of mineralogical composition of the coal, degree of coal pulverization, type of furnace and oxidation conditions, and the way the fly ash is collected and handled (Mamlouk & Zaniewski, 2017; Siddique & Iqbal Khan, 2011).

2.5.2 Chemical and Physical Properties

Fly ash particles have a diameter that ranges from 0.1 mm to 1 μm (70 to 90% of fly ash has a diameter less than 45 μm). Fly ash is a unique material in that the material particles are spherical in shape. The small spherical particles can improve the workability and reduce the porosity when mixed with other materials. Fly ash is primarily composed of silica (SiO_2), alumina (Al_2O_3), iron oxide (Fe_2O_3), and lime (CaO). There are different types of fly ash that are readily available. Class F fly ash is defined by ASTM C618 as a fly ash with pozzolan properties. Class C fly ash is defined as fly ash with pozzolan and cementitious properties. Class F fly ash typically has less than 5% CaO but sometimes has up to 10%. Class C fly ash has CaO contents ranging from 15 to 30% CaO (Mamlouk & Zaniewski, 2017).

2.5.2 Spray Dryer Absorber (SDA)

Spray Dryer Absorber (SDA) materials are byproducts of flue gas desulfurization (FGD) air quality control systems often referred to as SDA scrubbers or SDA ash. SDA scrubber systems typically use aqueous calcium or sodium-based reagents as sorbents to reduce the sulfur dioxide (SO_2) emissions from the flue gasses at coal-fired power plants. Depending on where

the sorbents are injected in the process, the SDA system byproducts may be removed from the flue gas and captured with the coal fly ash or downstream of the main fly ash removal device. Slaked lime slurries are incorporated into this process by being sprayed into the flue gas, dried, and then collected. The SDA materials can be collected with fly ash, or these materials can be combined with both fly ash and the lime particulate (EPRI 2007).

2.5.3 Using Spray Dryer Absorber Products

According to the American Coal Ash Association (ACAA 2017) 111.4 million tons of Coal Combustion Products (CCP) are being produced but only 64.44% are currently being utilized in different applications. The remaining 35.56% goes to landfills. Moreover, only 0.92% of the CCPs used are being used as mineral filler in asphalt cement. The utilization is mostly focused on Class C fly ash while high carbon CCPs, such as Spray Dryer Absorbers (SDA), remain vastly underutilized. Out of approximately 2.5 million tons of SDA produced only 15.56% are currently being use in applications in mining and the oil/gas field services industries. This leaves 84.44% of the material to be disposed in landfills. This trend proves that new markets and innovative uses of CCPs, especially SDA materials, are needed to enhance the utilization of a waste material that otherwise will be stored in landfills.

2.5.4 Effect of Coal Combustion Products (CCPs) in Asphalt Mixtures

In the past, mineral fillers have been added to asphalt mixtures were found to improve certain characteristics of the mix. Mineral fillers are defined by ASTM as finely divided mineral matter such as rock dust, slag dust, hydrated lime, hydraulic cement, fly ash, or other suitable mineral matter. In more recent years, CCPs, such as fly ash, was suggested as a mineral filler in asphalt mixtures. Fly ash was used in asphalt mixtures to reduce the asphalt content, increase

stability, and improve bond strength between the asphalt binder and the aggregates (Brown, McRae, & Crawley, 1989). In other studies, fly ash was added to HMA mixtures to extend the material service life due to enhanced moisture resistance, rutting resistance, fatigue resistance, low-temperature thermal cracking resistance, aging resistance, and workability (Anderson, Brock & Tarris, 1982).

Adding fly ash to asphalt mixtures has been found to enhance moisture resistance. Resisting moisture damage is critical for asphalt as pavement retains strength when the voids are penetrated with water. In terms of moisture resistance, Carpenter (1952) found that by specimens with Class F fly ash retained great compressive strengths when immersed in water. Zimmer (1970) found that adding fly ash had resulted in improved strength when the specimens were immersed in water. Henning (1974) investigated these effects by using Class C fly ash in asphalt concrete. Adding 4% of fly ash resulted in higher stability and flow, lower air voids, and improved stability after being immersed in water. Howell, Hudson, and Warden (1952) also found that fly ash was a great filling material in terms of mixing, compacting, material stability, and resistance to water damage.

Galloway (1980) studied the addition of lignite fly ash and indicated that fly ash as mineral filler retards the rate of age hardening of asphalt cement. Furthermore, Rosner et al. (1982) used two fly ashes (Class C and Class F) as a mineral filler and an anti-stripping agent for asphalt concrete mixtures to resist moisture damage in pavements. The asphalt concrete samples were tested against moisture damage by determining the indirect tensile strength of dry and moisture-conditioned specimens following AASHTO T-165. The conditioned specimens were immersed in a warm water bath at 140°F (60°C) for one day. The retained strength refers to the value calculated for the conditioned specimens compared with the dry specimens. Rosner

et al. determined that the retained strength of the samples increased as additional fly ash was used in the prepared mixtures. In most cases, the retained strengths of fly ash mixtures were considerably greater than those using other filler materials.

Researchers have also found that adding fly ash to asphalt has improved the strength. Suheibani (1986) evaluated fly ash as an asphalt extender by using indirect tensile strength, creep and resilient modulus tests. An asphalt extender is a material that can replace asphalt and thus saves asphalt binder. It was found that adding Class F fly ash had improved fatigue life, rut depth resistance, and tensile strength. Goetz, Razi, and Tons (1983) had also evaluated the use of Class F fly ash as an asphalt extender. A full evaluation was developed on moisture damage, thermal cracking, rutting, fatigue life, and asphalt hardening in mixtures. The results of the experiment demonstrated improvements in reduced asphalt hardening, improved moisture and freeze-thaw damage resistance, rutting resistance, increased fatigue life, higher density, and higher tensile strength.

Cabrera and Zoorob (1994) established that, based on a workability index at various temperatures, the fly ash based hot-mixed asphalt could be mixed at temperature as low as 120°C compared with 160°C for the conventional control mix. Fly ash mixes were compacted at temperatures from 85°C to 110°C without any detrimental effects on engineering and performance properties. It is important to note that the conventional mix required a compaction temperature range of 132°C to 135°C. The authors reported considerable energy savings through placement of asphalt mixtures with fly ash at lower temperatures compared with conventional mixes.

Bautista et al. (2015) studied the effects of Coal Combustion Products (CCPs) in asphalt mastics (mixture of asphalt binder and filler materials). The study evaluated different dosages

(5, 10, 15, 25, and 40% by volume) of Class C, Class F, and SDA (Spray Dryer Absorber) materials in different Performance Graded asphalt binders. These CCP mastics were then referenced with mastics composed of a limestone filler. Mastics were tested for shear using DSR (Dynamic Shear Rheometer), viscosity using Rotational Viscometer, aging resistance, rutting resistance using MSCR (Multiple Stress Creep and Recovery), fatigue resistance using DSR, and thermal-cracking resistance using BBR (Bending Beam Rheometer). The experimental results demonstrated, for all Performance Grades, that many of the mastics performed better than the reference limestone filler. It was demonstrated that adding CCPs to asphalt mastics, especially at larger dosages, enhanced properties such as workability, rutting resistance, recovery, aging resistance, and low-temperature resistance.

2.6 PORTLAND CEMENT

2.6.1 Portland Cement Products

Portland cement is the most widely used construction material that is manufactured in the world. Portland cement was first patented by Joseph Aspdin in 1824 in England and was named after the limestone cliffs on the Isle of Portland. This product was then first produced in Coplay, Pennsylvania in 1871 and was then utilized as a commercial product. This material has been used in structures such as bridges, buildings, tunnels, dams, and pavements (Mamlouk & Zaniewski, 2017).

2.6.2 Chemical and Physical Properties

The production of portland cement begins by reducing the size of stone from a 125 mm size down to a 20 mm size and then stored. The primary components of raw materials are calcium oxide (from limestone, chalk, and oyster shell) and a combination of silica and alumina (from clay, shale and blast furnace slag). The raw materials must contain appropriate amounts of

calcium, silica, alumina, and iron components. Raw materials are ground to powder and blended. The raw mixture then converts to cement clinker in a kiln at 1400 – 1650°C. Clinker with gypsum is then ground into portland cement and shipped. A small amount of gypsum is added to regulate the setting time of the cement and to improve shrinkage and strength development properties. Clinker is ground so fine that nearly all of it passes through a 45 µm sieve with an average around 15 µm (Figure 2.15).

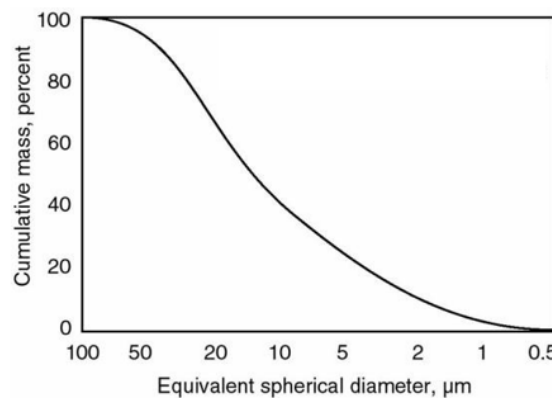


Figure 2.15: Typical Particle Size Distribution Curve for Portland Cement

The raw materials used in the production of portland cement (lime, silica, alumina, and iron oxide) form complex chemical compounds by means of calcination. During the calcination process (that takes place in the kiln), the main constituents develop four main compounds which are described in Table 2.2 (Mamlouk & Zaniewski, 2017).

Table 2.2: Main Compounds of Portland Cement

Compound	Chemical Formula	Common Formula	Usual Range by Weight (%)
Tricalcium Silicate	3 CaO·SiO ₂	C ₃ S	45 - 60
Dicalcium Silicate	2 CaO·SiO ₂	C ₂ S	15 - 30
Tricalcium Aluminate	3 CaO·Al ₂ O ₃	C ₃ A	6 - 12
Tetracalcium Aluminoferrite	4 CaO·Al ₂ O ₃ ·Fe ₂ O ₃	C ₄ AF	6 - 8

C₃S and C₂S, when hydrated, provide the desired concrete properties, however, C₃A and C₄AF are used to reduce the temperature required to produce C₃S and C₂S. C₃A hydrates rapidly, which significantly limits the workability of the cement products; hence, gypsum is added to retard this reaction for the first 24 hours of hydration.

Portland cements are composed of hydraulic cement particles that set and harden through a chemical reaction with water called hydration (Figure 2.16). During this reaction, a node forms on the surface of each cement particle and the node grows and expands until it links up with nodes from other cement particles. This hydration process is broken up into a through-solution process and a topochemical process. The through-solution process dominates the early stages of hydration, whereas the topochemical process is a solid-state chemical reaction occurring at the surface of the cement particles (Mamlouk & Zaniewski, 2017).

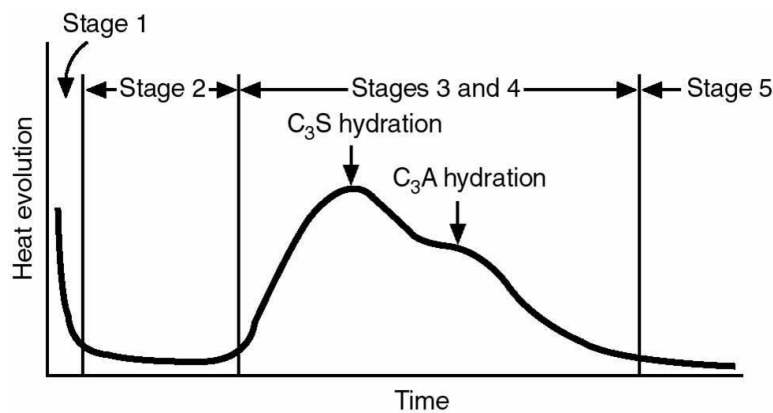
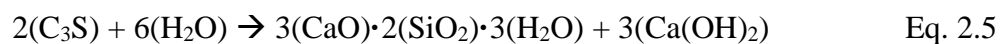


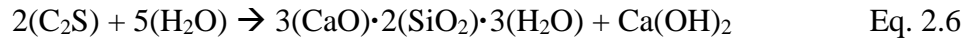
Figure 2.16: Hydration Process of Portland Cement

Tricalcium silicate (C₃S) compounds set within a few hours and are responsible for high early strength (7-days). The reaction gives out a large quantity of heat.



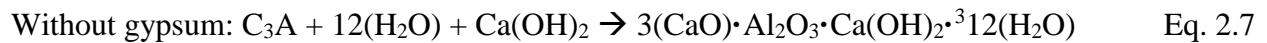
Tricalcium Silicate + Water = Calcium Silicate Hydrates + Calcium Hydroxide

Dicalcium silicate (C₂S) reacts very slowly with water and the heat of hydration is low. It does not produce strength until 28 days, but its final strength can be similar to C₃S.

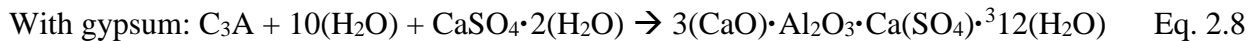


Dicalcium Silicate + Water = Calcium Silicate Hydrates + Calcium Hydroxide

Tricalcium aluminate (C₃A) without gypsum reacts with water rapidly causing flash setting which does not exhibit any strength.

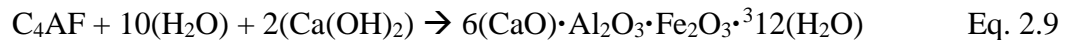


Tricalcium Aluminate + Water + Calcium Hydroxide = Calcium Aluminate Hydrate



Tricalcium Aluminate + Water + Gypsum = Calcium Monosulfoaluminate Hydrate

Tetracalcium aluminoferrite (C₄AF) has a similar reaction as C₃A but at a slower rate. The slow process results in progressive stiffening, hardening, and strength development.



Tetracalcium Aluminoferrite + Water + Calcium Hydroxide = Calcium Aluminoferrite Hydrate

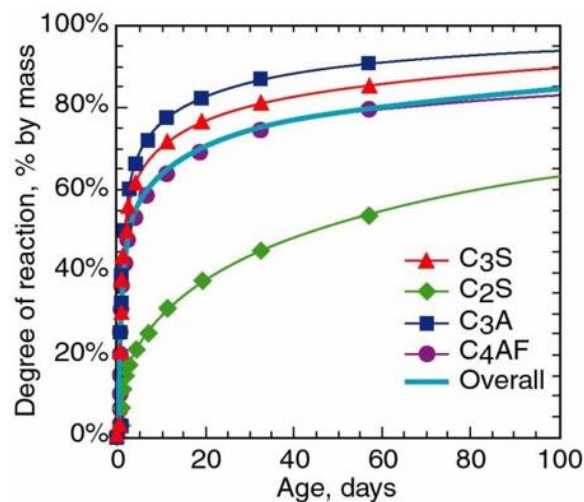


Figure 2.17: Degree of Reaction of Portland Cement Compounds During Hydration

2.6.3 Effect of Portland Cement Products in Asphalt Mixtures

Portland cement has not been widely utilized in asphalt concrete. Furthermore, portland cement has not been evaluated as a self-healing material when blended with an asphalt binder. The addition of portland cement in asphalt concrete is a rather new development in the construction industry and has been typically added to the asphalt matrix to work as a filler material rather than for self-healing potential.

Al-Qadi, Gouru, and Weyers (1994) investigated the use of an asphalt concrete composite with high air void contents (25-30%) filled with resin-modified cement grout. In this research project the resin-modified cement grout consisted of portland cement, fly ash, sand, water, and chemical admixture and these mixtures were considered asphalt-portland cement concrete composite (APCCC). Since the added cement grout consisted of hydrated portland cement the pavement evaluated a hybrid material that possessed flexibility and rigidity. These specimens were then compared to standard Hot Mix Asphalt (HMA) samples and also standard portland cement samples. The testing protocol for this research study included stability, indirect tensile strength, compressive strength, resilient modulus, water sensitivity, freezing and thawing, and chloride intrusion resistance. The samples experienced three different curing conditions: no moist curing, one-day moist curing, and three-day moist curing. This study concluded that the durability properties were enhanced for the APCCC mixtures when compared to the standard HMA samples. The chloride intrusion into APCCC specimens were also less than the standard portland cement concrete.

Al-Khateeb and Al-Akhras (2011) evaluated properties of portland cement in a PG64-10 asphalt binder using the standard Superpave® testing protocol with the Dynamic

Shear Rheometer (DSR). This study investigated different cement-to-asphalt (C/A) ratios (0.05, 0.10, 0.15, 0.20, 0.25, and 0.30) by volume of asphalt binder. The results proved that the use of portland cement increased the viscosity and the rutting parameter $G^*/\sin(\delta)$. The C/A of 0.15 was determined to provide the optimum balance increase in the rotational viscosity and $G^*/\sin(\delta)$. The C/A had insignificant effects on the Newtonian behavior and the elastic behavior of the asphalt mastics.

El-Maaty Behiry (2013) studied the effects of hydrated lime and portland cement on moisture damage resistance in asphalt mixtures. The mixtures were compacted to an average air void content of 1.5, 4, and 6%. The conditioned specimens were then exposed to tap water and sea water for conditioning periods of 1, 3, 7, and 14 days. From the testing, it was determined that both the lime and portland cement modified asphalt mixtures increased Marshall stability, resilient modulus, tensile strength, and resistance to moisture damage. The use of hydrated lime demonstrated better results than the portland cement mixtures.

Likitlersuang and Chompoorat (2016) researched the effects of cement and fly ash modified asphalt concrete mixtures. In this research study asphalt mixtures consisted on AC60/70 asphalt binder and incorporated portland cement and fly ash class C as fillers at different contents and mixed with limestone. The mixtures were then tested for indirect tensile strength, resilient modulus, and dynamic creep. Wet conditioning was used as a method to evaluate moisture susceptibility. The results of this research proved that portland cement and fly ash were both beneficial to strength, stiffness, and stripping resistance of the asphalt binder from the aggregates. As the stiffness increased with an increase in cement and fly ash contents, the rutting resistance also increased.

Termkhajornkit, Nawa, Yamashiro, and Saito (2009) explored the idea of self-healing by researching concrete susceptibility to both autogenous and drying shrinkage controlled cracking. As these cracks typically develop within 28 days, it was hypothesized that the fly ash particles would continue to hydrate after the testing period and prolong the service life of the pavement. For this reason, the samples produced consisted of both fly ash and portland cement. This study tested compressive strength, porosity, chloride diffusion coefficients, hydration reactions, and hydrate products. The results demonstrated that the fly ash and portland cement systems had self-healing capabilities for cracks that developed from shrinkage since the total hydrated particles continued to increase after 28 days for mixtures with increased fly ash contents (Figure 2.18). The ordinary portland cement (OPC) mixtures did not experience any additional hydration after 28 days.

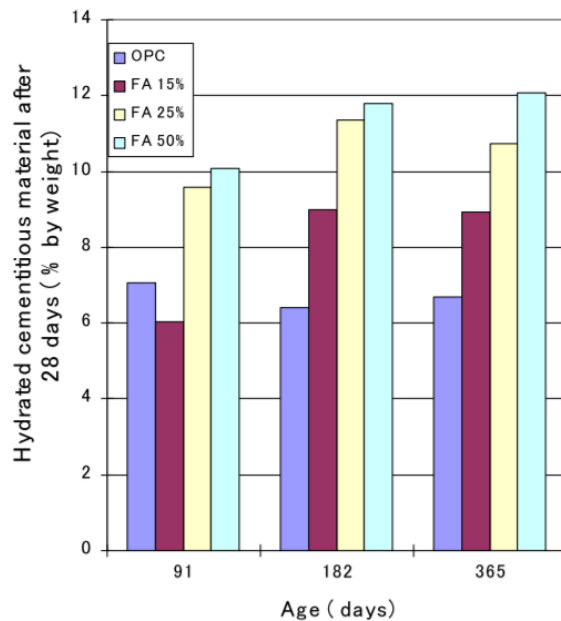


Figure 2.18: The Amount of Cementitious Particles that Hydrated after 28 Days

CHAPTER 3

MATERIALS AND TESTING METHODS

3.1 CHARACTERIZATION OF REACTIVE POWDERS

The reactive powders used in this research study were collected from different portland cement manufacturers in the United States. The purpose of this research study was to determine which reactive powder mastics or mixtures performed the best when compared to a control limestone mastic or mixture. Limestone was used as a control filler since this is a common industry material that is blended in asphalt mixtures. The specific types of reactive powders were chosen to vary drastically in both chemical and physical properties to evaluate the associated effects that such reactive powders can have on asphalt performance. For this reason, it was important to classify the powder materials for chemical oxides, Loss on Ignition (LOI), crystallography, specific gravity, particle size distribution (PSD), and particle shape based on the experimental matrix displayed in Table 3.1. This table demonstrates the reactive powder characterization, filler property, and the test method used to determine the specific property.

Table 3.1: Testing Matrix for Characterization of Reactive Powders

Filler Characterization	Reactive Powder Property	Test Method
Chemical Characterization	Chemical Oxides	X-Ray Fluorescence
	Loss on Ignition (LOI)	Thermogravimetric Analyzer
	Crystallography	X-Ray Diffraction
Physical Characterization	Specific Gravity	Helium Pycnometer
	Particle Size Distribution (PSD)	Laser Light Scattering
	Particle Shape	Scanning Electron Microscope (SEM)
	Rigden Voids	Fractional Void Test

3.1.1 Chemical Properties

Chemical property testing was performed on the 1 limestone powder, 1 SDA powder, and the 5 portland cement reactive powders. The chemical properties that were tested were chemical oxides, Loss on Ignition (LOI), and crystallography.

3.1.1.1 Chemical Composition

Chemical oxides were tested in accordance to ASTM C114 using X-Ray Fluorescence (XRF) to evaluate the chemical composition of the reactive powders and control limestone filler. It was important to investigate the chemical composition of the powders to evaluate the effects that the chemical oxides can have on the performance of the asphalt mastics and asphalt mixtures. ASTM C150 is the standard specification for portland cement and ASTM C618 is the standard specification commonly used to define coal fly ash and raw or natural pozzolan for use in concrete. These standards were used when classifying the powders that were used in this research study. Limitations were based on $\text{SiO}_2 + \text{Al}_2\text{O}_3 + \text{Fe}_2\text{O}_3$ contents in the SDA material which is classified as SAF content. The chemical oxides tested were silicon dioxide (SiO_2), aluminum oxide (Al_2O_3), iron oxide (Fe_2O_3), calcium oxide (CaO), magnesium oxide (MgO), sulfur trioxide (SO_3), sodium oxide (Na_2O), potassium oxide (K_2O), titanium dioxide (TiO_2), phosphorus pentoxide (P_2O_5), manganese oxide (Mn_2O_3), and strontium oxide (SrO).

3.1.1.2 Loss on Ignition (LOI)

Loss on Ignition (LOI) was tested according to ASTM C311 to assess the organic contents of the powder materials. The materials tested were required to be dried in an oven at $750 \pm 50^\circ\text{C}$ in a controlled environment with an inert gas, then exposed to oxygen to allow the

volatile matter to escape due to rapid oxidation. The procedure concluded once there was no more mass change. The results of this test were evaluated based on the percentage of total mass loss on the point of ignition.

3.1.1.3 Crystallography

Material crystallography was evaluated using X-Ray Diffraction (XRD). X-Ray Diffraction (XRD) is a type of microstructural investigation technique used to analyze crystalline materials by evaluating the atomic planes of a crystal and can be used to determine phase composition, unit cell lattice parameters, residual strains, crystal structure, and even crystal size.

The samples that were used in this study were tested to determine whether they were crystalline or amorphous. To prepare the powder samples for XRD, the samples were carefully placed onto the shallow well of the XRD holder and once there was a small amount of material, the metal spatula was used to flatten the mound and this packed the sample into a dense configuration. The surface of the material needed to be flat and dense to ensure that the X-ray absorption didn't reduce the intensity of low angle peaks. Once the sample was prepared on the holder, the sample was placed into the main compartment of the XRD machine and magnetically locked into place.

The model of the XRD machine that was used during the experiment was a Bruker D8 Discover and data was collected from the DIFFRAC.COMMANDER software. The X-rays used were soft X-rays and these X-rays were produced from an anode consisting of a water-cooled block of copper. High-speed electrons were detected by colliding with the metal target. This experimental procedure evaluated the powder materials from 5 to 50 2θ .

3.1.2 Physical Properties

Physical property testing was performed on the 1 limestone powder, 1 SDA powder, and the 5 portland cement reactive powders. The physical properties that were tested were specific gravity (SG), particle size distribution (PSD), particle shape, and Rigden voids.

3.1.2.1 Specific Gravity

The specific gravity (SG) was measured with the Helium Pycnometer test in accordance with ASTM D5550. The specific gravity was a significant parameter since it was used to calculate the Rigden voids and for converting mass to volume which was also important as all comparisons in this research study were made for a specific volume of material.

3.1.2.2 Particle Size Distribution (PSD)

The particle size distributions (PSD) of the powders were determined using laser diffraction according to ASTM D4464-10. This test method can measure the equivalent spherical diameter for particle sizes in the range of 1 to 300 μm . To conduct the laser diffraction test, a sample of material was dispersed in distilled water or a compatible organic liquid (alcohol) and circulated through the path of a laser light beam. When the light beam hit a particle, it was scattered. This scattered light was then collected by a photo detector and converted to an electrical signal and analyzed with the assumption that all the particles were spherical. From the PSD curves the D_{10} , D_{50} , and D_{90} values were determined. The diameters D_{10} , D_{50} , and D_{90} correspond to the portion of the material that is 10%, 50% and 90% finer, respectively.

3.1.2.3 Shape

A TOPCON® SM-300 Scanning Electron Microscope (SEM) was used to investigate particle size and shape. A small amount of powder was adhered to double sided carbon black tape, which was attached to a sample holder. The sample was then coated with a thin layer of gold to make it electrically conductive. Once properly aligned, the SEM was focused, and images were taken.

3.1.2.4 Rigden Voids

The fractional void test, also known as the Rigden Voids Test (RV) was developed by Rigden (1947) in order to obtain a simple filler characteristic that could be related to the performance of asphalt binders. The significance of the Rigden voids test has been validated by different researchers (Ishai and Craus, 1977; Van Der Heide and Van Zantvliet, 1982; Ishai and Craus, 1996, and Faheem et al., 2012). Several studies have demonstrated that higher stiffening effect is related to higher RV values, suggesting that more asphalt binder is required to fill the voids, reducing the separation between the filler particles (Rigden, 1947; Warden et al., 1959; Rao and Sen, 1973; Ishai and Craus, 1977; Taybeali et al., 1998; Silva et al., 2005; Faheem et al., 2012). In this research, Rigden voids testing was conducted according to the European Standard EN 1097-4.

3.2 SUPERPAVE® ASPHALT MASTIC TESTING PROTOCOL

This section explains the experimental testing matrix for both the control asphalt mastics and the mastics with reactive powders. Table 3.2 presents the mastic experimental testing matrix. This phase focused on testing for properties required by Superpave® performance specification to understand the level of interaction and the feedback for WMA mixture design.

Under this phase, the viscosity of unaged asphalt mastics was measured with a Brookfield Rotational Viscometer (RV) as an estimate of the workability. The Dynamic Shear Rheometer (DSR) was used to determine the rutting and fatigue resistance for RTFO and PAV aged mastics by measuring Superpave® $G^*/\sin(\delta)$, non-recoverable compliance (J_{nr}), % Recovery at high temperature, and Superpave® $G^*\sin(\delta)$ at intermediate temperature. For aging resistance of mastics, the PAV aged G^* and unaged G^* were compared. Finally, thermal cracking resistance was determined using the Bending Beam Rheometer (BBR) at low service pavement temperature to measure the creep stiffness $S(t)$ and m -value.

Table 3.2: Testing Matrix for Mastic Study

Mastic Property	Measured Indicator	Test Method	Aging	Asphalt Binders	Powders	Conc.	Temp.
Complex Modulus and Phase Angle	G^* and δ	DSR (25 mm)	Unaged	2	7	3	PG
Constructability	Viscosity	Rotational Viscometer	Unaged				135°C
Rutting Resistance	$G^*/\sin(\delta)$	DSR (25 mm)	RTFO				PG
	J_{nr} and %Recovery	MSCR (25 mm)	RTFO				PG
Fatigue Resistance	$G^*\sin(\delta)$ and Aging Index	DSR (8 mm)	Unaged				Intermediate PG
			PAV				
Thermal Cracking	$S(t)$ & m	BBR	PAV				-PG

3.2.1 Mastic Preparation

The mixing techniques for the reactive powders, limestone filler, and asphalt binder was optimized to avoid the incorporation of excess air into the mastic blend through the use of an adequate mixing apparatus, mixing speed, properly aligned propeller and mixing temperature controlled by the hot plate. A mechanical stirrer (Cowles Dissolver) was used at a mixing speed of 1,300 rpm and the required mass of powder was calculated based on the mass of the asphalt binder using the volume concentration and specific gravity of the material. Asphalt binder was mixed with the powders for 30 minutes at $135 \pm 5^\circ\text{C}$. During this mixing time, a portion of powders were added at 5 minutes increments.

3.2.1.1 Mixing Procedure

The following is the proposed procedure for blending the powders with asphalt binder:

1. Preheat powder in oven at $135 \pm 5^\circ\text{C}$.
2. Heat asphalt at $135 \pm 5^\circ\text{C}$
3. Place empty quarter of a gallon paint can on top of piece of wood or plywood on scale to prevent heat from reaching the platen
4. Zero the scale.
5. Pour target mass of asphalt into the can (recommended 500 – 600 grams in a quarter of a gallon can)
6. Determine the mass of filler required based on the mass of asphalt according to the target filler concentration by mass.
7. Put the can of asphalt in the heat mantel and adjust temperature to $135 \pm 5^\circ\text{C}$
8. Heat asphalt in the mantel for 10 minutes
9. Insert the mechanical stirrer such that it is located at the bottom third of the can depth. (Use dispersing stirrer to prevent filler agglomeration)
10. Start mechanical stirrer at 1300 revolutions per minutes.
11. Put an aluminum foil over the can and make a hole to allow space for adding fly ash into it and make sure to prevent dust going into air.
12. Add filler in small increments while stirring, targeting mixing time of 30 minutes
13. After all the filler is added continue stirring for five minutes. This makes the total stirring time to be 30 minutes.
14. After blending, the mix will be poured into smaller ointment tins. (50 – 60 grams each in 8 oz ointment tins)
15. Cover the ointment tins and store at room temperature for future testing.

3.2.2 Aging Procedures

3.2.2.1 Rolling Thin Film Oven (RTFO)

The Superpave® PG binder specification calls for short-term aged asphalt binder to be tested at high service temperatures to determine the resistance to rutting damage. The Rolling Thin Film Oven (RTFO), described under AASHTO standard designation T240, simulates the aging of the asphalt binder at mixing and construction stages. Asphalt binder is exposed to elevated temperatures to simulate the aging at manufacturing and placement. The RTFO also provides a quantitative measure of the volatiles lost during the aging process.

The basic RTFO procedure requires placement of unaged asphalt binder samples into cylindrical glass bottles and mounting these bottles in a rotating carriage within an oven. The carriage rotates within the oven for 85 minutes while the 163°C (325°F) temperature facilitates the aging of the samples. Samples are then stored for physical properties tests or processing with the Pressure Aging Vessel (PAV).



Figure 3.1: Rolling Thin Film Oven (RTFO)

3.2.2.2 Pressure Aging Vessel (PAV)

After considering short-term aging, the Superpave® PG binder specifications also consider long-term aging of asphalt binder for testing at intermediate temperature to determine the fatigue damage resistance and at low temperature to determine the thermal damage resistance. According to AASHTO standard R28 RTFO aged asphalt binder is exposed to heat and pressure to simulate in-service aging over a 7 to 10 year period in the Pressure Aging Vessel (PAV) unit. The basic PAV (Figure 3.2) procedure further ages the RTFO processed asphalt binder samples by placing the specimens into stainless steel pans, and then placing these for 20 hours in a heated vessel pressurized to 305 psi (2.10 MPa or 20.7 atmospheres). The heating temperature depends on the climate for which the asphalt binder is going to be used. Typically, it ranges from 90°C to 110°C. The final material is degassed for 30 minutes in a vacuum oven at 170°C. Samples were then stored for the tests of performance.



Figure 3.2: Pressure Aging Vessel (PAV)

3.2.3 Brookfield Rotational Viscometer (RV)

The Rotational Viscometer (Figure 3.3) was used under the Superpave® testing protocol to measure the asphalt viscosity at high construction temperatures (above 100°C). Since at such high temperatures the behavior of the most asphalt binders is totally viscous, a viscosity measurement is sufficient to represent the workability of the asphalt.

According to ASTM D4402, during this test the torque on a rotating spindle in a thermostatically controlled sample holder with asphalt is measured to determine the relative resistance to rotation. The torque and speed are used to estimate the viscosity of the asphalt in pascal seconds (Pa.s), milipascal seconds (mPa.s) or centipoises (cP). As with other viscoelastic material, the behavior of asphalt cement is affected by temperature and load. The temperature at which asphalt is heated has an influence on flow characteristics. The higher the temperature the more flowable (less viscous) the material will be. During the production process of Hot Mix Asphalt (HMA) it is important to determine the right temperature at which asphalt binder needs to be heated for sufficient flowability required for a proper mixing with aggregates and to assure that the end product can be pumped, handled, and compacted.

The Superpave® binder specifications set the viscosity limit for unfilled asphalts at a maximum of 3 Pa.s at 135°C. For the Rotational Viscometer (RV) test the viscosity at 135°C is reported as the average of three readings. Viscosity of mastics was measured at 135°C using a #27 spindle. The test started with 30 minutes of conditioning of the specimen at the testing temperature. During the last 10 minutes of equilibrium the spindle started to rotate at 20 rpm for 900 seconds. The viscosity measurements were taken every 300 seconds of testing, recording the

average of the apparent viscosity to evaluate the effect of reactive powders and reference filler on mastics workability.

Although mastics are known to be shear dependent materials, the shear rate speed was kept at 20 rpm because it is the most commonly used shear rate in binder testing in accordance with Superpave® binder protocol. Work conducted under the NCHRP 9-45 found that the relative ranking of mastics did not change as a function of shear rate (Bahia et al. 2011).



Figure 3.3: Rotational Viscometer (RV) (Pavement Interactive, 2015)

3.2.4 Dynamic Shear Rheometer (DSR)

3.2.4.1 Time Sweep

One way to characterize the viscoelastic materials is by dynamic testing through the application of a sinusoidal stress (strain) load to the material. In this case, the response strain (stress) is usually sinusoidal. A time lag between the stress sinusoid and the strain sinusoid is observed. This time lag is known as the phase angle (δ). The Dynamic Shear Rheometer (DSR) measures a specimen's complex shear modulus (G^*) and phase angle (δ). The G^* means the

sample's total resistance to deformation when repeatedly sheared, while δ is the lag between the applied shear stress and the resulting shear strain. Figure 3.4 reveals this phenomenon, where Δt is equal to the time lag.

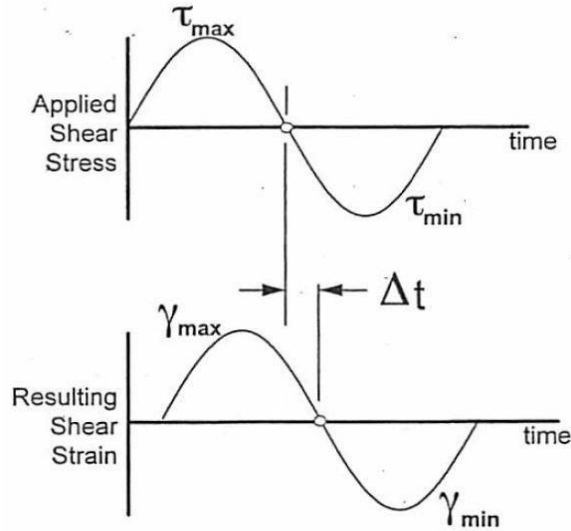


Figure 3.4: Stress-Strain Response of Viscoelastic Materials (after the Asphalt Institute 2003)

For elastic materials, the stress/strain reaction to load is immediate resulting in the $\delta = 0^\circ$. For viscous materials, since the stress is proportional to the strain rate, the $\delta = 90^\circ (\pi/2)$. For viscoelastic materials the δ is in between 0° and $90^\circ (\pi/2)$.

The stress and strain function on Figure 3.4 can be expressed mathematically by:

$$\sigma(t) = \sigma_0 \sin(\omega t + \delta) \quad \text{Eq. 3.1}$$

$$\epsilon(t) = \epsilon_0 \sin(\omega t) \quad \text{Eq. 3.2}$$

where:

σ_0 = peak stress ;

ϵ_0 = peak strain ;

ω = frequency of loading, rad/s ;

T = period.

For analysis, the stress function can be broken into two functions of the same frequency (Macosko 1994), one in phase with the strain ($\sin \omega t$) and another out of phase with the strain ($\cos \omega t$) (Eq. 3.3).

$$\sigma(t) = \sigma_0 \sin \delta \cos \omega t + \sigma_0 \cos \delta \sin \omega t \quad \text{Eq. 3.3}$$

The function that is in phase ($\sin \omega t$) represents the elastic component ($\delta = 0^\circ$) and the function that is out of phase represents the viscous component ($\delta = 90^\circ$). Since Hooke's Law is also applicable to shear stress (τ) and shear strain (γ), Eq. 3.3 can be written as:

$$\tau(t) = \tau_0 \sin \delta \cos \omega t + \tau_0 \cos \delta \sin \omega t \quad \text{Eq. 3.4}$$

By dividing Eq. 3.4 by the shear strain (γ_0), two dynamic moduli can be identified. One with the in-phase function called Shear Storage Modulus (G') (Eq. 3.5) and another with the out-phase function called Shear Loss Modulus (G'') (Eq. 3.6).

$$G' = \frac{\tau_0 \cos \delta}{\gamma_0} \quad \text{Eq. 3.5}$$

$$G'' = \frac{\tau_0 \sin \delta}{\gamma_0} \quad \text{Eq. 3.6}$$

In viscoelastic materials, the Shear Storage Modulus (G') represents the elastic portion and it is a measure of the stored energy. On the other hand, the Shear Loss Modulus (G'') represents the viscous portion and it is a measure of the energy dissipated as heat (Meyers and Chawla, 1999).

Using trigonometry, it can be seen that:

$$\tan \delta = \frac{G''}{G'} \quad \text{Eq. 3.7}$$

The prime and double prime notation has its origin in complex numbers (Macosko, 1994). In this way a Complex Shear Modulus (G^*) can be defined as:

$$G^* = G' + iG'' \quad \text{Eq. 3.8}$$

Where G' is the real component and G'' the imaginary component of the Complex Shear Modulus (G^*).

The Complex Shear Modulus (G^*) represents the stiffness of material for a specific frequency of loading and its graphical representation is reported in Figure 3.5. It is observed that the higher the time lag between the stress and strain (δ), the higher the G'' is and the more viscous the material is. Then again, the smaller the time lag between the stress and strain (δ), the higher the G' is and the more elastic the material is.

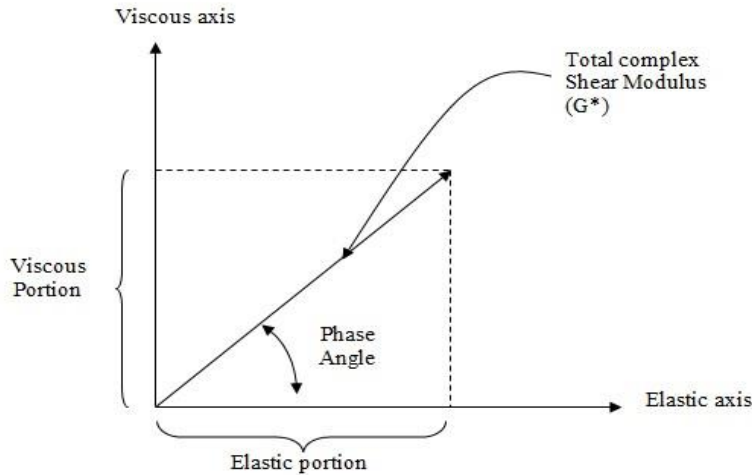


Figure 3.5: Complex Shear Modulus Representation

The specified DSR oscillation rate of 10 radians/second (1.59 Hz) was selected to simulate the shearing action (an average traffic speed according to the standard) corresponding to traffic

speed of about 55 mph (90 km/h). The G^* and δ are used as predictors of HMA rutting and fatigue cracking. In early pavement life, rutting is the main concern, while upon aging the fatigue cracking becomes the major concern.

To measure the asphalt cement rutting resistance at high pavement service temperatures the Superpave® system uses a rutting factor $G^*/\sin(\delta)$. According to AASHTO M320, when unaged asphalt cement is tested under the dynamic loading at the maximum pavement service temperature, this factor must be equal or greater than 1.00 kPa. On the other hand, when Rolling Thin Film Oven (RTFO) aged asphalt binder is tested under the dynamic loading at the maximum pavement service temperature this factor must be equal or greater than 2.20 kPa.

According to AASHTO T315, under a controlled strain test the target strain level for unaged materials should be 12%. This target strain level is defined by the Superpave® as strain level where the asphalt binder is still within the linear viscoelastic region. Under this phase of the research all the tests were conducted on asphalt mastics, so the strain level was reduced to 5% for unaged asphalt binder.

To measure the asphalt cement fatigue cracking resistance at intermediate pavement service temperatures the Superpave® system uses a fatigue factor $G^*\sin(\delta)$. When asphalt cement aged in the RTFO and Pressure Aging Vessel (PAV) is tested under the dynamic loading at the intermediate pavement service temperature the fatigue factor has a maximum limit of 5,000 kPa. According to Superpave®, the intermediate testing temperature depends on the asphalt binder used and it is determined by adding the high and low PG temperatures, dividing it by two and adding 4°C. Similar to unaged materials, for this research, the target strain level for PAV aged materials was reduced to 0.6% so the material is tested in the linear viscoelastic

region. The target strain value for PAV aged asphalt binder according to AASHTO T325 is 1%. These strain levels were selected based on limited experiments to assure the linear viscoelastic response.

3.2.4.2 Multiple Stress Creep and Recovery (MSCR)

The Multiple Stress Creep and Recovery (MSCR) test, using the Dynamic Shear Rheometer, is a recent development to the Superpave® Performance Graded (PG) asphalt binder specification. This test is conducted according to the AASSHTO standard T350 at a high pavement service temperature and is related to pavement damage resistance to rutting. This test method is comparable to elastic recovery, toughness, and force ductility of the asphalt binders.

The $G^*/\sin(\delta)$ test conducted by DSR is not sufficient to characterize the rutting resistance of polymer modified binders; therefore, it is usually coupled with this test to characterize the deformation resistance and recovery influenced by the polymer modification (D'Angelo, 2009). In this test method a load of 0.1 kPa is applied initially for 1 sec (conditioning load) and released (recovered) for 9 sec, and then this process continues for a total of 10 cycles. Afterwards, a load of 3.2 kPa is applied for 1 sec and recovered for 9 sec for another 10 cycles (Figure 3.6). In this research, an additional load of 10 kPa was used to complement the standard 0.1 kPa and 3.2 kPa sequence. This test is run on RTFO aged samples at high PG grade temperature.

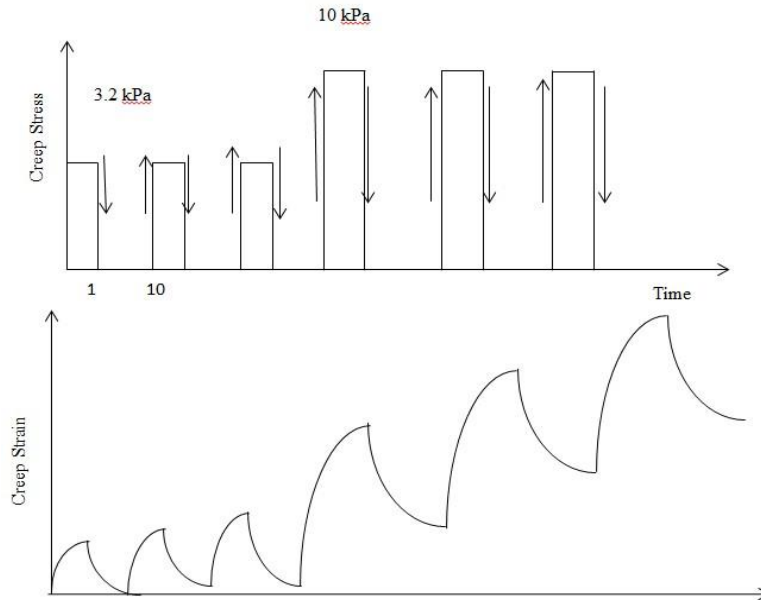


Figure 3.6: Multiple Stress Creep and Recovery Test Principle

The calculation method for non-recoverable creep compliance (inverse of complex modulus), J_{nr} is demonstrated by Figure 3.7. The percent recovery is calculated from the resulting strain values demonstrated by Figure 3.8. Research demonstrated that J_{nr} is highly correlated with pavement rutting (D'Angelo 2009). As the asphalt binder becomes stiffer, the J_{nr} becomes lower and % Recovery goes higher.

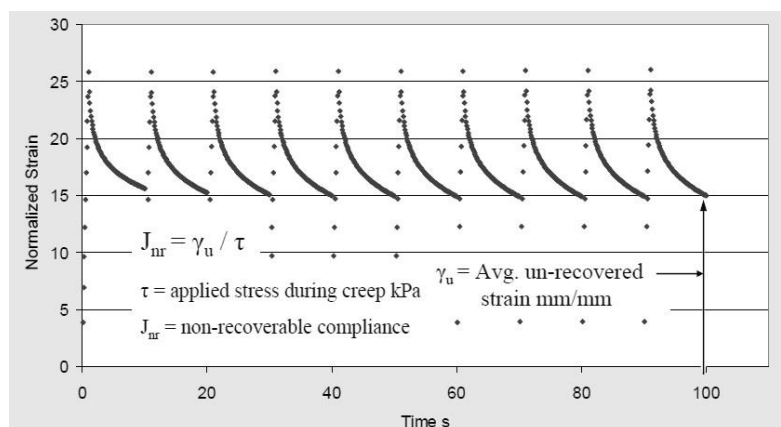


Figure 3.7: The Determination of J_{nr} (after D'Angelo, 2009)

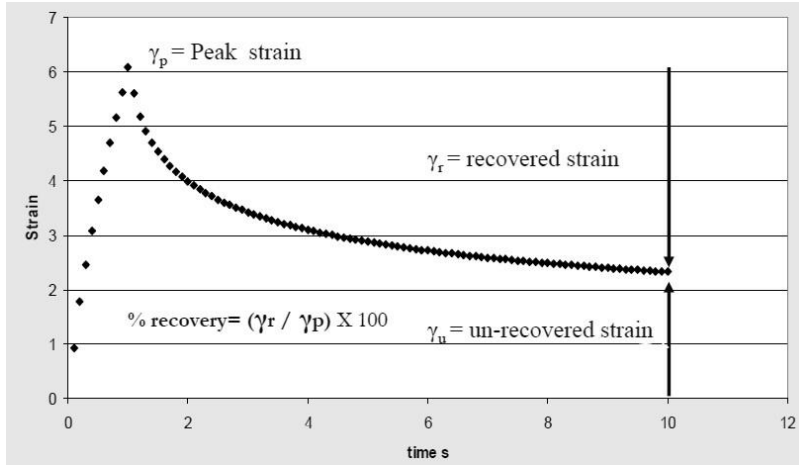


Figure 3.8: The Determination of % Recovery (after D'Angelo, 2009)

3.2.5 Bending Beam Rheometer (BBR)

To measure the asphalt cement thermal cracking resistance at low pavement service temperatures the Superpave® system measures the creep stiffness $S(t)$ and the slope of the creep stiffness (m-value). Creep is defined as a progressive deformation of a material under constant stress so when a creep experiment is conducted the stress is increased instantly from 0 to σ_0 and the strain $\epsilon(t)$ is recorded versus time.

As reported in Figure 3.9, a typical creep response of a viscoelastic material can be demonstrated by the instantaneous deformation at t_0 as soon as the stress is applied, then an increase in strain from t_0 to t_1 when the applied stress is continued and observed and once the stress has been removed the material responds with partial or total recovery (Lakes 2009).

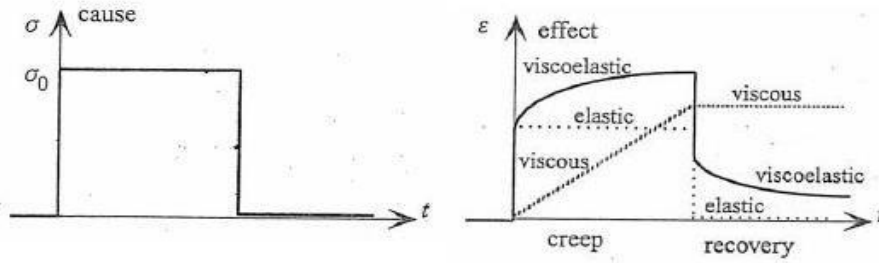


Figure 3.9: Creep and Recovery Stress (σ) and Strain (ϵ) Versus Time (t)

The Bending Beam Rheometer (Figure 3.10) test was conducted according to the standard AASHTO T313. Low temperature cracking is generally found in older, brittle pavements; therefore, the test is performed on the long-term aged material, after Pressure Aging Vessel (PAV). When asphalt cement aged in the RTFO and PAV is tested under the creep loading at low pavement service temperature the creep stiffness $S(t)$ is calculated using the Bernoulli beam classic theory as a function of time, sample geometry and deflection (Eq. 3.9).

$$S(t) = \frac{P L^3}{4bh^3 \delta(t)} \quad \text{Eq. 3.9}$$

where:

$S(t)$ = creep stiffness (MPa) at time t ;

P = applied constant load, (N);

L = distance between beam supports, 102 mm;

b = beam width, 12.5 mm;

h = beam thickness, 6.25 mm;

$\delta(t)$ = deflection (mm) at time, t .

According to Superpave® methodology, the creep stiffness $S(t)$ for asphalt binders must not exceed 300 MPa. Also, the slope of the creep stiffness is calculated as an indication of the relaxation of the asphalt binder at low temperatures and it is called m -value. The m -value must

be at least 0.300. The standard states that the stiffness value at 60 seconds is reported because it is correlated to 2 hours of actual traffic loading, which results in pavement cracking. The test is conducted at the low PG temperature plus 10°C, and the time temperature superposition is applied to calculate the response at the low PG temperature; this allows for shorter testing times (Ng Puga, 2013). Therefore, for PG58-28 the test was conducted at -18°C rather than -28°C and for PG52-34 the test was conducted at -24°C rather than -34°C.



Figure 3.10: Bending Beam Rheometer

3.3 SUPERPAVE® ASPHALT MIXTURE TESTING PROTOCOL

This section explains the experimental testing matrix for both the control asphalt mixtures and the mixtures with reactive powders in terms of aggregate coating, workability, aging resistance, moisture damage resistance, fatigue-cracking resistance, and low-temperature thermal-cracking resistance. Table 3.3 presents the experimental testing matrix for all asphalt mixtures. For all of these tests, at least two samples were tested, and averages were determined. For the aggregate coating, workability, and aging comparison, nine replicates were produced and compared. For the moisture damage resistance, fatigue cracking resistance, and thermal

cracking resistance, two replicates were produced and tested. The experimental testing methods are described in detail in the next sections.

Table 3.3: Testing Matrix for Mixture Study

Mixture Property	Measured Indicator		Aging	Asphalt Binders	Powders	Mixture Types	Conc.
Aggregate Coating	Asphalt Binder Film Thickness		Short-Term	WMA PG58-28 WMA PG52-34	3	6	1
Workability	% Air at 8 Gyration		Short-Term				
Aging Comparison			Long-Term				
Moisture Damage	TSR	Dry	Long-Term				
		Saturated					
		Conditioned					
Fatigue	E* using IDT	Intermediate Temp.	Long-Term				
Thermal Cracking	G _f & S(t)	Low Temp.	Long-Term				

3.3.1 Mixture Preparation

For this research there were two different types of mix designs: control mixtures and reactive powder hybrid asphalt mixtures. The control mixtures used a total added binder content of 5.8%. The mixtures containing reactive powders had 25% (by volume) bitumen replacement which means that the total added binder content was reduced to 4.4%. The aggregate quantities were constant throughout all the mixtures to allow for a more even comparison between the two different mixture types. All mixtures were modified with Evotherm by Ingevity® to create a WMA (Warm Mix Asphalt). The total mass of the mixtures as well as the added binder mass are shown in the equations below:

$$Total\ Asphalt\ Mixture\ Mass = \frac{Aggregate\ Mass}{1 - P_b} \quad Eq. 3.10$$

$$\text{Added Binder Mass } (P_b) = \left[\frac{\text{Aggregate Mass}}{1-P_b} \right] - \text{Aggregate Mass} \quad \text{Eq. 3.11}$$

where:

Aggregate Mass = Total mass of aggregates (4700 g or 1500 g);

P_b = added binder content.

The total mixture mass and added binder mass for a batch both depend on the specific test that the mixtures were used for. The mass of all the aggregates was 4700 g when compacting to determine the bulk specific gravity. The mass of all the aggregates was only 1500 g for the batch used to determine the maximum specific gravity. These quantity requirements are specified by ASTM D6857/D6857M-11 procedure for determining the maximum specific gravity (G_{mm}) and in ASTM D6752/D6752M-11 for the bulk specific gravity (G_{mb}).

3.3.1.1 Mixing Procedure

The asphalt mixing method was in accordance to AASHTO T312-12. Once all the materials were weighed, the aggregates were then mixed thoroughly, and then put in the oven to warm up to the designated temperature. As a reminder, for the hybrid mixtures, the reactive powder was added to the mixed aggregates prior to being placed in the oven. All mixture types were mixed at 120°C and then compacted at 115°C. The compaction temperatures were lowered from the mixing temperatures to mimic the temperature loss during delivery which is typically experienced in real-world applications. The appropriate amount of asphalt binder was also warmed up to the mixing temperature. When all the materials reached the mixing temperature, the aggregates were placed into a hot mixing bucket and a crater was formed in the center of the

bucket. The asphalt material was weighed into the mixture to achieve the desired batch weight. The mixing bucket was then placed into the Humboldt asphalt mixer and mixed for 3 minutes at 60 RPMs. It was noted that all the aggregates were thoroughly coated once the mixing was completed.

3.3.2 Aging Procedures

3.3.2.1 Short-Term Aging

Short-term aging conditioning was performed in accordance to AASHTO R30-02. Short-term aging is supposed to mimic the short-term effects that result from HMA mixtures being produced, placed, and compacted. After mixing the aggregates and asphalt binder together, the loose material was placed in a pan and spread to an even thickness ranging between 25 and 50 mm. This mixture was then placed into a forced-draft oven for $2 \text{ h} \pm 5 \text{ min}$ at a temperature equal to the mixture's compaction temperature $\pm 3^\circ\text{C}$ to simulate a short-term aging. The mixture was stirred after $60 \pm 5 \text{ min}$ to maintain a uniform conditioning. After the $2 \text{ h} \pm 5 \text{ min}$, the mixture was removed from the forced-draft oven and ready for compaction.

3.3.2.2 Long-Term Aging

The long-term aging procedure that was used was in accordance to AASHTO R30-02 and methods adapted by Elwardany, Rad, Castorena, & Kim (2010). These methods evaluate the aging of mixtures with either compacted specimens or loose mixtures and the methodology mimics a 5 to 10 year aging process. After the short-term aging, the mixtures were then placed into the force-draft oven for $24 \pm 0.5 \text{ h}$ at a temperature equal to the compaction temperature of 115°C . After $24 \pm 0.5 \text{ h}$ the specimens were then available to be compacted and tested.

3.3.3 Asphalt Mixture Volumetrics

3.3.3.1 Aggregate Volumetrics

There are many different volumetric parameters of aggregates that are important to understand and evaluate asphalt mixtures. The basis of these calculations is reported in Figure 3.11 (Asphalt Institute, 2001).

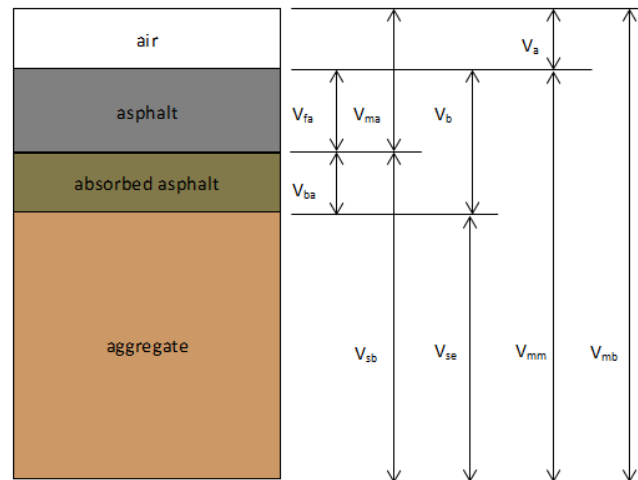


Figure 3.11: Component Diagram of Compacted HMA Specimen

$\%VMA$ = Volume of voids in mineral aggregate;

$\%V_{mb}$ = Bulk volume of compacted mix;

$\%V_{mm}$ = Voidless volume of paving mix;

$\%VFA$ = Volume of voids filled with asphalt;

$\%V_a$ = Volume of air voids;

$\%V_b$ = Volume of asphalt;

$\%V_{ba}$ = Volume of absorbed asphalt;

$\%V_{sb}$ = Volume of mineral aggregate (by bulk specific gravity);

$\%V_{se}$ = Volume of mineral aggregate (by effective specific gravity).

Aggregates in asphalt mixtures can absorb both water and asphalt binder. The most critical variables when evaluating aggregate and binder interactions is the volume of voids in the mineral aggregates, the volume of air voids in the mixture, and the volume of voids filled with asphalt. These parameters affect bonding strength as well as the coating film thickness and are directly related to the overall strength as well as moisture damage resistance.

3.3.3.2 Determination of G_{mm} and G_{mb}

The ASTM D6857/D6857M-11 procedure was used to determine the maximum specific gravity (G_{mm}) of the mixtures using a vacuum sealed material method and ASTM D6752/D6752M-11 specification was used to determine the bulk specific gravity (G_{mb}) of the mixtures using a vacuum sealed material method. After the asphalt mixtures were heated for both cases the samples were then cooled down for 16 ± 1 h at room temperature (AASHTO R30-02). Once the samples were cooled, the InstroTek CoreLok vacuum machine was used for the test.

For the maximum specific gravity, the loose rice samples were evenly spread out onto a pan and the particles were separated, taking care to avoid fracturing the aggregates. The particles of the fine aggregate portion were broken up so that the aggregate size was not larger than 6.3 mm. The bags, along with the asphalt mixture, were weighed. The sample was then placed into the CoreLok machine and the air was vacuumed out. Once the machine stopped, the sealed sample was submerged in water and the sealed bag was then cut across the top for water to enter. The bags were opened by hand in order to allow water to enter the bags completely and then the sample was weighed again. By using the CoreLok computer program, the G_{mm} was calculated directly.

For the bulk specific gravity, once the compacted sample was cooled, it was then weighed. The sample was then placed into a bag and placed into the CoreLok machine in order to remove the air from the chamber and bag. The sealed sample was removed from the CoreLok machine once the test was completed and then the sealed sample was weighed underwater. After the scale stabilized the weight was recorded. It was important to reweigh the sample, without the bag, out of water to ensure that no water had entered the bag while it was submerged. By using the CoreLok computer program, G_{mb} was calculated directly.

Using both G_{mm} and G_{mb} values, the $\%G_{mm}$ could be calculated based on the equation below. With this calculation, it is important to understand that 100% minus the $\%G_{mm}$ is the percent air in the mixture.

$$\%G_{mm} = \frac{G_{mb}h_m}{G_{mm}h_x} * 100\% \quad \text{Eq. 3.12}$$

where:

$\%G_{mm}$ = corrected relative density expressed as a percent of the maximum theoretical specific gravity;

G_{mb} = bulk specific gravity of the extruded specimen;

G_{mm} = max specific gravity of the of the mix;

h_m = height of the extruded specimen (mm);

h_x = height of the specimen after x gyrations (mm).

3.3.3.3 Volumetric Calculations of Asphalt Mixture

In order to properly analyze the compacted paving mixture it was important to evaluate and calculate volumetric parameters of the mixture. The equations below were used to evaluate the mixture based on Superpave® protocol.

3.3.3.3.1 Bulk Specific Gravity of Aggregates

$$G_{sb} = \frac{P_1 + P_2 + \dots + P_N}{\frac{P_1}{G_1} + \frac{P_2}{G_2} + \dots + \frac{P_N}{G_N}} \quad \text{Eq. 3.13}$$

where:

G_{sb} = bulk specific gravity for the total aggregate;

P_1, P_2, P_N = individual percentages by mass of aggregate;

G_1, G_2, G_N = individual (e.g. coarse, fine) bulk specific gravity of aggregates.

3.3.3.3.2 Effective Specific Gravity of Aggregates

$$G_{se} = \frac{P_{mm} - P_b}{\frac{P_{mm}}{G_{mm}} - \frac{P_b}{G_b}} \quad \text{Eq. 3.14}$$

where:

G_{se} = effective specific gravity of aggregate;

G_{mm} = maximum specific gravity of paving mixtures (no air voids);

P_{mm} = percent by mass of total loose mixture = 100;

P_b = asphalt content, percent by total mass of mixture;

G_b = specific gravity of asphalt.

3.3.3.3.3 Asphalt Absorption

$$\%P_{ba} = 100\% * \frac{G_{se}-G_{sb}}{G_{sb}*G_{se}} * G_b \quad \text{Eq. 3.15}$$

where:

$\%P_{ba}$ = absorbed asphalt, % by mass of aggregate;

G_{se} = effective specific gravity of aggregate;

G_{sb} = bulk specific gravity of aggregate;

G_b = specific gravity of asphalt.

3.3.3.3.4 Effective Asphalt Content

$$\%P_{be} = P_b - \frac{P_{ba}}{100} * P_s \quad \text{Eq. 3.16}$$

where:

$\%P_{be}$ = effective asphalt content, % by total mass of mixture;

$\%P_b$ = asphalt content, % by total mass of mixture;

$\%P_{ba}$ = absorbed asphalt, % by mass of aggregate;

$\%P_s$ = aggregate content, % by total mass of mixture.

3.3.3.3.5 Voids in Mineral Aggregate (VMA)

$$\%VMA = 100 - \frac{G_{mb} * P_s}{G_{sb}} \quad \text{Eq. 3.17}$$

where:

VMA = voids in the mineral aggregate, % of bulk volume;

G_{sb} = bulk specific gravity of total aggregate;

G_{mb} = bulk specific gravity of compacted mixture;

$\%P_s$ = aggregate content, % by total mass of mixture.

3.3.3.3.6 Percent Air Voids

$$\%V_a = 100 * \frac{G_{mm} - G_{mb}}{G_{mm}} \quad \text{Eq. 3.18}$$

where:

$\%V_a$ = air voids in compacted mixture, % of total volume;

G_{mm} = maximum specific gravity of paving mixture;

G_{mb} = bulk specific gravity.

3.3.3.3.7 Voids in the Mineral Aggregate Filled with Asphalt (VFA)

$$\%VFA = 100 * \frac{VMA - V_a}{VMA} \quad \text{Eq. 3.19}$$

where:

$\%VFA$ = voids filled with asphalt, % of VMA;

$\%VMA$ = voids in the mineral aggregate, % of bulk volume;

$\%V_a$ = air voids in compacted mixture, % of total volume.

3.3.3.3.8 Powder Proportion (Powder-to-Binder Ratio)

$$PB = \frac{P_{0.075}}{P_{be}} \quad \text{Eq. 3.20}$$

where:

$P_{0.075}$ = aggregate content passing the 0.075 mm sieve, percent by mass of aggregate;

P_{be} = effective asphalt content, percent by total mass of mixture.

After calculating these values, comparisons were then made with the Superpave® limitations in Table 3.4 (Asphalt Institute, 2001). This table reports on limitations for the voids in the mineral aggregate (VMA), voids filled with asphalt (VFA), and a dust-to binder ratio. When evaluating the mixture, comparisons were evaluated by using a nominal maximum aggregate size of 12.5 mm.

Table 3.4: Superpave® Volumetric Mixture Design Requirements

Design ESALs (millions)	Required Density (% of Theoretical Maximum Specific Gravity)			Voids-in-the Mineral Aggregate (Percent), minimum					Voids Filled With Asphalt (Percent)	Powder-to-Binder Ratio
	N_{ini}	N_{des}	N_{max}	Nominal Maximum Aggregate Size, mm						
				37.5	25.0	19.0	12.5	9.5		
< 0.3	≤ 91.5	96.0	≤ 98.0	11.0	12.0	13.0	14.0	15.0	70 - 80	0.6 - 1.2
0.3 to < 3	≤ 90.5								65 - 78	
3 to < 30	≤ 89.0								65 - 75	
≥ 30										

* Design ESALs are the anticipated project traffic level expected on the design lane over a 20-year period.

3.3.4 Workability

The workability performance was evaluated by comparing the short-term aged control mixtures with the short-term aged hybrid reactive powder mixtures. Using the Superpave® Gyrotory Compactor, it was determined how easily the mixtures are compacted based on the compaction effort. Lower compaction efforts allowed the densification curve to reach higher values of %G_{mm}, or lower %V_a. The purpose of this testing was to evaluate the compactability of the developed mixtures. If the reactive powder hybrid mixtures reached higher values of %G_{mm}, then the workability was considered to be reduced which is desired.

The Strategic Highway Research Program (SHRP) developed the laboratory compaction method with several goals in mind. It was critical to develop a compaction method that was able to produce asphalt samples with realistic densities under realistic pavement climates and loading conditions. The method needed to be able to handle larger aggregate sizes and also be able to measure the compactability so that the compaction problems could be evaluated. The device needed to output parameters such as a vertically applied pressure, an angle of gyration, and a specimen height over time. The SHRP researchers then developed the Superpave® Gyrotory Compactor (SGC), shown in Figure 3.12, to handle these requirements.



Figure 3.12: Superpave® Gyratory Compactor

The SGC is a piece of equipment that has a base that rotates at 30 rotations, or gyrations, per minute at an inclined angle of 1.25° . The specimen is placed into a compaction mold, Figure 3.13, which is 150 mm in diameter. The loading system applies a load of 600 kPa of compaction pressure on the specimen while the base and compaction rotate together. The computer program then measures the gyration number, the angle, the pressure (kPa), and the specimen height (mm). The specimen height is important to record because the density can be calculated from the values. From these values, the percent air in the material after compaction can also be calculated which is a critical characteristic for asphalt pavements.

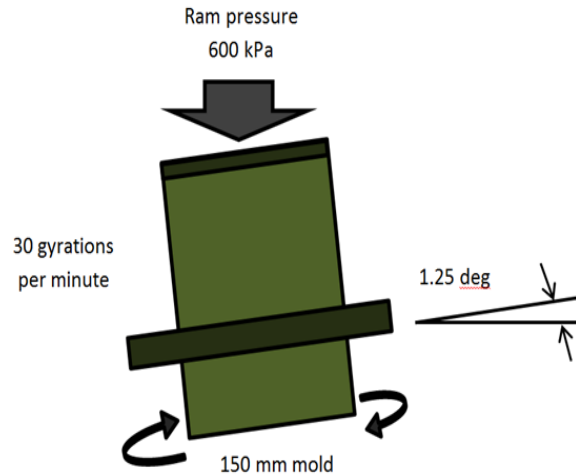


Figure 3.13: Superpave® Gyrotory Compactor Mold

Asphalt mixtures are designed for a specific compaction effort. When using a SGC the compaction effort can be directly related to the number of gyrations necessary to achieve the appropriate amount of air voids. In Superpave® these variables can be expressed as the design number of gyrations, N_{des} . The N_{des} is the design number of gyrations to achieve the specific compaction degree and a density of the asphalt mix that is expected in the field after the designed amount of traffic. Generally, after N_{des} gyrations, the compacted asphalt specimen will have 4 percent air voids.

The other gyration levels that are important are N_{ini} and N_{max} . The N_{ini} is the initial number of gyrations and this is a measure of mixture compactibility. Tender mixtures tend to compact too quickly which is undesirable. At N_{ini} the compacted specimen should generally have about 11 percent air voids. The N_{max} is the maximum number of gyrations that should produce a density that should never be exceeded in the field. At N_{max} , the number of air voids should generally be less than 2 percent. Mixtures with less than 2 percent tend to be more prone to rutting and fracture (Roberts et al., 1996). All values of N_{ini} , N_{des} , and N_{max} are used in the

design process as a function of traffic levels and this traffic level is represented by the design ESALs (Equivalent Single Axel Load).

Determining the number of wheel/axel loads a pavement will experience during its life-cycle can be difficult to estimate. The repeated loading and unloading of these wheel/axel forces cause damage to the pavement and there needs to be an estimation of traffic loads when analyzing the pavement design. The ESALs are used to convert ordinary daily traffic loads to magnitudes and repetitions to mimic a standard number of equivalent loads. A standard axel load of 80.0 kN is used to estimate the pavement performance over its lifetime.

The percentage of air voids is generally expressed in terms of $\%G_{mm}$. The $\%G_{mm}$ is the corrected relative density expressed as a percent of the maximum theoretical specific gravity. For most densification curves, the x-axis is represented by the number of gyrations while the y-axis is represented by $\%G_{mm}$. When evaluating $\%G_{mm}$ it is important to understand that the percentage of air voids ($\%V_a$) is basically 100 minus the $\%G_{mm}$ at that given point. So, if trying to achieve 4% air voids, the $\%G_{mm}$ would be 96%. Figure 3.14 visually represents the densification curve and where certain points such as N_{ini} , N_{des} , and N_{max} should be on the plot.

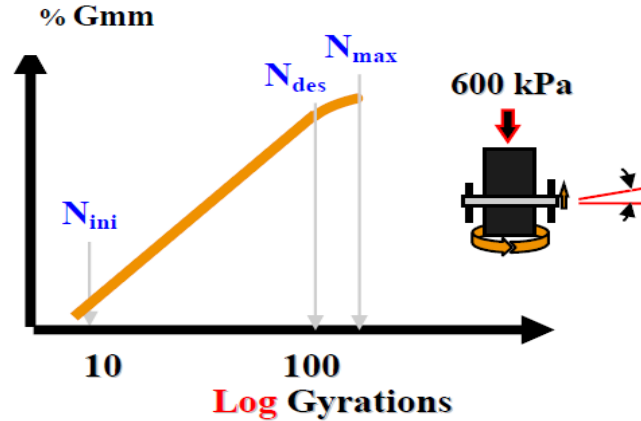


Figure 3.14: Maximum Theoretical Specific Gravity vs. Number of Gyration (Faheem et al. 2008)

Table 3.5 further summarizes the Superpave® compaction efforts and N_{des} characteristic values for different roadway applications.

Table 3.5: Superpave® Gyratory Compaction Parameters for Different Roadway Applications

Design ESALs (millions)	Compaction Parameters			Typical Roadway Applications
	N_{ini}	N_{des}	N_{max}	
< 0.3	6	50	75	Very light traffic (local/county roads; city streets where truck traffic is prohibited)
0.3 to < 3	7	75	115	Medium traffic (collector roads; mostly county roadways)
3 to < 30	8	100	160	Medium to high traffic (city streets; state routes; US highways; some rural interstates)
≥ 30	9	125	205	High traffic (most of the interstate system; climbing lanes; truck weighing stations)

The AASHTO T312-12 procedure was followed for compacting the asphalt samples using a Pine Co. Superpave Gyratory Compactor (SGC). The compaction mold and base plate were placed in the oven and preheated at the required compaction temperature for a minimum of 30 minutes prior to the beginning of the compaction. The control mixtures and the hybrid reactive powder mixtures were both compacted at 115°C. Approximately 4700 g of asphalt

material was used for compaction and this was necessary when determining the bulk specific gravity. Approximately 1500 g of asphalt material was used as a loose mixture to determine the maximum specific gravity.

Once the compaction temperature was achieved, the mold and base plate were removed from the oven and a paper disk was placed at the bottom of the mold. The mixture was placed into the mold in one lift, then it was leveled, and then another paper disk was placed on top of the material inside the mold. The charged mold was placed into the gyratory compactor and centered beneath the ram. A pressure of 600 ± 18 kPa was applied to the specimen at an angle of 1.25° , while the rotating base spun at a constant 30 gyrations per minute. The Superpave Gyratory Compactor recorded the exact height, pressure, and angle of the compacted sample for each gyration (as these parameters are used for developing the compaction densification curve).

To fully understand the workability of the mixtures, 100 gyrations were used to effectively analyze the entire compaction curve. Once the test was completed, the angle was removed from the mold as well as the ram pressure and then the ram was retracted from the mold. The specimens were then extruded from the mold and the paper disks were also removed. The same procedure was used when compacting the duplicate sample. The compacted specimen was important for evaluating the bulk specific gravity and the loose mixture was important for evaluating the maximum specific gravity.

3.3.5 Aggregate Coating

Aggregate coating was evaluated based on physical observations as well as calculated parameters. Pictures were taken to make the side-by-side comparisons between the control samples and the hybrid samples. Since the total binder content for the control mixtures was

5.8%, whereas the total binder content for the hybrid powder hybrid mixtures was only 4.4%, it was important to evaluate the aggregate coating to ensure proper long-term performance.

The percent of asphalt, as well as the diameter, particle size distribution, and surface area of the aggregate particles, have an effect on the thickness of the asphalt film. The asphalt film thickness decreases when the average diameter of the aggregate particle decreases because the surface area increases. For this reason, the surface area factors (Table 3.6) can be used to evaluate, or estimate, the total aggregate surface area in a given asphalt mixture. This assumes that all of the particles are rounded, however it serves as a good approximation. The surface area can be calculated by multiplying the surface area factor by the percent passing that specific sieve size. The units of the results are square feet per pound of aggregate (Roberts et al., 1996).

Table 3.6: Surface Area Factors for Different Aggregate Sizes

Sieve Size	Surface Area Factors
Percent Passing Maximum Sieve Size	2
Percent Passing No. 4	2
Percent Passing No. 8	4
Percent Passing No. 16	8
Percent Passing No. 30	14
Percent Passing No. 50	30
Percent Passing No. 100	60
Percent Passing No. 200	160

Once the surface area of the aggregates is determined (converted to m^2/kg), a volumetric analysis needs to be conducted in order to find the film thickness. The equations below demonstrate the necessary steps to calculate the variables needed to find film thickness:

$$\text{Total volume } P_{bv} = \frac{(\text{total weight of mixture}) * (P_b)}{G_b} \quad \text{Eq. 3.21}$$

$$P_{ba} = \frac{G_{se} - G_{sb}}{G_{sb} * G_{se}} * G_b \quad \text{Eq. 3.22}$$

$$P_{baw} = (P_{ba}) * (\text{total weight of mixture} * (1 - P_b)) \quad \text{Eq. 3.23}$$

$$P_{bav} = \frac{\text{Weight of absorbed asphalt}}{G_b} \quad \text{Eq. 3.24}$$

$$P_{bev} = 100\% * \frac{G_{se} - G_{sb}}{G_{sb} * G_{se}} * G_b \quad \text{Eq. 3.25}$$

where:

P_{bv} = total volume of asphalt cement, by total mass of mixture (mL);

P_b = asphalt content, by total mass of mixture;

P_{ba} = absorbed asphalt content, by total mass of mixture;

G_{se} = effective specific gravity of aggregate;

G_{sb} = bulk specific gravity of aggregate;

G_b = specific gravity of asphalt;

P_{baw} = weight of absorbed mixture (g);

P_{bav} = volume of absorbed asphalt (mL);

P_{bev} = effective volume of asphalt (mL);

After these variables are determined, the film thickness can then be calculated using the equation below:

$$T_F = 1000 * \frac{V_{asp}}{SA * W} \quad \text{Eq. 3.26}$$

where:

T_F = Average film thickness (microns);

V_{asp} = Effective volume of asphalt cement (liters);

SA = Surface area of the aggregate (m² per kg of aggregate);

W = weight of aggregate (kg).

With this equation it is important to understand that when the surface area estimations were made, the units need to be converted from square feet per pound to m² per kg of aggregate. Once these units are converted, the equation can be used.

3.3.6 Aging Resistance

Aging resistance was measured as a comparison in compaction efforts between the long-term aged materials and the short-term aged materials. As the material ages it becomes stiffer. Since the experimental matrix required that the long-term aged materials be re-compacted to 93% G_{mm}, a comparison was made between the two different aging conditions. The aging index was calculated as the difference in air content at 8 gyrations for long-term aged materials versus the air content at 8 gyrations for short-term aged materials. Lower aging indexes demonstrate a higher aging resistance. If the aging index is low, this means that the material resists the stiffening effects of age-hardening. Therefore, the aging index is calculated using the equation below:

$$\text{Aging Index} = A\%_{LT} - A\%_{ST} \quad \text{Eq. 3.27}$$

where:

A%_{LT} = Percent air at 8 gyrations for long-term aged materials;

A%_{ST} = Percent air at 8 gyrations for short-term aged materials.

3.3.7 Moisture Damage

3.3.7.1 Specimen Conditioning

This testing procedure is in accordance to AASHTO T283-07. Moisture damage is the result from water or air damaging the bond between the aggregate particles and the layer of asphalt binder. It is required that the compacted asphalt mixtures resist this damage to a certain degree when saturated with water. Specimens were therefore prepared and conditioned to evaluate proper moisture damage resistance. Duplicate samples were tested for each situation.

After the asphalt mixtures were long-term aged and compacted to 93% G_{mm} , these were then core drilled and saw cut to a 101.6 ± 2.0 mm diameter and a 50.8 ± 2.0 mm thickness. Typical core drilling procedures were followed as well as saw cutting. Two specimens were collected (after core drilling and saw cutting) from each compacted sample. The samples from the compacted cores were randomly chosen for each testing procedure.

After the 101.6 ± 2.0 mm diameter by 50.8 ± 2.0 mm thick specimens were produced, the samples were separated into subsets and then the subsets were placed under three different environments: dry, saturated, and conditioned. The dry samples were placed into a leak-proof plastic bag and then placed in a water bath at $25 \pm 0.5^\circ\text{C}$ for $2 \text{ h} \pm 10 \text{ min}$ with a minimum of 25 mm of water above the surface of the specimen. The specimens were then ready to be tested with the Indirect Tension Machine.

The saturated and conditioned specimens were submerged in a water container with a minimum of 25 mm of water above their top surface, and with also 25 mm of water below the bottom surface (a perforated spacer was used to raise the specimen off the base of the water container). Using the Instron Corelok machine, the samples were then vacuumed to remove

the air, and thus insert the water into the void spaces. After the machine completed the cycle, the samples were left in the water bath for approximately 5 to 10 minutes. After this time period the samples were taken out of the water bath and the degree of saturation (S') was calculated by using the equations below:

$$S' = \frac{100 * J'}{V_a} \quad \text{Eq. 3.28}$$

$$V_a = \frac{P_a * E}{100} \quad \text{Eq. 3.29}$$

$$J' = B' - A \quad \text{Eq. 3.30}$$

where:

V_a = volume of air voids (cm^3);

P_a = air voids, (percent);

E = volume of the specimen, (cm^3).

J' = volume of absorbed water, (mL);

B' = mass of the saturated, surface-dry specimen after partial vacuum saturation, (g);

A = mass of the dry specimen in air, (g).

A requirement from AASHTO T283-07 is that all of the saturated and conditioned specimens need to have a degree of saturation between 70 and 80%. If the degree of saturation is less than 70% the specimen needs to be vacuumed so that the degree of saturation increases. If the degree of saturation is higher than 80%, the specimen must be discarded due to excessive damage. The degree of saturation is important because this presents an allowable range where the asphalt pavement is not excessively damaged, but at the same time demonstrates realistic water penetration. This procedure is critical to evaluate the bonding between the asphalt binder

and the aggregate particles. If the bond between these materials is significantly damaged due to water penetration, the materials will separate, and the mixture becomes weak which is undesirable.

After all the saturated specimens reached the appropriate range between 70 and 80%, the specimens were then placed into a water bath at $25 \pm 0.5^{\circ}\text{C}$ for $2 \text{ h} \pm 10 \text{ min}$ with a minimum of 25 mm of water above the surface of the specimen. The specimens were then ready to be tested with the Indirect Tension Machine. After the conditioned specimens were saturated, they were then placed in a water bath at $60 \pm 1^{\circ}\text{C}$ for $24 \pm 1 \text{ h}$. The specimens were submerged so that at least 25 mm of water was above the top surface of the asphalt specimen. After $24 \pm 1 \text{ h}$, the specimens were removed from the water bath and then placed into a different water container that was $25 \pm 0.5^{\circ}\text{C}$ for $2 \text{ h} \pm 10 \text{ min}$ with at least 25 mm of water above the top surface. Maintaining the temperature for this water bath was critical since the samples were warmer than $25 \pm 0.5^{\circ}\text{C}$. Once this time had elapsed, the specimens were then removed from the water bath and then tested using the IDT.

3.3.7.2 Indirect Tensile Test (IDT)

The Humboldt Indirect Tensile Machine (IDT) was used to evaluate the moisture damage resistance in accordance to ASTM D4123. This machine uses a single compressive load that acts parallel to the vertical plane of the specimen. As the vertical compressive load pushes down on the specimen (at a rate of 50 mm/min.), horizontal tensile forces begin to develop. (Figure 3.15). The required thickness of the loading strip for a 101.6 mm diameter asphalt specimen is 12.7 mm and this was used for this study. This specific thickness provides a uniform loading condition which produces a nearly uniform stress distribution

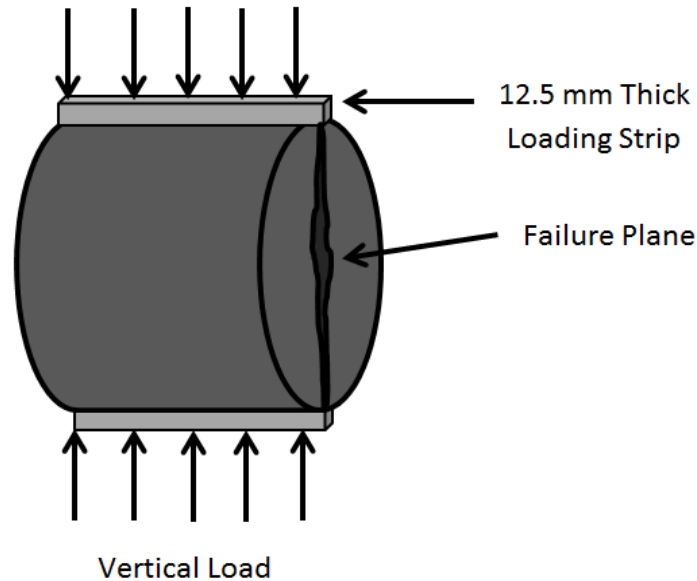


Figure 3.15: Indirect Tension Test at Failure

The IDT provides two important properties that are very useful in HMA mixture analysis: moisture damage resistance and tensile strain at failure. For moisture damage resistance, the tensile strength of a conditioned compacted asphalt sample was compared to that of a vacuum-saturated, compacted asphalt sample. This value can be expressed as a Tensile Strength Ratio (TSR). The higher the value for the TSR, the better the mixture performed in terms of moisture damage resistance. A lower value indicates poor performance of the specimen. AASHTO T283-07 requires a TSR of at least 80%. The other beneficial variable that can be calculated from the IDT is the tensile strain at failure which can help predict the cracking potential. Mixtures that are able to resist cracking generally can tolerate higher strains at failure which is beneficial to the asphalt pavement.

Equations for tensile stress and tensile strain have been developed (Anagnos & Kennedy, 1972; Hadley, Hudson & Kennedy, 1970, 1972) and are reported below:

$$\sigma_x = \frac{2P}{\pi dt} \quad \text{Eq. 3.31}$$

$$\sigma_y = \frac{6P}{\pi dt} \quad \text{Eq. 3.32}$$

where:

σ_x = horizontal tensile stress at center of specimen, (MPa);

σ_y = vertical tensile stress at center of specimen, (MPa);

P = applied load, (N);

d = diameter of specimen, (mm);

t = thickness of specimen, (mm).

$$\varepsilon_f = 0.52x_t \quad \text{Eq. 3.33}$$

where:

ε_f = tensile strain at failure (mm/mm);

x_t = horizontal deformation across the specimen (in.).

$$TSR = \frac{S_c}{S_s} \quad \text{Eq. 3.34}$$

where:

S_c = average tensile strength of conditioned specimen (MPa);

S_s = average tensile strength of saturated specimen (MPa).

The methods explained in this section were used to convert the loads and deflections to stresses and strains. Moisture damage resistance was also calculated, and evaluations have been made.

3.3.8 Fatigue-Cracking Resistance

Fatigue testing was performed to evaluate the effects of fatigue-cracking resistance in ASHphalt mixtures. Fatigue cracking is a result of repeated loads at intermediate temperatures. Over the life-cycle of the asphalt pavement, the material begins to deteriorate due to cyclic loading. As traffic loading overstresses the asphalt material, the pavement begins to crack. The factors affecting fatigue cracking are the asphalt content, air void content, aggregate characteristics, temperature, and traffic. Also, asphalt binders that become stiffer during aging also develop poor fatigue characteristics. Ideally, asphalt materials should act as a soft, elastic material when loaded and unloaded. Since fatigue cracking is an undesirable characteristic of asphalt pavements, it was vital to evaluate this parameter and potential contribution of reactive powders.

Figure 3.16 demonstrates a typical fatigue testing curve. The horizontal axis represents the number of cycles and the vertical axis represents the displacement of the material. As seen from Figure 4.16 there are different zones within this type of fatigue curve. The most critical section of this curve that is evaluated in this research is the secondary fatigue section and the point where the tertiary fatigue section starts. During the secondary fatigue stage, the material undergoes a constant cyclic loading and the material deforms at a constant rate. The slope of this line represents the constant deformation per cycle in which the material is deforming. This is important because it demonstrates a perfect elastic deformation over time. The tertiary portion represents the point at which the material is failing. This section was important to understand where the material fails (N_f). Even though the curve continues in the tertiary fatigue section, the material was considered to have failed when the tertiary fatigue section started.

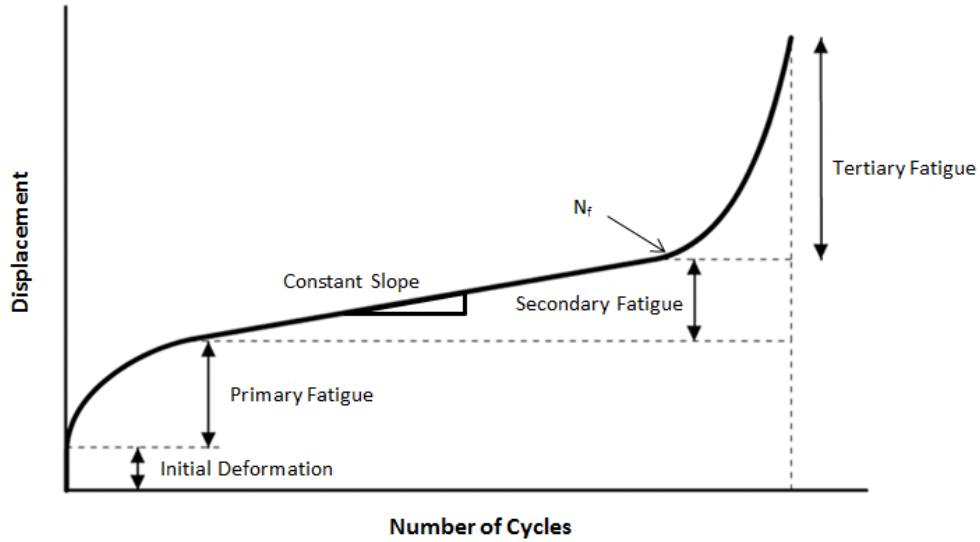


Figure 3.16: Typical Fatigue Curve

The complex modulus, E^* , represents the storage and loss moduli of a viscoelastic material. The complex modulus is a complex number that relates the stress and strain and this can be modeled from the equation below:

$$E^* = E' + iE'' \quad \text{Eq. 3.35}$$

where:

E = storage modulus or elastic component of the complex modulus (MPa);

E'' = loss modulus or the viscous component (MPa).

The complex modulus can also be determined by evaluating the stress and strain rate at different locations. By calculating the ratio of the stress amplitude and the strain-rate from the cyclic test, the dynamic modulus is represented as:

$$E^* = \frac{\sigma_o}{\varepsilon_o} \quad \text{Eq. 3.36}$$

where:

σ_o = stress amplitude (MPa);

ε_o = strain-rate (mm/cycle).

Since the amplitude of the load cycle remains constant (i.e., stress remains constant), the deformation (i.e., strain) is the only variable changing. E^* remains constant over the secondary fatigue section since the stress is constant and the strain-rate is increasing at a constant rate. Therefore, it is actually critical to evaluate the number of cycles till E^* drops in magnitude and this is represented by N_f which is where the tertiary fatigue starts. Since E^* is a function of stress and strain, the strain rate influences E^* since stress is considered constant. The E^* finally reduces as the strain rate increases (since it is the denominator of the function). When the tertiary fatigue section starts, the strain rate increases and thus E^* decreases. In this research evaluation, N_f is used to determine the point at which E^* drops.

Fatigue testing was performed as a modified test from AASHTO T322-03, AASHTO T342-11, and methods adapted by Shu, Huang, & Vukosavljevic (2007). In these procedures, fatigue is evaluated by using different parameters such as loading curve, temperature, load amplitude, and a frequency in which the load is applied. For this study, fatigue was evaluated by using a sine wave loading condition, a test temperature of $20 \pm 1^\circ\text{C}$, a 2% pre-loading condition, a 25% ultimate loading condition, and a frequency of 10 Hz (Figure 3.17). For all specimens, the same loading condition was used to directly compare the specimens. The loading conditions were calculated based on the ultimate loads obtained from the dry specimens tested in IDT.

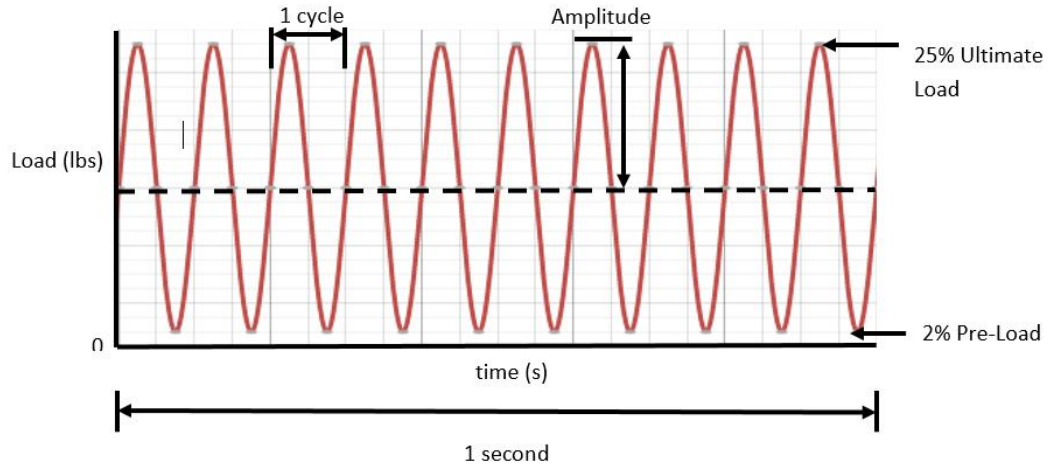


Figure 3.17: 10 Hz Sine Wave Representation of Fatigue Test

A sine wave was used to represent a cyclic loading condition to the specimen as it was tested in fatigue. The equation that was used to represent the loading cycle is shown below:

$$y(t) = A * \sin(2\pi ft + \varphi) \quad \text{Eq. 3.37}$$

where:

A = Amplitude (peak from the reference line) (N);

f = frequency (number of oscillations, or cycles, per second) (Hz);

t = time (s);

φ = phase (where the oscillation is at $t = 0$) (radians).

To evaluate the fatigue cracking resistance, a MTS 858 Mini Bionix II loading frame was used with a MTS 651 Environmental Chamber (Figure 3.18). This environmental chamber was connected to a temperature controller to ensure the temperature in the chamber was accurate. The chamber was also insulated to ensure the appropriate temperature did not fluctuate dramatically throughout testing. The same testing frame from the IDT, with a 12.7 mm loading

strip, was also attached to the MTS frame (Figure 4.18). This equipment recorded data by using MTS data acquisition software.



Figure 3.18: MTS Environmental Chamber with IDT Testing Frame

The samples that were used for fatigue testing were 101.6 ± 2.0 mm diameter by 50.8 ± 2.0 mm thick with duplicates tested. An important aspect of this type of testing was to evaluate both the horizontal and vertical displacements. The applied load and vertical displacement were both recorded directly from the MTS testing frame. After the sample was loaded, it was then tested according to specified protocol using the MTS software.

3.3.9 Thermal-Cracking Resistance

Thermal-cracking resistance was used as a parameter to evaluate the low-temperature response of fly ash-based asphalt mixtures. Thermal cracking is an important parameter to

evaluate in climates with cold weather because these types of cracks are directly related to low temperatures. Reducing the asphalt mixture stiffness can reduce the effects of thermal cracking and this is critical for low-temperature evaluations. Stiffer asphalt mixtures usually perform worse in lower temperatures whereas asphalt binders that are soft typically perform better. Asphalt binders that are excessively aged also have poor performance in lower temperatures because the binder has been exposed to higher amounts of age-hardening due to excessive oxidation.

Low-temperature thermal cracking resistance was evaluated by using the Semi-Circular Bending Test (SCB). The SCB is a 3-point bending test using semi-circular specimens, with a notch cut in the bottom, at lower temperatures to evaluate Fracture Energy (G_f) and Stiffness (S). The Fracture Energy, G_f (J/m^2), is the energy required to create a unit surface area of a crack. This is obtained by dividing the work of fracture (area under the load vs. load line displacement curve, Figure 3.19) by the ligament area (ligament length and thickness of specimen). The Stiffness, S (kN/mm), is the slope of the linear portion of the load-line displacement curve (Figure 3.20).

$$G_f = \frac{W_f}{A_{lig}} \quad \text{Eq. 3.38}$$

$$W_f = \int P du = W + W_{tail} \quad \text{Eq. 3.39}$$

$$A_{lig} = (r - a) * t \quad \text{Eq. 3.40}$$

where:

$W_f = \int P du = W + W_{tail}$, work of fracture (J);

P = applied load (N);

u = load line displacement (m);

A_{lig} = ligament area (m²);

r = specimen radius (m);

a = notch length (m);

t = specimen thickness (m).

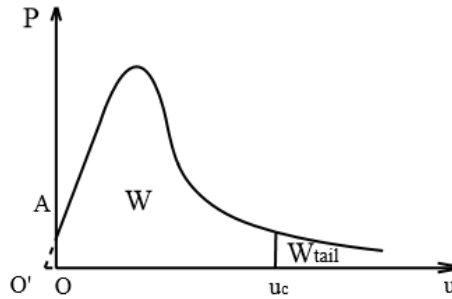


Figure 3.19: Low-Temperature Load vs. Load-Line Displacement Representation

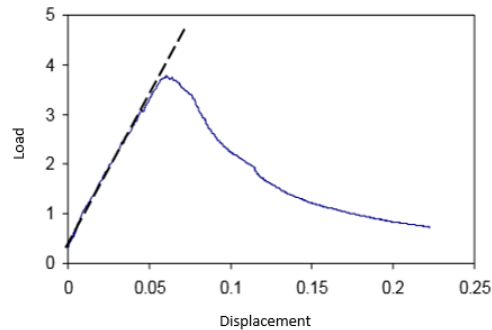


Figure 3.20: Stiffness (S) Determination of Low-Temperature Testing

Samples were cut in half (laterally) and then cut to a 25.4 ± 2.0 mm thickness. A 1.5 ± 0.3 mm by 10.0 ± 0.5 mm notch was centrally cut at the base of the specimen. The test temperature was set to $-18 \pm 1^\circ\text{C}$ and the loading rate was 0.03 mm/min. The samples were conditioned for 2 ± 0.2 h at $-18 \pm 1^\circ\text{C}$ prior to testing (duplicates were tested). For all specimens, the same loading condition was used to directly compare the specimens.

The SCB test was performed using the MTS 858 Mini Bionix II loading frame, the MTS 651 Environmental Chamber, and a 3 point-testing frame. The test was finished once the load dropped below 0.5 kN. This machine was used to evaluate both the vertical load and the vertical load-line displacement.

3.4 DURABILITY TESTING

This section explains the experimental testing matrix for both the control asphalt mastics and mixtures as well as reactive powder asphalt mastics and mixtures in terms of durability testing (all asphalt materials were long-term aged and all asphalt mixtures were compacted to 93% G_{mm}). Table 3.7 presents the experimental testing matrix for all mastics and mixtures. For these tests, two samples were tested, and averages were determined. The durability testing that was performed evaluated self-healing, freeze-thaw exposure, and salt-scaling. The experimental testing methods are described in detail in the next sections.

Table 3.7: Testing Matrix for Durability Study

Mixture Property	Measured Indicator		Aging	Asphalt Binder	Powders	Mixture Types	Conc.
Freeze-Thaw	Mass Change	Freeze-Thaw Cycles	Long-Term	WMA PG58-28 WMA PG52-34	3	6	1
IDT Freeze-Thaw	Tensile Strength	Freeze-Thaw Cycles	Long-Term				
Salt Scaling	Mass Loss	Salt Scaling Cycles	Long-Term				

3.4.1 Self-Healing

Mastic durability testing was used to prove the idea of microstructural self-healing. For this specific testing the mastics were RTFO and PAV aged, and then applied to a 5 mm x 5 mm limestone tile as a thin liquid film at 115°C. Once the thin film of mastic adhered to the limestone tile and solidified at room temperature it was then exposed to rapid freezing by means of liquid nitrogen (-195.79°C). The long-term aged mastic (brittle from long-term aging) developed cracks and was then placed in a curing chamber for 3 days so that the unhydrated reactive powders could activate and hydrate. The idea was for the hydrated portland cement to bridge the walls of the open cracks and fill the opening. The hydrated portland cement would therefore heal the propagating crack, reduce the rate of crack propagation, and protect the aggregate from environmental exposure. These materials were evaluated under Scanning Electron Microscope (SEM) and images were investigated to understand the microstructure.

3.4.2 Mixture Durability Testing

Mixture durability testing was evaluated for both freeze-thaw and salt-scaling based on the experimental testing protocol in Table 3.7. As mentioned, the materials in this section were long-term aged and compacted to 93% G_{mm} as this is typical in the field.

3.4.2.1 Freeze-Thaw

Freeze-thaw damage resistance was an important parameter to evaluate since this is a critical durability concern, especially in climates with colder weather. The material expands and contracts due to temperature change which creates the internal stresses. As these stresses become too large the material can crack, water can penetrate, and then the material can fail. Therefore, increasing the resistance to freeze-thaw deformation can result in longer lasting materials. Since the asphalt binder is a flexible material, the material was long-term aged for this testing to mimic the brittleness effects caused by age-hardening and oxidation. This testing was also important to understand the effects of water exposure over a long period of time and how water can influence the hybrid material behavior. The reactive powder mixtures contained the unhydrated portland cement and adding water to the hybrid reactive powder mixture could potentially cause the particles to hydrate and act a self-healing agent.

3.4.2.1.1 Standard Freeze-Thaw

The standard freeze-thaw testing was performed as a modified test in accordance to ASTM C666 (Procedure A) which evaluates the mass change of asphalt mixture samples due to rapid freezing and thawing in water. This procedure was used to evaluate the samples for 300 freeze-thaw cycles in a standard freeze-thaw chamber by measuring the mass loss every 36 cycles. The samples used in this section were 101.6 ± 2.0 mm diameter by 25.4 ± 2.0 mm thick

with duplicates tested. The testing procedure requires the samples to be conditioned in water at $4.5 \pm 1^\circ\text{C}$ and then placed into the environmental chamber for testing. The freezing and thawing cycles consisted of lowering the testing temperature from 4 to -18°C and then raising the temperature from -18 to 4°C in not less than 2 h and not more than 5 h (not less than 25% of the time shall be used for thawing). At the end of the cooling period the temperatures at the center of the specimens shall be $-18 \pm 2^\circ\text{C}$ and at the end of the thawing period the temperature shall be $4 \pm 2^\circ\text{C}$. At no point was it permitted for the specimens to reach a temperature lower than -19°C nor higher than 6°C .

3.4.2.1.2 IDT Freeze-Thaw

The Humboldt Indirect Tensile Machine was used to evaluate the IDT freeze-thaw exposure for 0, 10, 20 cycles as a modification of ASTM T283-07 (the testing specifications for using the IDT equipment are the same as described in Section 3.3.7.2). The samples that were tested were 101.6 ± 2.0 mm in diameter and 50.8 ± 2.0 mm in thickness. Sample preparations for IDT freeze-thaw exposure were similar to those described in Section 3.3.7.1. However, for this testing, 1 cycle of freeze-thaw exposure consisted of a dry sample being saturated to 70 – 80% degree of saturation, wrapped in plastic, placed in a sealed bag containing 10 mL of water, placed into a freezer at -18°C for 24 ± 1 h, placed into a water bath at $60 \pm 1^\circ\text{C}$ for 24 ± 1 h, then dried at $25 \pm 0.5^\circ\text{C}$ for 24 ± 1 h. All samples were tested in the dry condition and duplicates were evaluated.

3.4.2.2 Salt-Scaling

Salt-scaling was evaluated to understand the resistance to surface scaling of an exposed horizontal asphalt surface that was subjected to freezing and thawing cycles in the presence of

deicing chemicals. Salt-scaling is the flaking of a surface of hardened concrete or flaking of a surface of aggregate due to the deterioration caused by the deicing agent. This type of environmental exposure is very common in climates with colder temperatures because salt is used to remove the ice on pavements even though these chemicals cause durability concerns. For this reason, salt-scaling testing was important to evaluate the effects of the reactive powders on the performance of developed hybrid asphalts.

This testing was performed on gyratory compacted specimens (93% G_{mm}) in accordance to the procedure described in RILEM TC176-IDC: 'Internal Damage of Concrete due to Frost Action' CIF-Test: Capillary Suction, Internal Damage and Freeze Thaw Test – Reference Method. This testing procedure is a modification ASTM C672 which is the standard test procedure for the scaling resistance of concrete surfaces exposed to deicing chemicals. With this procedure, the unsealed face of the sample was submerged 6 mm face down in a 3% salt solution. The samples that were tested were 152.4 ± 2.0 mm in diameter and 50.8 ± 2.0 mm in thickness. The samples were then exposed to 50 freeze-thaw cycles. Each of the cycles consisted of 16 – 18 h in the freezing environment followed by a storage at $23 \pm 2^\circ\text{C}$ and a relative humidity of 45 – 55% for 6 – 8 h. The salt solution was added before each freezing phase of the cycle. After each 5 cycles the salt solution was removed and the face of the sample was washed and strained through a filter to collect all flake materials. The flake solution was dried in an oven at 105°C to a constant mass and then the residue was cumulatively weighed, and the mass was recorded. Duplicate samples were tested to determine average mass loss.

3.5 FIELD IMPLEMENTATION TESTING

This section explains the experimental testing matrix for the field implementation testing protocol. Table 3.8 presents the experimental testing matrix for all asphalt mixtures. All testing methods for this phase are described in detail in Section 3.3. For the aggregate coating, workability, and aging comparison, six replicates were produced and compared. For the moisture damage resistance, fatigue cracking resistance, and thermal cracking resistance, two replicates were produced and tested. The experimental testing methods were described in detail in the previous sections.

Table 3.8: Testing Matrix for Field Implementation Study

Mixture Property	Measured Indicator		Aging	Asphalt Binders	Powders	Mixture Types	Conc.
Aggregate Coating	Asphalt Binder Film Thickness		Short-Term	2	2	9	1
Workability	% Air at 8 Gyration		Short-Term				
Aging Comparison			Long-Term				
Moisture Damage	TSR	Dry	Long-Term				
		Saturated					
		Conditioned					
Fatigue	E* using IDT	Intermediate Temp.	Long-Term				
Thermal Cracking	G _f & S(t)	Low Temp.	Long-Term				

CHAPTER 4

RESULTS AND DISCUSSION

4.1 REACTIVE POWDER CHARACTERIZATION

Reactive powders that were used in this study were evaluated for both chemical and physical properties. In this study there was 1 reference limestone powder, 1 SDA powder, and 5 portland cement reactive powders which were collected from different parts of the United States. Table 4.1 lists the specific sources of these powders and their associated abbreviations which are used in the remaining sections. The reactive powders covered a wide range of both chemical and physical properties to completely assess the effects that these parameters had on the performance of the composite materials. In this section, the chemical and physical properties are characterized by investigating the chemical and physical properties.

Table 4.1: Filler Materials used in Mastic Testing

Type	Origin/Supplier	Abbreviation
Control	Payne & Dolan Limestone Filler	LS
Reactive Powders	Weston Spray Dryer Absorber	SDA
	Lafarge Type I	LF
	St. Mary Type I	SM
	Buzzi Unicem CSA	CSA
	Lafarge Oil Well	OW
	Kerneos High Alumina	HA

4.1.1 Chemical Properties

Chemical property testing was performed on the investigated powders. The chemical properties that were tested were chemical oxides, Loss on Ignition (LOI), and crystallography.

4.1.1.1 Chemical Oxide Composition

Chemical oxide composition was tested using X-Ray Fluorescence (XRF) in accordance to ASTM C114. It was important to investigate the chemical composition of the powders to fully understand the effects the reactive powders had on the performance of the asphalt mastics and asphalt mixtures. The ASTM C150 is the standard specification for portland cement and ASTM C618 is the standard specification used for coal fly ash and natural pozzolans for use in concrete. These standards were used when classifying the reactive powders and limestone filler that were used in this research study. The limitations were based on $\text{SiO}_2 + \text{Al}_2\text{O}_3 + \text{Fe}_2\text{O}_3$ contents for the SDA material which is classified as SAF content. Figure 4.1 to 4.3 show the range of the oxides which were important in determining the SAF content.

Figure 4.1 demonstrates that the SDA material had the highest SiO_2 content of 27.22% and the control limestone powder had the lowest SiO_2 content of 3.33%. Other materials such as LF, SM, and OW cements also had high SiO_2 contents when compared to the control limestone. Figure 4.2 reports the HA cement having the most extreme Al_2O_3 content of 38.67% and the control limestone having the lowest Al_2O_3 content of 0.63%. Figure 4.3 reports the HA cement also having the highest Fe_2O_3 content of 15.46% and the control limestone having the lowest Fe_2O_3 content of 0.31%.

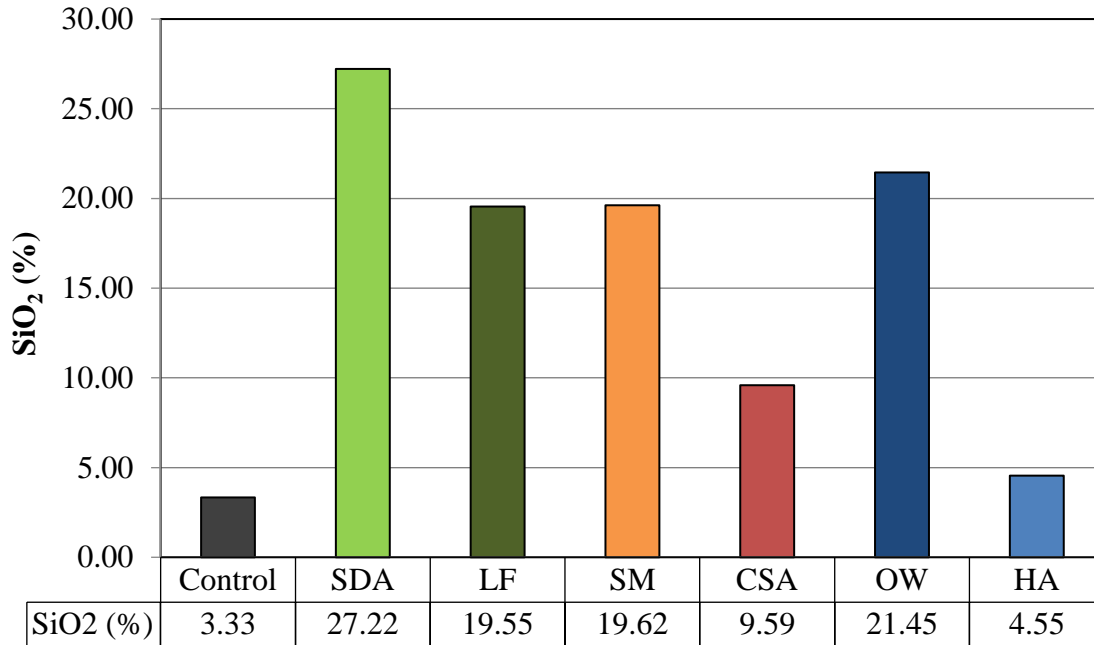


Figure 4.1: SiO₂ Content for Investigated Powders

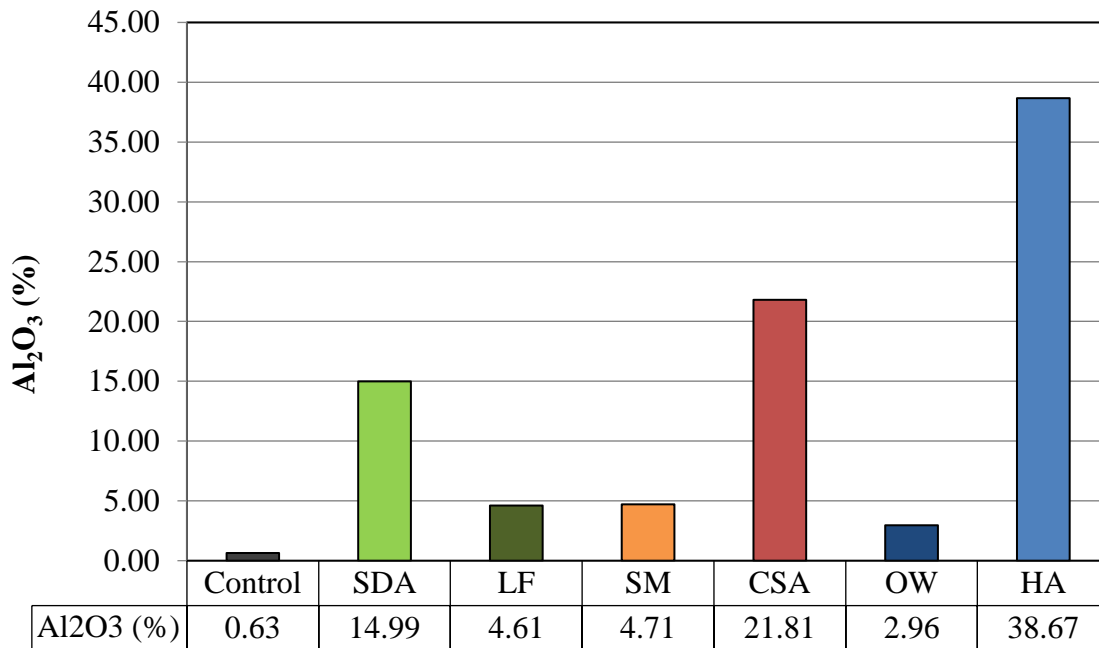


Figure 4.2: Al₂O₃ Content for Investigated Powders

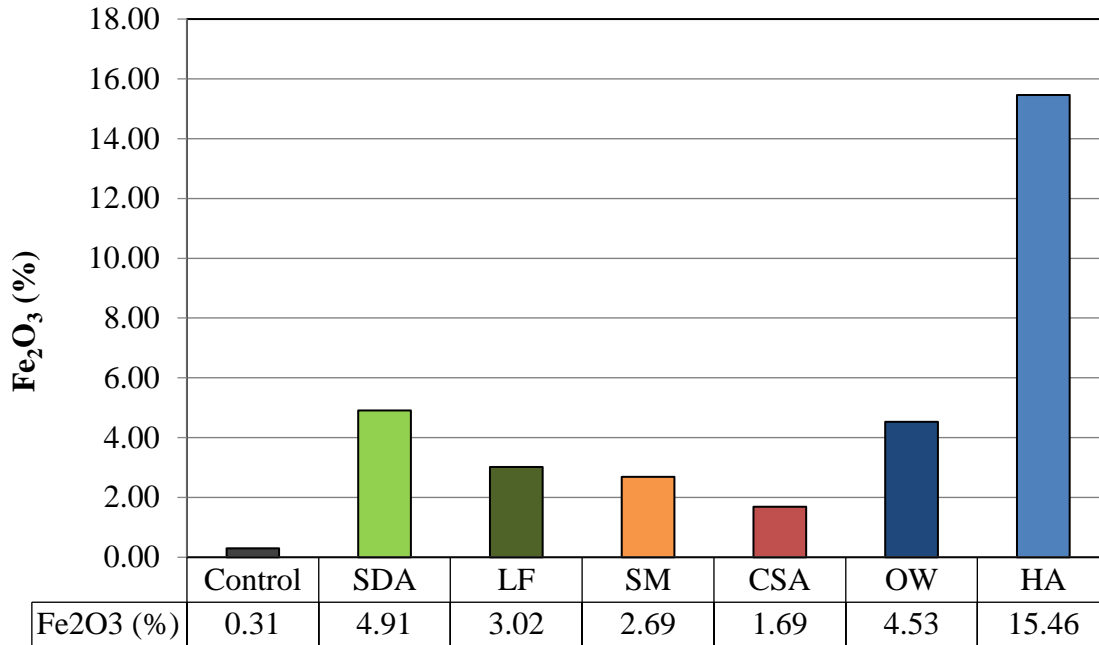


Figure 4.3: Fe₂O₃ Content for Investigated Powders

Other chemical oxides that were reported to influence the performance of asphalt mastics were both CaO and SO₃ (Ahmed et al., 2010; Wang et al., 2011, DeFoe, 1983; Liao & Huang, 2008; Wu, 2009). Figure 4.4 displays the CaO content being the highest for LA cement at 64.18%, and relatively high for SM, and OW cements and the SDA material had the lowest CaO content of 28.15%. Figure 4.5 reports the SO₃ content being the highest for CSA at 19.06% and the lowest for the control limestone at only 0.07%.

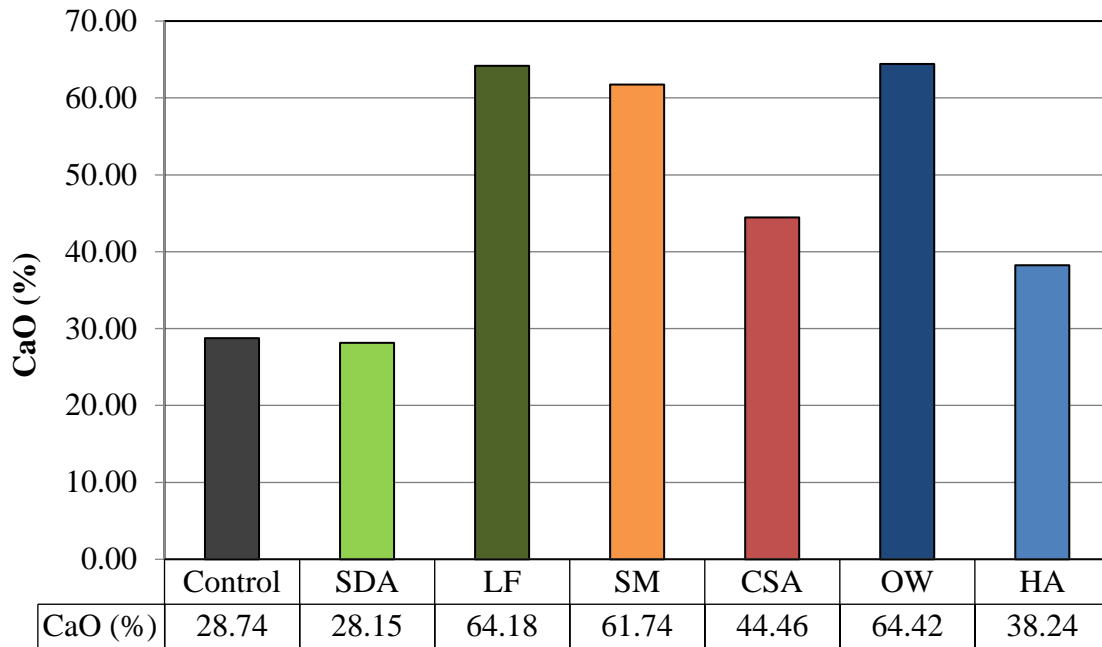


Figure 4.4: CaO Content for Investigated Powders

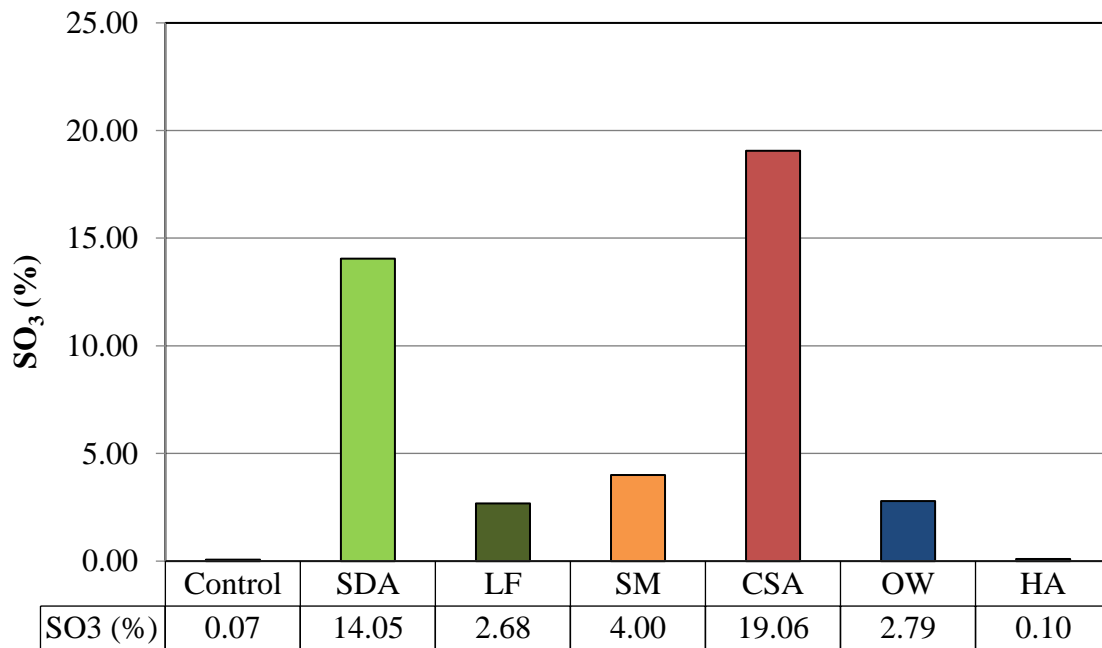


Figure 4.5: SO₃ Content for Investigated Powders

Based on the previous results the filler materials were all summarized using a ternary diagram shown in Figure 4.6 which illustrates the distribution of aluminum oxide (Al_2O_3), calcium oxide (CaO), and silicon dioxide (SiO_2). From the ternary diagram it can be seen that the control limestone had a large quantity of CaO and SiO_2 but also had a low quantity of Al_2O_3 . The SDA material had a balance of both CaO and SiO_2 but at the same time also had a high quantity of Al_2O_3 when compared to the control limestone. The reactive powders (cements) all generally had high contents of CaO , SiO_2 , and Al_2O_3 and the CSA and HA cements had the high quantities of Al_2O_3 .

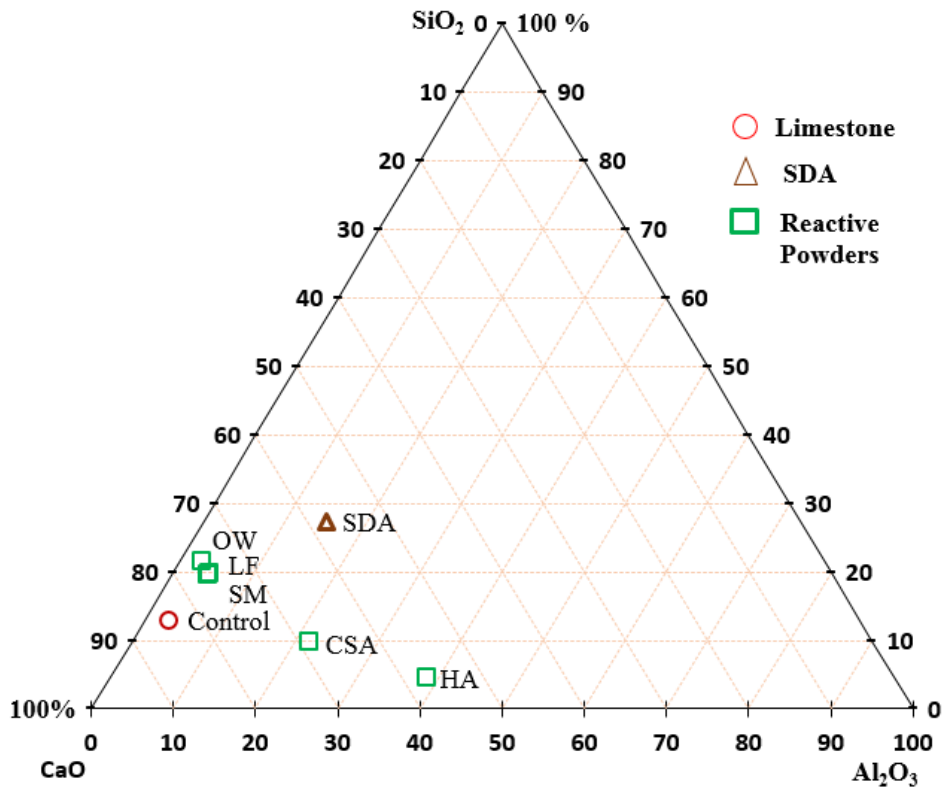


Figure 4.6: Ternary Diagram for Investigated Powders

The remaining chemical oxides that were tested are summarized below in Table 4.2 and it can be observed that other chemical oxides such as Na₂O and P₂O₅ are low (< 1%) in terms of overall chemical compositions but vary quite a bit in terms of relative composition.

Table 4.2: Chemical Oxide Contents for Investigated Powders

Sample ID	SiO ₂ (%)	Al ₂ O ₃ (%)	Fe ₂ O ₃ (%)	CaO (%)	MgO (%)	SO ₃ (%)	Na ₂ O (%)	K ₂ O (%)	TiO ₂ (%)	P ₂ O ₅ (%)	Mn ₂ O ₃ (%)	SrO (%)	LOI (%)
Control	12.77	3.16	2.05	57.82	2.61	2.71	0.15	0.33	0.18	0.11	0.06	0.04	45.33
SDA	27.22	14.99	4.91	28.15	4.00	14.05	1.21	0.40	1.12	0.78	0.04	0.25	1.13
LF	19.55	4.61	3.02	64.18	2.50	2.68	0.21	0.48	0.28	0.12	0.11	0.07	1.82
SM	19.62	4.71	2.69	61.74	3.93	4.00	0.16	1.00	0.29	0.10	0.15	0.06	1.62
CSA	9.59	21.81	1.69	44.46	1.49	19.06	0.12	0.27	0.64	0.19	0.07	0.08	0.59
OW	21.45	2.96	4.53	64.42	2.89	2.79	0.11	0.20	0.20	0.12	0.06	0.09	0.00
HA	4.55	38.67	15.46	38.24	0.70	0.10	0.06	0.10	1.84	0.12	0.12	0.02	0.47

4.1.1.2 Loss on Ignition (LOI)

The Loss on Ignition (LOI) contents for the filler materials were evaluated based on ASTM C311 using a TGA701 Thermogravimetric Analyzer. Figure 4.7 demonstrates the results of LOI and it can be seen that the LOI content for the control limestone filler was the highest at 45.33% (due to the decomposition of CaCO₃) and the other reactive powders had low LOI contents.

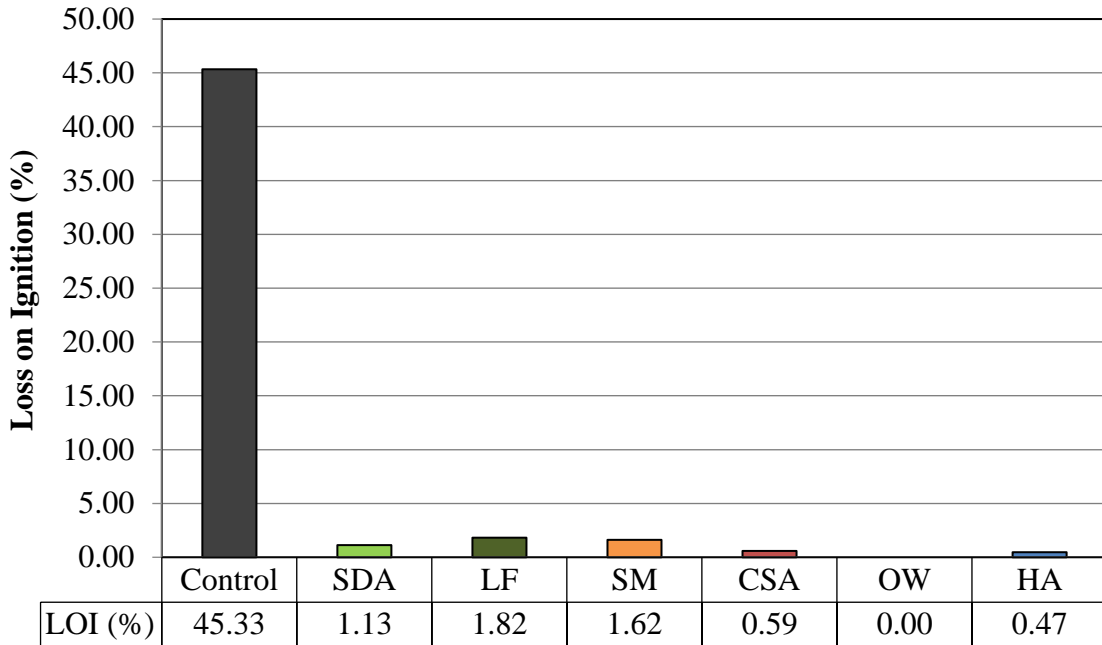


Figure 4.7: Loss on Ignition (LOI) for Investigated Powders

4.1.1.3 Crystallography

Material crystallography was evaluated using X-Ray Diffraction (XRD). The XRD is a microstructural investigation technique used to analyze crystalline materials by evaluating the atomic planes of a crystal and can be used to determine the phase composition, unit cell lattice parameters, residual strains, crystal structure, and even crystal size.

In this study, XRD was primarily used to look at the crystallinity of all the filler materials based on XRD intensity plots. Figure 4.8 reports on the XRD results for the control limestone and these results demonstrate that the control limestone filler is a crystalline material based on the high intensity peak of 452.58 CPS at 30.93 2 θ .

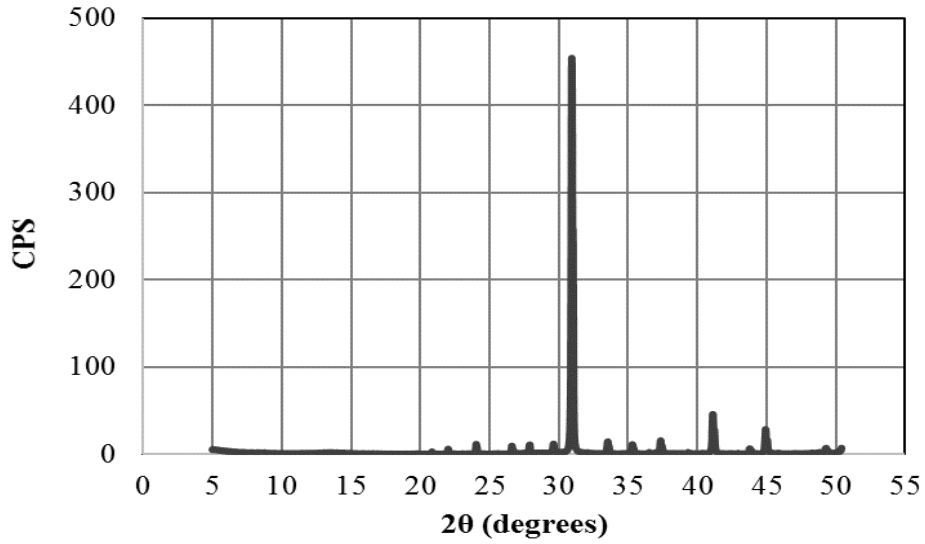


Figure 4.8: XRD for Control Limestone

Figure 4.9 displays the XRD results for the Spray Dryer Absorber (SDA) material. From the XRD analysis the SDA material had high backgrounds and low intensity peaks which suggests an abundance of amorphous glass phases due to quartz being the dominant phase.

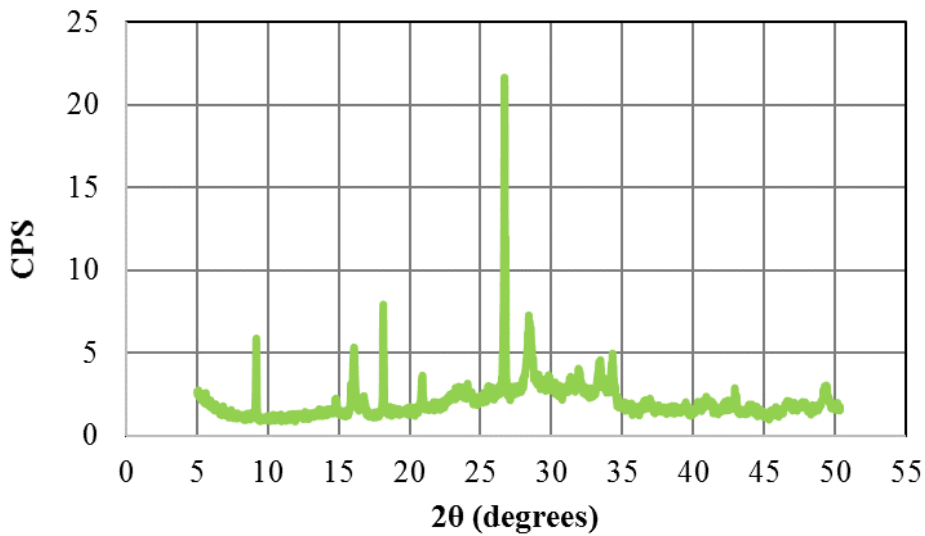


Figure 4.9: XRD for Spray Dryer Absorber (SDA)

Figure 4.10 displays the XRD results for all the reactive powders. It can be observed that the reactive powders can all be classified as crystalline materials based on the low backgrounds and high intensity peaks. All the reactive powders had relatively the same intensity and the same incident angle. The LF cement had a max intensity peak of 44.47 CPS at 32.24 2θ , SM cement had a max intensity peak of 34.34 CPS at 32.23 2θ , CSA cement had a max intensity peak of 73.41 CPS at 23.71 2θ and another large peak of 72.26 CPS at 25.45 2θ , OW cement had a max intensity peak of 61.59 CPS at 32.26 2θ , and HA cement had a max intensity peak of 26.21 CPS at 30.01 2θ .

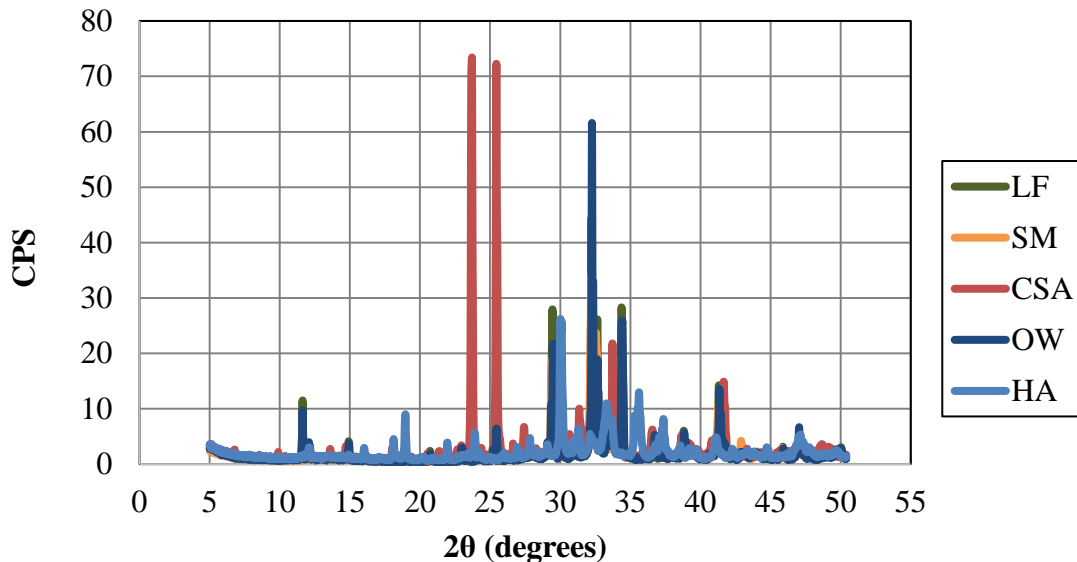


Figure 4.10: XRD for Reactive Powders

4.1.2 Physical Properties

Physical property testing was performed on the 1 limestone powder, 1 SDA powder, and the 5 portland cement reactive powders. The physical properties that were tested were specific gravity (SG), particle size distribution (PSD), particle shape, and Rigden voids.

4.1.2.1 Specific Gravity

Specific gravity (SG) was evaluated based on ASTM D5550-06 using a Helium Pycnometer. Figure 4.11 presents the results of the specific gravity testing. The results prove that the specific gravity for the all materials are similar, however HA cement had the highest SG of 3.22 and the SDA had the lowest SG of 2.63. The SG values were important for this research study since these were used for Rigden Void (RV) determination as well as for conversion of mastic and WMA volumetrics.

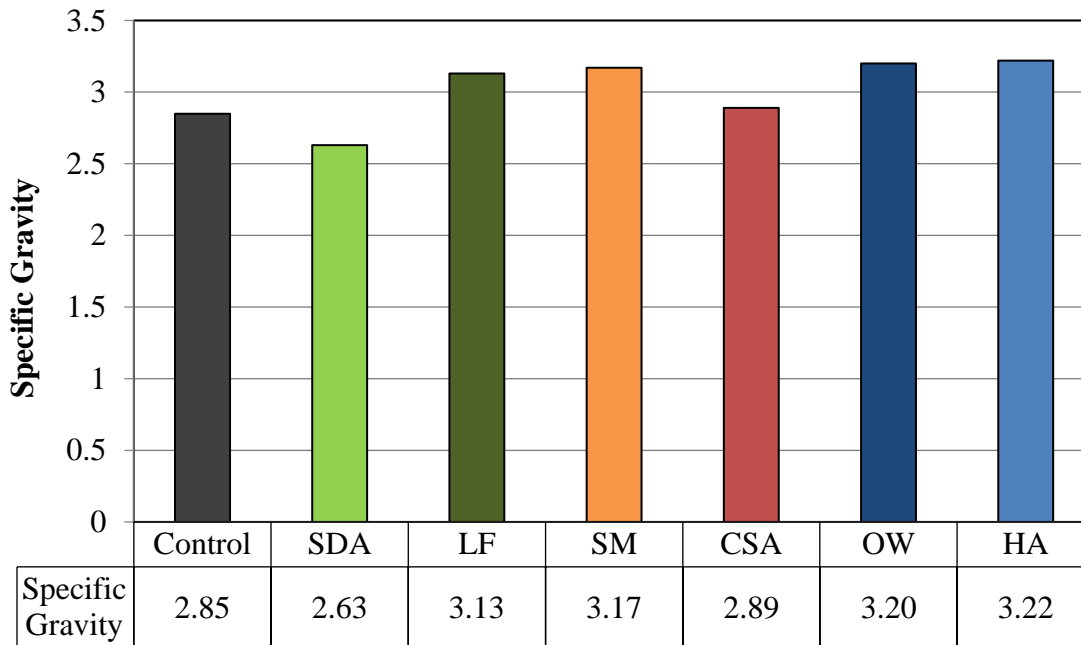


Figure 4.11: Specific Gravity of Investigated Powders

4.1.2.2 Particle Size Distribution (PSD)

The particle size distributions (PSD) of all powder materials were evaluated based on ASTM D4464-10 using laser light scattering. This specific technique has capabilities of measuring particles from 1 to 300 μm , and can determine D_{10} , D_{50} , and D_{90} values. Figure 4.12

presents the particle size distribution curves for all powders and it can be seen that the control limestone had the largest average particle sizes out of all materials whereas the SDA material had the smallest average particle sizes when compared to all other materials. The reactive powder particle sizes generally ranged between the SDA and the control limestone filler. The maximum particle size ranged between 200 – 300 μm for the control limestone, 200 – 300 μm for SDA, 60 – 80 μm for LF, 50 – 60 μm for SM, 60 – 80 μm for CSA, 100 – 200 μm for OW, and 50 – 70 μm for HA.

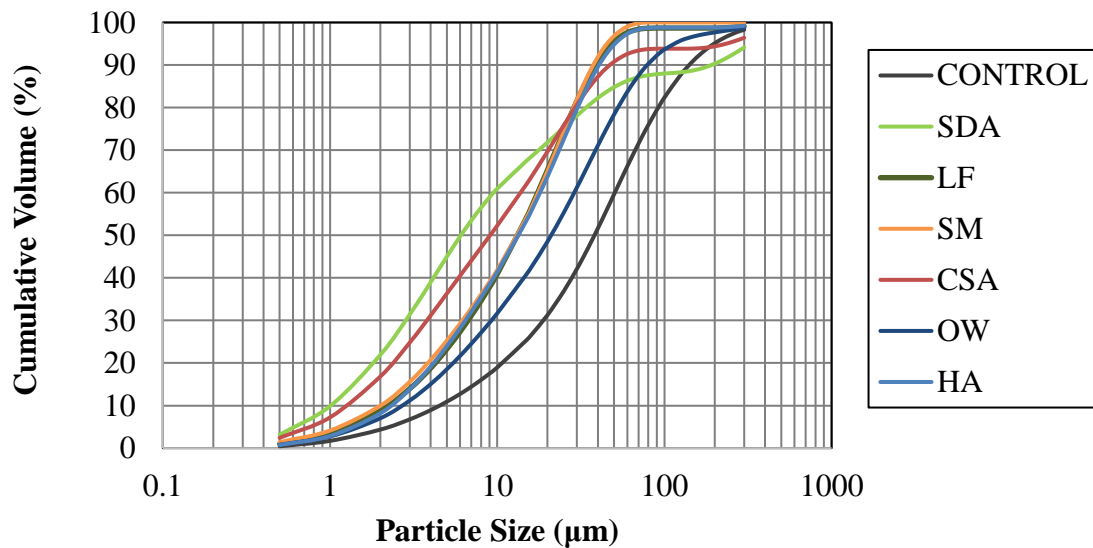


Figure 4.12: Particle Size Distribution (PSD) of Investigated Powders

From the PSD curves, values of D_{10} , D_{50} , and D_{90} were obtained. Figure 4.13 reports the D_{10} values for all investigated materials. It can be observed that the SDA material is characterized by smaller particles since the D_{10} value is only at 1.01 μm when compared to all other powders and the control limestone had much coarser particles since the D_{10} value is 4.52 μm . The D_{10} of reactive powders generally ranged from 1.28 – 2.71 μm .

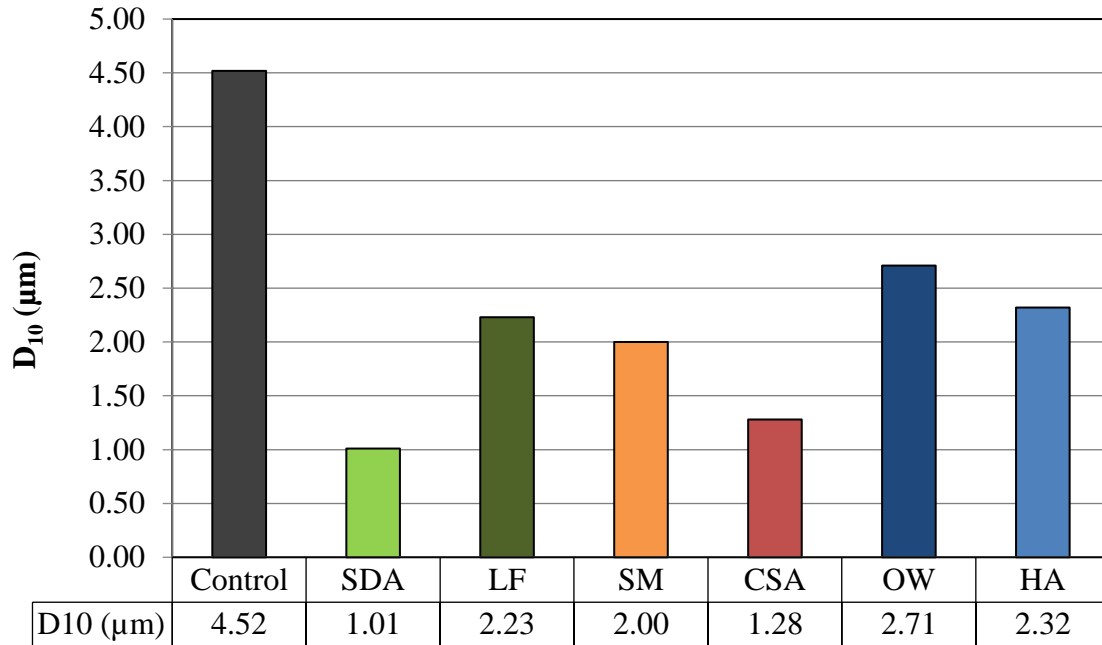


Figure 4.13: D₁₀ Values of Investigated Powders

Figure 4.14 presents the D₅₀ values for all investigated powders and it can be seen that these results represent the same trend with the control limestone filler being the coarsest material and the SDA being very fine. The SDA material had a D₅₀ of only 6.06 µm and the control limestone had a D₅₀ of 38.10 µm. The reactive powders ranged between 13.20 – 21.00 µm.

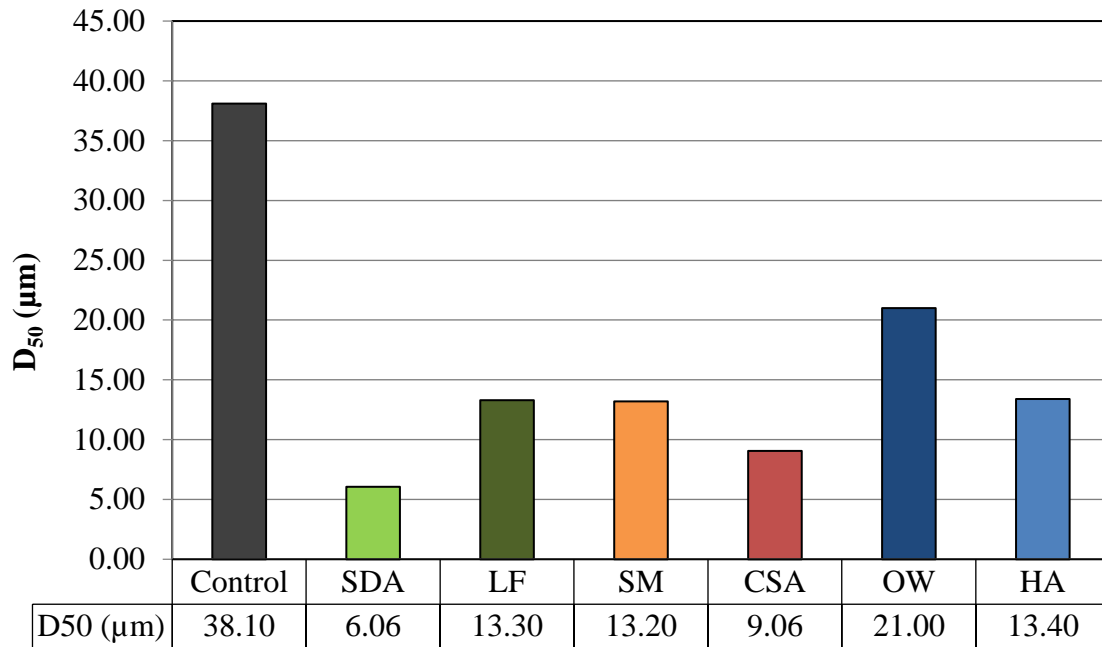


Figure 4.14: D₅₀ Values of Investigated Powders

Figure 4.15 demonstrates the D₉₀ values for all investigated powders. It is interesting that the trends observed for D₁₀ and D₅₀ changed as the particles got closer to D₉₀. The D₉₀ results demonstrate that the SDA becomes the coarsest as compared to all other materials, possibly due to agglomeration. The SDA had a D₉₀ of 192.00 µm and the control limestone had a D₉₀ of 141.00 µm. The reactive powders were all within the same range for D₉₀ values from 37.60 – 78.90 µm.

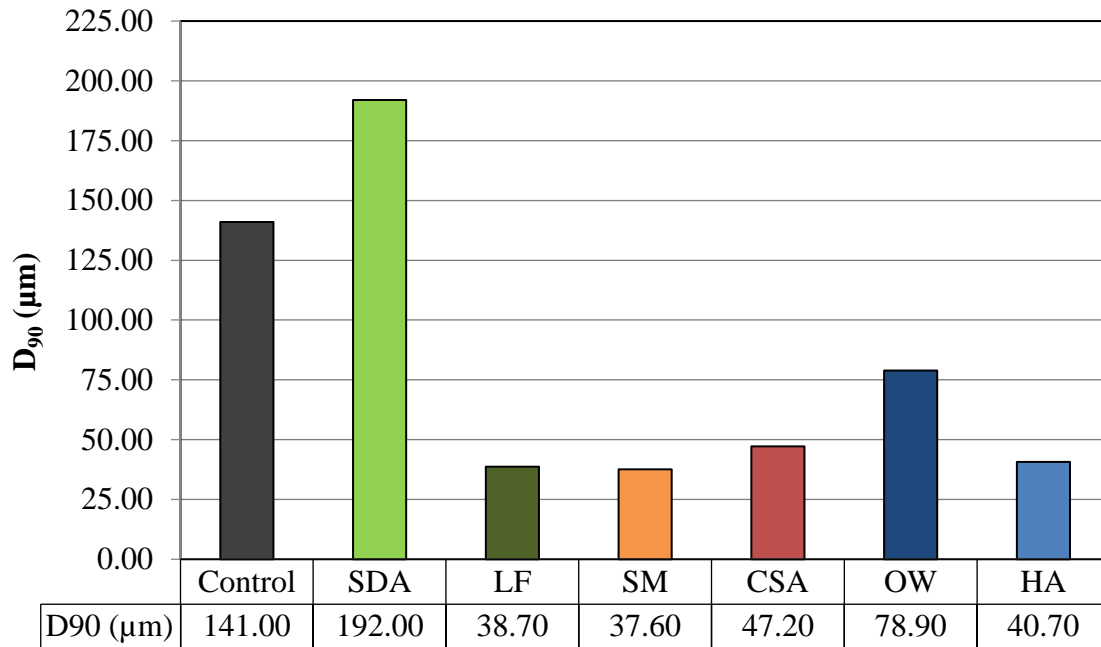


Figure 4.15: D₉₀ Values of Investigated Powders

4.1.2.3 Particle Shape

Particle shape was evaluating using a TOPCON® SM-300 Scanning Electron Microscope (SEM) in accordance to ASTM E986. A SEM is an electron imaging microscope that has the spatial resolution to examine microscopic structure by scanning material surfaces. The SEM is used for inspecting topographies of specimens at very high magnifications. Materials can be analyzed for physical defects, bond failures, fracture surfaces, and cracks. The SEM image is formed by a focused electron beam that scans over the surface area of a specimen. In this research study, the control limestone powder, SDA powder, and portland cement reactive powder were all evaluated to examine the surface texture and shape.

Figure 4.16 reports the SEM images for all types of powders. The control limestone powder is composed of individual flake shaped particles whereas the SDA material is composed

of mostly individual spherical particles. The portland cement is represented by small flake particles with larger rigid forms. The particle sizes also correlate well with the particle size distributions (PSD) which were already discussed in the previous section.

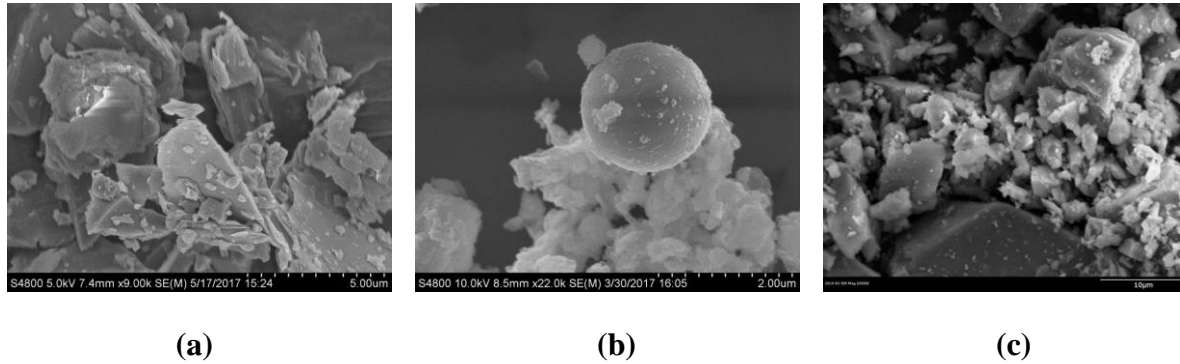


Figure 4.16: SEM Images of (a) Control Limestone (b) Spray Dryer Absorber (SDA) (c) Portland Cement Reactive Powder

4.1.2.4 Rigden Voids

The Rigden voids (RV) test, also known as the fractional voids test, was performed in accordance to EN1097-4. This test was developed to evaluate the particle packing of filler materials which was directly associated with the testing performance of asphalt mastics. Rigden voids are important when understanding the interactions between filler void characteristics and asphalt binders and the associated stiffness properties that result from these interactions.

Figure 4.17 reports on the Rigden voids for all the investigated materials. The Rigden voids for the SDA material is the highest at 41.71%, whereas the Rigden voids for the control limestone is the lowest at 26.80% (due to a larger particle range). The reactive powders have a uniform range between 31.11 – 35.06%.

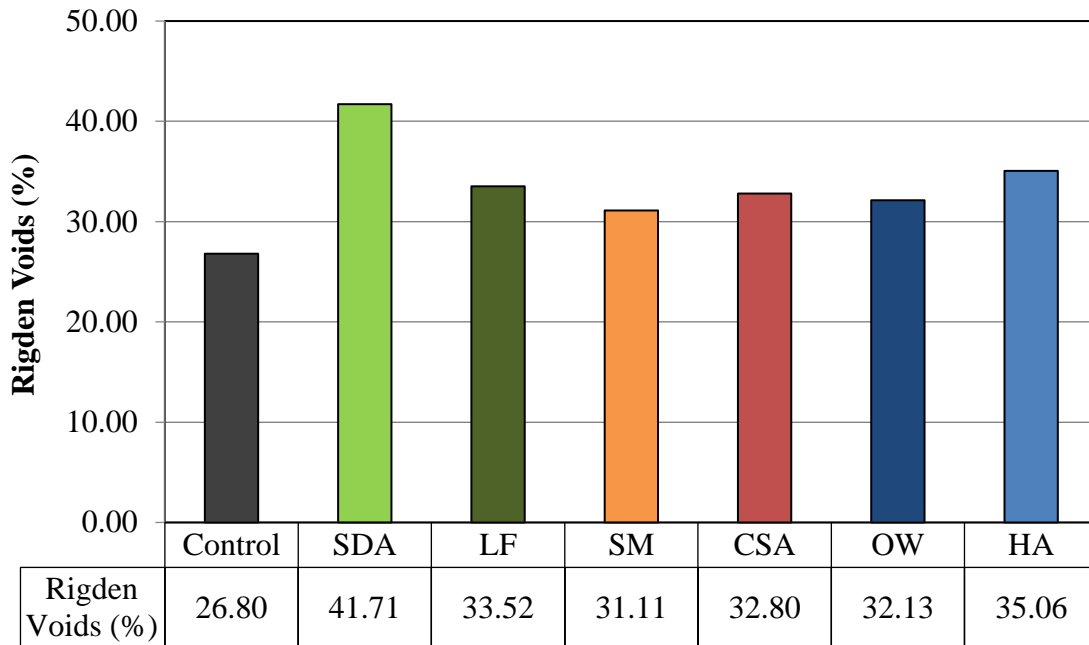


Figure 4.17: Rigden Voids (RV) of Investigated Powders

4.2 MASTIC TESTING (NON-PERFORMANCE RELATED INDICATORS)

The reactive powders that were evaluated for chemical and physical properties were added to WMA PG58-28 and WMA PG52-34 asphalt binders at concentrations of 0 (reference), 5, 15, 25% by volume of binder replacement and tested. These asphalt binders were also modified with Evotherm by Ingevity® which is a Warm Mix Asphalt modifier composed of approximately 60-70% alkyl acid phosphates and 30-40% modified tall oil fatty acids. Testing comparisons for HMA PG58-28 and WMA PG58-28 binders were assessed and compared with performance of HMA PG52-34 and WMA PG52-34 binders.

4.2.1 Complex Shear Modulus (G^*)

The Dynamic Shear Rheometer (DSR) was used in accordance to AASHTO T315 to determine the specimen's response to shear and report on the complex shear modulus (G^*) and the phase angle (δ) at the high PG temperature (58°C for PG58-28 and 52°C for PG52-34). The G^* is the measure of the total resistance to shear deformation while the sample is repeatedly sheared and δ is the phase angle between the recoverable and non-recoverable deformation. Larger values of G^* are typically desirable as this indicates a better resistance to shear deformation. This section summarizes the results for unaged mastic DSR testing for WMA PG58-28 and WMA PG52-34 mastics at all powder concentrations. The non-performance related indicators are only used to evaluate the interactions between the unaged WMA binders and the powders at different concentrations since the powders range in chemical and physical properties as was reported in the previous sections.

Table 4.3 compares the results for G^* and δ for unaged HMA PG58-28 and WMA PG58-28 asphalt binders. The results demonstrate that the HMA binder is stiffer than the WMA since the G^* is larger. This is potentially due to the Evotherm WMA binder modifier acting as a softening (plasticizing) agent which helps to reduce the mixing temperature. The phase angle, on the other hand, stays relatively the same regardless of stiffness.

Table 4.4 compares the test results for G^* and δ for HMA PG52-34 and WMA PG52-34 unaged asphalt binders. Similarly to the PG58-28 binders, the results indicate the reduced G^* values for the WMA binder when compared to the HMA binder with the phase angle not changing. These results also suggest that the decrease in G^* for the WMA binder is a result of the Evotherm WMA modification acting as a softening agent.

Table 4.3: DSR Measured Indicators for Unaged PG58-28 HMA and Unaged PG58-28 WMA (Evotherm) at 58°C

	PG58-28 (HMA)	PG58-28 (WMA)
Test Temp. (°C)	58	58
G* (Pa)	1378.46	1346.80
Phase Angle	87.23	87.09

Table 4.4: DSR Measured Indicators for Unaged PG58-28 HMA and Unaged PG58-28 WMA (Evotherm) at 52°C

	PG52-34 (HMA)	PG52-34 (WMA)
Test Temp. (°C)	52	52
G* (Pa)	1545.84	1495.93
Phase Angle	85.69	85.47

Figure 4.18 demonstrates the results for all G* values for the unaged WMA PG58-28 mastics. The stiffness of these mastics varies drastically depending on both the quantity and type of filler material. Typically, larger values of G* are desirable as this reduces the overall shear deformation when repeatedly sheared. For this reason, values at each concentration are compared to the control limestone filler and larger values of G* are highlighted. For example, at 15% concentration by volume, the CSA mastic had a G* of 2153.40 Pa and this was larger than that of the control limestone G* of 1944.59 Pa which means that the response of CSA based mastic at 15% concentration was more desirable than the mastic with control limestone. Other mastics also had an increase in G* at different concentrations.

From the results, at lower concentrations the effects of the powders are not very defined, but at higher concentrations such as 25%, the effects are exaggerated and can be observed clearly. The SDA mastics indeed had the most dramatic increase in stiffness when compared to all other filler materials. The SDA mastic had a G* value of 3008.23 Pa at 25% concentration by

volume. When compared to the plain unfilled binder, the use of SDA at 15% concentration by volume increased the G^* of the mastic by 94.65% and by 123.36% at 25% concentration. As a comparison, the use of OW cement at 15% concentration by volume only increased the G^* of the mastic by 36.36% and 83.60% at 25% concentration.

Figure 4.19 displays the results for all G^* values for the unaged WMA PG52-34 mastics. The results indicate similar behavior of those obtained from the WMA PG58-28 asphalt mastics. The SDA mastics are clearly the stiffest materials, especially at 15% and 25% by volume concentrations. For the WMA PG52-34 mastics, when compared to the plain unfilled binder, the SDA mastic increased G^* by 79.20% at 15% concentration by volume and by 112.35% at 25% concentration by volume. As a comparison, the OW mastics only increased the G^* by 35.08% at 15% concentration by volume and the SM mastics only increased G^* by 90.68% at 25% concentration by volume. All mastics increased G^* when compared to the control limestone at 25% concentrations.

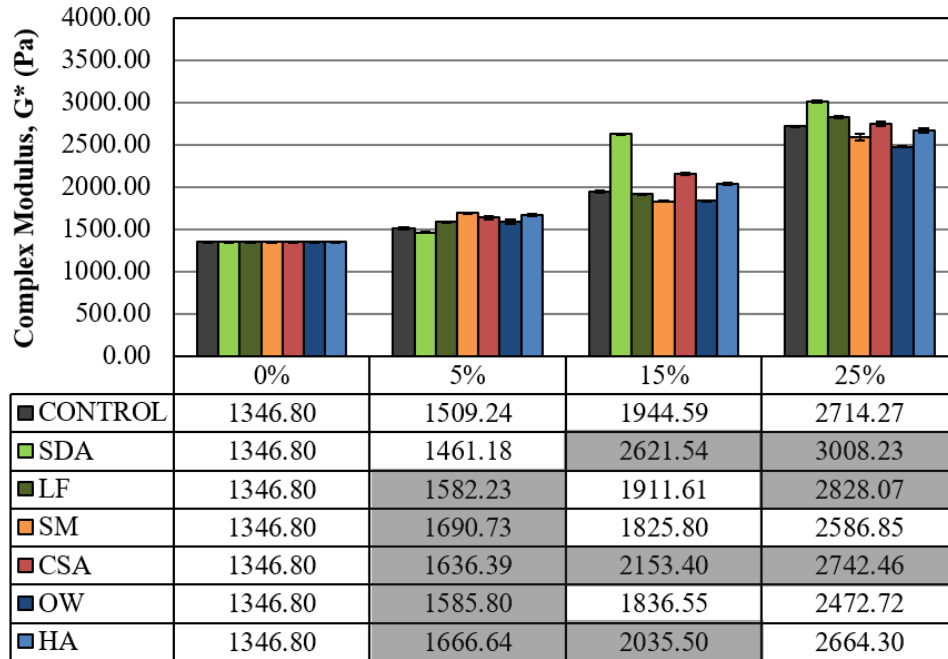


Figure 4.18 Complex Modulus (G^*) for Unaged PG58-28 WMA (Evotherm) Mastics at 58°C

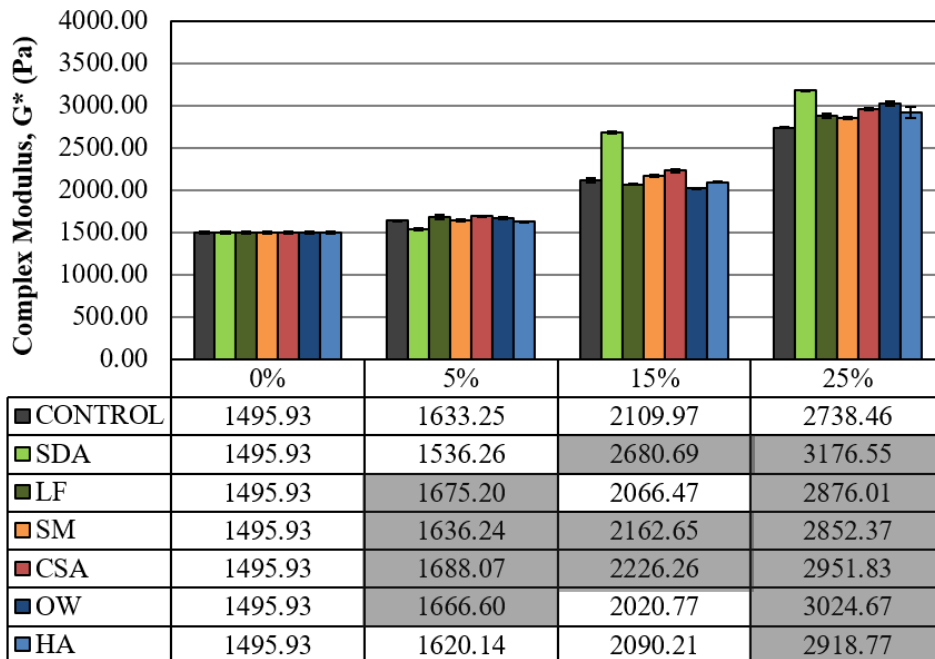


Figure 4.19: Complex Modulus (G^*) for Unaged PG52-34 WMA (Evotherm) Mastics at 52°C

As previously mentioned, the non-performance related indicators G^* and δ are simply used to evaluate the differences between mastics and more specifically used to evaluate the interactions between the powders and asphalt binders.

4.2.1.1 Relative Complex Shear Modulus (G^*r)

To directly compare the complex modulus (G^*) of the mastics, it was important to determine the relative complex shear modulus (G^*r). The relative complex shear modulus is the ratio of the complex modulus of the asphalt mastics over the complex modulus of the plain unfilled asphalt binder. By evaluating G^*r it is easier to understand the relationships between the asphalt binders and the powders.

Figure 4.20 and Figure 4.21 displays the relative complex modulus (G^*r) for WMA PG58-28 asphalt mastics and for WMA PG52-34 asphalt mastics. As observed from these graphs, the relative complex modulus curves are generally linear up to about 15% concentration by volume for both binder types but past this point the curves tend to become nonlinear as the slopes begin to increase at a higher rate. Beyond 15% concentration by volume the curves become asymptotic and more difficult to predict.

Most of the mastics are stiffer when compared to the control limestone filler at 5% concentration, however, when concentrations increase, the SM and OW cement mastics both become softer than the control, especially with the WMA PG58-28 binder. On the other hand, the SDA mastics and CSA mastics at concentrations higher than 5% result in a stiffer material than the control limestone mastics. This increase in G^*r indicates that the material requires more compaction efforts. Since the mastic results have the same trends between the asphalt binders, it is clear that G^* values depend on the filler type rather than the binder type.

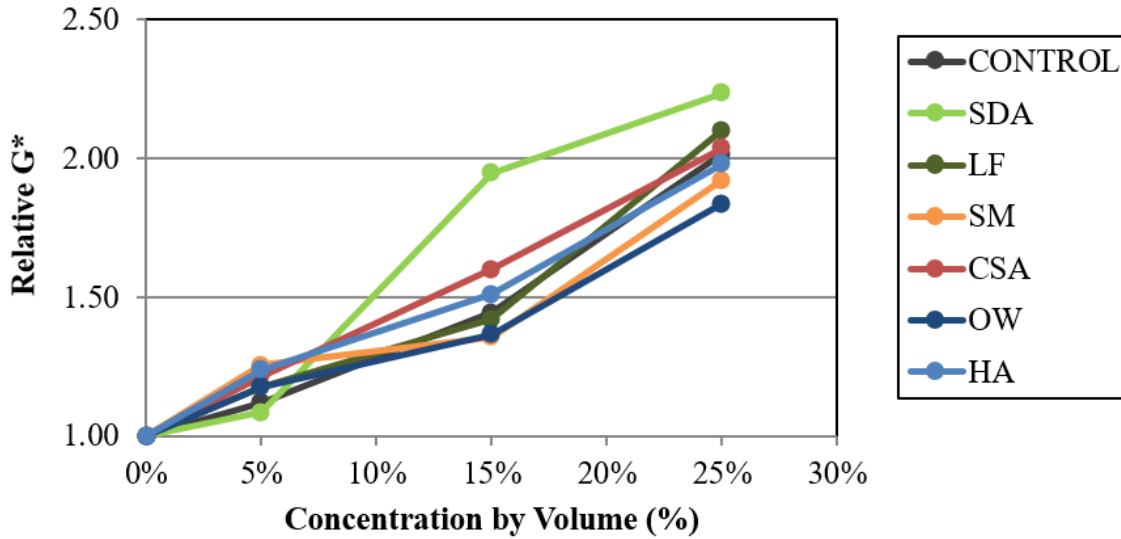


Figure 4.20: Relative Complex Modulus (G^*) for Unaged PG58-28 WMA (Evotherm) Mastics at 58°C

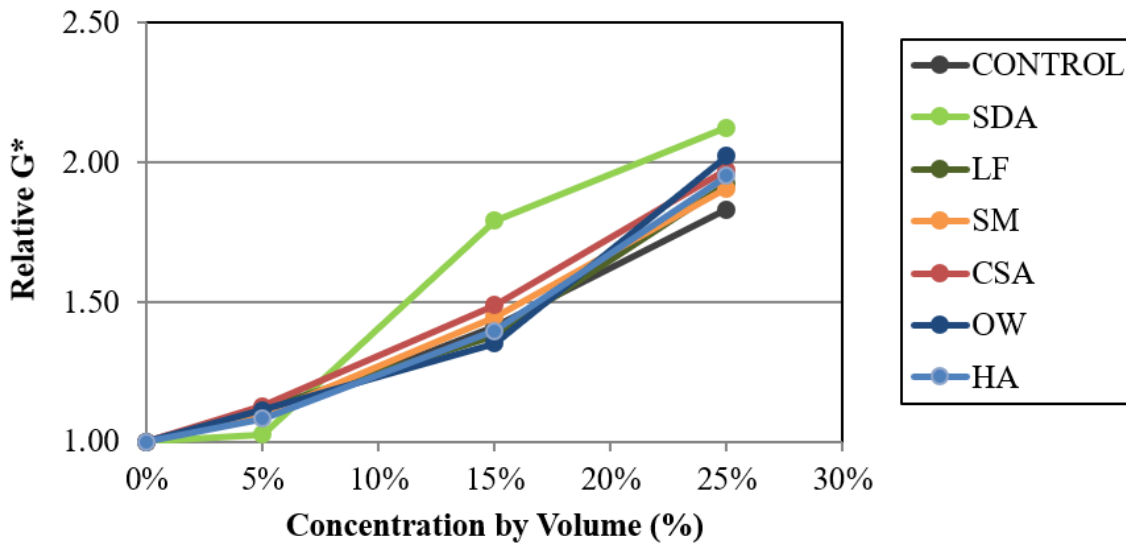


Figure 4.21: Relative Complex Modulus (G^*) for Unaged PG52-34 WMA (Evotherm) Mastics at 52°C

4.2.1.2 Relative Phase Angle (δ_r)

To directly compare the phase angle (δ) values between the asphalt mastics, a relative phase angle (δ_r) was calculated. The phase angle is the lag between the elastic and inelastic (viscous) behavior of the asphalt binder. When the phase angle is low the binder experiences a

more elastic response. The relative phase angle is the ratio of the phase angle of the asphalt mastic over the phase angle of the plain unfilled asphalt binder. By evaluating δ_r it is easier to understand the relationships between the asphalt binders and the powders.

Table 4.5 and Table 4.6 report on the relative phase angle (δ_r) for WMA PG58-28 and WMA PG52-34 asphalt mastics. From these tables it is evident that the phase angle is unaffected by the filler type and concentration since the relative phase angle does not change. Regardless of filler type or concentration, the δ_r is always relatively 1.00.

Table 4.5: Relative Phase Angle (δ_r) for Unaged PG58-28 WMA (Evotherm) Mastics at 58°C

Sample ID	Relative Phase Angle (δ_r)			
	0%	5%	15%	25%
Control	1.00	0.99	0.99	0.99
SDA	1.00	1.00	1.00	1.00
LF	1.00	0.99	1.00	0.99
SM	1.00	0.99	1.00	0.99
CSA	1.00	0.99	0.99	0.99
OW	1.00	0.99	0.99	0.98
HA	1.00	0.99	0.99	0.98

Table 4.6: Relative Phase Angle (δ_r) for Unaged PG52-34 WMA (Evotherm) Mastics at 52°C

Sample ID	Relative Phase Angle (δ_r)			
	0%	5%	15%	25%
Control	1.00	1.01	1.01	1.01
SDA	1.00	1.02	1.02	1.02
LF	1.00	1.01	1.02	1.01
SM	1.00	1.01	1.01	1.01
CSA	1.00	1.01	1.01	1.01
OW	1.00	1.01	1.01	1.00
HA	1.00	1.01	1.01	1.01

4.3 MASTIC TESTING (PERFORMANCE RELATED INDICATORS)

The testing requirements for the Superpave® binder testing protocol do not assess the performance of asphalt mastics but rather asphalt binders only. The purpose of this research study was to adopt the Superpave® binder testing protocol for asphalt mastics and make comparisons between the mastics and mastic performance. It was important to use this protocol to make conclusions on the fundamental properties of the mastics based on the experimental results. Therefore, for this research study, Superpave® limitations were not followed (as these were developed for plain binders) but rather used as a guideline to evaluate the relative effects that the filler and reactive powders had on the overall performance and compared different powders with the reference LS filler. Duplicates were used for all tests and the coefficient of variations (CV) were all below 15%.

4.3.1 Constructability

Workability was evaluated by comparing the viscosity of the unaged mastics at high construction temperatures using the guidelines of ASTM D4402-12. The constructability of the asphalt mastic at a high temperature was an important parameter to evaluate as it indicates the workability efforts associated with aggregate coating, mixing, and compacting the asphalt mixtures since the asphalt binder is completely viscous at these temperatures.

In this study, the viscosity was measured using a Brookfield Rotational Viscometer (RV) with a #27 spindle size at 135°C. The Superpave® testing protocol limits the viscosity for unfilled unaged binders to be less than 3.0 Pa-s. If the viscosity is above 3.0 Pa-s the binder has a viscosity which is high and, therefore, there is additional compaction effort requiring

supplementary compaction energy. For this reason, lower values of viscosity are desirable as the specific temperature as this reduces the efforts for compaction.

Table 4.7 reports on the viscosity comparisons between the unaged HMA PG58-28 and WMA PG58-28 binders. It can be observed that the HMA PG58-28 binder yields a higher viscosity value when compared to the WMA PG58-28 binder. This reduction in viscosity is directly related to the Evotherm Warm Mix Asphalt modifier and this performance is desirable as it reduces the overall viscosity. This decrease in viscosity can therefore be correlated to a reduction in compaction efforts.

Table 4.8 reports on the viscosity comparisons between the unaged HMA PG52-34 and WMA PG52-34 binders. Similarly to the PG58-28 binders, the viscosity decreased when the Evotherm Warm Mix modifier was used. This decrease in viscosity is very small but regardless, this results in lower compaction efforts when compared to the reference HMA and this is a desirable effect at the compaction temperatures.

Table 4.7: Viscosity for Unaged PG58-28 HMA and Unaged PG58-28 WMA (Evotherm) at 135°C

	PG58-28 (HMA)	PG58-28 (WMA)
Test Temp. (°C)	135	135
Viscosity (Pa-s) ≤ 3.0 Pa-s	0.30	0.28

Table 4.8: Viscosity for Unaged PG52-34 HMA and Unaged PG52-34 WMA (Evotherm) at 135°C

	PG52-34 (HMA)	PG52-34 (WMA)
Test Temp. (°C)	135	135
Viscosity (Pa-s) ≤ 3.0 Pa-s	0.22	0.21

Figures 4.22 and 4.23 report on the viscosity of the unaged WMA mastics. The results demonstrate that the increase in filler content hinders the viscosity of the asphalt mastic. As the concentration increases, the viscosity increases, especially at higher concentrations. For both the WMA PG58-28 and WMA PG52-34 mastics all materials are below Superpave® specifications of 3.0 Pa-s. Due to high surface area and high RV, the SDA material yields the highest viscosity at 15% and 25% concentrations, which is undesirable, particularly at higher concentrations, since this increases the mixing and compaction efforts. When compared to the original WMA PG58-28 unfilled asphalt binder the SDA mastic at 25% by volume concentration increased the viscosity by 210.71% which is significant. On the other hand, the control limestone filler only increased the viscosity by 114.29%. The overall viscosity performance trends can also be correlated to stiffness which was observed by G^* values. Materials such as SM and OW mastics were only observed to have the same viscosity as the control at 5% which is a desirable effect (highlighted in the plots) but increase beyond the control viscosity at higher concentrations.

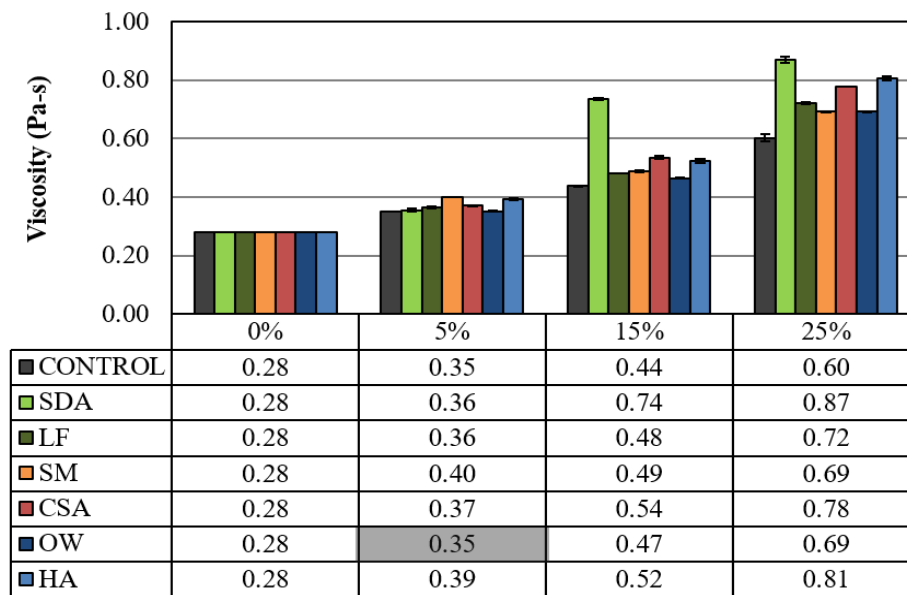


Figure 4.22: Viscosity for Unaged PG58-28 WMA (Evotherm) Mastics at 58°C

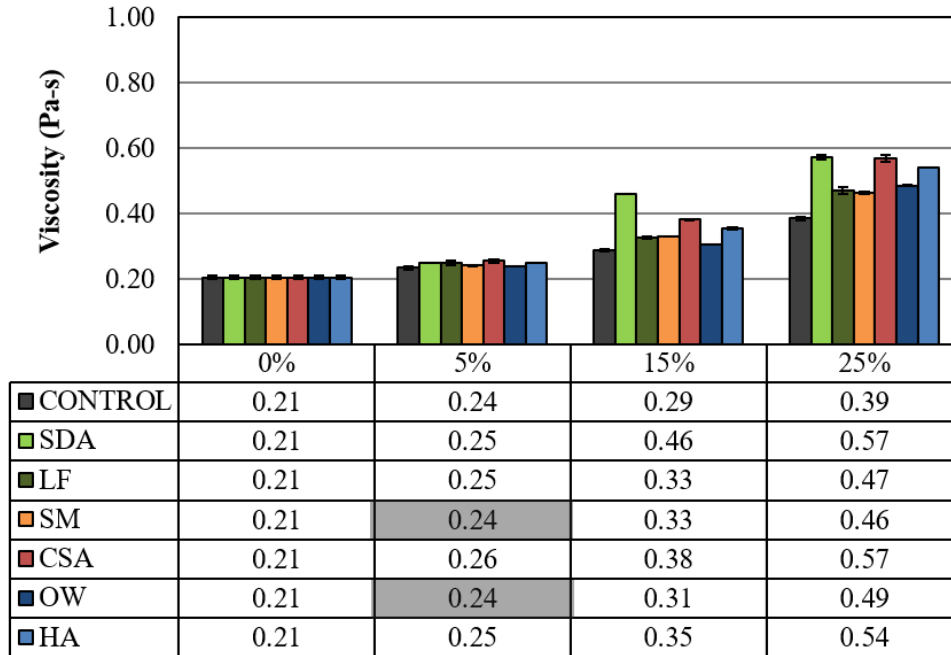


Figure 4.23: Viscosity for Unaged PG52-34 WMA (Evotherm) Mastics at 52°C

4.3.2 Rutting Resistance

Rutting in asphalt mixtures refers to the progressive permanent deformation of material under repeated load which can occur from consolidation or through plastic flow. Rutting results from permanent distortion of the material at higher temperatures due to wheel track loading affecting short-term aged materials, which is the most common form of permanent deformation. A Superpave® rutting factor $G^*/\sin(\delta)$ is used to evaluate asphalt binders at the high PG temperature (58°C for PG58-28 and 52°C for PG52-34) under the testing protocol to assess rutting resistance. In this research study the rutting factor was used to compare all asphalt mastics to understand the effects of the powder materials and to see if rutting resistance could be enhanced. In this regard, higher values of $G^*/\sin(\delta)$ are desirable as this indicates better rutting resistance.

Still, according to the Superpave® testing protocol, the rutting factor $G^*/\sin(\delta)$ is not an effective parameter to characterize asphalt binders for rutting resistance. Therefore, Superpave® specifications require that the rutting factor $G^*/\sin(\delta)$ must be paired with a Multiple Stress Creep and Recovery (MSCR) test conducted at the high PG temperature to evaluate rutting resistance. For the MSCR test, a Non-Recoverable Compliance (J_{nr}) and % Recovery are evaluated to understand the response of the mastics. The J_{nr} values represent the residual strain of the material after the creep and recovery cycle, whereas the % Recovery is used to evaluate the elastic response of the asphalt binder. Here, lower values of J_{nr} are desirable and higher values of % Recovery are desirable.

4.3.2.1 Superpave® Rutting Factor ($G^*/\sin(\delta)$)

Rutting resistance testing was performed in accordance to AASHTO T315 specifications with the DSR to evaluate the rutting factor $G^*/\sin(\delta)$. According to the standard, to reduce rutting, $G^*/\sin(\delta)$ must be larger than 1.00 kPa for unaged asphalt binders and larger than 2.20 kPa for RTFO aged asphalt binders. Higher values of $G^*/\sin(\delta)$ are desirable as this promotes a more elastic response which is desirable for rutting resistance.

Table 4.9 and Table 4.10 report on the performance of unaged asphalt binders. As previously observed, the WMA binders exhibit a softening affect due to the use of Evotherm modifier. The $G^*/\sin(\delta)$ values are lower for the WMA binders as compared to the HMA binders which means that the WMA binders are potentially more likely to experience rutting. However, these differences are extremely small which means that the overall performance should not change dramatically. Regardless, both the PG58-28 and PG52-34 binders meet the Superpave® testing specifications since all values of $G^*/\sin(\delta)$ are greater than 1.00 kPa.

Table 4.9: $G^*/\sin(\delta)$ for Unaged PG58-28 HMA and Unaged PG58-28 WMA (Evotherm) at 58°C

	PG58-28 (HMA)	PG58-28 (WMA)
Test Temp. (°C)	58	58
$G^*/\sin(\delta)$ (kPa) \geq 1.00 kPa	1.38	1.35

Table 4.10: $G^*/\sin(\delta)$ for Unaged PG52-34 HMA and Unaged PG52-34 WMA (Evotherm) at 58°C

	PG52-34 (HMA)	PG52-34 (WMA)
Test Temp. (°C)	52	52
$G^*/\sin(\delta)$ (kPa) \geq 1.00 kPa	1.55	1.50

Table 4.11 and Table 4.12 show the $G^*/\sin(\delta)$ results for the RTFO aged asphalt binders. These results demonstrate similar trends observed from the unaged asphalt binders when tested for rutting resistance. The WMA binders are slightly softer than the HMA binders which makes sense because this testing is performed at the high PG temperature. Here, both the PG58-28 and PG52-34 asphalt binders both meet the Superpave® testing protocol requirements since the $G^*/\sin(\delta)$ values are greater than 2.20 kPa.

Table 4.11: $G^*/\sin(\delta)$ for RTFO Aged PG58-28 HMA and RTFO Aged PG58-28 WMA (Evotherm) at 58°C

	PG58-28 (HMA)	PG58-28 (WMA)
Test Temp. (°C)	58	58
$G^*/\sin(\delta)$ (kPa) \geq 2.20 kPa	3.52	3.29

Table 4.12: $G^*/\sin(\delta)$ for RTFO Aged PG52-34 HMA and RTFO Aged PG52-34 WMA (Evotherm) at 52°C

	PG52-34 (HMA)	PG52-34 (WMA)
Test Temp. (°C)	52	52
$G^*/\sin(\delta)$ (kPa) \geq 2.20 kPa	3.66	3.58

The results for RTFO aged rutting resistance testing are reported in Figure 4.24 and Figure 4.25. The results prove that the addition of the powders increases the rutting factor $G^*/\sin(\delta)$ and, therefore, increase the rutting resistance. As powder concentration increases, the $G^*/\sin(\delta)$ also increases as compared to the original RTFO plain binder for both WMA PG58-28 and WMA PG52-34 binders. For the WMA PG58-28 asphalt binders it is evident that the SDA mastics and CSA cement mastics experience greater rutting resistance at all levels when compared to the control limestone filler since the rutting factor $G^*/\sin(\delta)$ is greater (these values are highlighted on the plots). It is interesting to note that LF cement mastics increased rutting resistance only at 25% concentration (by volume) and HA cement mastics only increased the rutting resistance at 5% concentration by volume. For WMA PG52-34, the SDA mastics only experienced improved rutting resistance at 15% and 25% concentrations (by volume) as compared to the control limestone filler.

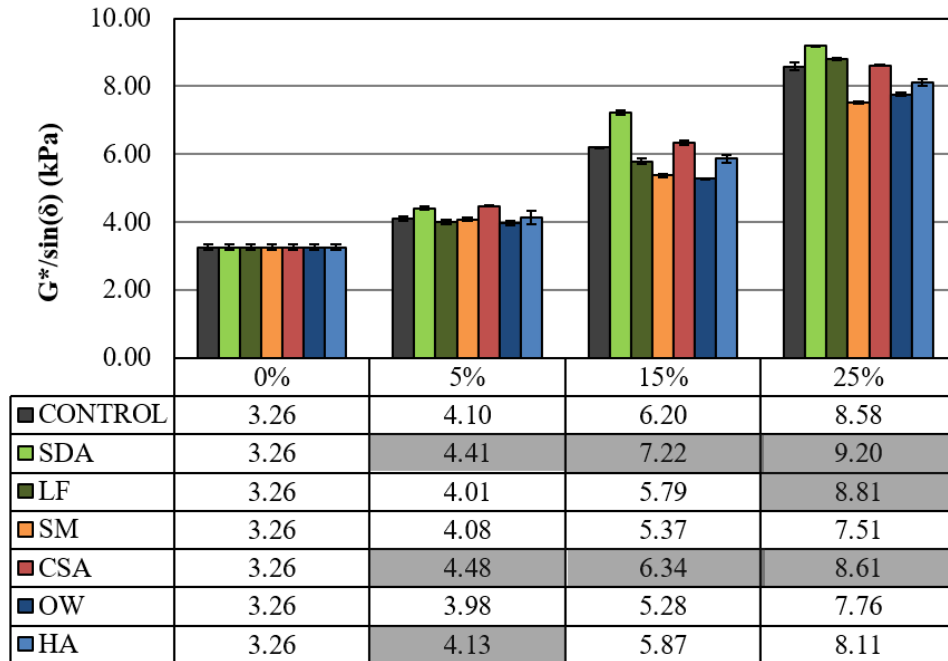


Figure 4.24: $G^*/\sin(\delta)$ for RTFO Aged PG58-28 WMA (Evotherm) Mastics at 58°C

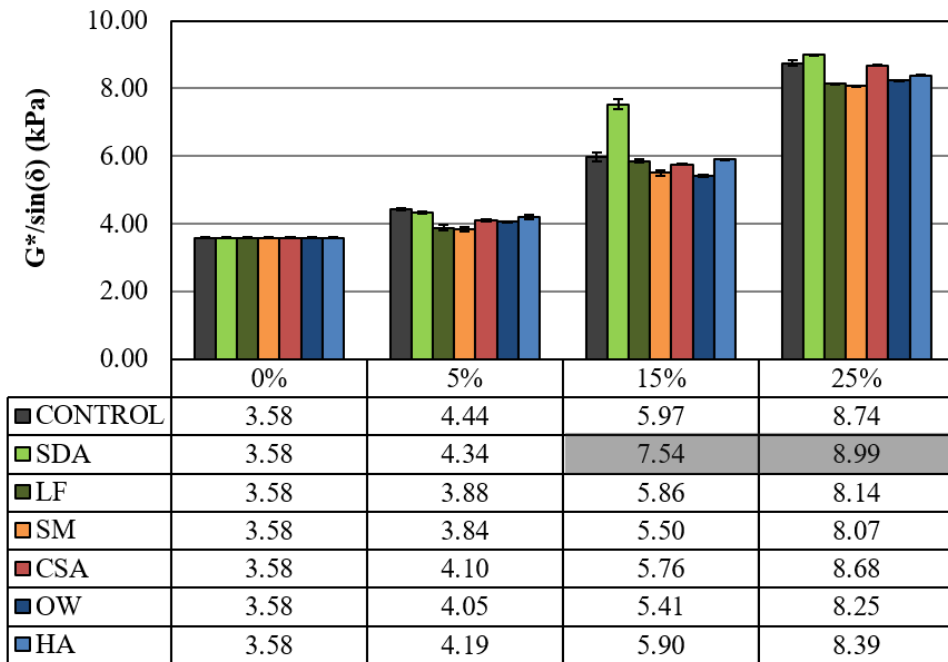


Figure 4.25: $G^*/\sin(\delta)$ for RTFO Aged PG52-34 WMA (Evotherm) Mastics at 52°C

4.3.2.2 Non-Recoverable Compliance (J_{nr})

The Multiple Stress Creep & Recovery (MSCR) testing was performed in accordance to ASTM T315 and AASHTO T350-14 with the DSR at the high PG temperature on RTFO aged materials to evaluate both Non-Recoverable Compliance (J_{nr}) and % Recovery. The testing stress of 0.1 kPa was used for conditioning and testing stresses of 3.2 and 10.0 kPa were used to illustrate the rutting resistance of the asphalt mastics. Previous studies proved the stress sensitivity correlations between J_{nr} values at 3.2 kPa and 10.0 kPa levels for mastics at 5, 10, 15, 25, and 40% concentrations by volume (Bautista, 2014). The trends between the different stress levels had strong linear correlations and was determined that the stress dependencies of the results could be ignored since the characteristics affected by the Newtonian behavior of the asphalt binders. For this reason, this research reports on the testing at 3.2 kPa stress levels. Here, lower values of J_{nr} and higher values of % Recovery are desirable.

Table 4.13 and Table 4.14 report on the results for the RTFO aged PG58-28 and PG52-34 binders. The results demonstrate that the HMA binders experience a greater resistance to rutting as the J_{nr} values are lower than that for the WMA binders. These results reflect on the performance of WMA Evotherm additive once again as this causes a softening effect. The differences between the test results are minor which concludes that there would not be a significant difference in field performance.

Table 4.13: J_{nr} for RTFO Aged PG58-28 HMA and RTFO Aged PG58-28 WMA (Evotherm) at 58°C

	PG58-28 (HMA)	PG58-28 (WMA)
Test Temp. (°C)	58	58
J_{nr} (1/kPa)	2.77	3.17

Table 4.14: J_{nr} for RTFO Aged PG52-34 HMA and RTFO Aged PG52-34 WMA (Evotherm) at 52°C

	PG52-34 (HMA)	PG52-34 (HMA)
Test Temp. (°C)	52	52
J_{nr} (1/kPa)	2.47	2.49

The MSCR testing results are reported in Figure 4.26 for WMA PG58-28 mastics and in Figure 4.27 for WMA PG52-34 mastics. These results prove that the RTFO aged mastics had a better rutting resistance as the J_{nr} values are all less than the RTFO aged unfilled asphalt binders. This trend demonstrates a reduction in J_{nr} with an increase of concentration of filler material and this leads to better performance when related to rutting resistance. The mastics experience an enhanced elastic behavior under the 3.2 kPa loading condition and continue to perform better with increased powder concentrations.

When evaluating the mastics, it is clear that the HA cement mastics performed better than the control limestone filler since the J_{nr} values are less at all concentrations for both WMA PG58-28 and WMA PG52-34 binders. The LF mastics performed better than the control mastic at both 5% and 25% concentrations for both asphalt binders and SM mastics performed better than the control filler at 15% and 25% concentrations for both asphalt binders. Other mastics such as CSA also experienced better performance than the control limestone mastics. An important observation is that all mastics improved rutting resistance at 25% concentration by volume for the WMA PG52-34 binder when compared to the control.

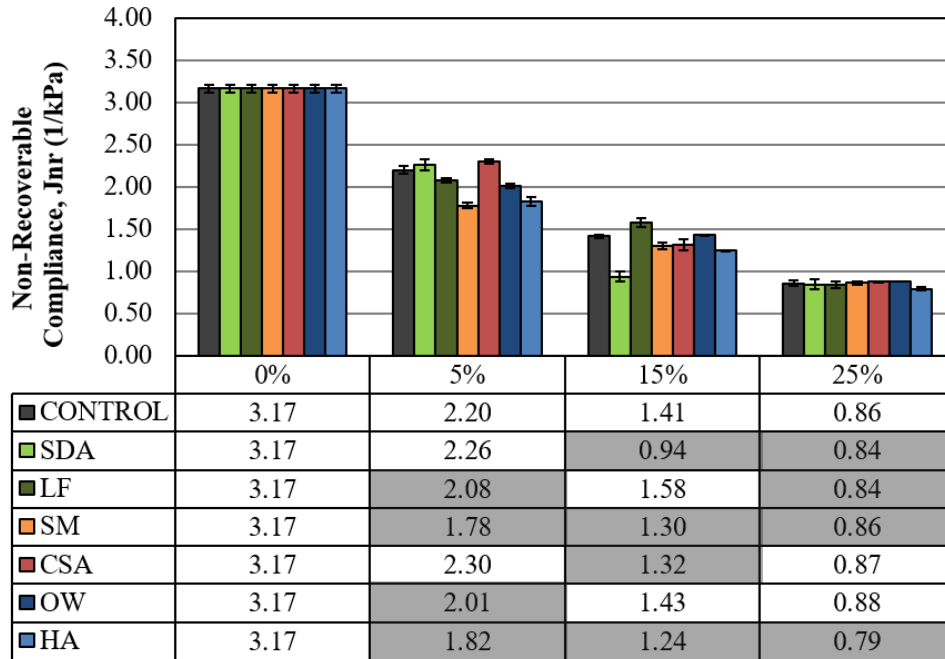


Figure 4.26: J_{nr} for RTFO Aged PG58-28 WMA (Evotherm) Mastics at 58°C

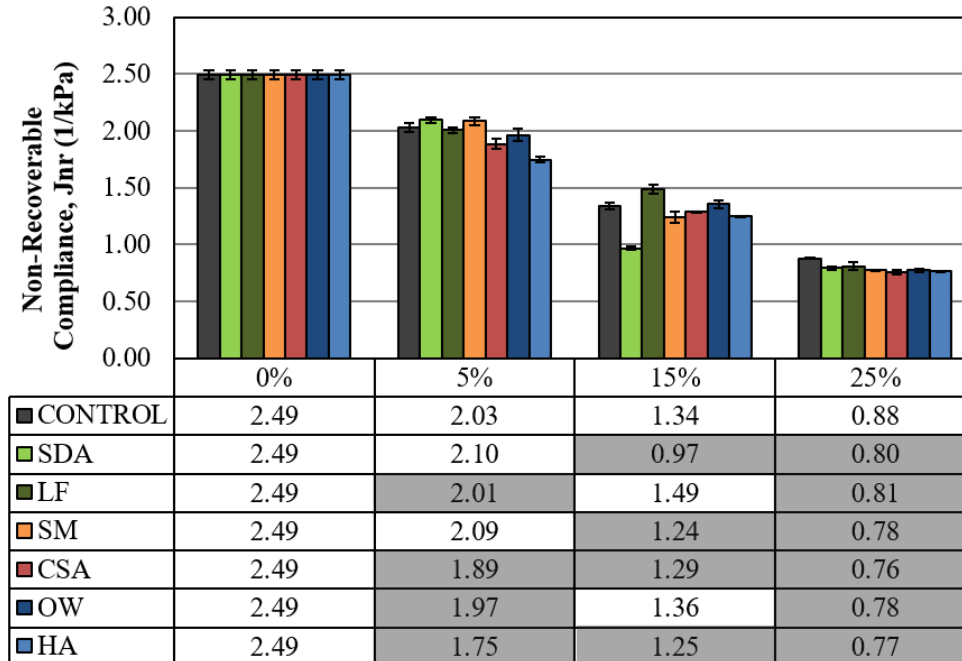


Figure 4.27: J_{nr} for RTFO Aged PG52-34 WMA (Evotherm) Mastics at 52°C

4.3.2.3 % Recovery

The % Recovery data was also calculated from the MSCR testing at the 3.2 kPa stress intensity level. Table 4.15 and Table 4.16 report on the RTFO aged PG58-28 binder and the RTFO aged PG52-34 binder. It can be observed that the HMA binders experienced a greater % Recovery when compared to the WMA binders. The % Recovery was 3.95% for the HMA PG58-28 binder and decreased to 3.33% for the WMA PG58-28 binder. Similarly, the % Recovery was 7.64% for the HMA PG52-34 binder which decreased to 6.77% for the WMA PG52-34 binder.

Table 4.15: % Recovery for RTFO Aged PG58-28 HMA and RTFO Aged PG58-28 WMA (Evotherm) at 58°C

	PG58-28 (HMA)	PG58-28 (WMA)
Test Temp. (°C)	58	58
% Recovery	3.95	3.33

Table 4.16: % Recovery for RTFO Aged PG52-34 HMA and RTFO Aged PG52-34 WMA (Evotherm) at 52°C

	PG52-34 (HMA)	PG52-34 (WMA)
Test Temp. (°C)	52	52
% Recovery	7.64	6.77

Table 4.17 lists the results for both the WMA PG58-28 mastics and the WMA PG52-34 mastics. The results report on the % Recovery and also the relative recovery. The relative recovery is the mastic recovery divided by the plain (unfilled) binder recovery. From the table it is evident that the % Recovery increases for all WMA PG58-28 asphalt mastics when compared to the plain binder. As an example, the CSA cement mastic based on WMA PG58-28 at 25% by volume concentration increased the % Recovery by 80.91%. For every WMA PG58-28 mastic there is at least a 15% increase in recovery and in some cases the increase in recovery is more

than 100% as it is evident from the control at 25% concentration, the OW cement mastic at 25% concentration, and the HA mastic at 25% concentration. For the WMA PG52-34 mastics there are only a few mastics that result in an increase in % Recovery and these are the control mastics and the HA cement mastics.

Table 4.17: % Recovery for RTFO Aged Binders and Mastics

Sample ID	Concentration (%)	% Recovery		Relative Recovery	
		PG58-28 (WMA)	PG52-34 (WMA)	PG58-28 (WMA)	PG52-34 (WMA)
-	0	3.30	6.77	1.00	1.00
Control	5	6.23	7.41	1.89*	1.09
	15	5.78	7.79	1.75*	1.15*
	25	8.38	9.46	2.54**	1.40*
SDA	5	5.10	5.14	1.55*	0.76
	15	5.64	5.57	1.71*	0.82
	25	6.32	6.70	1.91*	0.99
LF	5	5.03	5.27	1.52*	0.78
	15	4.38	5.24	1.33*	0.77
	25	5.60	6.79	1.70*	1.00
SM	5	5.53	5.80	1.67*	0.86
	15	5.38	6.38	1.63*	0.94
	25	5.75	7.44	1.74*	1.10
CSA	5	4.76	6.28	1.44*	0.93
	15	5.21	6.39	1.58*	0.94
	25	5.97	7.23	1.81*	1.07
OW	5	5.90	6.38	1.79*	0.94
	15	5.08	5.99	1.54*	0.88
	25	6.59	7.20	2.00**	1.06
HA	5	5.11	7.23	1.55*	1.07
	15	5.48	5.95	1.66*	0.88
	25	7.69	8.41	2.33**	1.24*

* Highlighted and bold numbers indicate more than 15% increase in recovery

** Highlighted and bold numbers indicate more than 100% increase in recovery

These results may be deceiving though as the unmodified asphalt binders experience rather negligible results. The overall % Recovery is still relatively low in terms of overall performance when the concentrations increase and thus there would not result in significant improvement. However, even though the improvement may be minor there is generally still an increase in % Recovery as the concentration levels increase and this is an important discovery.

4.3.3 Fatigue Resistance

Fatigue resistance testing was performed in accordance to AASHTO T315 using the DSR equipment to evaluate a fatigue factor $G^*\sin(\delta)$ at intermediate temperatures (19°C for PG58-28 and 13°C for PG52-34). Fatigue cracking in asphalt refers to failure due to repeated loads at a typical service temperature over a long period of time. The Superpave® specifications require that the asphalt binder be evaluated under intermediate temperature conditions when the asphalt material has been PAV aged. The fatigue factor $G^*\sin(\delta)$ is assessed by applying an oscillating load at a low shear strain which is measured in the linear viscoelastic region. The Superpave® specifications also require that $G^*\sin(\delta)$ be less than or equal to 5,000 kPa. Low values of $G^*\sin(\delta)$ are desirable as this indicates a better resistance to fatigue deformation.

Table 4.18 and Table 4.19 report the results of HMA and WMA fatigue testing. The results indicate that the HMA and WMA binders both meet the Superpave® specifications since $G^*\sin(\delta)$ are both lower than 5,000 kPa. These tables also demonstrate that the addition of the Evotherm WMA modifier increases the effects of fatigue resistance as the $G^*\sin(\delta)$ is lower when compared to the HMA binder. For the PG58-28 binder the $G^*\sin(\delta)$ is reduced by 12.98% and for the PG52-34 binder the $G^*\sin(\delta)$ is reduced by 47.34% indicating the WMA binder performed better under cyclic loading conditions.

Table 4.18: $G^*\sin(\delta)$ for PAV Aged PG58-28 HMA and PAV Aged PG58-28 WMA (Evotherm) at 19°C

	PG58-28 (HMA)	PG58-28 (WMA)
Test Temp. (°C)	19	19
$G^*\sin(\delta)$ (kPa) $\leq 5,000$ kPa	3830.00	3390.00

Table 4.19: $G^*\sin(\delta)$ for PAV Aged PG52-34 HMA and PAV Aged PG52-34 WMA (Evotherm) at 13°C

	PG52-34 (HMA)	PG52-34 (WMA)
Test Temp. (°C)	13	13
$G^*\sin(\delta)$ (kPa) $\leq 5,000$ kPa	3489.00	2368.00

Figure 4.28 and Figure 4.29 indicate that the increase in filler content decreases the fatigue resistance since the mastic becomes too stiff at elevated concentrations. For the WMA PG58-28 binder, only the SM, CSA, and control mastics meet specifications up to 15% concentration (by volume) and the control mastics still meet the specifications at 25%. For the WMA PG52-34 binder, the SDA, LF, SM, CSA, HA, and control limestone mastics meet specifications up to 15% and the control mastics still meet the specifications at 25%. The CSA and OW cement mastics were the only materials that increased the rutting resistance for the WMA PG58-28 binder at 5% concentrations by volume when compared to the control. On the other hand, the control filler outperformed all mastics for WMA PG52-34 except for SDA, CSA, and LF at 15% concentration by volume.

It is interesting to investigate the mastic behavior of the CSA and OW cement mastics for the WMA PG58-28 binder as these materials decreased the stiffness at 5% concentrations. As reported by Figure 4.28, there was a decrease in $G^*\sin(\delta)$ values and this decrease in stiffness could indicate the asphalt being an extender.

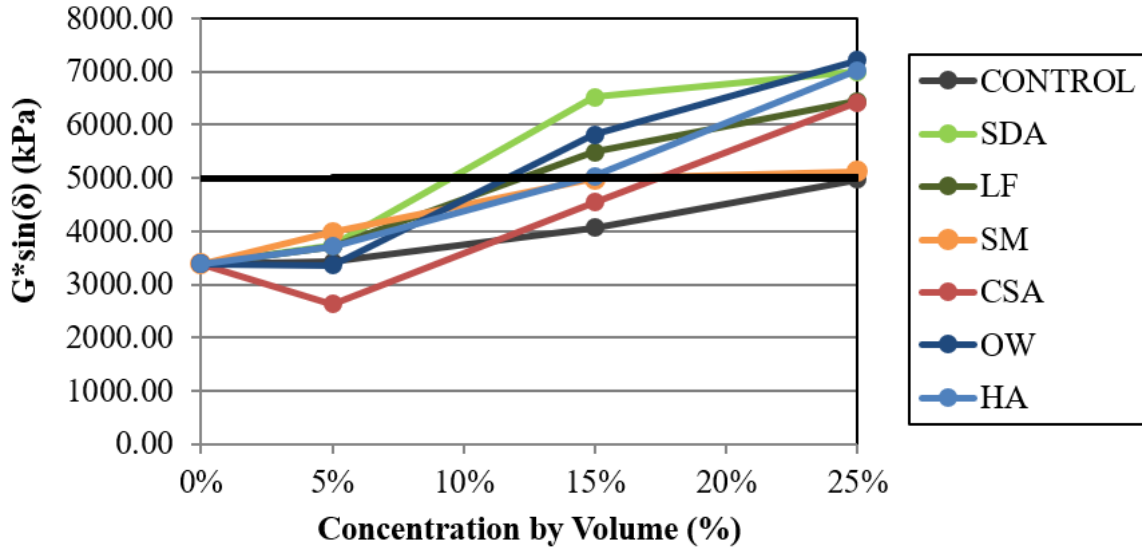


Figure 4.28: $G^*\sin(\delta)$ for PAV Aged PG58-28 WMA (Evotherm) Mastics at 19°C

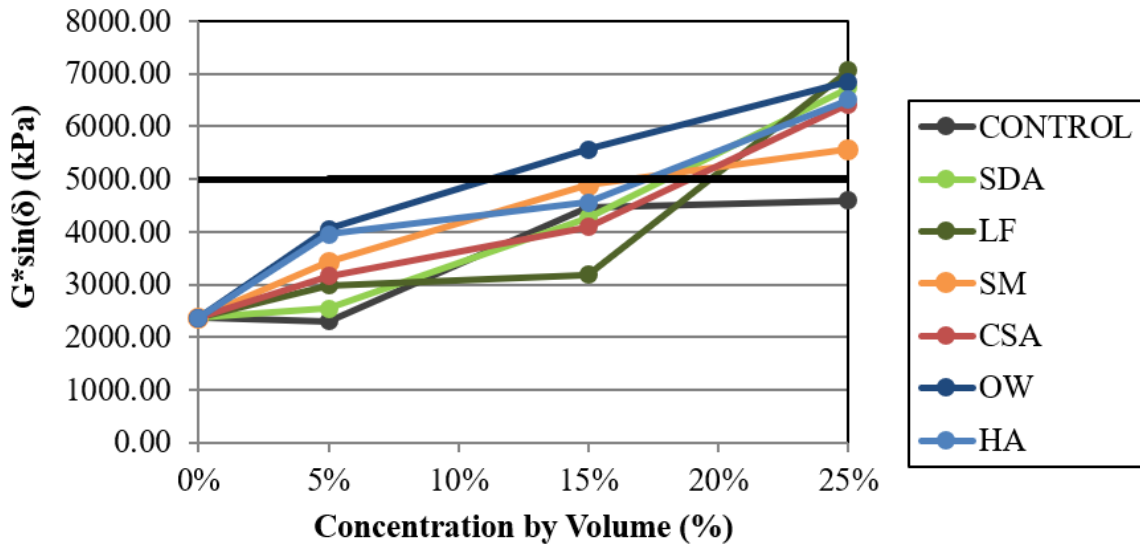


Figure 4.29: $G^*\sin(\delta)$ for PAV Aged PG52-34 WMA (Evotherm) Mastics at 13°C

4.3.4 Aging Resistance

Throughout the RTFO and PAV aging processes associated with the asphalt testing the asphalt become more brittle due to age hardening. For this reason, it was important to evaluate the effects of aging resistance by comparing the unaged asphalt mastics with PAV aged

materials. An aging index was used to directly compare the G^* of the PAV aged materials to the G^* of the unaged materials, both of which were tested at intermediate temperatures (19°C for PG58-28 and 13°C for PG52-34). This testing was important since it assessed the potential ability of the asphalt mastics to reduce the rate of aging when compared to the control limestone mastics. Here, lower values of aging index are desirable as this indicates a slower rate of age hardening which can lead to longer life cycles.

Table 4.20 and Table 4.21 report on the initial results from the PG58-28 and PG52-34 binders. These results indicate that the HMA PG58-28 asphalt binder had a lower aging index than the WMA PG58-28 binder. However, the aging index for the HMA PG52-34 binder had a higher aging index than the WMA PG52-34 binder which indicates the potential differences in binder sensitivity. Regardless of the differences, all asphalt mastics were compared directly to the control limestone mastics at specific concentrations.

Table 4.20: Aging Index for PG58-28 HMA and PG58-28 WMA (Evotherm) at 19°C

	PG58-28 (HMA)	PG58-28 (WMA)
Test Temp. (°C)	19	19
Aging Index	5.53	6.55

Table 4.21: Aging Index for PG52-34 HMA and PG52-34 WMA (Evotherm) at 13°C

	PG52-34 (HMA)	PG52-34 (WMA)
Test Temp. (°C)	13	13
Aging Index	8.23	5.43

The mastic results for aging index are reported in Figure 4.30 and Figure 4.31. The results demonstrate that for the WMA PG58-28 binder the majority of asphalt mastics had a

reduced aging index at 5% concentrations by volume as compared to the control limestone mastics. The CSA cement mastics were the only type that had a reduction in aging index at the higher concentration of 25%. For the WMA PG52-34 binder, every mastic performed better than the control at 15% concentration. However, CSA mastics were the only type that had a reduction in aging index at a concentration of 5%. For this reason it seems that CSA demonstrates a consistent reduction in aging index when compared to the limestone filler and this indicates a potential for this material to reduce the effects of aging.

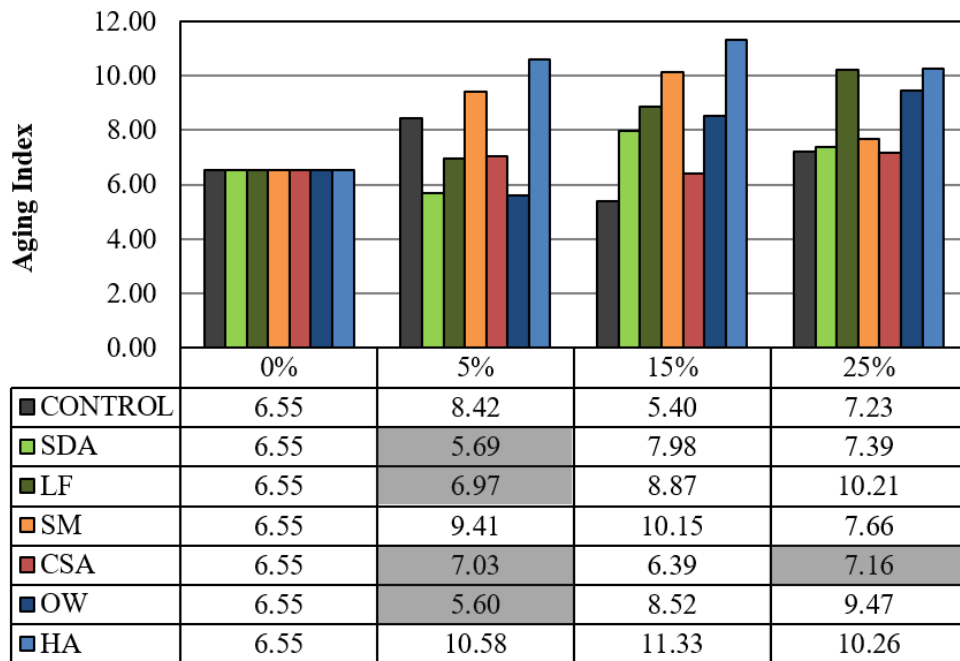


Figure 4.30: Aging Index for PG58-28 WMA (Evotherm) Mastics at 19°C

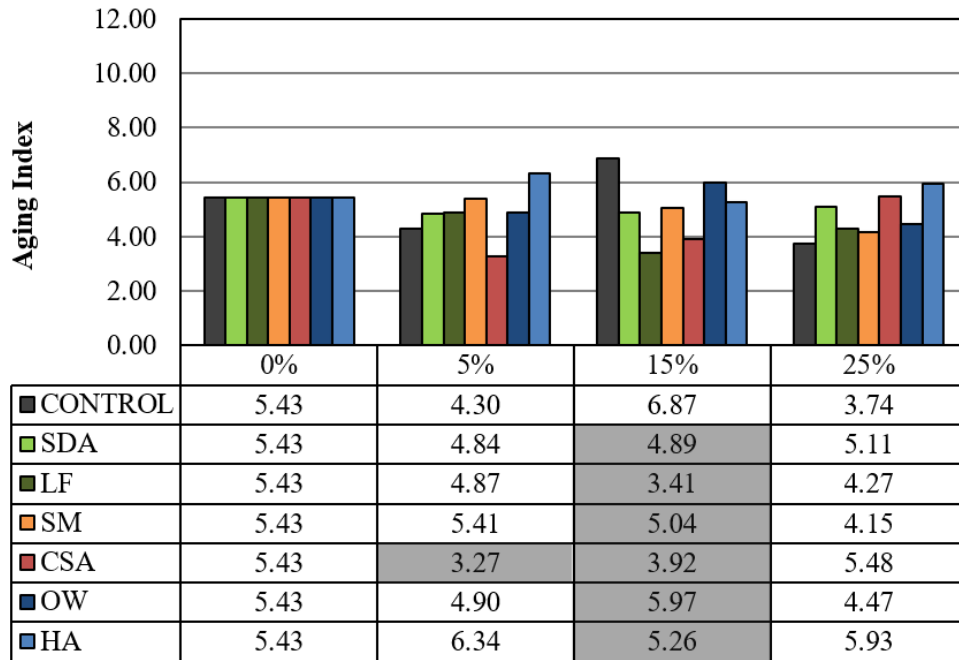


Figure 4.31: Aging Index for PG52-34 WMA (Evotherm) Mastics at 13°C

The results obtained in this section need to be investigated further to understand the effects of aging resistance. Aging resistance is an important parameter to evaluate as this can be directly correlated to the life cycle of the asphalt binder. Reducing the rate at which the asphalt binder ages would result in a longer lasting material and this is critical for field applications.

4.3.5 Thermal-Cracking Resistance

Thermal cracking is an important parameter to evaluate, especially in cold climates because these are non-load associated cracks. Thermal cracks are intermittent transverse cracks that form when the asphalt binder shrinks or contracts due to low temperatures. During this excessive shrinkage, the tensile stresses within the asphalt layer exceed the tensile capacity of the material. These cracks typically form with aged material and for this reason the testing performed for thermal-cracking resistance was PAV aged to mimic the field conditions.

Thermal-cracking resistance testing was evaluated in accordance to AASHTO T313 for PAV aged materials using a Bending Beam Rheometer (BBR). This test was performed to determine the creep stiffness $S(t)$ and m -value. The creep stiffness is the measurement of thermal stresses that result from the thermal contraction of the asphalt binder. Lower values of $S(t)$ are desirable as this indicates a more elastic material that can reduce thermal cracking. According to Superpave® specifications, $S(t)$ is required to be less than 300 MPa. The m -value is rate at which the asphalt binder relieves stresses through plastic flow which is essentially the slope of the creep stiffness curve. Higher values of m -value are desirable as this indicates a less brittle material that can relax thermal stresses. Superpave specifications require that the m -value is a minimum of 0.300. Thermal-cracking resistance testing was evaluated at the low PG temperature plus 10°C (-18°C for PG58-28 and -24°C for PG52-34).

4.3.5.1 Creep Stiffness (S_t)

This section presents the creep stiffness $S(t)$ results for the PG58-28 and PG52-34 binders. Table 4.22 and Table 4.23 report on the results of the HMA and WMA unfilled PAV aged asphalt binders. From these results it can be concluded that the WMA binders performed better when compared to the HMA binder since the $S(t)$ values are lower at the specific testing temperatures. This reduction in $S(t)$ demonstrates the softening affect from the Evotherm WMA additive and this is an important discovery. Nevertheless, all HMA and WMA unfilled binders met the Superpave® testing specifications.

Table 4.22: S(t) for PAV Aged PG58-28 HMA and PAV Aged PG58-28 WMA (Evotherm) at -18°C

	PG58-28 (HMA)	PG58-28 (WMA)
Test Temp. (°C)	-18	-18
S(t) (MPa) ≤ 300 MPa	211.00	198.50

Table 4.23: S(t) for PAV Aged PG52-34 HMA and PAV Aged PG52-34 WMA (Evotherm) at -24°C

	PG52-34 (HMA)	PG52-34 (WMA)
Test Temp. (°C)	-24	-24
S(t) (MPa) ≤ 300 MPa	225.00	198.00

Figure 4.32 and Figure 4.33 report on the creep stiffness of the WMA mastics at all concentrations. For the WMA PG58-28 binder, all mastics were stiffer than the control limestone mastic except for the OW cement mastic at 25% concentration. Also, the LF and OW cement mastics were most comparable to the control mastics. For the WMA PG52-34 binder, the LF, SM, and CSA cement mastics had a reduction in stiffness at 5% and 15% concentrations. The HA cement mastic at 15% concentration also had a reduction in S(t). Since LF cement mastics were comparable, if not better, than the control for both the WMA PG58-28 and WMA PG52-34 binders there is an importance to evaluate these mastics even further as low-temperature thermal cracking is a focus in this research.

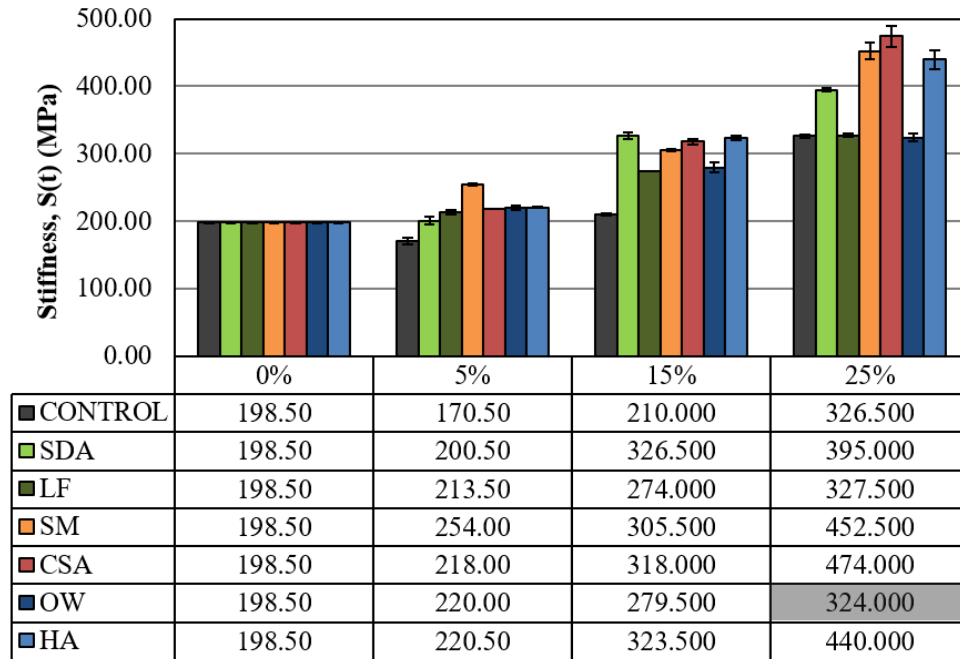


Figure 4.32: Stiffness $S(t)$ for PAV Aged PG58-28 WMA (Evotherm) Mastics at -18°C

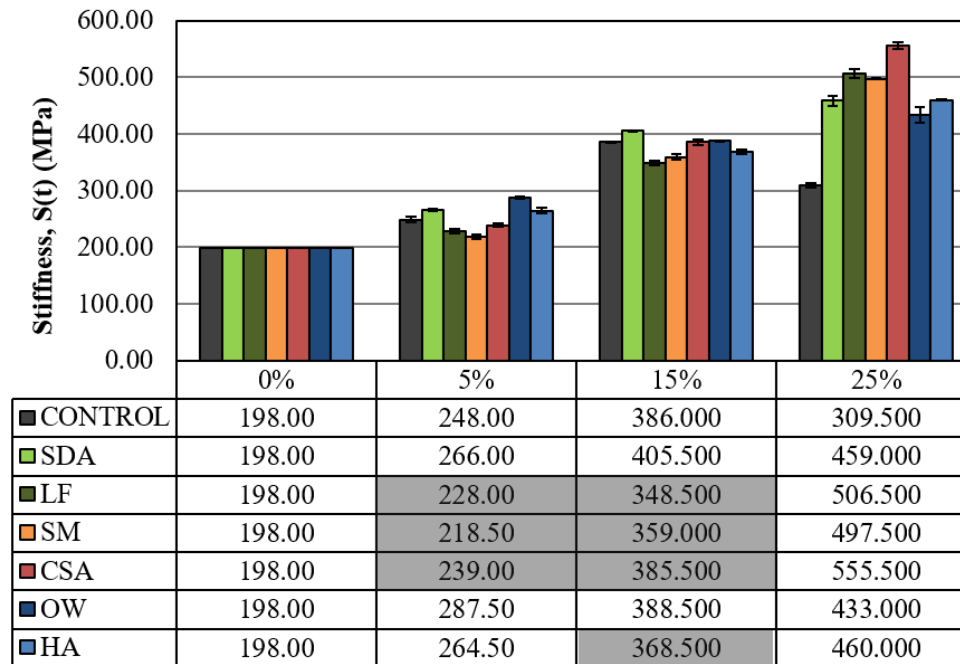


Figure 4.33: Stiffness $S(t)$ for PAV Aged PG52-34 WMA (Evotherm) Mastics at -24°C

4.3.5.2 m-value

This section presents the results for the m-value of the PG58-28 and PG52-34 binders. Table 4.24 and Table 4.25 report that the WMA binders were comparable to the HMA binder in that the m-value was approximately the same. Both binder types meet the Superpave® specifications since the m-values were greater than 0.300.

Table 4.24: m-value for PAV Aged PG58-28 HMA and PAV Aged PG58-28 WMA (Evotherm) at -18°C

	PG58-28 (HMA)	PG58-28 (WMA)
Test Temp. (°C)	-18	-18
m-value \geq 0.300	0.34	0.33

Table 4.25: m-value for PAV Aged PG52-34 HMA and PAV Aged PG5-34 WMA (Evotherm) at -24°C

	PG52-34 (HMA)	PG52-34 (WMA)
Test Temp. (°C)	-24	-24
m-value \geq 0.300	0.35	0.34

Figure 4.34 and Figure 4.35 demonstrate the m-value results for WMA mastics. The results indicate that the LF cement mastics for both WMA PG58-28 and WMA PG52-34 once again improved the performance at the 5% and 15% concentration levels as compared to the control mastics. The CSA and OW cement mastics also improved the low-temperature thermal cracking resistance when used at different concentrations. These results are significant, especially for applications in colder climates, as the low-temperature performance of these mastics was enhanced. Low-temperature cracking resistance is a critical area of focus in this research and these discovered improvements are important.

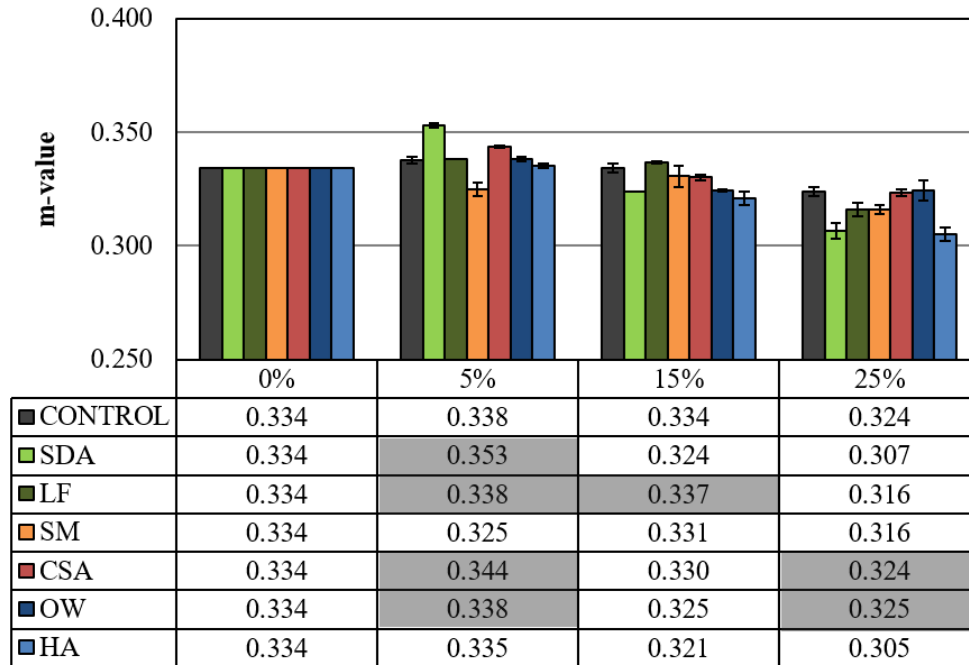


Figure 4.34: m-value for PAV Aged PG58-28 WMA (Evotherm) Mastics at -18°C

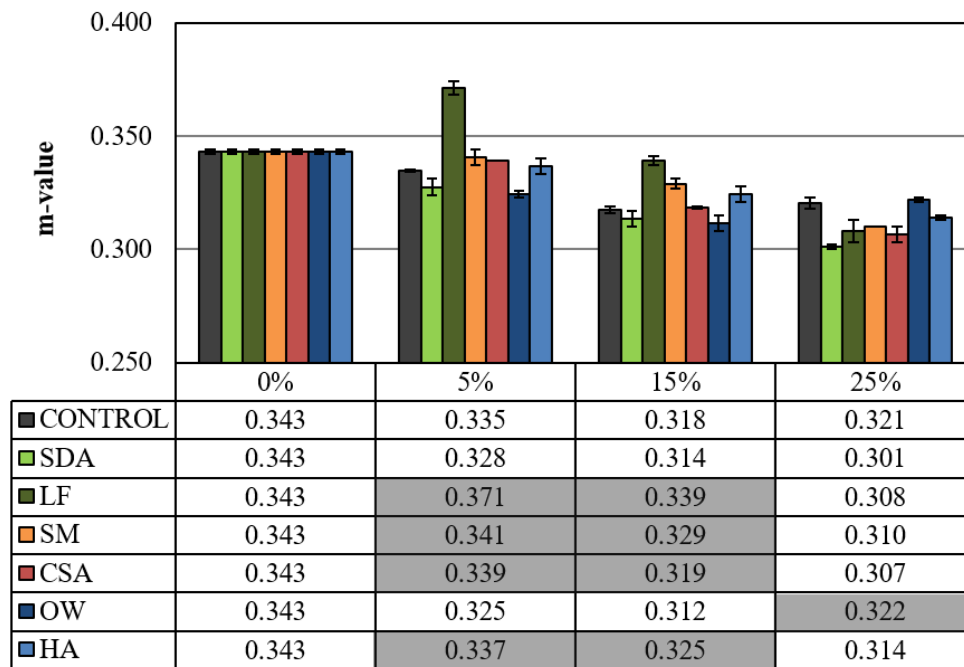


Figure 4.35: m-value for PAV Aged PG52-34 WMA (Evotherm) Mastics at -24°C

4.4 SUMMARY OF RESULTS

From the mastic research, the overall results were summarized using Table 4.26 to demonstrate the performance of each mastic. This table demonstrates the general trends for each type of asphalt mastic for each of the Superpave® tests. The arrows indicate the level of performance that was achieved for each type of mastic when compared to the control limestone mastics. An upward arrow indicates improved performance, a downward arrow indicates a decrease in performance, and a sideways arrow indicates no change in performance.

From the table it is evident that the SDA material behaved better for rutting resistance and, overall, about the same as the control mastics. This is a significant discovery as the performance was not hindered and yet the by-product SDA material can be utilized to replace the asphalt binder without any real detrimental consequences. The LF cement mastics hindered the performance at different testing levels, however, the low-temperature cracking resistance was improved, and this is an important discovery. Lastly, the CSA mastics improved the performance the most at many levels including rutting resistance, aging resistance, and low-temperature thermal cracking resistance. It is evident that due to its unique chemical composition the CSA cement mastics performed the best when compared to all other mastics.

Table 4.26: Performance Testing Summary of all Asphalt Mastics

Powder	Workability	Rutting Resistance	Fatigue Resistance	Aging Resistance	Low-Temp Resistance
SDA	↓	↑	↔	↔	↔
LF	↓	↔	↓	↓	↑
SM	↓	↔	↓	↓	↔
CSA	↓	↑	↔	↑	↑
OW	↔	↔	↓	↓	↔
HA	↓	↑	↓	↓	↔

Based on the results presented above, it was determined to evaluate LF and CSA further by introducing these reactive powders in asphalt mixtures at 25% concentration by volume and compare with a control mixture with limestone filler. These extended study results are presented in the next sections.

4.5 MIXTURE TESTING

From the mastic results presented in the previous sections, it was apparent that the LF and CSA based mastics performed the best when compared to the mastics with other powders including the control mastics with limestone. For this reason, the following section elaborates on the mixture testing for LF and CSA materials combined with both WMA PG58-28 and WMA PG52-34 binders. This section reports on performance of the mixtures based on the asphalt binder, reactive powders, aggregates (12.5 mm maximum aggregate size), and air (7%) (whereas the mastics only included the asphalt binder and the powder materials). The reactive powders were used at 25% by volume because using a larger quantity of the reactive powder would potentially develop a better understanding on the interactions between the powders and the bitumen. A larger quantity of the reactive powders could also help investigate the potential effect of these materials as a self-healing performance.

This section evaluates mixtures based on aggregate coating, constructability aging resistance, moisture damage resistance, fatigue resistance, and low-temperature thermal-cracking resistance. For the aggregate coating, workability, and aging comparison, six replicates were produced and compared. For the moisture damage resistance, fatigue resistance, and thermal-cracking resistance, two replicates were produced and tested. The experimental testing methods are described in detail in the next sections.

4.5.1 Asphalt Mixtures

For mixture testing, the LF and CSA cement powders were introduced to an asphalt mix at 25% replacement of the binder by volume. Mixtures prepared for this study used a job mix formula (JMF) approved by the Wisconsin DOT. The 4-MT mixtures had a NMAS of 12.5 mm. All mixtures used a WMA PG58-28 binder or a WMA PG52-34 binder. The 4-MT WMA control mixtures had a mix design with a 5.8% optimum asphalt content. The LF and CSA materials were added at 25% by binder volume replacement so these mixtures had a reduced 4.4% asphalt content. Here, the reactive powders were assumed as a part of the binder phase rather than as an aggregate component. A control mix was used to compare the impact of the added reactive powders on the performance indicators of mixtures.

4.5.2 Aggregate Blends

The aggregate JMF combinations are reported in Table 4.27. This table gives the specific aggregate blend percentages used to develop the mixtures. The RAP (Recycled Asphalt Pavement) material provided 1.2% asphalt binder so that the total added asphalt binder in the mix was reduced from 5.8% down to only 4.4% for the LS control mixture. Appropriately, the same method was used to reduce the amount of added asphalt binder for the LF and CSA mixtures.

Table 4.27: 4-MT JMF Aggregate Combinations

Aggregate Type	% Combination
5/8" Chips	9.0
3/8" Chips	10.0
Man Sand	18.0
Nat Sand	33.0
Limestone Fines	1.0
RAP	29.0

Table 4.28 displays the particle size distributions (PSD) values for each of the aggregate types and Figure 4.36 provides the actual PSD curves for each of the aggregate types. Both Table 4.28 and Figure 4.35 show the JMF particle size distribution which was determined based on the specific blend percentages given in Table 4.27.

Table 4.28: Particle Size Distributions (PSD) for all Aggregate Types

Sieve		5/8"	3/8"	Man	Nat	Limestone	RAP	JMF
(Std)	(mm)	Chips	Chips	Sand	Sand	Fines		
1"	25	100.0	100.0	100.0	100.0	100.0	100	100.0
3/4"	19	100.0	100.0	100.0	100.0	100.0	100	100.0
1/2"	12.5	84.3	100.0	100.0	100.0	100.0	100	98.6
3/8"	9.5	12.1	91.5	100.0	100.0	100.0	95.8	90.0
#4	4.75	1.1	1.5	85.8	98.1	100.0	73.9	70.5
#8	2.36	1.0	0.9	48.0	89.0	100.0	55	55.1
#16	1.18	1.0	0.9	24.7	80.5	100.0	41.6	44.3
#30	0.6	1.0	0.8	12.2	64.4	100.0	31.3	33.7
#50	0.3	0.9	0.8	5.7	24.5	100.0	20.2	16.1
#100	0.15	0.9	0.8	2.9	4.5	100.0	14	7.2
#200	0.075	0.7	0.6	1.9	2.1	100.0	10.8	5.3

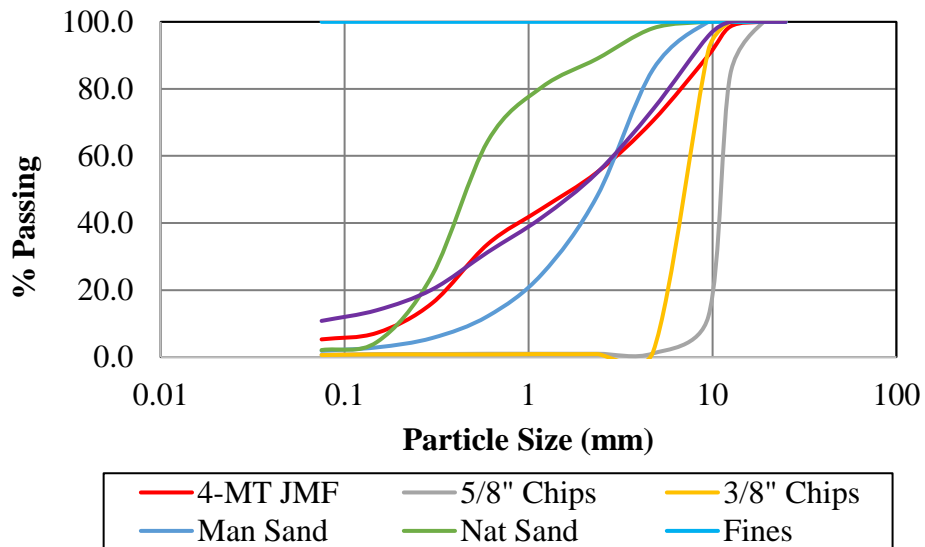


Figure 4.36: Aggregate Particle Size Distribution Curves

The particle size distribution (PSD) curve for the JMF mixture was then used to compare to the 0.45 power curve according to the maximum aggregate size that was used in the mix. It can be seen from Figure 4.37 that the JMF combination curve is very similar to the 0.45 power curve which represent an optimal aggregate configuration.

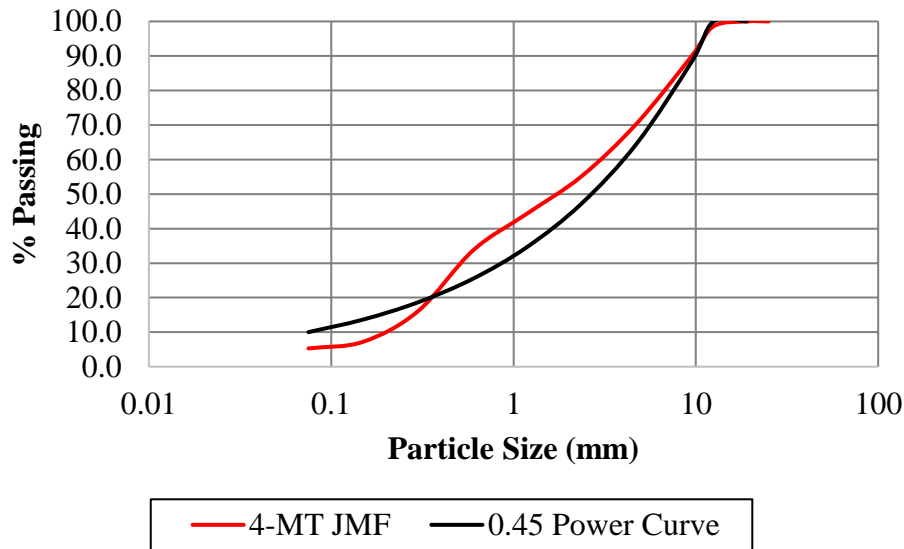


Figure 4.37: JMF Particle Size Distribution Curves

Even though the JMF particle size distribution looked similar to the 0.45 power curve, it was still critical to evaluate the Superpave® gradation limits. Figure 4.38 reports the gradation limits with the JMF combination particle size distribution. As seen from this figure, the 0.45 power curve represents the maximum density line where the particles fit together in the densest possible arrangement. The JMF particle size distribution line is within all the control points which is required since the control points function as extreme ranges through which gradation must pass. Lastly, the JMF combination curve does not pass through the restricted zone which means that the mixture is not over-sanded. This also means that the gradation veers from the 0.45 power curve which allows the asphalt mixture to have sufficient room for durability.

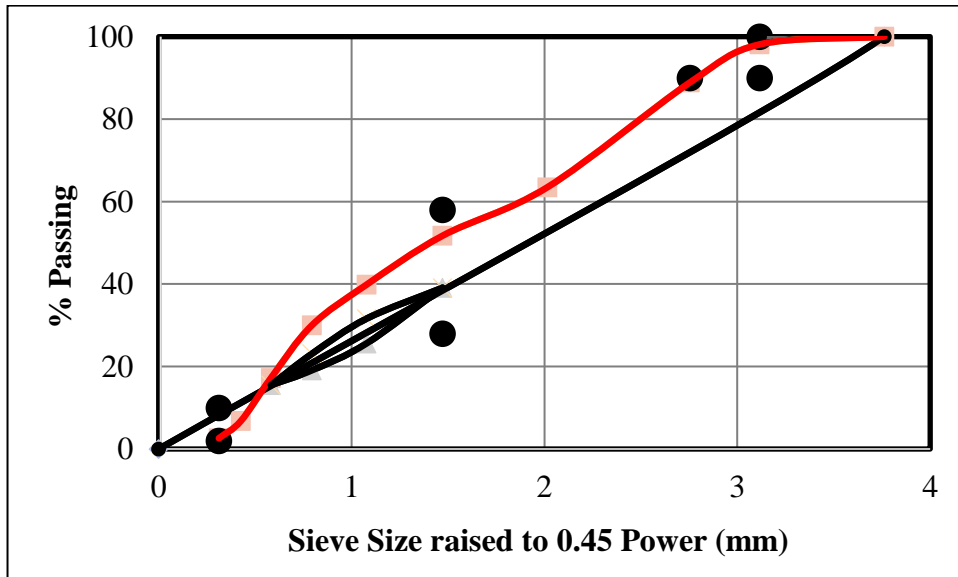


Figure 4.38: Superpave® Gradation Limitations

4.5.3 Aggregate Coating

Asphalt film thickness was used to evaluate proper aggregate coating for both control mixtures and reactive powder mixtures. This parameter was important to calculate since the mixtures with LF and CSA had 25% by volume binder replacement and this means that less binder is available to coat the aggregates. The calculated asphalt film thickness represents the average thickness of the asphalt that surrounds the aggregate particle, and this parameter has been related directly to durability. If the asphalt film thickness is too thin, air can enter the bulk of the material and oxidize the binder which can cause the asphalt to become brittle and fracture. Also, if the film thickness is too thin, water can enter through the binder and penetrate the aggregate particles which can cause moisture damage, leading to rutting, raveling, freeze-thaw damage, and bleeding.

Asphalt film thickness is not considered as a Superpave® design requirement, however evaluating aggregate coating is critical. It has been found that average values for asphalt film thickness should typically be between 6 to 8 μm (Hmoud, 2011). This thickness range has been found to establish a thick enough coating around the aggregate particles which prevents rapid oxidation, and moisture damage.

Table 4.29 reports the surface area factors, percent passing of the asphalt mixtures, and surface area of aggregates. From this table it can be seen that the total surface area of the aggregates used in all 4-MT WMA mixtures was approximately 6.45 m^2/kg .

Table 4.29: Calculated Surface Area of Aggregates

Sieve Size	Surface Area Factors	Percent Passing (%)	Surface Area (m^2/kg)
Max (19.0mm)	2	100.00	0.41
No.4 (4.75mm)	2	70.50	0.29
No.8 (2.36mm)	4	55.14	0.45
No.16 (1.18mm)	8	44.26	0.73
No.30 (0.6)	14	33.70	0.97
No.50 (0.3)	30	16.13	0.99
No.100 (0.15)	60	7.23	0.89
No.200 (0.075mm)	160	5.29	1.72
		SUM	6.45

The surface area was then used to calculate the film thickness which is reported in Table 4.30. From this table it is seen that the film thickness of the control mixtures was 8.24 μm and the film thickness of the reactive powder mixtures was 5.90 μm . This makes sense that the film thickness of the LF and CSA mixtures was less than the control mixtures because 25% by volume of asphalt binder was replaced with the reactive powder material. It is also important

that both mixture types were either close to the recommended range of 6 to 8 μm or above this range as this is critical for durability.

Table 4.30: Asphalt Film Thickness for Control and Reactive Powder Mixtures

Mixture	4-MT Control	4-MT Reactive Powder
Surface Area of Aggregates (ft²/lb)	31.51	31.51
Surface Area of Aggregates (m²/kg)	6.45	6.45
Bulk Specific Gravity of Aggregate	2.706	2.706
Effective Specific Gravity of Aggregate	2.756	2.756
Asphalt Specific Gravity	1.028	1.028
Asphalt Content (%)	5.8%	4.4%
Total Weight (g)	4700.00	4700.00
Asphalt Volume (mL)	265.18	201.17
Asphalt Absorbed (by weight of aggregate)	0.689	0.689
Weight of Absorbed Asphalt (g)	30.51	30.97
Volume of Absorbed Asphalt (mL)	29.68	30.12
Effective Volume of Asphalt (mL)	235.49	171.04
Film Thickness (Tf) (microns)	8.24	5.90

After the film thickness was calculated it was also important to visually inspect the coating of the aggregates. During the mixing process, there were no problems observed in terms of aggregate coating. The asphalt binder seemed to coat the aggregates at the same rate for both the control mixtures and reactive powder mixtures. Figure 4.39 displays representative aggregates for each mixture type. From this figure it is clear that no major differences can be reported.

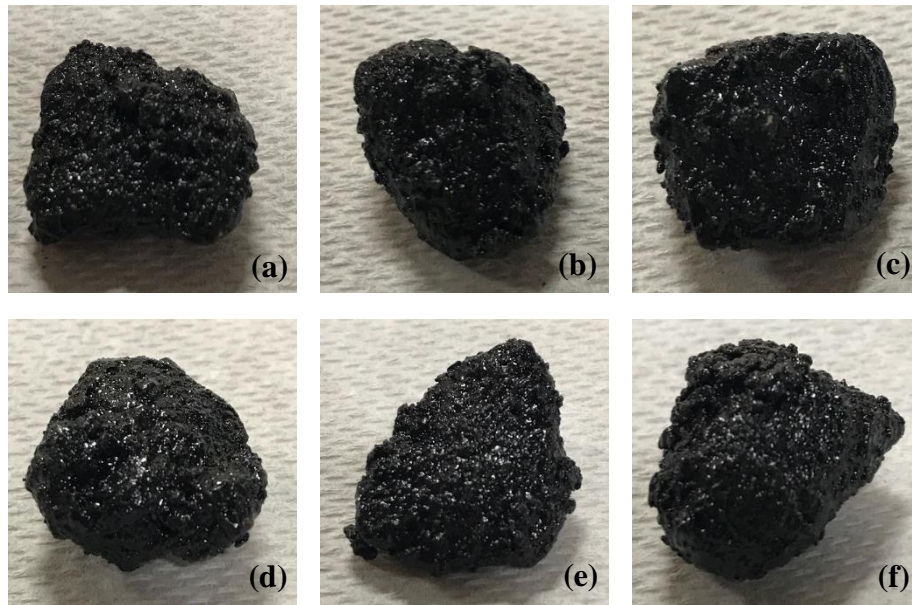


Figure 4.39: Aggregate Coating (a) WMA PG58-28 LS Control (b) WMA PG58-28 LF (c) WMA PG58-28 CSA (d) WMA PG52-34 LS Control (e) WMA PG52-34 LF (f) WMA PG52-34 CSA

4.5.4 Constructability

Workability was evaluated by comparing the densification curves of the control mixtures (with limestone) and the mixtures with LF and CSA reactive powders. All compaction comparisons for workability were evaluated for short-term aged materials because this demonstrates the physical condition in which the material is mixed, placed, and compacted in the field. Here, lower compaction efforts demonstrated better workability properties. For all evaluations, all WMA mixtures were mixed at 120°C and compacted at 115°C.

Figure 4.40 demonstrates the workability results for WMA PG58-28 mixtures and Figure 4.41 demonstrates the workability results for the WMA PG52-34 mixtures. Every mixture was compacted to 100 gyrations to understand the material behavior over a wide range of gyrations. It can be seen that every specimen was compacted to approximately 96-97% G_{mm} (3-4% air voids) and this is a critical parameter to evaluate in terms of Superpave® compaction

efforts. The densification curves show that the 25% binder replacement by volume for the LF and CSA mixtures hindered the workability when compared to the LS control mixtures because the required compaction efforts were higher. Both Figure 4.39 and Figure 4.40 demonstrate that the CSA mixtures required the most compaction efforts when compared to all other mixtures.

For the WMA PG58-28 mixtures the maximum %Gmm at 100 gyrations was 96.80% for LS, 96.40% for LF, and 96.24% for CSA. For the WMA PG52-34 mixtures the maximum %Gmm at 100 gyrations was 96.88% for LS, 96.47% for LF, and 96.42% for CSA. It is important to note that even though there was a reduction in workability the difference is rather small when understanding that there was a 25% binder replacement by volume for the reactive powder mixtures and this is an important factor to consider.

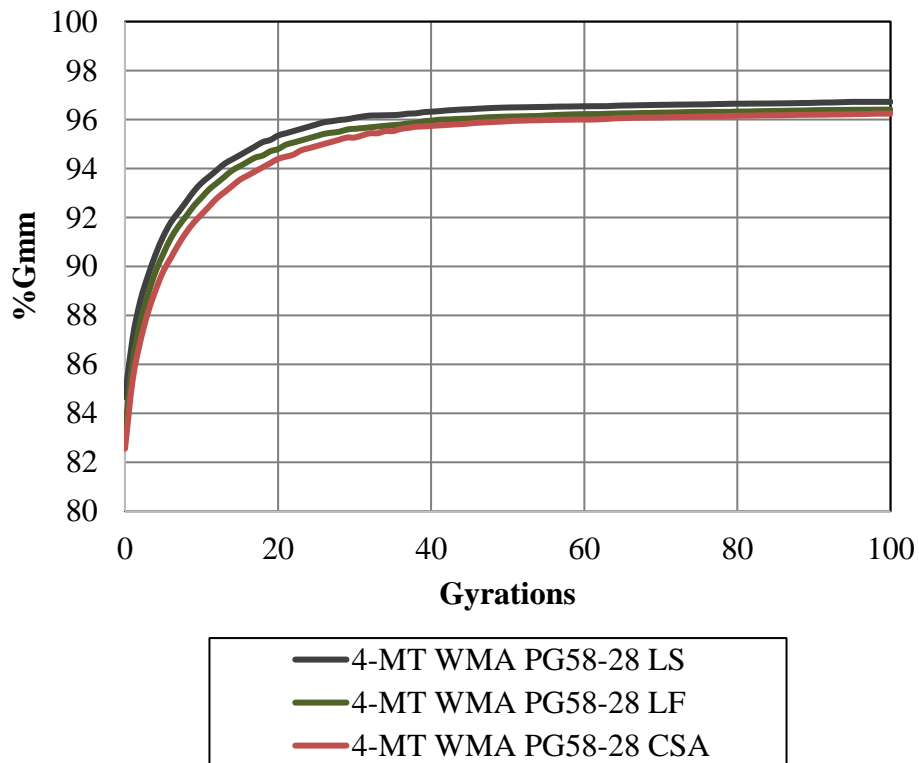


Figure 4.40: Densification Curve for 4-MT WMA PG58-28 Mixtures

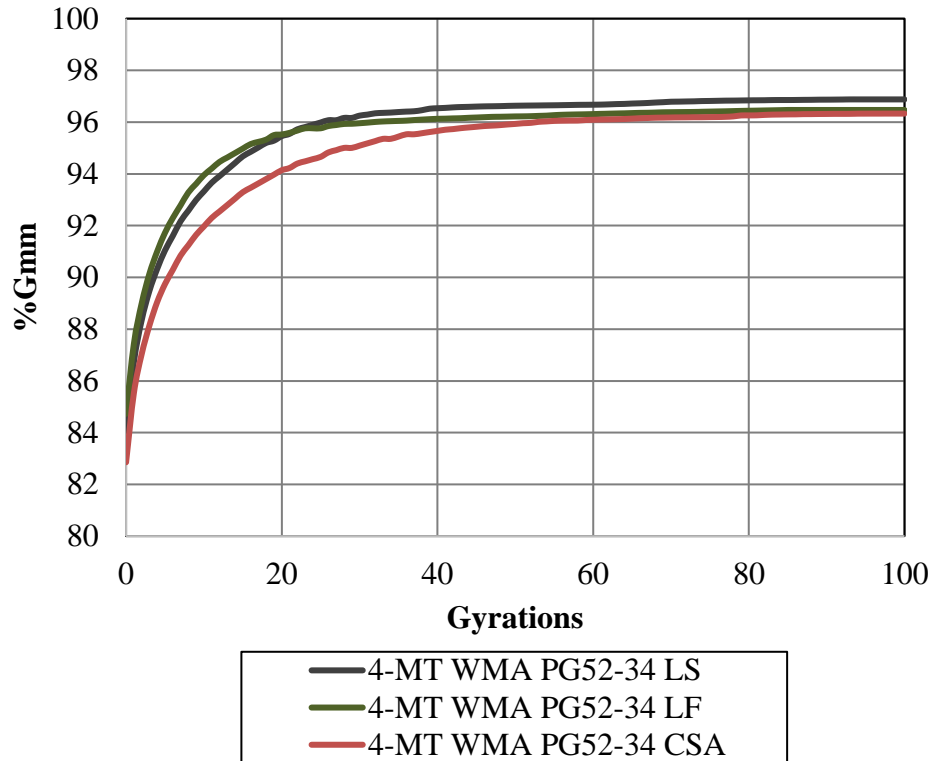


Figure 4.41: Densification Curve for 4-MT WMA PG52-34 Mixtures

The compaction volumetrics were evaluated to understand the differences between the control LS mixtures and reactive powder mixtures with LF and CSA cement. Table 4.31 displays the mixture volumetrics for the WMA PG58-28 mixtures and Table 4.32 displays the mixture volumetrics for the WMA PG52-34 mixtures. From these table it can be seen that the bulk specific gravity (G_{mb}) and the maximum specific gravity (G_{mm}) both increased due to the addition of the reactive powders. The reason for this increase is because the specific gravity of the reactive powders (LF, 3.13; CSA, 2.89) were higher than the specific gravity of asphalt binder (1.028). Since 25% of binder was being replaced with the reactive powder (by volume), the bulk and max specific gravities increased due to the proportional increase in the aggregate quantities.

Other volumetrics that demonstrate the differences are the added binder content (P_b), aggregate content (P_s), effective asphalt content (P_e), voids in the mineral aggregate (VMA), air voids (V_a), voids filled with asphalt (VFA), and the dust-to-binder ratio (powder-to-binder ratio). Since 25% (by volume) of asphalt content was being replaced with the reactive powder materials, the added binder content, effective asphalt binder content, voids in the mineral aggregate, and the voids filled with asphalt were all reduced as a result. The reduction in these parameters can be correlated directly to the asphalt film thickness because the film thickness was reduced as well for reactive powder mixtures (i.e., indicating less binder content). However, considering that more powder (material that passes the No. 200 sieve) was added to the reactive powder mixtures, the dust-to-binder ratio increased to 1.3 as compared to the control mixture with 0.7.

Table 4.31: WMA PG58-28 Asphalt Mixture Volumetrics

Mixture	4-MT WMA PG58-28 LS	4-MT WMA PG58-28 LF	4-MT WMA PG58-28 CSA
Gmm	2.535	2.586	2.579
Gmb	2.454	2.493	2.482
Gsb	2.706	2.706	2.706
Gse	2.756	2.756	2.756
Gb	1.028	1.028	1.028
Design Pb (%)	5.8	4.4	4.4
Pba (%)	0.7	0.7	0.7
Ps (%)	94.2	95.7	95.6
Pbe (%)	5.2	3.7	3.7
VMA (%) > 14%	14.6	11.9	12.3
Va (%) = 4.0%	3.2	3.6	3.8
VFA (%) (65-75)	78.1	69.7	69.5
Dust-to-Binder Ratio (0.6-1.2)	0.7	1.3	1.3

Table 4.32: WMA PG52-34 Asphalt Mixture Volumetrics

Mixture	4-MT WMA PG52-34 LS	4-MT WMA PG52-34 LF	4-MT WMA PG52-34 CSA
Gmm	2.531	2.578	2.569
Gmb	2.452	2.487	2.477
Gsb	2.706	2.706	2.706
Gse	2.756	2.756	2.756
Gb	1.028	1.028	1.028
Design Pb (%)	5.8	4.4	4.4
Pba (%)	0.7	0.7	0.7
Ps (%)	94.2	95.6	95.6
Pbe (%)	5.1	3.7	3.7
VMA (%) > 14%	14.6	12.1	12.5
Va (%) = 4.0%	3.1	3.5	3.6
VFA (%) (65-78)	78.7	70.9	71.3
Dust-to-Binder Ratio (0.6-1.2)	0.7	1.3	1.3

When evaluating the Superpave® volumetric mixture design requirements it was noted that the VMA needs to be above 14% (based on a nominal maximum aggregate size of 12.5 mm), the VFA needs to be between 65 and 78% (0.3 to < 3 ESALs in millions) or 65 and 75% (3 to < 30, 30 ≤ ESALs in millions), and the dust-to-binder ratio needs to be between 0.6 and 1.2. Evaluating the mixture volumetrics in Table 4.31 and Table 4.32 it can be observed that for the control mixtures with limestone all of these parameters are satisfied. For the reactive powder mixtures used at higher replacement volumes of 25%, however, even though all of the requirements are fulfilled, the VMA is slightly less than 14% and the dust-to-binder ratio is slightly higher than 1.2. Findings from this research, though, could be used to implement new limits affecting mix designs and this is an objective of the reported research.

4.5.5 Aging Resistance

The aging resistance was evaluated by comparing the aging index of all the mixtures. The aging index was calculated as the difference in air content at 8 gyrations for long-term aged materials versus the air content at 8 gyrations for short-term aged materials. Here, lower aging indexes demonstrate higher aging resistance. If the aging index is low, this means that the material resists the stiffening effects of age-hardening. The short-term aging procedure used in this research mimics the aging due to mixing, placing, and compacting whereas the long-term aging procedure used in this research represents 5 to 10 years of aging in the field. Comparing the material in these different aging conditions was critical because resisting the effects of age-hardening could potentially increase the life expectancy of the material since it would become stiffer at a slower rate.

Figure 4.42 and Figure 4.43 display the percentage of air for both the short-term and long-term compacted specimens at 8 gyrations (N_{ini}) for the WMA PG58-28 mixtures and WMA PG52-34 mixtures, respectively. Age hardening increases the stiffness of the material which means the compaction effort needs to increase. These figures visually demonstrate this hardening effect due to aging since the percent air increased from the compaction of short-term aged compaction to the long-term aged mixture. It is important to note that mixtures with similar percentages of air at 8 gyrations can resist the effects of aging. Materials with poor aging resistance reveal higher deviations in percentages of air at different aging conditions. Since there is a lower compaction in the long-term aged mixtures at 8 gyrations, these materials demonstrate age-hardening due to the increase in compaction effort.

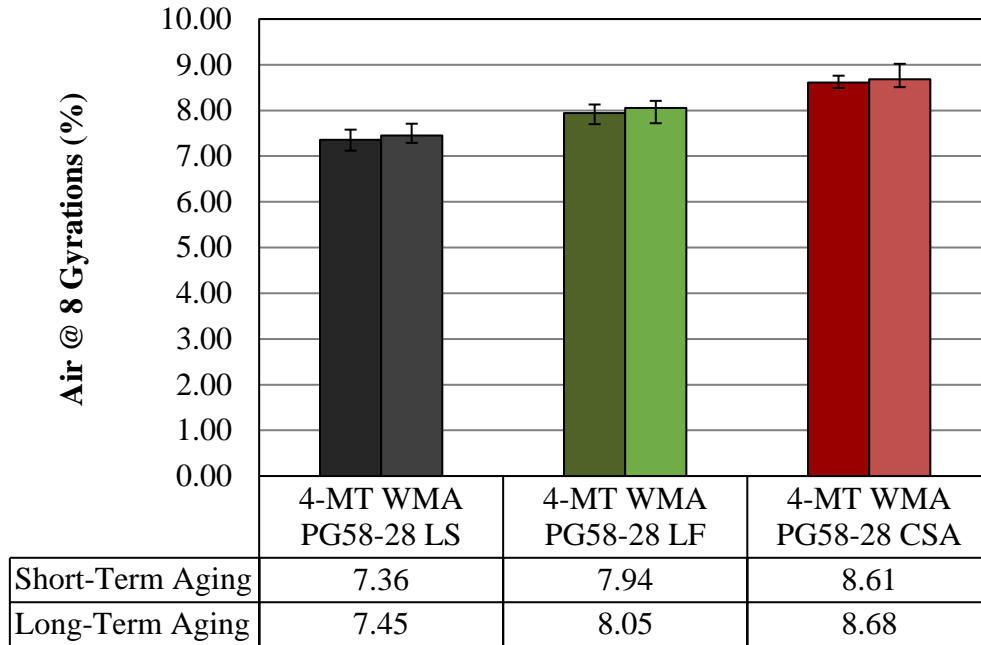


Figure 4.42: Percent Air at 8 Gyration for Short-Term and Long-Term Aged WMA PG58-28 Mixtures

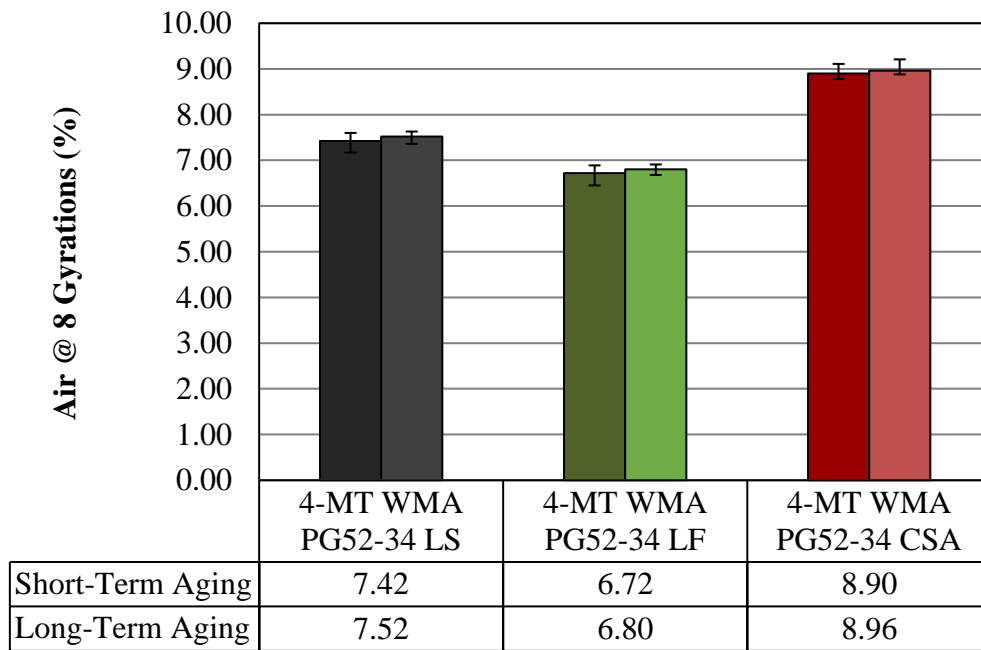


Figure 4.43: Percent Air at 8 Gyration for Short-Term and Long-Term Aged WMA PG52-34 Mixtures

Figure 4.44 and Figure 4.45 report the results of the aging resistance testing. These results demonstrate that lower values of aging index are desirable since this means the material is less prone to age hardening and can resist the long-term stiffening. All long-term aged materials experienced age hardening since the aging index is greater than 1.0, which was expected. Figure 4.44 explains that the WMA PG58-28 CSA mixtures were the only reactive powder mixtures that reduced the rate of age hardening as compared to the control LS mixtures since the aging index was 28.57% lower. Figure 4.45 explains that the WMA PG52-34 LF and CSA mixtures both increased the age hardening resistance since the aging index values were lower than the control LS mixtures. Here, the WMA PG52-34 CSA mixtures demonstrated the best aging index since the aging index was 66.67% lower than the control LS mixture.

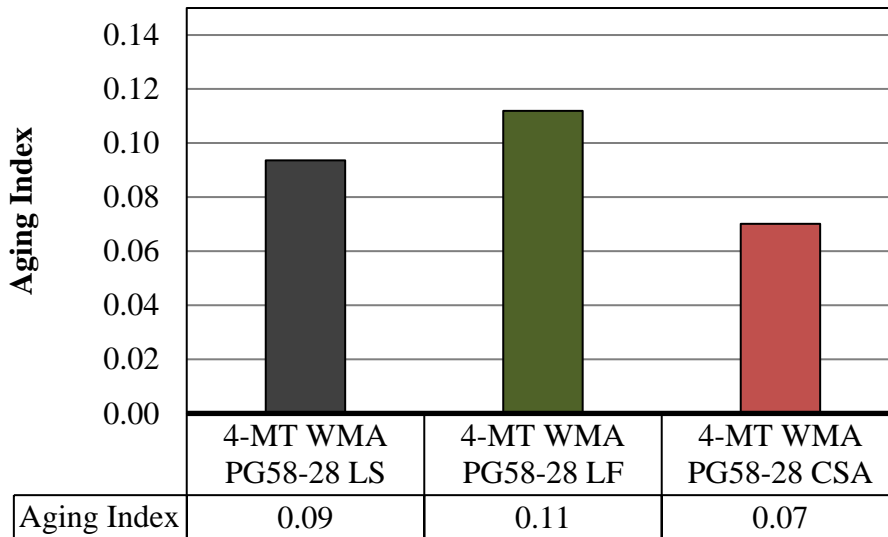


Figure 4.44: Aging Index for WMA PG58-28 Mixtures

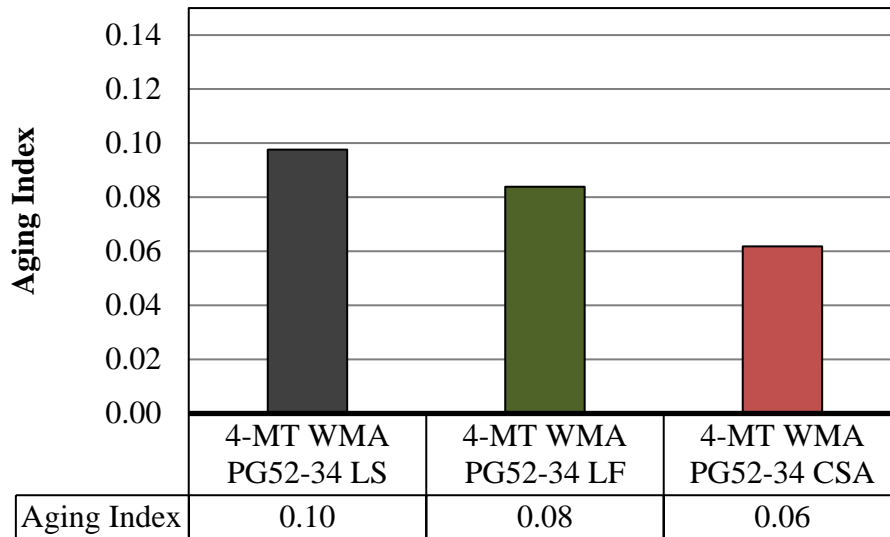


Figure 4.45: Aging Index for WMA PG52-34 Mixtures

4.5.6 Moisture Damage

Moisture damage was used as a parameter to evaluate the durability of asphalt pavements. Asphalt specimens were tested under different conditions to understand the effects of moisture damage. The samples that were tested in dry, saturated, and conditioned environments. The dry samples were placed into a leak-proof plastic bag and then placed in a water bath at $25 \pm 0.5^\circ\text{C}$ for $2 \text{ h} \pm 10 \text{ min}$ and then tested using IDT. The saturated and conditioned specimens were both vacuum-saturated to a degree of saturation of 70 to 80%. The saturated specimens were then placed into a water bath at $25 \pm 0.5^\circ\text{C}$ for $2 \text{ h} \pm 10 \text{ min}$ and then tested with the IDT. The conditioned samples were placed in a water bath at $60 \pm 1^\circ\text{C}$ for $24 \pm 1 \text{ h}$, then placed in a water bath at $25 \pm 0.5^\circ\text{C}$ for $2 \text{ h} \pm 10 \text{ min}$ and then tested with the IDT.

The results of the Indirect Tensile Test (IDT) for dry, saturated, and conditioned sample are reported in Table 4.33 and Table 4.34. These results demonstrate that all the reactive powder mixtures for both WMA PG58-28 and WMA PG52-34 mixtures developed higher

strengths when compared to the control LS mixture, however, flow (displacement) was reduced in most cases. Typically, load and displacement have an inverse relationship which means that when the maximum load increases the maximum flow tends to decrease. For dry WMA PG58-28 samples, the CSA mixture had the highest ultimate strength of 9.96 kN whereas the control mixture had the lowest ultimate load of 7.65 kN. The control samples had the highest flow (displacement) of 4.29 mm whereas the LF samples had the lowest flow of 3.92 mm. This case demonstrated the inverse relationship between load and deformation. For dry WMA PG52-34 samples, the LF mixture had the highest ultimate strength of 6.29 kN whereas the control mixture had the lowest strength again of only 4.96 kN. For this case the control samples had the lowest flow of only 3.98 mm and the CSA samples had the highest flow of 4.23 mm.

Table 4.33: Moisture Damage Load and Flow Results for WMA PG58-28 Mixtures

Binder	Environment	Sample	Max Load (kN)	Max Flow (mm)
WMA PG58-28	Dry	LS	7.65	4.29
		LF	9.67	3.92
		CSA	9.96	4.19
	Saturated	LS	7.23	4.20
		LF	8.47	3.81
		CSA	9.36	3.73
	Conditioned	LS	6.98	4.14
		LF	8.01	4.17
		CSA	9.01	3.98

Table 4.34: Moisture Damage Load and Flow Results for WMA PG52-34 Mixtures

Binder	Environment	Sample	Max Load (kN)	Max Flow (mm)
WMA PG52-34	Dry	LS	4.96	3.98
		LF	6.29	4.01
		CSA	5.96	4.23
	Saturated	LS	4.87	3.89
		LF	6.27	3.71
		CSA	5.78	3.77
	Conditioned	LS	4.58	3.89
		LF	5.83	3.70
		CSA	5.43	3.81

Figure 4.46 and Figure 4.47 demonstrate the horizontal tensile stress. These results give a visual correlation to the maximum load results represented in Table 4.33 and Table 4.34. These figures reflect that the maximum horizontal stresses for the reactive powder samples were higher than the control LS samples at all environmental conditions. For dry WMA PG58-28 samples, CSA samples had the highest maximum horizontal stress at all environmental conditions. For dry WMA PG52-34 samples, LF samples had the highest maximum horizontal stress at all environmental conditions. The displayed trend indicates that as the environmental exposure worsens, the ultimate stress decreases.

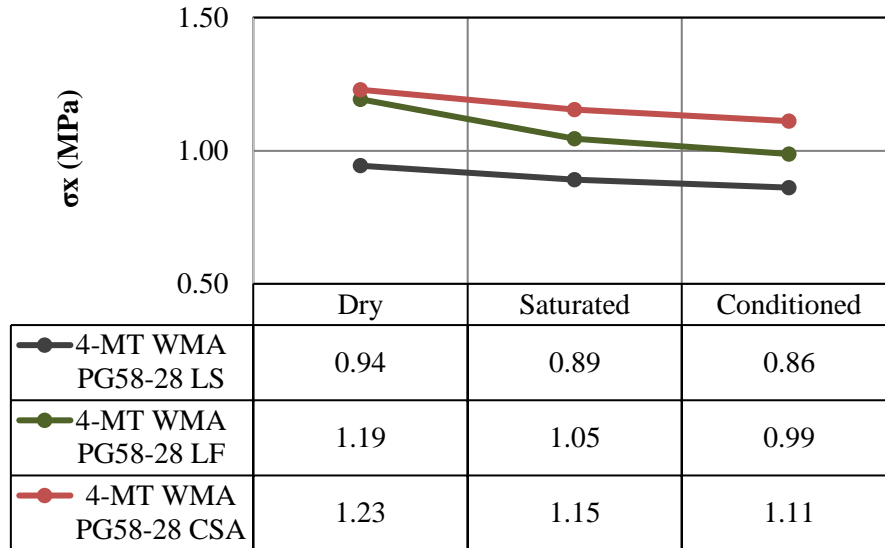


Figure 4.46: Horizontal Tensile Stress at Center of Specimen for WMA PG58-28 Mixtures

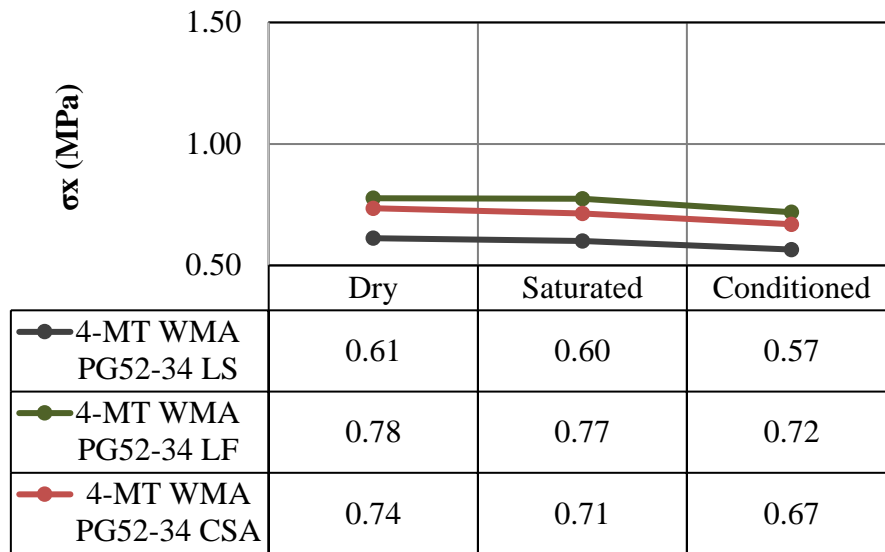


Figure 4.47: Horizontal Tensile Stress at Center of Specimen for WMA PG52-34 Mixtures

Figures 4.48 and Figure 4.49 demonstrates the ultimate vertical compressive stress of the mixtures which directly correlate with the horizontal tensile stress results. These figures proved that the maximum vertical stresses for the reactive powder samples were higher than the control LS samples at all environmental conditions. For dry WMA PG58-28 samples, CSA cement samples had the highest maximum vertical stress at all environmental conditions. For

dry WMA PG52-34 samples, LF cement samples had the highest maximum vertical stress at all environmental conditions.

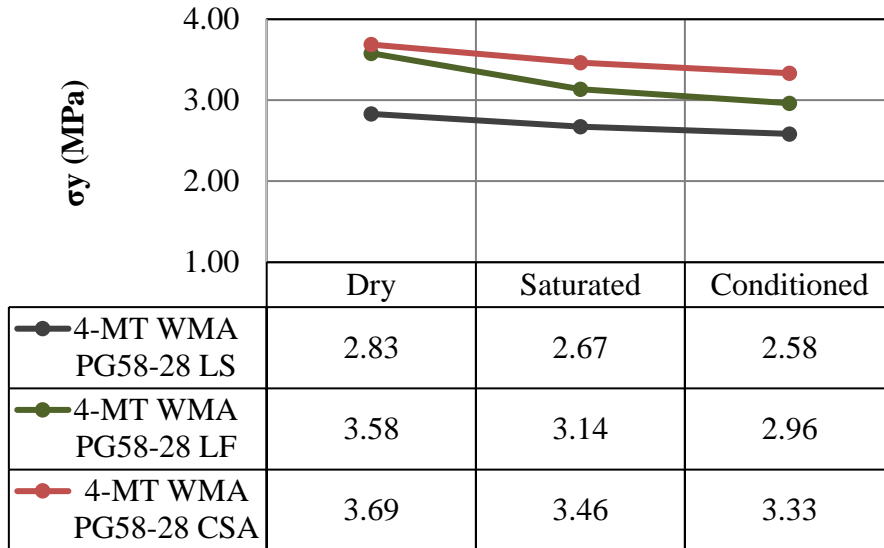


Figure 4.48: Vertical Compressive Stress at Center of Specimen for WMA PG58-28 Mixtures

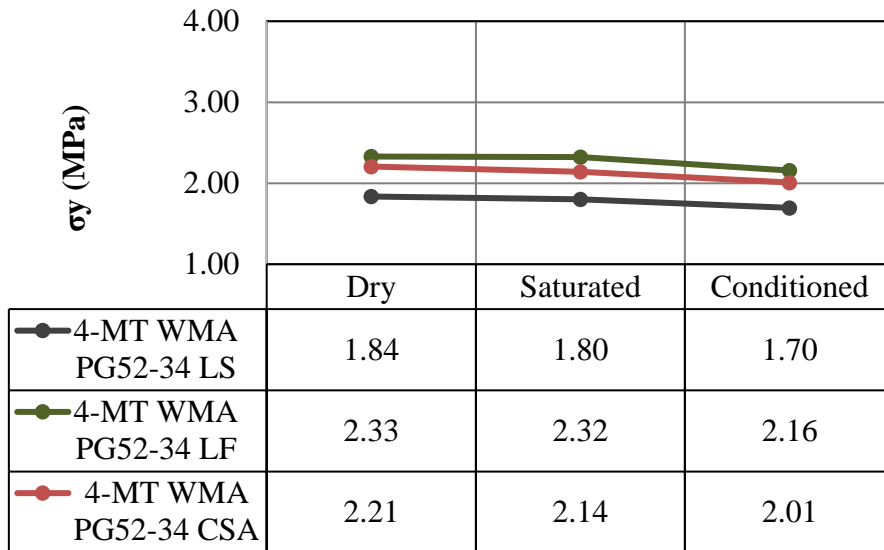


Figure 4.49: Vertical Compressive Stress at Center of Specimen for WMA PG52-34 Mixtures

Figure 4.50 and Figure 4.51 reports on the tensile strain at failure for the WMA PG58-28 mixtures and WMA PG52-34 mixtures. These results give a visual representation of the maximum flow (displacement) results represented in Table 4.33 and Table 4.34. These figures demonstrate the effects of moisture damage on the ability for asphalt pavements to deform. For dry WMA PG58-28 samples the LS samples had the highest strain at failure of 0.088 mm/mm and for the dry WMA PG52-34 samples the CSA cement samples had the highest strain at failure of 0.087 mm/mm. For saturated specimens the strain at failure is reduced in all cases when compared to the dry specimens. The ultimate strain (related to flow) increased for the LF and CSA cement samples for both WMA PG58-28 and WMA PG52-34 when comparing the conditioned to the saturated samples. This demonstrates that as the environmental exposure progressed, the ultimate strain upon loading developed better results. This discovery should be investigated further as this might be related to self-healing aspects since the unhydrated portland cement in the aged matrix could be activated due to water exposure.

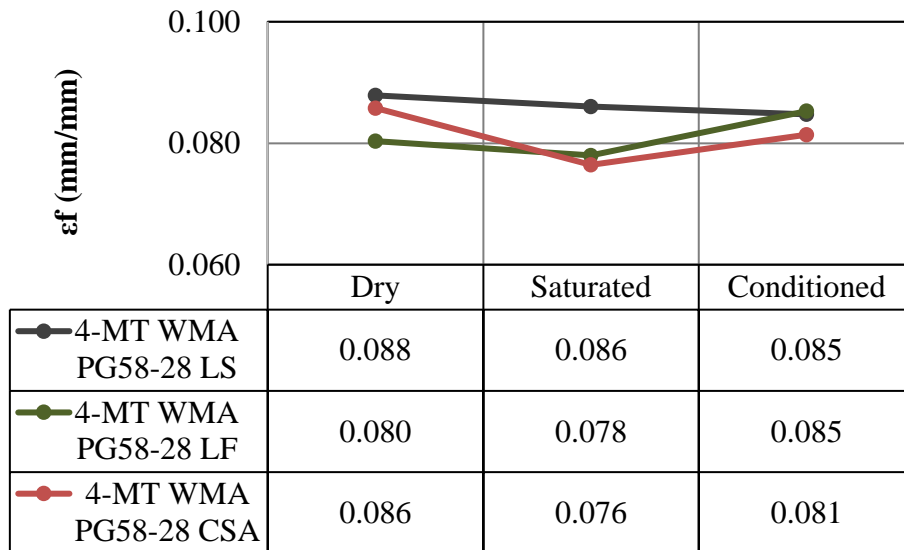


Figure 4.50: Tensile Strain at Failure for WMA PG58-28 Mixtures

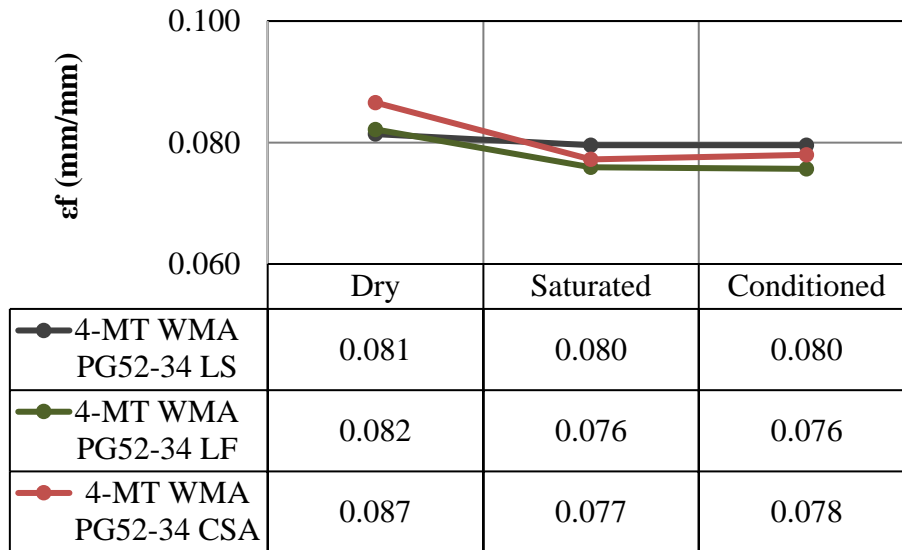


Figure 4.51: Tensile Strain at Failure for WMA PG52-34 Mixtures

The Tensile Strength Ratio (TSR) was calculated and compared for conditioned and saturated samples (Figure 4.52 and Figure 4.53). The TSR values are required to be at or above 0.80; the results demonstrate that all mixtures fulfilled this requirement. Higher values of TSR are desired as this indicates a better performance in terms of moisture damage resistance. It can be observed that the control LS mixture developed better TSR values when compared to the other reactive powder mixtures. When comparing the conditioned samples with the saturated samples the control samples produced a TSR of 0.966 for the WMA PG58-28 mixtures and a TSR of 0.941 for the WMA PG52-34 mixtures. Still, the differences between the control and reactive powder samples are very small and might be misleading. For example, for the WMA PG58-28 samples, the LS only developed a TSR that was 2.22% higher than the LF cement samples and 0.42% higher than the CSA cement samples. Also, for the WMA PG52-34 samples, the LS only developed a TSR that was 1.29% higher than the LF cement samples and 0.32% higher than the CSA cement samples. Here, longer testing time is required to activate the self-healing features of the reactive powders.

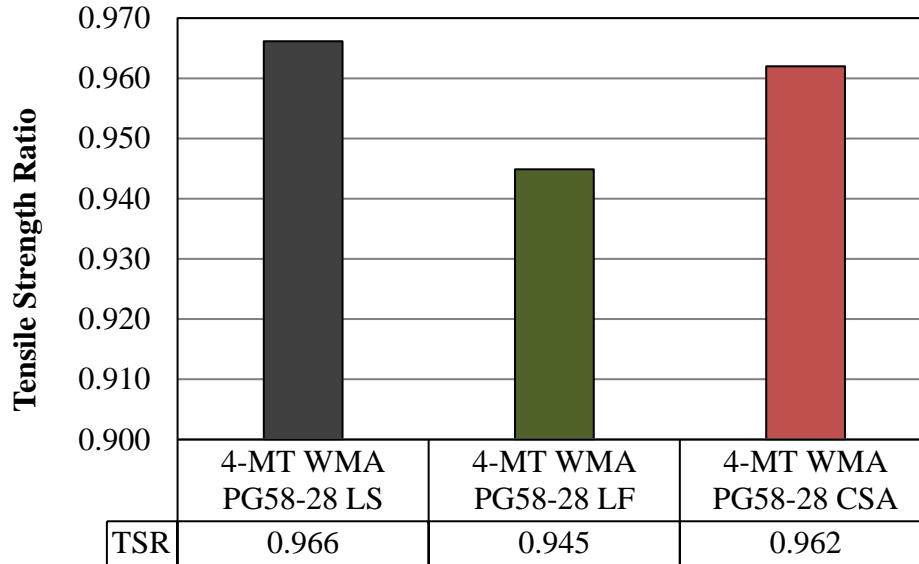


Figure 4.52: TSR for WMA PG58-28 Mixtures

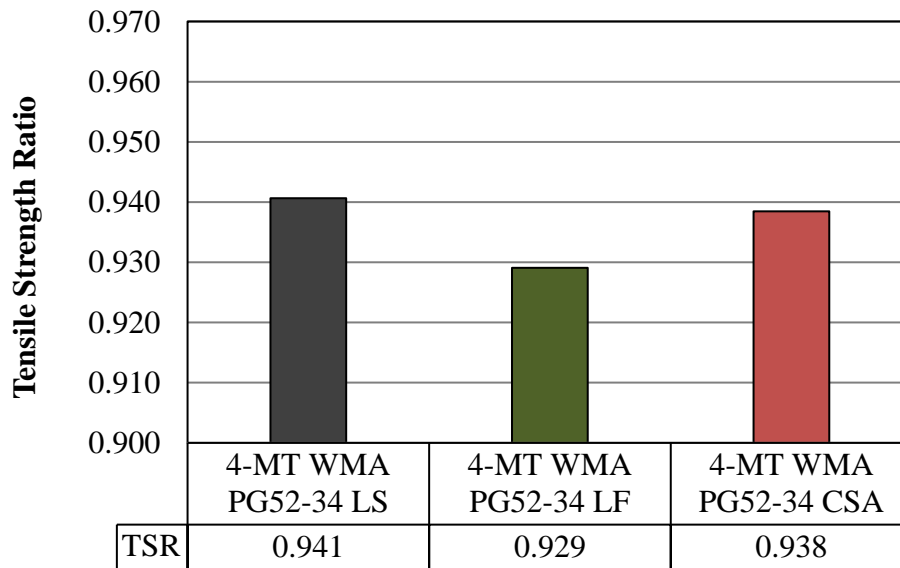


Figure 4.53: TSR for WMA PG52-34 Mixtures

4.5.7 Fatigue Resistance

Fatigue resistance was evaluated to understand the number of cycles each specimen could withstand till failure. The fatigue test that was used to evaluate the slope of the secondary fatigue section as well as the failure point (N_f) which is where the tertiary fatigue section started. It was determined that at this point, the complex modulus (E^*) started to decrease since

the slope of the deformation (strain) line increased. Asphalt pavements that demonstrated smaller deformation rates, as well as demonstrated higher amounts of cycles till failure were considered to be desired.

For this study, fatigue was assessed by using a sine wave loading condition, a test temperature of 20 to 25°C, a 2% pre-loading condition, a 25% ultimate loading condition, and a frequency of 10 Hz. After evaluating the IDT results for the dry samples it was decided to use a constant ultimate load of 7.65 kN for the WMA PG58-28 based samples and an ultimate load of 4.96 kN. For WMA PG58-28 samples, there was a 25% ultimate load of 1.91 kN, a 2% pre-loading of 0.15 kN, and an amplitude of 0.88 kN. For WMA PG52-34 based samples, there was a 25% ultimate load of 1.24 kN, a 2% pre-loading of 0.10 kN, and an amplitude of 0.57 kN. The fatigue test was designed to run until the materials failed.

The results of the fatigue testing are reported in Figure 4.54 and Figure 4.55. These results display the actual vertical deformation for fatigue slopes (from the secondary fatigue sections) of the WMA PG58-28 and WMA PG52-34 materials. Lower values of the fatigue slopes are desirable as this indicates a lower deformation rate under the cyclic loading. The CSA cement mixtures performed the best as these mixtures demonstrated the lowest deformation rate of 1.69E-06 mm/cycle in the vertical direction for the WMA PG58-28 samples and 1.20E-06 mm/cycle for the WMA PG52-34 samples. The LF cement mixtures also performed considerably better than the control mixtures for both binder types. The control LS samples performed the worst as these samples deformed at a rate of 7.28E-06 mm/cycle for the WMA PG58-28 samples and 6.34E-06 mm/cycle for the WMA PG52-34 samples.

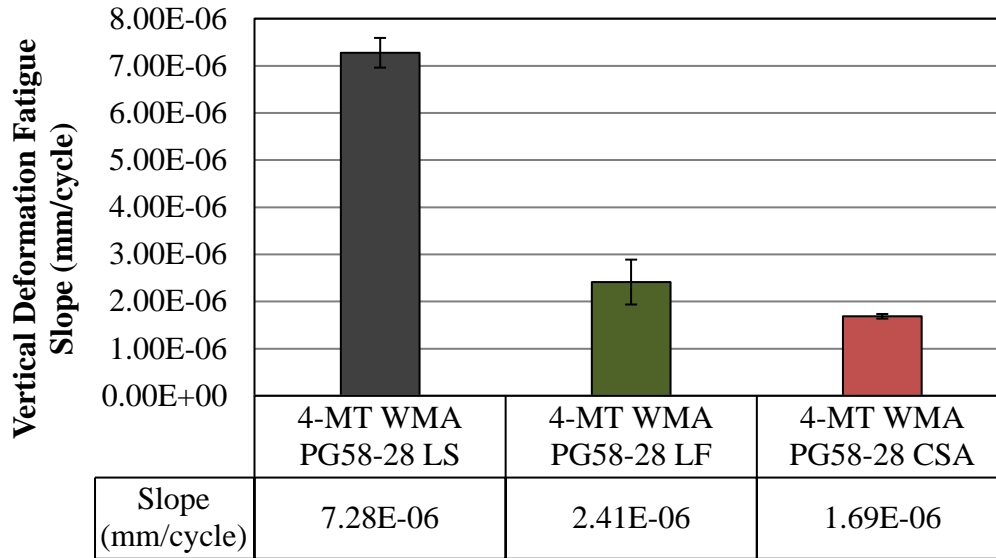


Figure 4.54: Vertical Deformation Fatigue Slope for WMA PG58-28 Mixtures

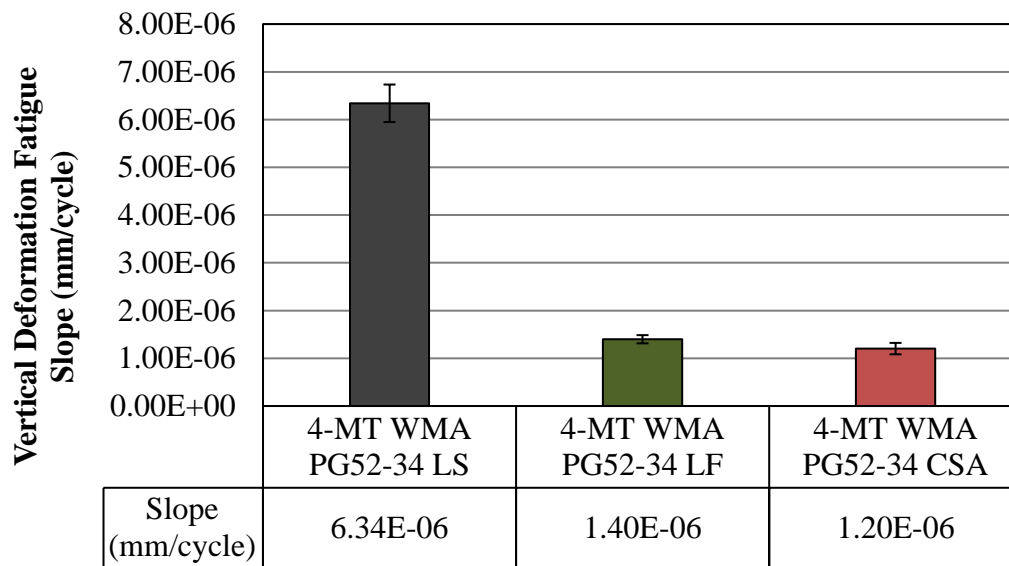


Figure 4.55: Vertical Deformation Fatigue Slope for WMA PG52-34 Mixtures

Figure 4.56 and Figure 4.57 demonstrate the number of cycles that the samples could withstand till there was a drop in E^* (complex modulus). This drop in E^* is directly correlated to N_f as this is the defined point of failure. The results demonstrate a direct correlation to the vertical deformation fatigue slope. In this case the CSA cement samples performed the best for both binder types and the control LS performed the worst for both binder types. The CSA

cement samples for WMA PG58-28 were able to withstand 184,750 cycles till failure and for WMA PG52-34 were able to withstand 158,750 cycles till failure. Therefore, LF samples were very comparable to the CSA cement samples. The control samples were only able to achieve 46.68% as many cycles till failure for the WMA PG58-28 binder when compared to the CSA samples and only able to achieve 62.20% as many cycles till failure for the WMA PG52-34 binder when compared to the CSA cement samples. These results can be correlated to the IDT results in that the samples with higher ultimate strengths and flow could last longer under the fatigue loading. The CSA and LF cement mixtures both demonstrated superior strengths when compared to the control mixture in IDT and comparable flow properties and it was established for fatigue that these materials performed better when exposed to similar loading.

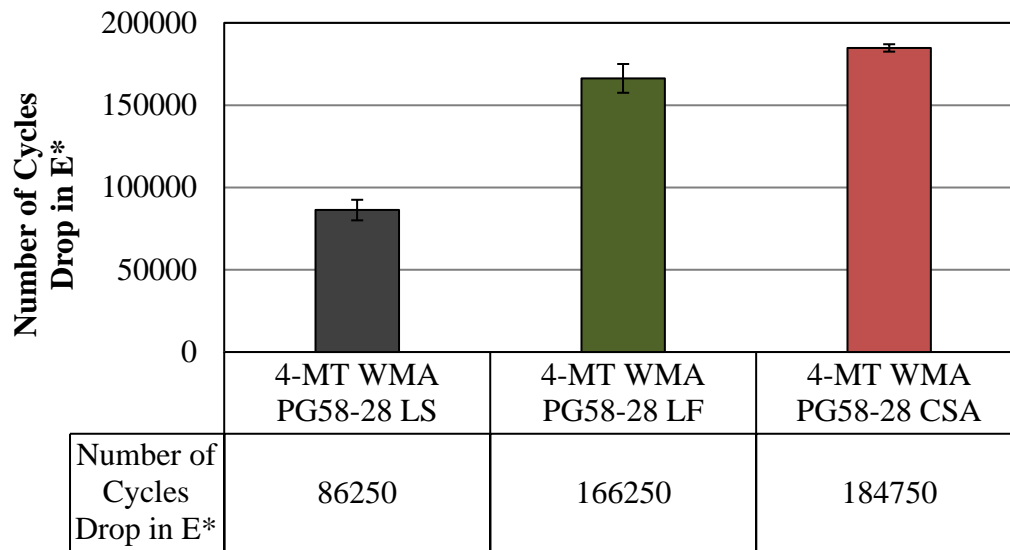


Figure 4.56: Number of Cycles Drop in E* for WMA PG58-28 Mixtures

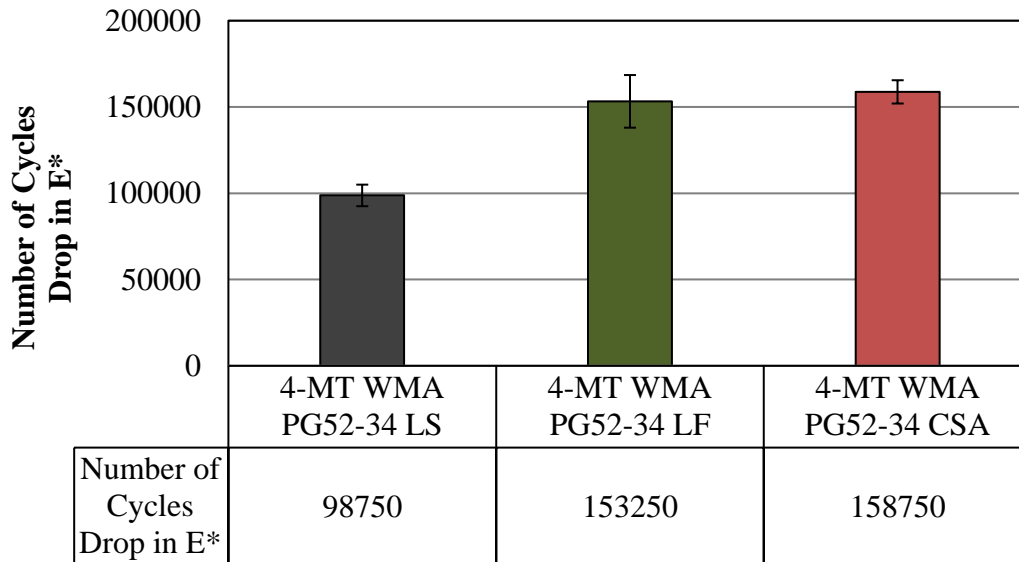


Figure 4.57: Number of Cycles Drop in E* for WMA PG52-34 Mixtures

The results of this study prove that the reactive powder mixtures perform better in respect to intermediate-temperature fatigue resistance. Every reactive powder mixture demonstrated smaller deformation fatigue slopes, and these mixtures were all able to withstand a higher number of loading cycles until failure.

4.5.8 Thermal-Cracking Resistance

The Semi-Circular Bending (SCB) test was used to determine the low-temperature (-18°C) properties such as Fracture Energy (G_f), Fracture Toughness (K_{IC}), and Stiffness (S). Asphalt mixtures become brittle at low temperatures and when the developing thermal stresses become too large, the pavement cracks as a result. Therefore, asphalt materials that are too brittle at low temperatures are undesirable whereas materials that are more elastic perform better since these are able to recover from the emerging stresses. For this testing, higher values of G_f are desirable as this demonstrates larger amounts of energy that is necessary to fracture the specimen. On the other hand, lower stiffness values are desirable as

this demonstrates a more ductile material that can recover from the stresses that are developed due to traffic loads.

The SCB test was performed at -18°C by applying a vertical load on the specimen at a rate of 0.03 mm/min and the test was completed once the load decreased to 0.5 kN . Figure 4.58 and Figure 4.59 demonstrate the Fracture Energy (G_f) of investigated asphalt materials. As previously mentioned, larger values of G_f are desirable as this demonstrates larger energy required to create a unit surface area of crack. This is obtained by dividing the work of fracture (area under the load vs. load line displacement curve) by the ligament area. The experimental results prove that both the LF and CSA cement mixtures performed better than the control LS mixture in terms of G_f . For the WMA PG58-28 binder, the CSA cement samples performed the best since G_f was 1.46 J/m^2 when compared to the control samples which had a G_f of only 1.23 J/m^2 . These results are extremely significant since this demonstrates improved performance of the reactive powder mixtures at low temperature.

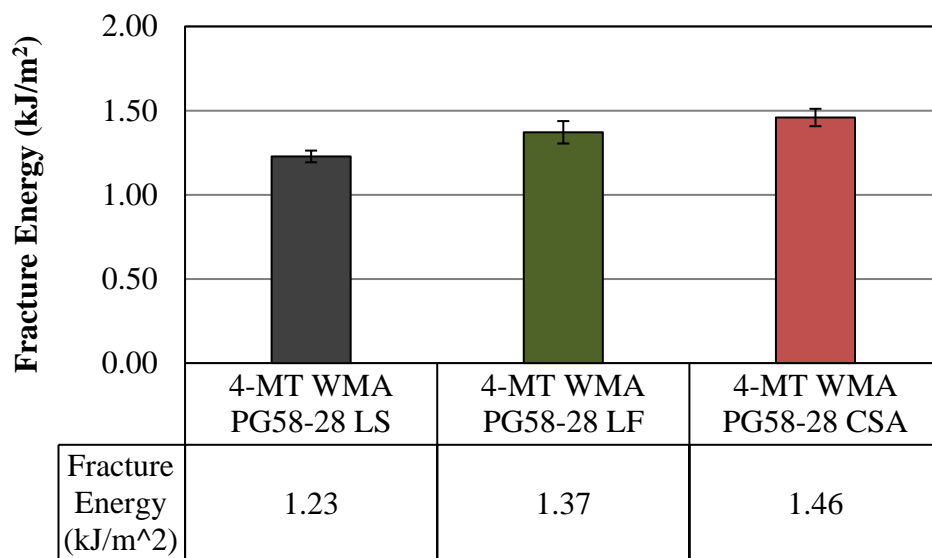


Figure 4.58: Fracture Energy (G_f) for WMA PG58-28 Mixtures

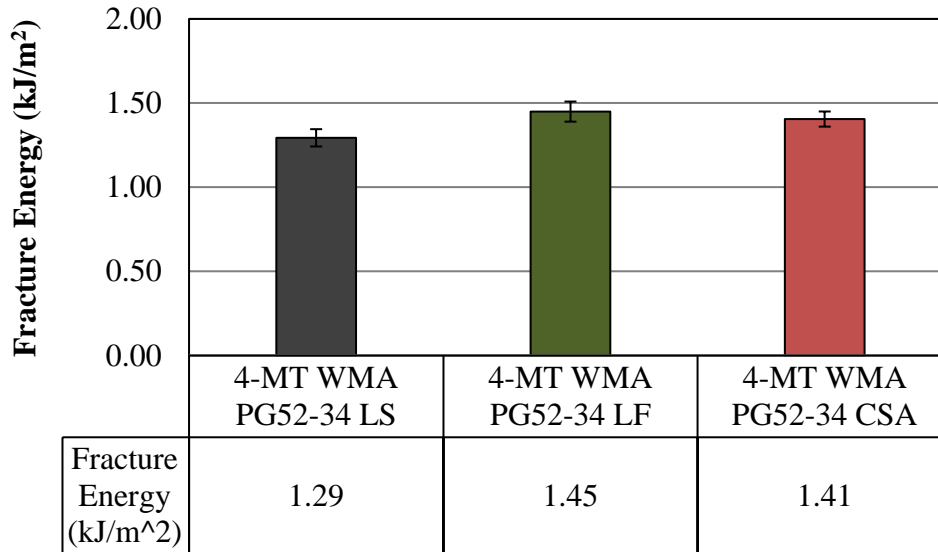


Figure 4.59: Fracture Energy (G_f) for WMA PG52-34 Mixtures

The stiffness $S(t)$ is represented as the slope of the linear portion of the load-line displacement curve. Lower stiffness values are desirable since this demonstrates a more elastic material that can recover from low-temperature stress accumulations. Figure 4.60 and Figure 4.61 reports the stiffness results from the SCB testing. The results prove that the use of reactive powder components hindered the stiffness of the materials and this makes sense since there is a 25% replacement by volume of binder. This means that the reactive powder samples were more brittle at the lower temperature when compared to the control samples. Here, the 25% binder replacement by volume is significant and could have slightly detrimental effects. However, the overall results of the reactive powder mixtures are comparable to those of the control mixtures. The control LS $S(t)$ for the WMA PG58-28 was 10.70 kN/mm whereas the LF was 20.84% higher and the CSA was 26.73% higher. The control LS $S(t)$ for the WMA PG52-34 was 10.15 kN/mm whereas the LF was 21.58% higher and the CSA was 18.33% higher. This is relatively low considering a 25% asphalt binder replacement by volume.

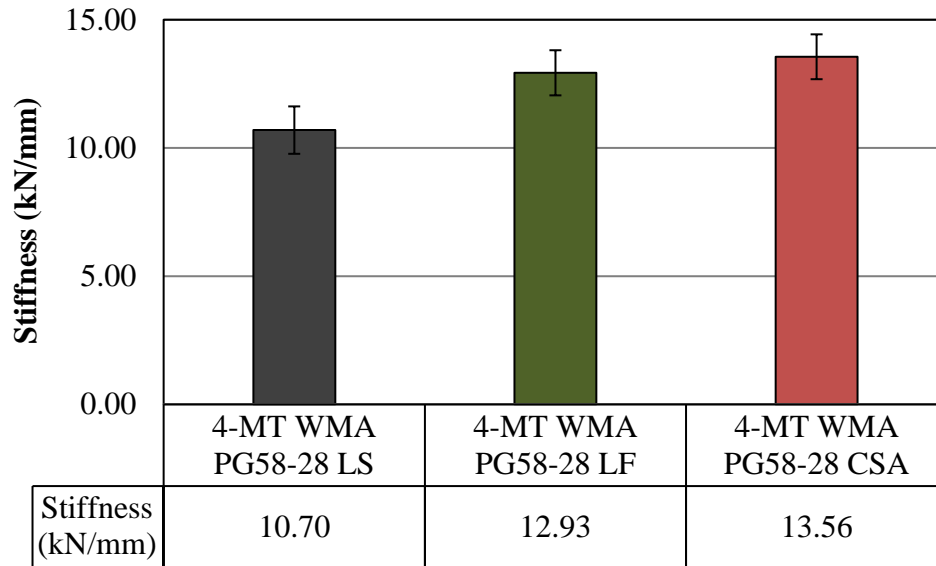


Figure 4.60: Stiffness S(t) for WMA PG58-28 Mixtures

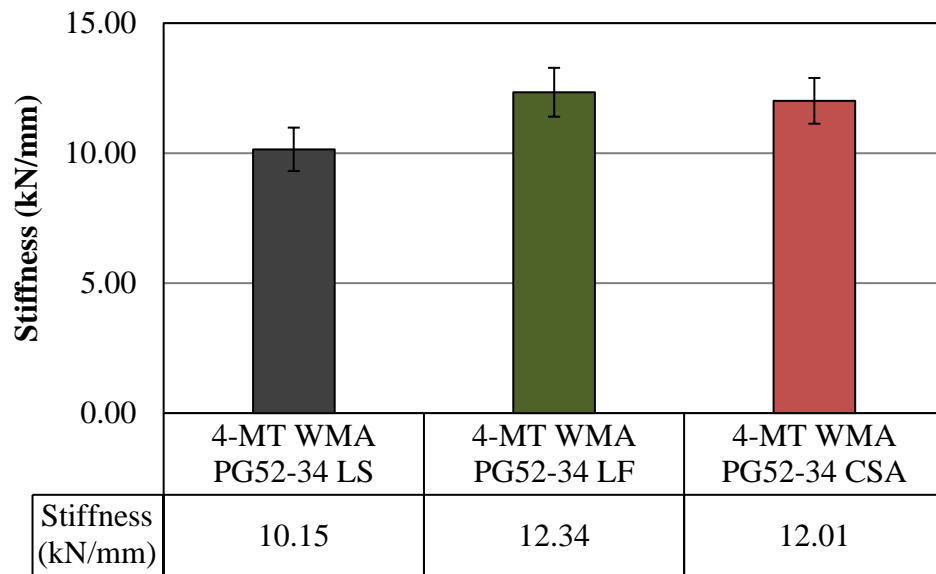


Figure 4.61: Stiffness S(t) for WMA PG52-34 Mixtures

In terms of thermal-cracking resistance, it can be concluded that reactive powder mixtures resisted the effects of low-temperature cracking better than the control mixtures for Fracture Energy (G_f) evaluations. However, the reactive powder mixtures were unable to outperform the control LS mixture for the stiffness $S(t)$ evaluations. Thermal-cracking resistance is an important area of focus, especially for regions that experience cold winter

seasons. For this reason, additional testing should be performed at these low temperatures to assess the response of reactive powders in terms of the overall performance.

4.6 DURABILITY TESTING

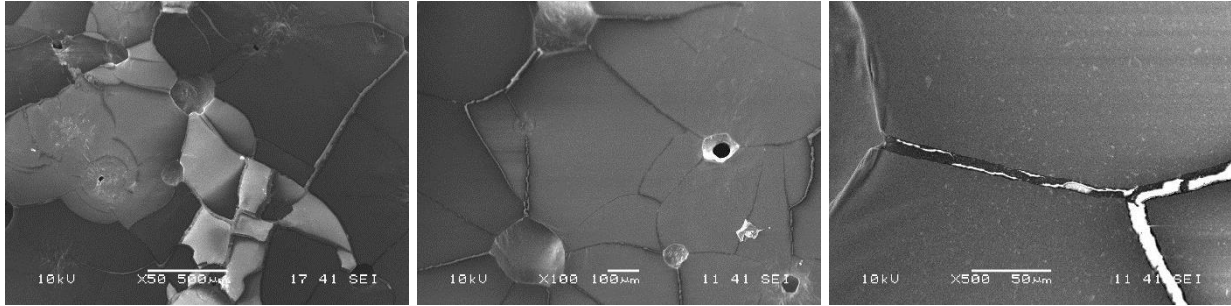
This section explains the experimental testing results for both the control asphalt mastics and mixtures as well as reactive powder asphalt mastics and mixtures in terms of durability testing (all asphalt materials were long-term aged and all asphalt mixtures were compacted to 93% G_{mm}). For these tests, two samples were tested, and averages were determined. The durability testing that was performed evaluated self-healing, freeze-thaw exposure, and salt-scaling.

4.6.1 Self-Healing

Mastic durability testing was used to prove the idea of self-healing at the matrix level. LF and CSA cements, as well as control limestone, were considered with WMA PG58-28 and mastics were produced at a powder concentration of 50% (by volume replacement). This high level of concentration was used to develop a better potential for self-healing as there were more particles incorporated within the asphalt matrix. The mastics were long-term aged using the RTFO and PAV, and then applied to a 5 mm x 5 mm limestone tile as a thin film at 115°C. The thin film solidified at room temperature and was then exposed to rapid freezing by means of liquid nitrogen. The long-term aged mastic (brittle from long-term aging) developed cracks and was placed in a curing chamber for 3 days so that the unhydrated reactive powders could activate and hydrate. These materials were evaluated under Scanning Electron Microscope (SEM) and microstructural images were investigated to understand the potential for self-healing.

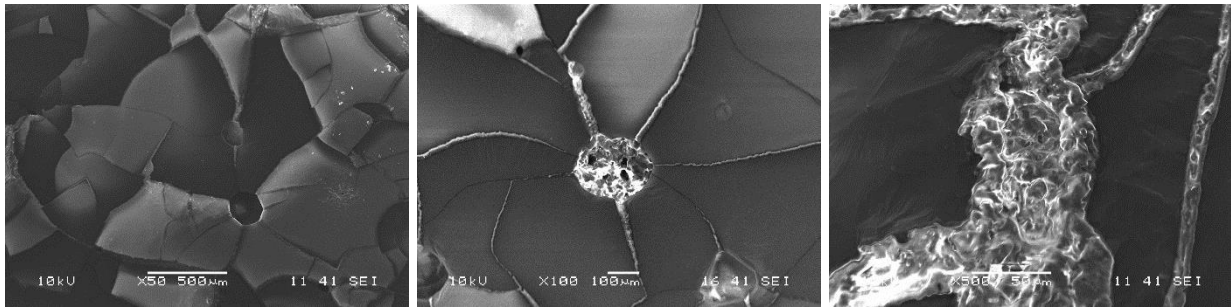
Figure 4.62, 4.63, and 4.64 represent the SEM images of the mastic after durability testing. These results give a clear indication of the self-healing potential for the reactive powder

hybrid asphalt mastics. For the control limestone mastic, it is evident that the limestone powder cannot participate in self-healing as the cracks were exposed with virtually no fill material which opens the pathway for aggressive chemicals. Since the cracks were exposed in this case, the environmental exposure effects can deteriorate the material quicker. On the other hand, the cement powder mixtures had a clear potential for filling the cracks as the hydrated cement expanded from the original source (unhydrated cement particles) and adhered to the crack in its entirety. There was also an excess of activated portland cement that emerged from the internal crack and expanded well beyond the crack channel and even adhered to the surrounding asphalt material. This mechanism of self-healing supports the major objective of this research explaining why reactive powder hybrid asphalt mixtures should be adopted in the field, especially when the durability parameters are included in the design. This is an extremely significant discovery as this proves the idea of self-healing and gives credibility to the proposed developments.



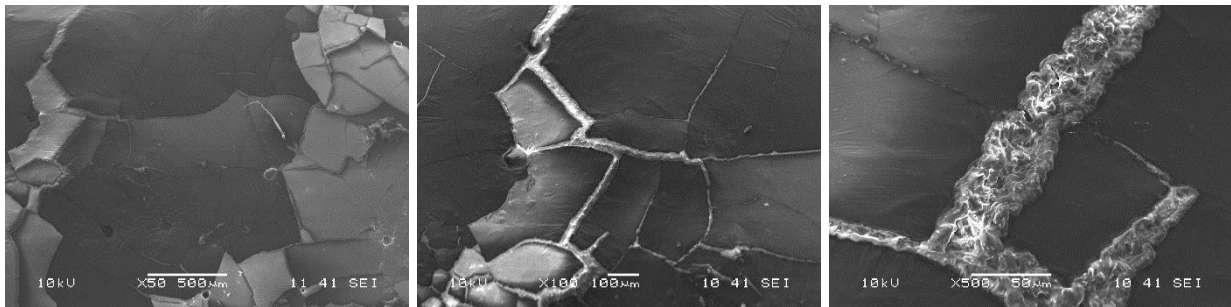
(a) (b) (c)

Figure 4.62: SEM Images of Control Limestone Mastic at (a) 50X (b) 100X (c) 500X



(a) (b) (c)

Figure 4.63: SEM Images of LF Mastic at (a) 50X (b) 100X (c) 500X



(a) (b) (c)

Figure 4.64: SEM Images of CSA Mastic at (a) 50X (b) 100X (c) 500X

4.6.2 Mixture Durability Testing

Asphalt mixture durability testing was evaluated for both freeze-thaw and salt-scaling. The mixtures used for durability testing had a 12.5 mm maximum aggregate size, long-term aged, and compacted to 93% G_{mm} . The LF and CSA reactive powders were added at 25% by

volume replacement to mixtures with WMA PG58-28 and WMA PG52-34 binders and were compared to the control limestone mixtures. The larger quantities of reactive powders was important as this helped build conclusions to better understand the interactions between the materials and self-healing.

4.6.2.1 Freeze-Thaw

The resistance to freeze-thaw damage was an important parameter to evaluate since this is a critical durability concern in climates with colder weather. The material expands and contracts due to freezing and thawing which creates considerable internal stresses. When the internal stresses exceed the material capacity, the composite material can develop macro cracks, and water can penetrate, and then the bulk of the material can fail. Therefore, increasing the resistance to freeze-thaw deformation can result in longer lasting materials. This testing was also important to understand the effects of water exposure over a longer period of time and potentially observe how water can influence the hydration process in hybrid materials.

4.6.2.1.1 Standard Freeze-Thaw

The standard freeze-thaw testing was performed as a modified test in accordance to ASTM C666 (Procedure A) which evaluates the mass change of asphalt mixture samples due to rapid freezing and thawing in water. This procedure was used to evaluate the samples for 300 freeze-thaw cycles in a standard freeze-thaw chamber by measuring the mass loss every 36 cycles. These samples were conditioned in water at 4.5 ± 1 °C and then placed into the environmental chamber for testing. The freezing and thawing cycles consisted of lowering the testing temperature from 4 to -18°C and then raising the temperature from -18 to 4°C in not less than 2 h and not more than 5 h (not less than 25% of the time shall be used for thawing). At the end of the cooling period the temperatures at the center of the specimens shall be -18 ± 2 °C and

at the end of the thawing period the temperature shall be $4 \pm 2^{\circ}\text{C}$. At no point was it permitted for the specimens to reach a temperature lower than -19°C nor higher than 6°C .

Figure 4.65 and Figure 4.66 display the freeze-thaw testing results for both WMA PG58-28 mixtures and WMA PG52-34 mixtures. The results demonstrate that the CSA mixtures performed better than the control limestone mixtures for both WMA PG58-28 and WMA PG52-34 binders. The LF cement mixtures, however, only performed better than the control limestone mixtures for the WMA PG52-34 binder. For the WMA PG58-28 mixtures the total mass loss after 300 freeze-thaw cycles was 0.29% for the LS, 0.84% for the LF, and 0.17% for the CSA. For the WMA PG52-34 mixtures the total mass loss after 300 freeze-thaw cycles was 0.55% for the LS, 0.16% for the LF, and 0.41% for the CSA. This is an interesting research development as this concludes that the CSA cement material performed better than the control for freeze-thaw durability testing.

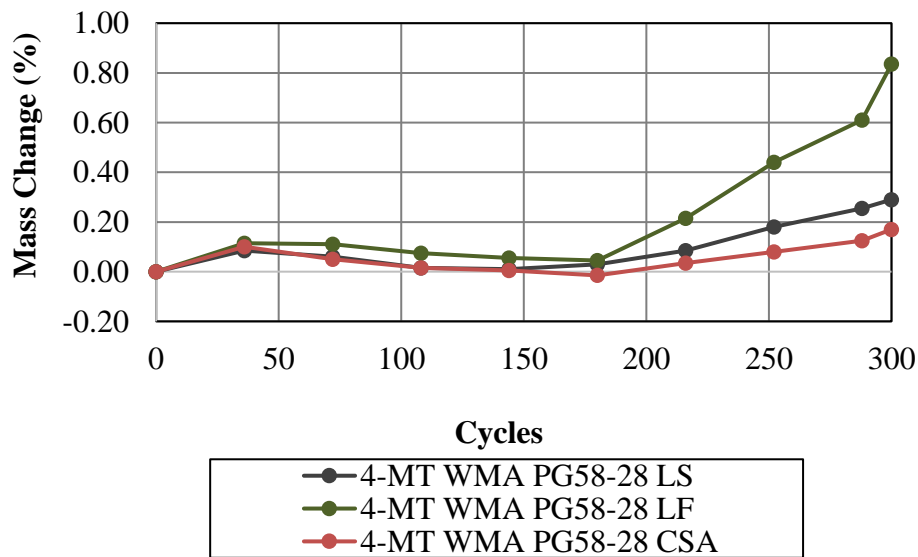


Figure 4.65: Freeze-Thaw Mass Change (%) for WMA PG58-28 Mixtures

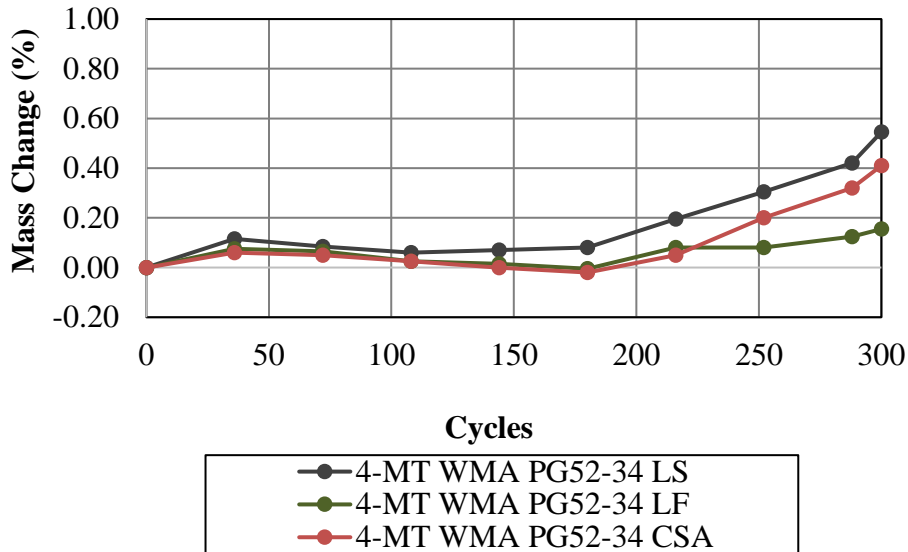


Figure 4.66: Freeze-Thaw Mass Change (%) for WMA PG52-34 Mixtures

4.6.2.1.2 IDT Freeze-Thaw

The Humboldt Indirect Tensile Machine was used to evaluate the IDT after freeze-thaw exposure after 0, 10, and 20 cycles as a modification of ASTM T283-07. For this testing, 1 cycle of freeze-thaw exposure consisted of a dry sample being saturated to 70 – 80% degree of saturation, wrapped in plastic, placed in a sealed bag containing 10 mL of water, placed into a freezer at -18°C for 24 ± 1 h, placed into a water bath at $60 \pm 1^{\circ}\text{C}$ for 24 ± 1 h, then finally dried at $25 \pm 0.5^{\circ}\text{C}$ for 24 ± 1 h. All samples were tested in the dry condition and duplicates were evaluated.

Figure 4.67 and Figure 4.68 demonstrate the horizontal tensile stress for the freeze-thaw exposed samples. These figures indicate that the maximum horizontal stresses for the reactive powder samples were higher than the control LS samples at all cycles. The CSA cement WMA PG58-28 samples had the highest maximum horizontal stress of 1.26 MPa after 20 cycles of freezing and thawing. For WMA PG58-28 samples, both the LF and CSA developed strength

gain from 10 cycles to 20 cycles and this could be potentially due to the hydration of the reactive powder. For the WMA PG52-34 mixtures, the CSA samples had the highest maximum horizontal stress of 0.75 MPa after 20 cycles of freezing and thawing. There is also a slight strength gain for the CSA mixtures from 0 cycles to 10 cycles as the horizontal stress increased.

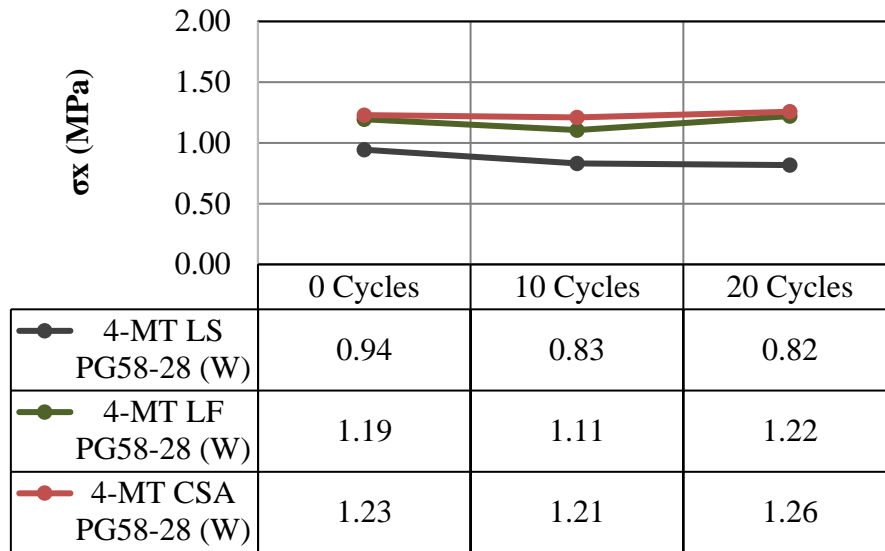


Figure 4.67: Freeze-Thaw Horizontal Tensile Stress at Center of Specimen for WMA PG58-28 Mixtures

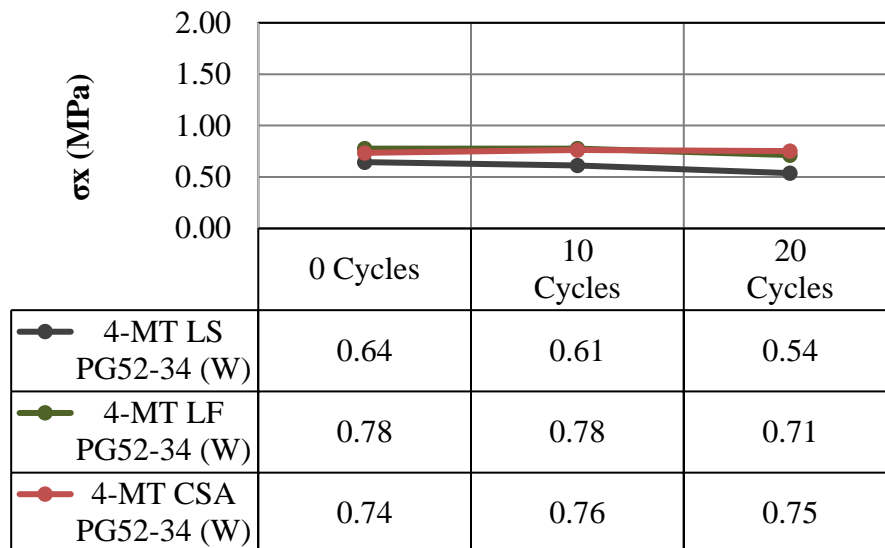


Figure 4.68: Freeze-Thaw Horizontal Tensile Stress at Center of Specimen for WMA PG52-34 Mixtures

Figures 4.69 and Figure 4.70 demonstrates the ultimate vertical compressive stress of the mixtures which directly correlate with the horizontal tensile stress results. These figures prove that the maximum vertical stresses for the reactive powder samples were higher than the control LS samples at all environmental conditions. For WMA PG58-28 mixtures, CSA samples had the highest maximum vertical stress at 20 cycles of 3.77 MPa. For WMA PG52-34 mixtures, CSA samples had the highest maximum vertical stress at 20 cycles of 2.26 MPa.

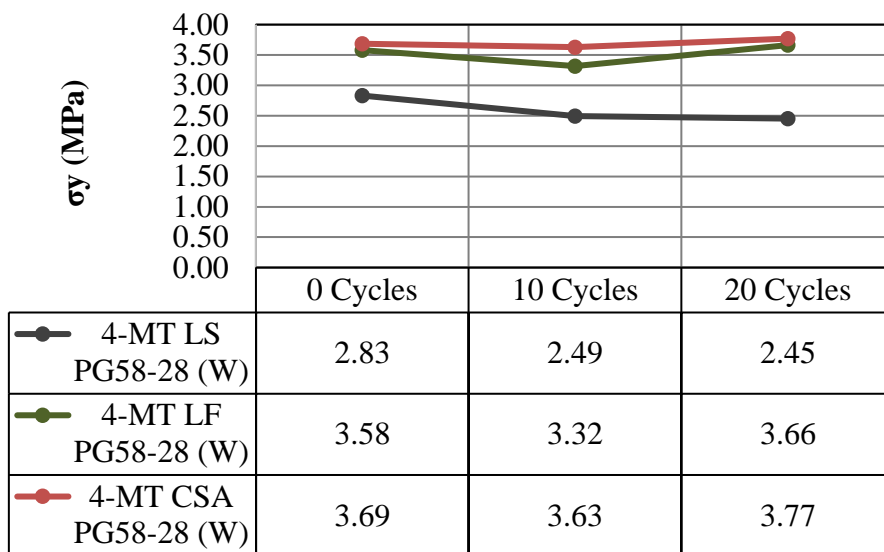


Figure 4.69: Freeze-Thaw Vertical Compressive Stress at Center of Specimen for WMA PG58-28 Mixtures

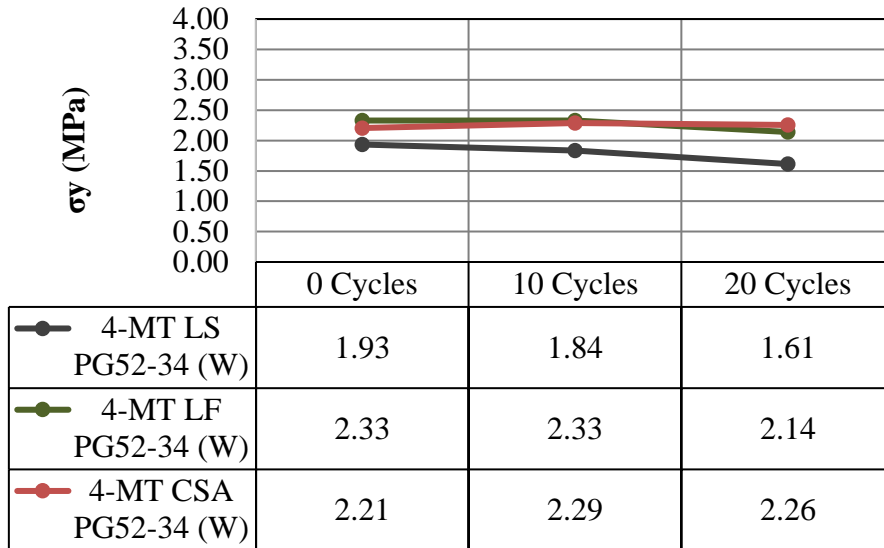


Figure 4.70: Freeze-Thaw Vertical Compressive Stress at Center of Specimen for WMA PG58-28 Mixtures

Figure 4.71 and Figure 4.72 report on the tensile strain at failure for the WMA PG58-28 mixtures and WMA PG52-34 mixtures. These figures illustrate the effects of freeze-thaw on the ability for asphalt pavements to deform. For WMA PG58-28 samples the LS samples had the highest strain at failure of 0.088 mm/mm at 20 cycles and for the WMA PG52-34 samples the CSA cement samples had the highest strain at failure of 0.085 mm/mm at 20 cycles. In all cases the ultimate strain (related to flow) decreased for all samples over the course of the freeze-thaw testing.

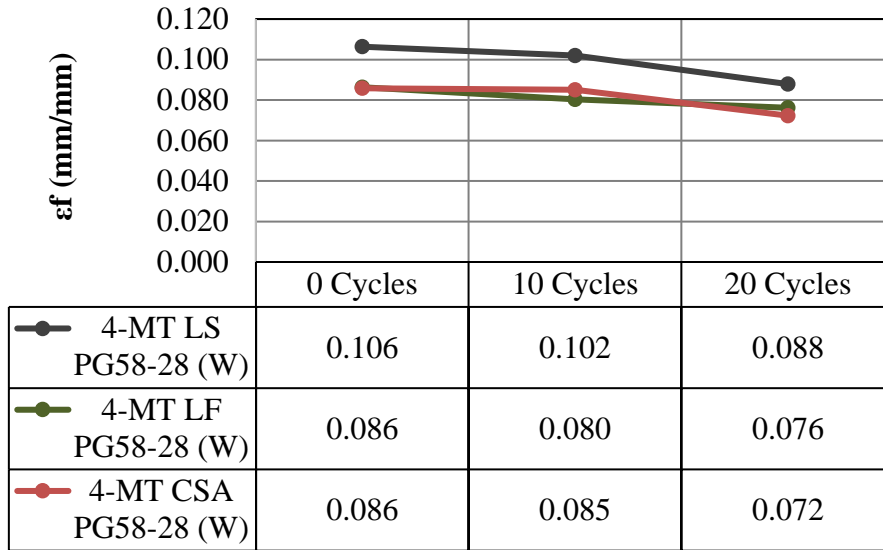


Figure 4.71: Freeze-Thaw Tensile Strain at Failure for WMA PG58-28 Mixtures

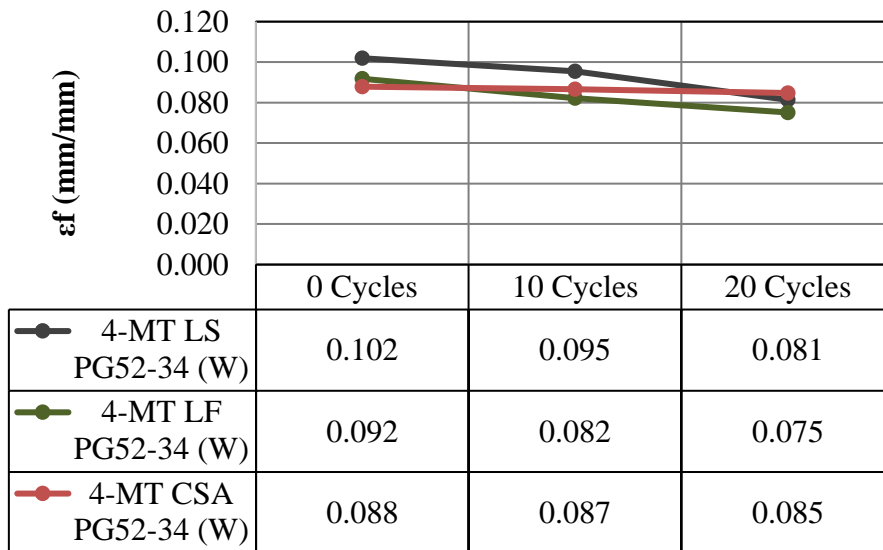


Figure 4.72: Freeze-Thaw Tensile Strain at Failure for WMA PG52-34 Mixtures

4.6.2.2 Salt-Scaling

Salt-scaling was evaluated to understand the resistance to surface scaling of a horizontal asphalt surface that was exposed to freezing and thawing cycles in the presence of deicing chemicals. Testing was performed on gyratory compacted specimens (93% G_{mm}) in accordance

to the procedure described in RILEM TC176-IDC: ‘Internal Damage of Concrete due to Frost Action’ CIF-Test: Capillary Suction, Internal Damage and Freeze Thaw Test – Reference Method. The unsealed face of the sample was submerged 6 mm face down in a 3% salt solution. The samples were then exposed to 50 freeze-thaw cycles. Each of the cycles consisted of 16 – 18 h in the freezing environment followed by a storage at $23 \pm 2^{\circ}\text{C}$ and a relative humidity of 45 – 55% for 6 – 8 h. The salt solution was added before each freezing phase of the cycle. After each 5 cycles the salt solution was removed and the face of the sample was washed and strained through a filter to collect all flake materials. The flake solution was dried in an oven at 105°C to a constant mass and then the residue was cumulatively weighed, and the mass was recorded.

Figure 4.73 and Figure 4.74 report on the results of the salt-scaling. These results demonstrate that there was no mass loss for specimens up to 45 cycles. For the WMA PG58-28 mixtures, the LF cement samples performed the best as there was no mass loss after 50 cycles and the LS and CSA cement samples both had a total mass loss of 8.20 g/m^2 . For the WMA PG52-34 mixtures, the LS samples performed the best as the total mass loss was 5.50 g/m^2 at 50 cycles whereas the LF and CSA cement samples had a total mass loss of 10.95 g/m^2 and 8.20 g/m^2 , respectively. This testing should be extended and investigated further as the results are not very conclusive. The failure was mainly due to weak aggregates and may not reflect the type of powder or binder.

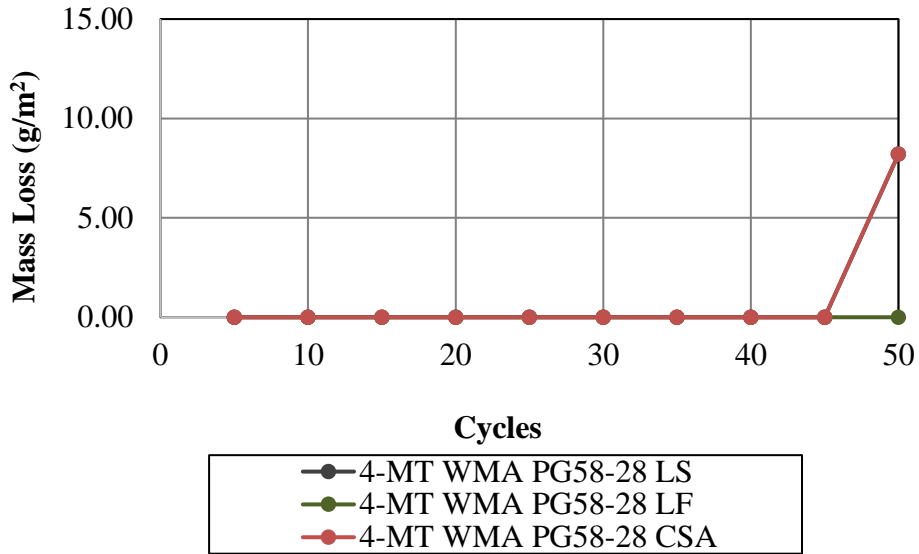


Figure 4.73: Salt-Scaling Mass Loss (g/m²) for WMA PG58-28 Mixtures

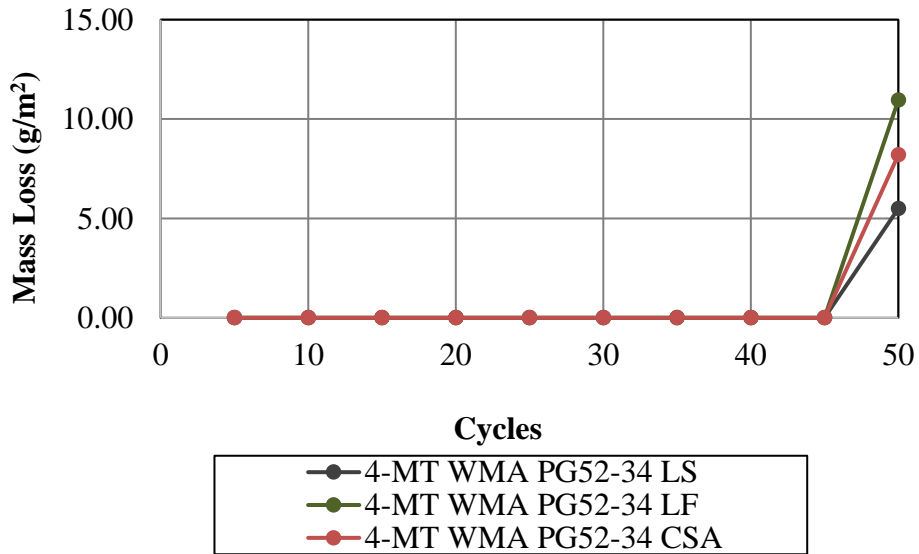


Figure 4.74: Salt-Scaling Mass Loss (g/m²) for WMA PG52-34 Mixtures

CHAPTER 5

STATISTICAL MODELING OF THE REACTIVE POWDER EFFECTS ON ASPHALT MASTICS

Statistical analysis of the experimental results was performed to find the correlations between non-performance and performance related indicators of reactive powders and the mastic types using a confidence level of 85%. Chemical and physical properties that affected the mastic performance based on this confident interval were chosen to perform multiple regression analysis to come up with equations that predict the performance of mastics. This section specifically discusses the multiple linear regression models for determining the complex shear modulus G^* , viscosity, and the rutting factor $G^*/\sin(\delta)$. Multiple regression analysis was then performed for asphalt mastics that introduced the reactive powder at a concentration of 25% by binder volume replacement for both WMA PG58-28 and WMA PG52-34 binders. The goal of this project was to maximize the use of reactive powders since 25% by binder volume replacement demonstrates a better potential for self-healing. It should be noted that the multiple linear regression models should be used with caution since these cannot predict the exact values and should only be used to potentially estimate the final predicted values. The reason for this is because the regression models are based on six reactive powders.

5.1 THE EFFECT OF REACTIVE POWDER PROPERTIES ON TESTING PARAMETERS

The results from the mastic testing study are reported in Table 5.1, 5.2, and 5.3. Table 5.1 summarizes the DSR results for the complex shear modulus (G^*) which is the non-performance related indicator that measures the total resistance to shear deformation. Table 5.2 lists the unaged rotational viscometer results for viscosity which is a performance related indicator that

measures the constructability. Table 5.3 displays the DSR results for RTFO aged rutting factor ($G^*/\sin(\delta)$) which is a performance related indicator that measures the rutting resistance.

Table 5.1: Complex Modulus (G^*) for Unaged WMA PG58-28 Mastics at 58°C and Unaged WMA PG52-34 Mastics at 52°C

Sample ID	G^* (Pa)					
	WMA PG58-28			WMA PG52-34		
	5%	15%	25%	5%	15%	25%
SDA	1461.18	2621.54	3008.23	1536.26	2680.69	3176.55
LF	1582.23	1911.61	2828.07	1675.20	2066.47	2876.01
SM	1690.73	1825.80	2586.85	1636.24	2162.65	2852.37
CSA	1636.39	2153.40	2742.46	1688.07	2226.26	2951.83
OW	1585.80	1836.55	2472.72	1666.60	2020.77	3024.67
HA	1666.64	2035.50	2664.30	1620.14	2090.21	2918.77

Table 5.2: Viscosity for Unaged Mastics based on WMA PG58-28 and WMA PG52-34 Binders at 135°C

Sample ID	Viscosity (Pa-s)					
	WMA PG58-28			WMA PG52-34		
	5%	15%	25%	5%	15%	25%
SDA	0.36	0.74	0.87	0.25	0.46	0.57
LF	0.36	0.48	0.72	0.25	0.33	0.47
SM	0.40	0.49	0.69	0.24	0.33	0.46
CSA	0.37	0.54	0.78	0.26	0.38	0.57
OW	0.35	0.47	0.69	0.24	0.31	0.49
HA	0.39	0.52	0.81	0.25	0.35	0.54

Table 5.3: $G^*/\sin(\delta)$ for RTFO Aged WMA PG58-28 at 58°C and RTFO Aged WMA PG52-34 Mastics at 52°C

Sample ID	$G^*/\sin(\delta)$ (kPa)					
	WMA PG58-28			WMA PG52-34		
	5%	15%	25%	5%	15%	25%
SDA	4.41	7.22	9.20	4.34	7.54	8.99
LF	4.01	5.79	8.81	3.88	5.86	8.14
SM	4.08	5.37	7.51	3.84	5.50	8.07
CSA	4.48	6.34	8.61	4.10	5.76	8.68
OW	3.98	5.28	7.76	4.05	5.41	8.25
HA	4.13	5.87	8.11	4.19	5.90	8.39

The complex modulus G^* , viscosity, and rutting factor $G^*/\sin(\delta)$ values can all be used as the basis of the output values when determining the multiple linear regression models. For this reason, the correlations were determined between the testing parameters and the chemical and physical properties of the reactive powder materials. These correlations were determined using the Pearson's correlation coefficient as well as the statistical significance p-value. The correlation analysis was used to determine if a linear relationship existed between the WMA mastics (independent variables) and the testing output parameters (dependent variables) by computing the linear correlation coefficient. The correlation coefficient (r-value) is a number that ranges from -1 to +1, where -1 implies a strong negative linear correlation, +1 implies a strong positive linear correlation, and when the r-value is 0 or close to zero, it implies that little or no correlation between the input parameter and test results exists, or possibly related in some other nonlinear way. For this project, only linear relationships were investigated. The formula for the linear correlation coefficient r-value is as follows:

$$r = \frac{n(\sum xy) - (\sum x)(\sum y)}{\sqrt{[n(\sum x^2) - (\sum x)^2][n(\sum y^2) - (\sum y)^2]}} \quad \text{Eq. 5.1}$$

where:

x = independent variable;

y = dependent variable;

n = number of data points.

The p-value was calculated using the Pearson coefficient to test the significance of the correlation coefficient. To test the significance of the r-value, a hypothesis-testing procedure is used to decide between a null hypothesis (H_0) or an alternative hypothesis (H_1). The null hypothesis for the project states $H_0: \rho = 0$, which means that there is no correlation between the

dependent and independent variables. The alternative hypothesis $H_1: \rho \neq 0$, which means there is a significant correlation between the dependent and independent variables. P-values are calculated by using the F-test method using the r-values calculated previously to determine if the null hypothesis should be accepted or rejected. The formula used to calculate the p-value using the F-test is seen below:

$$p_{value} = 1 - F_{DIST} \left(\frac{r^2 * (n-2)}{1-r^2} \right) \quad \text{Eq. 5.2}$$

where:

r = Pearson correlation coefficient;

n = number of data points.

Tables 5.4, 5.5, and 5.6 summarize the correlation matrices between the asphalt results and the chemical and physical properties of the components. In these tables the significance level p-value is reported on top and the Pearson correlation coefficient is provided in parenthesis below. The highlighted cells in the table demonstrate the chemical and physical properties that had a statistical correlation based on the 85% confidence interval (p-value ≤ 0.15) which also represents a high Pearson correlation coefficient.

Table 5.4 reports the summarized correlation matrix between the asphalt mastic complex shear modulus G^* at all concentrations and the chemical and physical properties. This table demonstrates that at low concentrations of 5% binder replacement by volume, the reactive powders did not have any effect (p-value > 0.15) on the mastic complex shear modulus G^* . However, at higher concentrations there are more correlations between the reactive powder properties and the testing parameter. Parameters with a positive Pearson correlation coefficient demonstrate that as the concentration increases the stiffness increases since G^* increases whereas

the parameters with a negative Pearson correlation coefficient demonstrate that as the concentration increases the stiffness decreases since G^* decreases. For example, the WMA PG58-28 mastic at 15% concentration had a p-value of 0.006 (Pearson correlation coefficient of -0.934) for specific gravity which indicates a good correlation but also proves that as the specific gravity increases the stiffness decreases. The results prove that specific gravity, D_{10} , D_{50} all decrease the stiffness as the concentration increases whereas D_{90} , Na_2O , P_2O_5 , SrO , SAF , and $Rigden$ voids all increase the stiffness as the concentration increases.

Table 5.4: Correlation Matrix Between the Reactive Powder Properties and Complex Modulus (G^*) of Mastics

Sample ID	WMA PG58-28			WMA PG52-34		
	5%	15%	25%	5%	15%	25%
Specific Gravity	0.090 (0.743)	0.006 (-0.934)	0.050 (-0.812)	0.211 (0.596)	0.006 (-0.938)	0.079 (-0.761)
D_{10} (μm)	0.372 (0.449)	0.037 (-0.839)	0.074 (-0.768)	0.331 (0.484)	0.026 (-0.865)	0.319 (-0.494)
D_{50} (μm)	0.478 (0.364)	0.050 (-0.811)	0.028 (-0.861)	0.281 (0.528)	0.052 (-0.808)	0.519 (-0.333)
D_{90} (μm)	0.015 (-0.897)	0.032 (0.850)	0.194 (0.615)	0.043 (-0.826)	0.020 (0.883)	0.003 (0.952)
Na_2O (%)	0.026 (-0.866)	0.019 (0.884)	0.064 (0.786)	0.028 (-0.861)	0.004 (0.948)	0.043 (0.826)
P_2O_5 (%)	0.031 (-0.854)	0.005 (0.944)	0.066 (0.782)	0.032 (-0.850)	0.001 (0.969)	0.022 (0.877)
SrO (%)	0.012 (-0.909)	0.037 (0.840)	0.130 (0.689)	0.098 (-0.733)	0.012 (0.908)	0.017 (0.890)
SAF (%)	0.133 (-0.685)	0.012 (0.908)	0.122 (0.700)	0.007 (-0.930)	0.029 (0.858)	0.061 (0.790)
$Rigden$ Voids (%)	0.048 (-0.815)	0.007 (0.931)	0.048 (0.816)	0.023 (-0.874)	0.024 (0.871)	0.050 (0.811)

Table 5.5 summarizes the correlation matrix between the asphalt mastic viscosity at all concentrations and the chemical and physical properties. This table demonstrates that there are low correlations at concentrations of 5% binder replacement by volume, however, at higher

concentrations there are more correlations between the reactive powder properties and the testing parameter. Parameters with a positive Pearson correlation coefficient demonstrate that as the concentration increases the viscosity increases whereas parameters with a negative Pearson correlation coefficient demonstrate that as the concentration increases the viscosity decreases. For example, the WMA PG58-28 mastic at 25% concentration had a p-value of 0.016 (Pearson correlation coefficient of 0.896) for Rigden voids which means that as the Rigden voids increases the viscosity increases. The results prove that specific gravity, D_{10} , D_{50} all decrease the viscosity as the concentration increases whereas D_{90} , Na_2O , P_2O_5 , SAF, and Rigden voids all increase viscosity as concentration increases.

Table 5.5: Correlation Matrix Between the Reactive Powder Properties and Viscosity of Mastics

Sample ID	WMA PG58-28			WMA PG52-34		
	5%	15%	25%	5%	15%	25%
Specific Gravity	0.364 (0.456)	0.012 (-0.908)	0.086 (-0.750)	0.300 (-0.511)	0.005 (-0.939)	0.095 (-0.736)
D_{10} (μm)	0.800 (0.134)	0.054 (-0.804)	0.118 (-0.704)	0.184 (-0.625)	0.015 (-0.899)	0.098 (-0.732)
D_{50} (μm)	0.927 (-0.049)	0.068 (-0.780)	0.074 (-0.768)	0.099 (-0.730)	0.022 (-0.876)	0.131 (-0.687)
D_{90} (μm)	0.237 (-0.571)	0.014 (0.901)	0.143 (0.673)	0.913 (0.058)	0.055 (0.801)	0.283 (0.527)
Na_2O (%)	0.384 (-0.438)	0.005 (0.943)	0.115 (0.709)	0.729 (0.183)	0.027 (0.864)	0.322 (0.492)
P_2O_5 (%)	0.371 (-0.450)	0.001 (0.979)	0.060 (0.792)	0.601 (0.273)	0.009 (0.922)	0.179 (0.631)
SAF (%)	0.684 (-0.214)	0.005 (0.941)	0.010 (0.918)	0.543 (0.315)	0.020 (0.882)	0.117 (0.706)
Rigden Voids (%)	0.460 (-0.378)	0.004 (0.948)	0.016 (0.896)	0.455 (0.382)	0.018 (0.887)	0.149 (0.666)

Table 5.6 summarizes the correlation matrix between the asphalt mastic rutting factor $G^*/\sin(\delta)$ and the chemical and physical properties of reactive powders at all concentrations.

This table also demonstrates that at low concentrations there are low correlations. Parameters with a positive Pearson correlation coefficient demonstrate that as the concentration increases the $G^*/\sin(\delta)$ increases (becomes stiffer) whereas parameters with a negative Pearson correlation coefficient demonstrate that as the concentration increases the $G^*/\sin(\delta)$ decreases (has a softening effect). For example, the WMA PG52-34 mastic at 15% concentration had a p-value of 0.009 (Pearson correlation coefficient of 0.922) for P_2O_5 which means that as the P_2O_5 increases the $G^*/\sin(\delta)$ increases. The results demonstrate that specific gravity, D_{10} , D_{50} , CaO all decrease $G^*/\sin(\delta)$ as the concentration increases whereas D_{90} , SO_3 , Na_2O , P_2O_5 , SrO, SAF, and Rigden voids all increase $G^*/\sin(\delta)$ as the concentration decreases.

Table 5.6: Correlation Matrix Between the Reactive Powder Properties and Rutting Factor $G^*/\sin(\delta)$ of Mastics

Sample ID	WMA PG58-28			WMA PG52-34		
	5%	15%	25%	5%	15%	25%
Specific Gravity	0.033 (-0.847)	0.005 (-0.941)	0.067 (-0.781)	0.166 (-0.646)	0.028 (-0.859)	0.011 (-0.912)
D_{10} (μm)	0.007 (-0.932)	0.020 (-0.883)	0.141 (-0.675)	0.314 (-0.499)	0.106 (-0.721)	0.042 (-0.827)
D_{50} (μm)	0.035 (-0.842)	0.022 (-0.876)	0.105 (-0.722)	0.358 (-0.461)	0.091 (-0.743)	0.095 (-0.736)
D_{90} (μm)	0.354 (0.464)	0.078 (0.763)	0.236 (0.572)	0.098 (0.733)	0.016 (0.895)	0.071 (0.774)
CaO (%)	0.073 (-0.770)	0.028 (-0.861)	0.228 (-0.579)	0.013 (-0.904)	0.064 (-0.786)	0.020 (-0.883)
SO_3 (%)	0.008 (0.928)	0.112 (0.713)	0.247 (0.561)	0.409 (0.418)	0.375 (0.447)	0.070 (0.776)
Na_2O (%)	0.304 (0.508)	0.039 (0.835)	0.139 (0.677)	0.180 (0.630)	0.002 (0.961)	0.087 (0.748)
P_2O_5 (%)	0.189 (0.620)	0.016 (0.894)	0.121 (0.701)	0.093 (0.739)	0.001 (0.970)	0.032 (0.850)
SrO (%)	0.286 (0.524)	0.064 (0.786)	0.168 (0.644)	0.210 (0.597)	0.021 (0.879)	0.081 (0.758)
SAF (%)	0.273 (0.536)	0.037 (0.840)	0.210 (0.598)	0.023 (0.875)	0.006 (0.937)	0.051 (0.810)
Rigden Voids (%)	0.285 (0.525)	0.018 (0.887)	0.085 (0.751)	0.045 (0.822)	0.001 (0.982)	0.048 (0.815)

Evaluating the statistical parameters was important to understand the correlations between the chemical and physical properties and the testing parameter such as G^* , viscosity, and $G^*/\sin(\delta)$. However, it was also important to understand the correlations between the chemical and physical properties among themselves to verify independence between these variables and to confirm multicollinearity. Tables 5.7, 5.8, and 5.9 establish the chemical and physical properties independent correlations for each of the separate variables. These tables report on the p-values on top and the Pearson correlations coefficient below. The highlighted values in the table demonstrate the chemical and physical properties that had a statistical correlation based on the 85% confidence interval ($p\text{-value} \leq 0.15$) which also represents a high Pearson correlation coefficient. A positive Pearson correlation coefficient represents a linear relationship between independent variables whereas a negative Pearson correlation coefficient represents an inverse relationship between independent variables.

Table 5.7 provides the correlation matrix for the parameters related to complex modulus G^* . This table demonstrates that the variables with high correlations related to G^* also have high correlations among themselves. For example, the p-value between the specific gravity and Rigden voids was 0.065 (Pearson correlation coefficient of -0.784) which demonstrates an inverse relationship.

Table 5.7: Correlation Matrix Between the Reactive Powder Properties Related to Complex Modulus (G^*) of Mastics

	SG	D₁₀	D₅₀	D₉₀	Na₂O	P₂O₅	SrO	SAF	RV
SG	1.000	0.008 0.926	0.046 0.820	0.050 -0.812	0.028 -0.861	0.012 -0.908	0.019 -0.884	0.105 -0.723	0.065 -0.784
D₁₀		1.000	0.006 0.939	0.232 -0.575	0.128 -0.692	0.088 -0.747	0.139 -0.678	0.215 -0.592	0.192 -0.617
D₅₀			1.000	0.354 -0.464	0.163 -0.649	0.132 -0.686	0.261 -0.548	0.179 -0.631	0.158 -0.655
D₉₀				1.000	0.003 0.952	0.002 0.962	0.002 0.967	0.031 0.853	0.020 0.883
Na₂O					1.000	0.016 0.984	0.003 0.958	0.083 0.754	0.002 0.962
P₂O₅						1.000	0.003 0.958	0.014 0.901	0.006 0.937
SrO							1.000	0.083 0.754	0.044 0.824
SAF								1.000	0.001 0.970
RV									1.000

Table 5.8 provides the correlation matrix for the parameters that were related to viscosity. This table also demonstrates that the variables with high correlations related to viscosity also have high correlations among themselves. For example, the p-value between P₂O₅ and SAF was 0.014 (Pearson correlation coefficient of 0.901) which demonstrates a direct relationship. Other variables such as D₁₀ and SAF demonstrate poor correlations as the p-value does not validate the 85% confidence interval.

Table 5.8: Correlation Matrix Between the Reactive Powder Properties Related to Viscosity of Mastics

	SG	D₁₀	D₅₀	D₉₀	Na₂O	P₂O₅	SAF	RV
SG	1.000	0.008 0.926	0.046 0.820	0.050 -0.812	0.028 -0.861	0.012 -0.908	0.105 -0.723	0.065 -0.784
D₁₀		1.000	0.006 0.939	0.232 -0.575	0.128 -0.692	0.088 -0.747	0.215 -0.592	0.192 -0.617
D₅₀			1.000	0.354 -0.464	0.163 -0.649	0.132 -0.686	0.179 -0.631	0.158 -0.655
D₉₀				1.000	0.003 0.952	0.002 0.962	0.031 0.853	0.020 0.883
Na₂O					1.000	0.016 0.984	0.027 0.863	0.011 0.915
P₂O₅						1.000	0.014 0.901	0.006 0.937
SAF							1.000	0.001 0.970
RV								1.000

Table 5.9 establishes the correlation matrix for the parameters related to the rutting factor $G^*/\sin(\delta)$. This table also demonstrates that the variables with high correlations related to $G^*/\sin(\delta)$ also have high correlations among themselves. For example, the p-value between Na₂O and P₂O₅ was 0.016 (Pearson correlation coefficient of 0.984) which demonstrates direct relationship in that both variables have the same effect of $G^*/\sin(\delta)$. Other variables such as CaO and SrO demonstrate poor correlations as the p-value > 0.15.

Table 5.9: Correlation Matrix Between the Reactive Powder Properties Related to Rutting Factor $G^*/\sin(\delta)$ of Mastics

	SG	D ₁₀	D ₅₀	D ₉₀	CaO	Na ₂ O	P ₂ O ₅	SrO	SAF	RV
SG	1.000	0.008 0.926	0.046 0.820	0.050 -0.812	0.116 0.708	0.028 -0.861	0.012 -0.908	0.019 -0.884	0.105 -0.723	0.065 -0.784
D ₁₀		1.000	0.006 0.939	0.232 -0.575	0.118 0.704	0.128 -0.692	0.088 -0.747	0.139 -0.678	0.215 -0.592	0.192 -0.617
D ₅₀			1.000	0.354 -0.464	0.088 0.747	0.163 -0.649	0.132 -0.686	0.261 -0.548	0.179 -0.631	0.158 -0.655
D ₉₀				1.000	0.190 -0.619	0.003 0.952	0.002 0.962	0.002 0.967	0.031 0.853	0.020 0.883
CaO					1.000	0.175 -0.635	0.095 -0.736	0.280 -0.530	0.018 -0.888	0.045 -0.821
Na ₂ O						1.000	0.016 0.984	0.002 0.962	0.027 0.863	0.011 0.915
P ₂ O ₅							1.000	0.003 0.958	0.014 0.901	0.006 0.937
SrO								1.000	0.083 0.754	0.044 0.824
SAF									1.000	0.001 0.970
RV										1.000

5.2 MULTIPLE LINEAR REGRESSION MODELS

Multiple linear regression analysis was performed to determine the equations representing the response of experimental performance parameters. The purpose of multiple linear regression analysis is to make predictions for the dependent variable by creating an equation based on the multiple independent variables that effect the dependent variable. The multiple linear regression equation has the general form:

$$y = a + b_1x_1 + b_2x_2 + \dots + b_nx_n \quad \text{Eq. 5.3}$$

where:

a = y-axis intercept;

b_n = partial regression coefficients;

x_n = independent variables.

The values used in computing the correlation coefficients are also used to calculate y-axis intercept and the partial regression coefficients. The formula for calculating the y-intercept is as follows:

$$a = \bar{Y} - b_1\bar{X}_1 - b_2\bar{X}_2 - b_3\bar{X}_3 - \dots - b_n\bar{X}_n \quad \text{Eq. 5.4}$$

where:

a = y-intercept;

\bar{Y}_n = average value of dependent variable;

\bar{X}_n = average value of independent variable;

b_n = partial regression coefficient.

The multiple linear regression models were developed to evaluate the testing parameters based on the chemical and physical properties with highest correlations. In determining testing parameters only four independent variables were used to develop the multiple linear regression models. These variables were specifically chosen based on the highest average correlations at the 15% and 25% concentrations for both WMA PG58-28 and WMA PG52-34 binders. Since there were no consistent correlations at the 5% concentration level, these results were excluded from the analysis when choosing the specific independent variables. Also, since the multiple linear

regression models were used to develop an analysis at higher concentrations the output models are specific to the 25% concentration mastics. This also means that these models are more appropriate for potentially self-healing compositions since there is more potential for this behavior at higher concentrations of reactive powders.

Table 5.10 lists the independent chemical and physical parameters that had the highest correlations to the dependent variable (G^*) for both the WMA PG58-28 asphalt mastics and WMA PG52-34 asphalt mastics. Specific gravity, Na_2O , P_2O_5 , and Rigden voids were used to develop the multiple linear regression models to determine G^* at 25% concentrations.

Table 5.10: Input Parameters Used to Determine the Multiple Linear Regression Models for Complex Modulus (G^*)

Sample ID	SG	Na_2O (%)	P_2O_5 (%)	Rigden Voids (%)
SDA	2.63	1.21	0.78	41.71
LF	3.13	0.21	0.12	33.52
SM	3.17	0.16	0.10	31.11
CSA	2.89	0.12	0.19	32.8
OW	3.20	0.11	0.12	32.13
HA	3.22	0.06	0.12	35.06

Table 5.11 lists the independent chemical and physical parameters that had the highest correlations to the dependent variable (viscosity) for both the WMA PG58-28 asphalt mastics and WMA PG52-34 asphalt mastics. Specific gravity, P_2O_5 , SAF, and Rigden voids were used to develop the multiple linear regression models to determine the viscosity at 25% concentrations.

Table 5.11: Input Parameters Used to Determine the Multiple Linear Regression Models for Viscosity

Sample ID	SG	P ₂ O ₅ (%)	SAF (%)	Rigden Voids (%)
SDA	2.63	0.78	98.24	41.71
LF	3.13	0.12	27.18	33.52
SM	3.17	0.10	27.02	31.11
CSA	2.89	0.19	33.09	32.8
OW	3.20	0.12	28.94	32.13
HA	3.22	0.12	58.68	35.06

Table 5.12 lists the independent chemical and physical properties that had the highest correlations to the dependent variable ($G^*/\sin(\delta)$) for both the WMA PG58-28 asphalt mastics and WMA PG52-34 asphalt mastics. Specific gravity, Na₂O, P₂O₅, and Rigden voids were used to develop the multiple linear regression models to determine $G^*/\sin(\delta)$ at 25% concentrations.

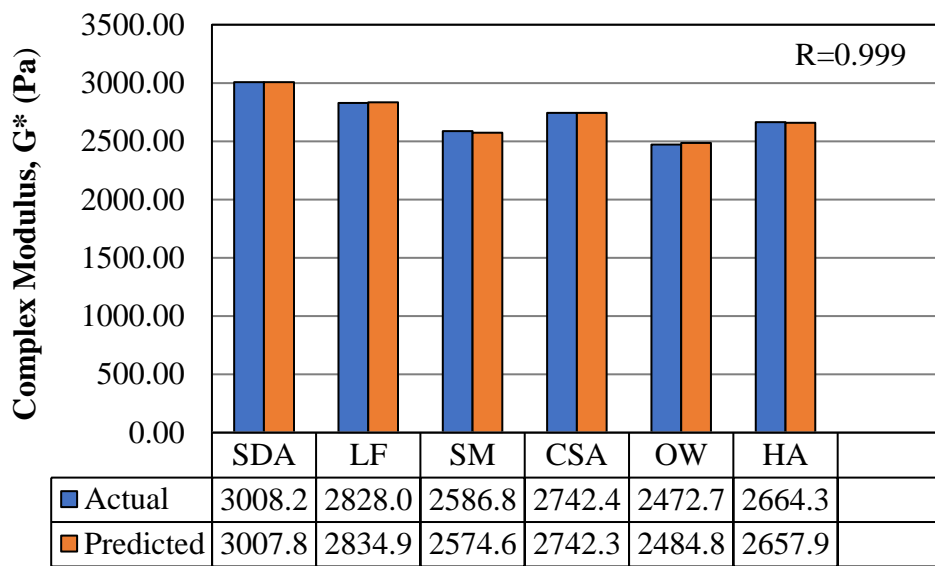
Table 5.12: Input Parameters Used to Determine the Multiple Linear Regression Models for Rutting Factor $G^*/\sin(\delta)$

Sample ID	SG	Na ₂ O (%)	P ₂ O ₅ (%)	Rigden Voids (%)
SDA	2.63	1.21	0.78	41.71
LF	3.13	0.21	0.12	33.52
SM	3.17	0.16	0.10	31.11
CSA	2.89	0.12	0.19	32.8
OW	3.20	0.11	0.12	32.13
HA	3.22	0.06	0.12	35.06

The variables were then used to develop the multiple linear regression models by determining the partial regression coefficients. These models were developed to predict the tested value based on the actual data acquired from testing. The models were then used to input the specific data points to evaluate the differences between the predicted values and the actual test data. The differences between the predicted and actual values is called the residual or predicted error. The residual is the difference between the actual test value and the predicted

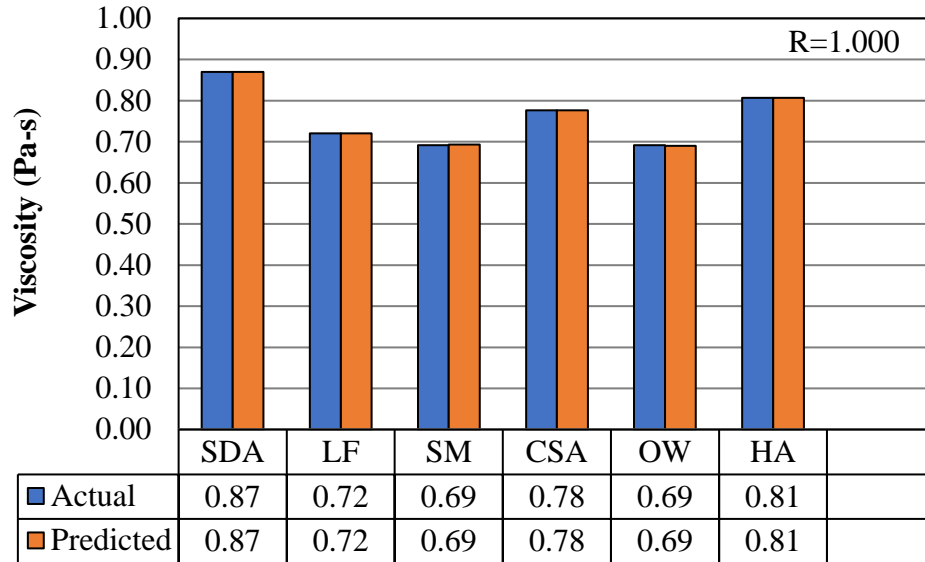
value, for which the predicted value is based on the multiple regression equation. A residual value of 0 signifies that the equation perfectly predicts the actual test value, hence the closer the residual values are to zero the better the fit and prediction. The figures presented in this section display the regression equation and the Pearson correlation coefficient relating the actual test value and the predicted value which are displayed within the figures. The figures also give a visual insight as to how well the actual test values compare to the predicted values that are calculated based on the regression model.

Here, Figure 5.1, Figure 5.2, and Figure 5.3 report on the results of the multiple linear regression models for the WMA PG58-28 asphalt mastics.



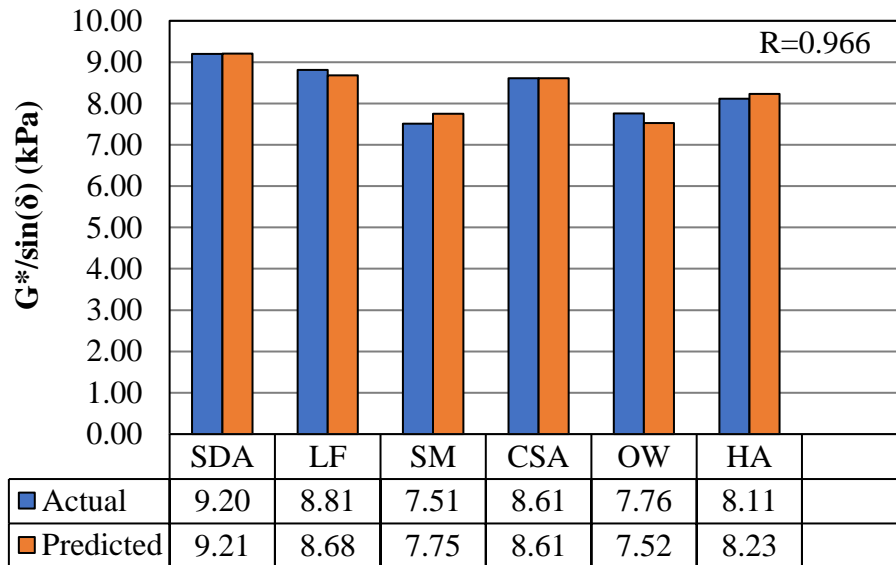
$$G^*_{PG58-28} (25\%) = 4586.299 - 1459.423 SG + 1228.278 Na_2O - 3821.647 P_2O_5 + 90.015 RV$$

Figure 5.1: Multiple Linear Regression Model for Determining Complex Modulus G* for WMA PG58-28 Mastics at 25% Concentration by Volume



$$\text{Viscosity}_{\text{PG58-28}} (25\%) = 1.374 - 0.324 \text{ SG} - 0.482 \text{ P}_2\text{O}_5 + 0.003 \text{ SAF} + 0.010 \text{ RV}$$

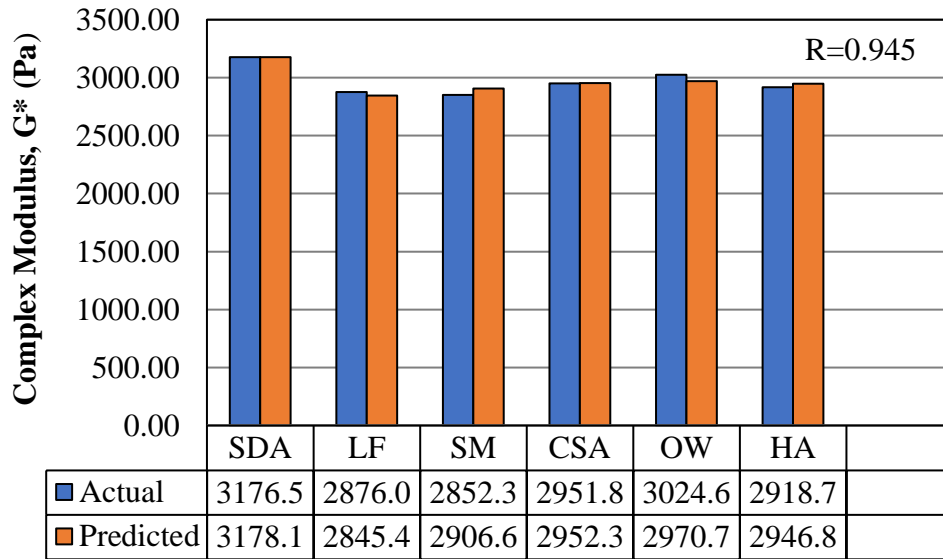
Figure 5.2: Multiple Linear Regression Model for Determining Viscosity for WMA PG58-28 Mastics at 25% Concentration by Volume



$$G^*/\sin(\delta)_{\text{PG58-28}} (25\%) = 15.386 - 5.443 \text{ SG} + 3.119 \text{ Na}_2\text{O} - 12.169 \text{ P}_2\text{O}_5 + 0.332 \text{ RV}$$

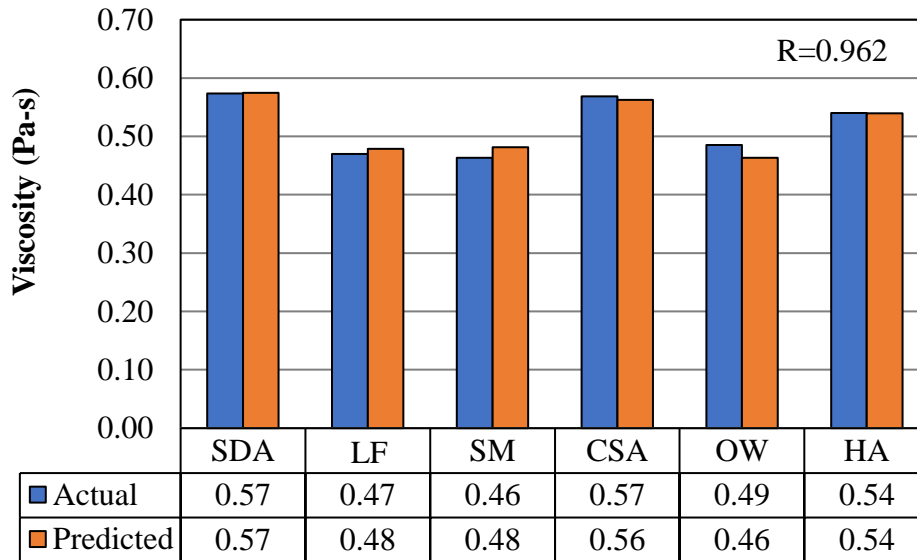
Figure 5.3: Multiple Linear Regression Model for Determining Rutting Factor $G^*/\sin(\delta)$ for WMA PG58-28 Mastics at 25% Concentration by Volume

Figure 5.4, Figure 5.5, and Figure 5.6 report on the results of the multiple linear regression models for the WMA PG52-34 asphalt mastics.



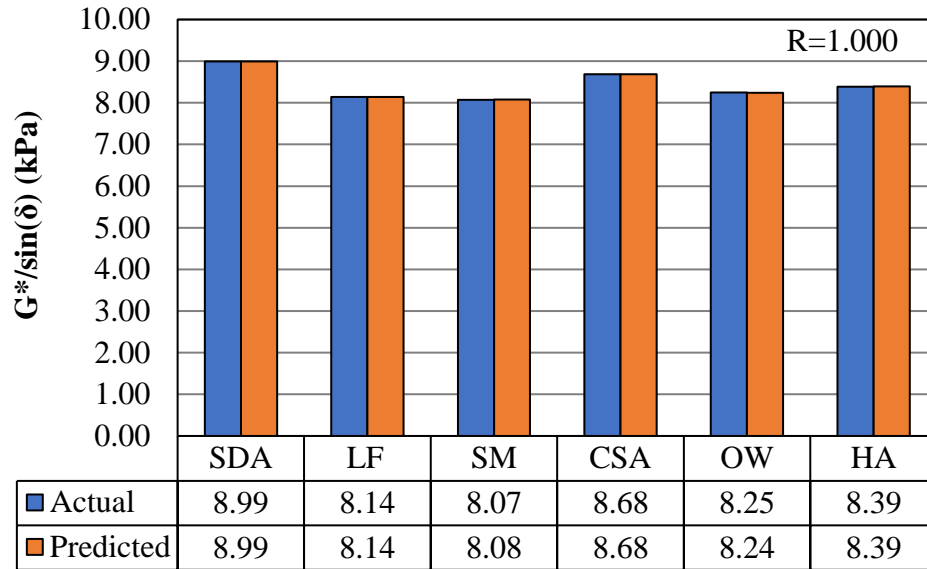
$$G^*_{PG52-34} (25\%) = 2025.467 + 459.912 SG - 625.983 Na_2O + 2073.808 P_2O_5 - 21.986 RV$$

Figure 5.4: Multiple Linear Regression Model for Determining Complex Modulus G* for WMA PG52-34 Mastics at 25% Concentration by Volume



$$Viscosity_{PG52-34} (25\%) = 1.794 - 0.387 SG - 0.446 P_2O_5 + 0.003 SAF - 0.004 RV$$

Figure 5.5: Multiple Linear Regression Model for Determining Viscosity for WMA PG52-34 Mastics at 25% Concentration by Volume



$$G^*/\sin(\delta)_{PG52-34} (25\%) = 9.508 - 0.705 SG - 1.853 Na_2O + 3.255 P_2O_5 + 0.025 RV$$

Figure 5.6: Multiple Linear Regression Model for Determining Rutting Factor $G^*/\sin(\delta)$ for WMA PG52-34 Mastics at 25% Concentration by Volume

The final multiple linear regression equations have been presented and can be used to predict the mastic behavior at 25% binder volume replacement by reactive powder cement components. It should be noted that the multiple linear regression models should be used with caution since these cannot predict the exact values and should only be used to potentially estimate the final values. The reason for this is because the multiple linear regression models are based on only five portland cement powders and SDA ash.

CHAPTER 6

FIELD IMPLEMENTATION STUDY

In the summer of 2016, a 1.61 km road near Wausau, Wisconsin (Figure 6.1) was paved using various control asphalt mixtures and SDA mixtures using the Weston SDA material (for SDA chemical and physical properties see Chapter 4, Section 4.1). In this project, there were two 0.52 km pavement sections with 3.96 m lane widths. One section used a 4-MT WMA SDA mixture (12.5 mm max aggregate size) with PG58-28 binder at 10% SDA ash replacement by binder volume in a 50.8 mm surface layer. The other section used a 4-MT WMA SDA mixture (12.5 mm max aggregate size) with PG52-34 binder at 10% SDA ash replacement by binder volume in a 50.8 mm surface layer. Both test sections were placed on a 101.6 mm base layer using 2-MT HMA (Hot Mix Asphalt) SDA mixture (25.0 mm max aggregate size) with PG58-28 binder at 10% SDA ash replacement by binder volume. Both test sections were placed and compacted with no apparent qualitative difference in flow from truck beds, flow through the paving equipment, compaction effort, labor, and cleaning of equipment. A total of 67.17 tons of SDA were used in this project.

Over 11,000 quad-axle truckloads used the haul road over a five-month period that was during record setting hot summer temperatures in 2016. Visual inspections indicated no observed rutting of the pavement test sections. Visual inspections were performed during the winter of 2017, and there was no observed indication of low-temperature cracking. The lowest recorded temperature for the season was -26°C.



Figure 6.1: Wausau, WI Road Paving Project

6.1 LABORATORY RESEARCH STUDY

This field implementation study investigated the control and SDA mixtures used in the Wausau Field Implementation Study. The purpose of this laboratory research was to evaluate the effect of SDA ash from the combustion of subbituminous coal on asphalt performance with respect to laboratory measured performance indicators at the asphalt mixture level using PG58-28 and PG52-34 binders. In this study, the SDA ash was introduced to an asphalt mixture as an enhancer that replaces 10% of the binder by volume and then these mixtures were compared to the control mixtures.

6.1.1 Experimental Design

This section explains the experimental testing matrix for both the control asphalt mixtures and the SDA mixtures in terms of aggregate coating, workability, aging resistance, moisture damage resistance, fatigue resistance, and thermal-cracking resistance. Table 6.1 presents the experimental testing matrix for the entire project along with the materials used for this project. For all of these tests, at least two samples were tested and averages were

determined. For the aggregate coating, workability, and aging comparison, six replicates were produced and compared. For the moisture damage resistance, fatigue cracking resistance, and thermal cracking resistance, two replicates were produced and tested. The experimental testing methods were described in detail in Section 3.3.

Table 6.1: Experimental Research Testing Matrix

Mixture Property	Measured Indicator		Aging	Asphalt Binders	Powders	Mixture Types	Conc.
Aggregate Coating	Asphalt Binder Film Thickness		Short-Term	PG58-28 PG52-34	SDA Control	2-MT 2-MT (A) 4-MT 4-MT (A) 4-MT (AL) 4-MT (W) 4-MT (WA) 4-MT (WAL) 6-MT (WA)	10% of Binder Replacement by Volume
Workability	% Air at 8 Gyration		Short-Term				
Aging Comparison			Long-Term				
Moisture Damage	TSR	Dry	Long-Term				
		Saturated					
		Conditioned					
Fatigue	E* using IDT	Intermediate Temp.	Long-Term				
Thermal Cracking	G _r & S(t)	Low Temp.	Long-Term				

- * 2-MT = 25.0 mm Max Aggregate Size
- * 4-MT = 12.5 mm Max Aggregate Size
- * 6-MT = 4.75 mm Max Aggregate Size
- * A = SDA Ash Replacement
- * L = Low Temperature Binder Grade (PG52-34)
- * W = Warm Mix Asphalt

6.1.2 Asphalt Mixtures

For mixture testing, the SDA material was introduced to an asphalt mix at 10% replacement of the binder by volume. Mixtures prepared for this study used a job mix formula (JMF) approved by the Wisconsin DOT. There were 9 different mixtures total as reported in Table 6.1. The 2-MT mixtures had a nominal maximum aggregate size (NMAS) of 25.0 mm, the 4-MT mixtures had a NMAS of 12.5 mm, and the 6-MT mixtures had a NMAS of 4.75 mm. All mixtures used a PG58-28 binder (HMA and WMA) except for 2 mixtures which used a

PG52-34 low binder grade. The 2-MT HMA control mix design had a 4.9% optimum asphalt content, the 4-MT HMA and WMA control mix design had a 5.6% optimum asphalt content, and the 6-MT WMA control mix design had a 6.7% optimum asphalt content. The SDA was assumed as part of the binder volume rather than as an aggregate component. A control mix was used to compare the impact of the added SDA on the performance indicators of mixtures. The control mixes were fabricated according to the JMF at the optimum asphalt content.

For all the testing results, the 2-MT HMA mixtures are compared, the 4-MT HMA mixtures are compared, and the 4-MT WMA and 6-MT WMA mixtures are compared.

6.1.3 Aggregate Blends

The aggregate JMF combinations are shown in Tables 6.2, 6.3, and 6.4. Table 6.2 lists the combinations for the 2-MT mixtures, Table 6.3 lists the combinations for the 4-MT mixtures, and Table 6.4 lists the combinations for the 6-MT mixtures.

Table 6.2: 2-MT JMF Aggregate Combinations

Aggregate Type	% Combination
1 1/2" Clean Bit Rock	45.0
7/8"x3/8" Bit Agg	14.0
3/8" Bit Agg	13.0
3/16" Washed Man Sand	10.0
3/4" RAP (4.6% AC)	15.0
Shingles (23.6% AC)	3.0

Table 6.3: 4-MT JMF Aggregate Combinations

Aggregate Type	% Combination
5/8"x3/8" Bit Agg	20.0
3/8"x1/8" Washed Chips	9.0
3/8" Bit Agg	26.0
3/16" Washed Man Sand	15.0
5/8" River Sand	12.0
3/4" RAP (4.6% AC)	15.0
Shingles (23.6% AC)	3.0

Table 6.4: 6-MT JMF Aggregate Combinations

Aggregate Type	% Combination
3/8" Bit Agg	16.0
1/4"x1/8" Chips	35.0
3/16" Washed Man Sand	12.0
3/8" River Sand	12.0
Fly Ash (SDA)	2.0
3/8" RAP (4.6% AC)	20.0
Shingles (23.6% AC)	3.0

The aggregate JMF particle size distribution curves are summarized by Figure 6.2. This figure provides the combination curves for the 2-MT, 4-MT, and the 6-MT mixtures as well as the appropriate 0.45 power curves according to the maximum aggregate size that was used in each mixture. Here, the combination curves are very similar to the 0.45 power curves which represent an optimal aggregate configuration. It is also important to note that all aggregate blends meet the Superpave® gradation limits.

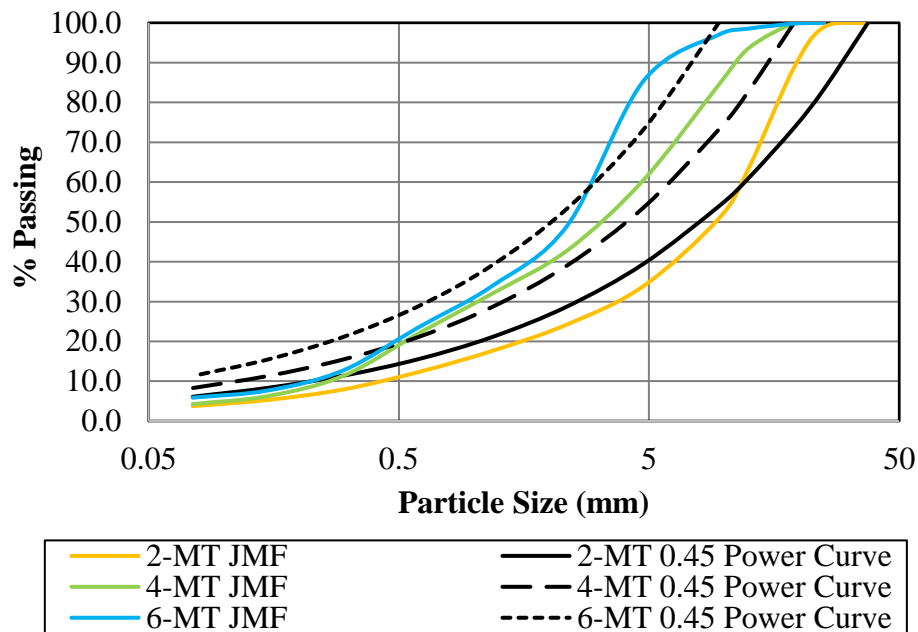


Figure 6.2: JMF Particle Size Distribution Curves

6.1.4 Aggregate Coating

Asphalt film thickness was used to evaluate a proper aggregate coating for both control and SDA mixtures. This parameter was important to calculate since the SDA mixtures had 10% (by volume) binder replacement with fly ash and this means that, potentially, less binder is available to coat the aggregates. The calculated asphalt film thickness represents the average thickness of the asphalt that surrounds the aggregate particle, and this has been related directly to aggregate protection and durability. If the asphalt film thickness is too thin, air can enter the compacted HMA more rapidly and this will oxidize the asphalt binder which can cause the HMA to become brittle and fracture by cracking. Also, if the film thickness is too thin, water can enter through the binder and penetrate the aggregate particles which can cause moisture damage, and this can lead to rutting, raveling, freeze-thaw damage, and bleeding.

Asphalt film thickness is not directly considered as a Superpave® design requirement, however evaluating aggregate coating is critical. It has been found that the average values for asphalt film thickness should typically be at least 6 to 8 μm (Hmoud, 2011). This thickness range has been found to establish a thick enough coating around the aggregate particles which will prevent rapid oxidation, and even prevent moisture damage.

Table 6.5 reports on the surface area factors, percent passing of the asphalt mixtures, and the surface area of aggregates. This table demonstrates that the total surface area of the aggregates used in the 2-MT mixtures was approximately $3.70 \text{ m}^2/\text{kg}$, the aggregates used in the 4-MT mixtures was approximately $5.01 \text{ m}^2/\text{kg}$, and the aggregates used in the 6-MT mixtures was approximately $6.05 \text{ m}^2/\text{kg}$.

Table 6.5: Calculated Surface Area of Aggregates

Sieve Size	Surface Area Factors	2-MT Percent Passing (%)	2-MT Surface Area (m^2/kg)	4-MT Percent Passing (%)	4-MT Surface Area (m^2/kg)	6-MT Percent Passing (%)	6-MT Surface Area (m^2/kg)
Max Aggregate Size	2	100.00	0.40	100.00	0.41	100.00	0.41
No.4 (4.75 mm)	2	33.89	0.14	60.50	0.25	85.40	0.35
No.8 (2.36 mm)	4	24.28	0.20	42.90	0.35	49.10	0.40
No.16 (1.18 mm)	8	17.61	0.28	32.00	0.52	33.90	0.56
No.30 (0.6 mm)	14	12.31	0.35	22.00	0.63	23.60	0.68
No.50 (0.3 mm)	30	7.93	0.48	11.30	0.69	12.70	0.78
No.100 (0.15 mm)	60	5.30	0.64	6.30	0.77	7.70	0.95
No.200 (0.075 mm)	160	3.73	1.21	4.20	1.38	5.90	1.93
		SUM	3.70	SUM	5.01	SUM	6.05

The surface area was then used to calculate the film thickness which is reported in Table 6.6. From this table it is evident that the film thickness of the 2-MT control mixtures was 12.95 μm and the film thickness of the 2-MT SDA mixtures was 11.50 μm . The film thickness of the 4-MT control mixtures was 10.99 μm and the film thickness of the 4-MT SDA mixtures was 9.69 μm . The film thickness of the 6-MT control mixtures was 11.51 μm and the film thickness of the 6-MT SDA mixtures was 10.24 μm . This makes sense that the film thickness of the SDA mixtures was less than the control mixtures because 10% (by volume) of asphalt binder was substituted with fly ash in the SDA mixtures. It is also important that all mixture types were above the recommended 6 to 8 μm range as this parameter can be critical for durability.

Table 6.6: Asphalt Film Thickness for Control and SDA Mixtures

Mixture	2-MT Control	2-MT SDA	4-MT Control	4-MT SDA	6-MT Control	6-MT SDA
Surface Area of Aggregates (m^2/kg)	3.69	3.69	5.01	5.01	6.05	6.05
Bulk Specific Gravity of Aggregate	2.671	2.671	2.667	2.667	2.659	2.659
Effective Specific Gravity of Aggregate	2.688	2.688	2.686	2.686	2.660	2.660
Asphalt Specific Gravity	1.028	1.028	1.028	1.028	1.028	1.028
Asphalt Content (%)	4.9%	4.4%	5.6%	5.0%	6.7%	6.0%
Total Weight (g)	4900.00	4900.00	4900.00	4900.00	4900.00	4900.00
Asphalt Volume (mL)	233.56	209.73	266.93	238.33	319.36	285.99
Asphalt Absorbed (by weight of aggregate)	0.243	0.243	0.273	0.273	0.015	0.015
Weight of Absorbed Asphalt (g)	11.34	11.40	12.61	12.69	0.66	0.67
Volume of Absorbed Asphalt (mL)	11.03	11.09	12.27	12.35	0.65	0.65
Effective Volume of Asphalt (mL)	222.53	198.64	254.66	225.98	318.71	285.34
Film Thickness (Tf) (microns)	12.95	11.50	10.99	9.69	11.51	10.24

After the film thickness was calculated it was also important to visually inspect the coating of the aggregates. During the mixing process, there were no problems observed in terms of aggregate coating. The asphalt binder seemed to coat the aggregates at the same rate for both the control mixtures and SDA mixtures. Figure 6.3 represents the aggregates for each mixture type. From this study, it is clear that no major differences can be reported. Here, all mixtures used PG58-28 binder unless a PG52-34 binder was specified.

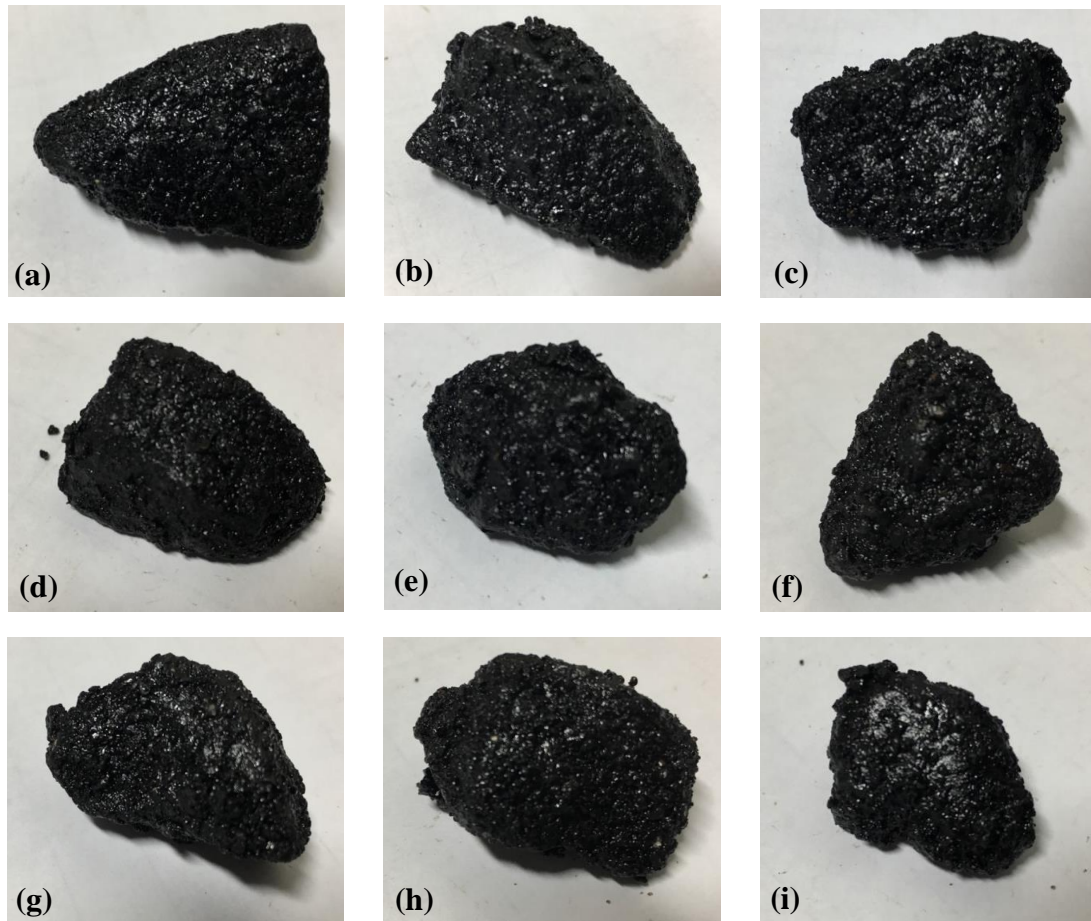


Figure 6.3: Aggregate Coating (a) 2-MT HMA Control (b) 2-MT HMA SDA (c) 4-MT HMA Control (d) 4-MT HMA SDA (e) 4-MT HMA SDA (PG52-34) (f) 4-MT WMA Control (g) 4-MT WMA SDA (h) 4-MT WMA SDA (PG52-34) (i) 6-MT WMA SDA

6.1.5 Constructability

Workability was evaluated by comparing the densification curves of the control mixtures and SDA mixtures. All compaction comparisons for workability were evaluated for short-term aged materials because this demonstrates the physical condition in which the material is mixed, placed, and compacted. Lower compaction efforts demonstrated better workability properties. For all evaluations, the HMA mixtures were mixed at 140°C and compacted at 135°C whereas the WMA mixtures were mixed at 120°C and compacted at 115°C. Every mixture was compacted to 100 gyrations to understand the material behavior over a wide range of gyrations.

Figure 6.4 demonstrates the workability results for the 2-MT (25.0 mm max aggregate size) HMA mixtures with a PG58-28 binder. It can be observed that the SDA mixture was compacted to approximately 96% G_{mm} (4% air voids) and this is a critical parameter to evaluate in terms of Superpave® compaction efforts. The control mixture demonstrated higher compaction efforts whereas the SDA mixture had a reduced compaction effort.

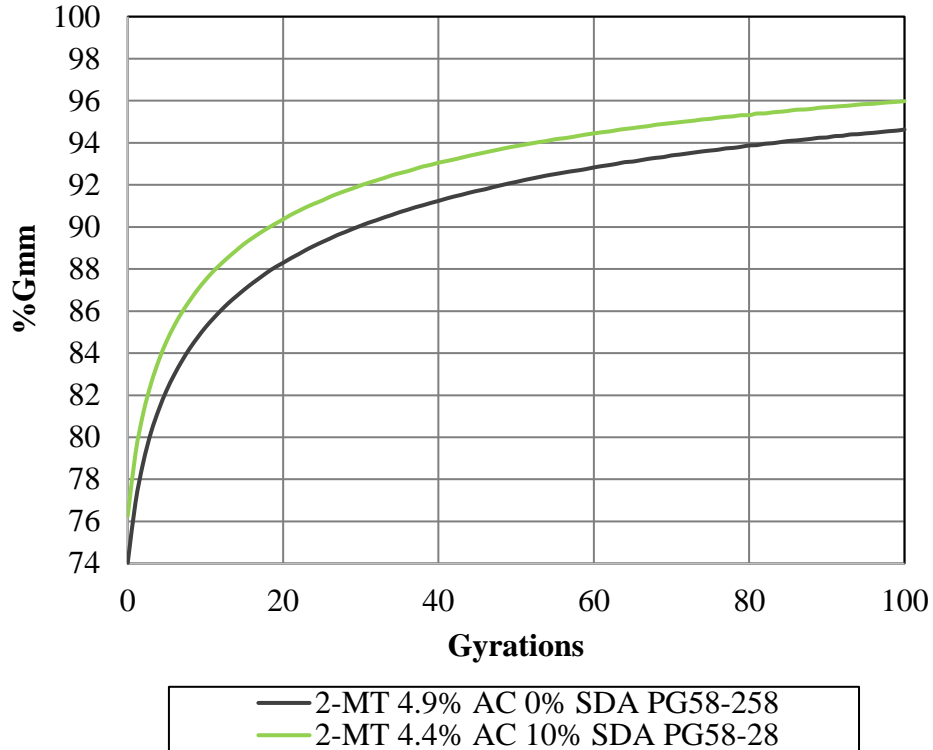


Figure 6.4: Densification Curves for 2-MT HMA Mixtures

Figure 6.5 reports on the workability results for 4-MT (12.5 mm max aggregate size) HMA mixtures with a PG58-28 binder and a PG52-34 binder. In this case, the 4-MT SDA mixture with PG52-34 binder demonstrated lower compaction efforts when compared to the control mixture. The 4-MT SDA mixture with PG58-28 binder, on the other hand, demonstrated lower compaction efforts than the control mixture at the beginning but then gradually required more compaction effort towards the end. This demonstrates an ideal situation because it indicates that the mixture can be easily compacted out in the field during construction to the required 7% air voids (93% G_{mm}) but then over time with vehicle compactions, it takes more effort to compact the mixture. Increasing the compaction efforts over time can increase rutting resistance because it takes more effort to vertically deform the material.

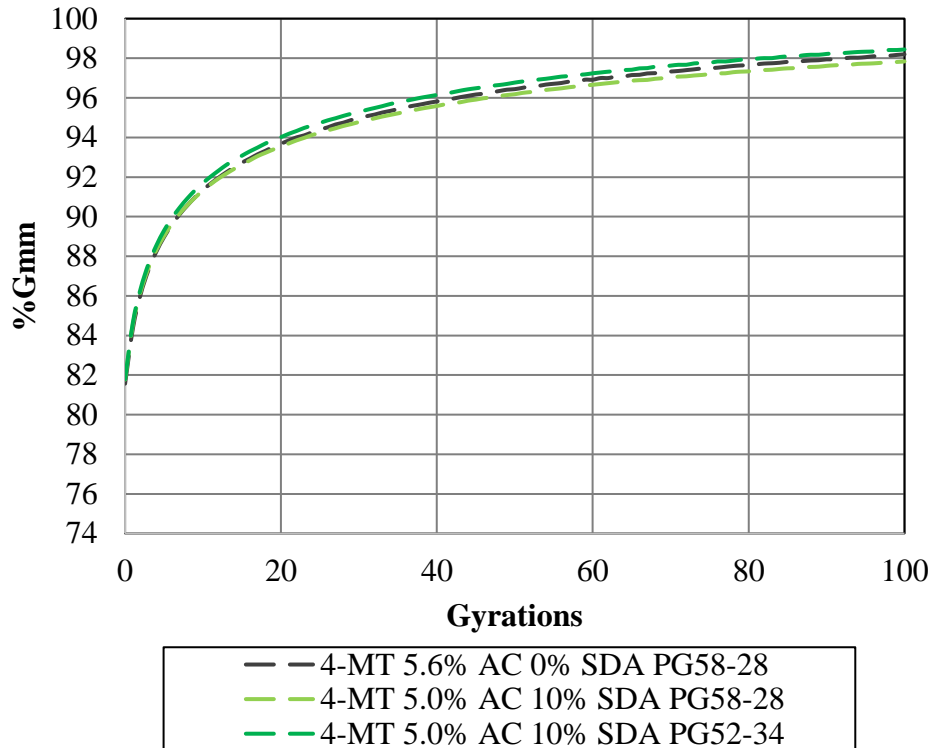


Figure 6.5: Densification Curves for 4-MT HMA Mixtures

Figure 6.6 demonstrates the workability results for 4-MT (12.5 mm max aggregate size) WMA mixtures with a PG58-28 binder and a PG52-34 binder and the 6-MT (4.75 mm max aggregate size) WMA mixture with PG58-28 binder. The 4-MT SDA mixture with PG52-34 binder and the 6-MT SDA mixture with PG58-28 binder demonstrate similar densification curves and are easier to compact than the control mixture. The 4-MT SDA mixture with PG52-34 binder requires the lowest compaction effort out of all the mixtures. The 4-MT SDA mixture with PG58-28 binder also demonstrates an ideal situation in which the compaction efforts towards the beginning (93% G_{mm}) are lower than the control mixture but then over time the slope of the densification curve is reduced below that of the control mixture which means that it takes more compaction energy to deform the material. This means that over time, the material behaves in a stiffer manner at elevated temperatures and this aids in improved rutting resistance.

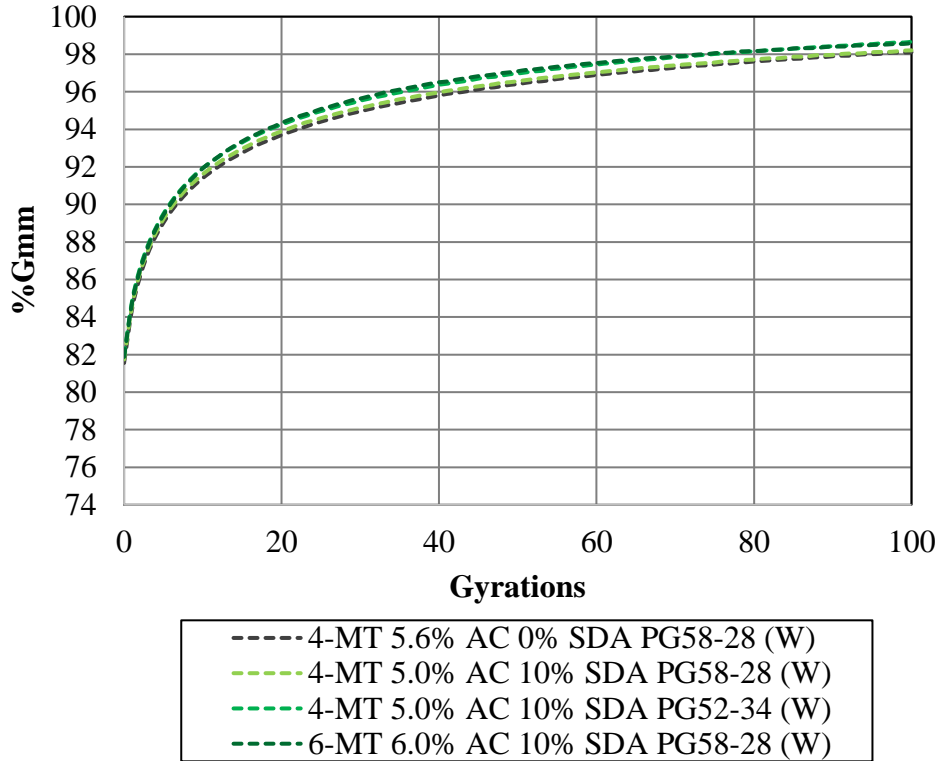


Figure 6.6: Densification Curves for 4-MT and 6-MT WMA Mixtures

The compaction volumetrics were evaluated to understand the differences between the control and SDA mixtures. Table 6.7, 6.8, and 6.9 report the mixture volumetrics for the 2-MT HMA mixtures, the 4-MT HMA (and WMA) mixtures, and the 6-MT WMA mixture, respectively. Based on the reported data, it can be concluded that the bulk specific gravity (G_{mb}) and the maximum specific gravity (G_{mm}) were both increased due to the addition of the SDA material. The reason for this increase is because the specific gravity of the SDA was higher than the specific gravity of asphalt binder (1.028). Since 10% of binder was being replaced with fly ash (by volume), the bulk and max specific gravities increased due to the proportional increase in the aggregate quantities.

Other volumetrics that demonstrate the differences are the added binder content (P_b), aggregate content (P_s), effective asphalt content (P_{be}), voids in the mineral aggregate (VMA), air voids (V_a), voids filled with asphalt (VFA), and the dust-to-binder ratio (powder-to-binder ratio). Since 10% (by volume) of asphalt content was being replaced with fly ash, the added binder content, effective asphalt binder content, voids in the mineral aggregate, and the voids filled with asphalt were all reduced as a result. The reduction in these parameters can be correlated directly to the asphalt film thickness because the film thickness was reduced as well for SDA mixtures (i.e., characterized by low binder contents). However, considering that more powder (material that passes the No. 200 sieve) was added to the SDA mixtures, the dust-to-binder ratio increased as a result when compared to the control mixture.

When evaluating the Superpave® volumetric requirements it was noted that the VMA needs to be above 12% for 2-MT mixtures, above 14% for 4-MT mixtures, and above 16% for 6-MT mixtures. Other design parameters require that the VFA needs to be between 65 and 75% ($3 < ESALs < 30$, $30 \leq ESALs$ in millions) for all mixtures, and the dust-to-binder ratio needs to be between 0.6 and 1.2 for all mixtures. Evaluating the mixture volumetrics it can be observed that for all mixtures, these parameters are satisfied.

Table 6.7: 2-MT HMA Mixture Volumetrics

Mixture	2-MT 4.9% AC 0% SDA PG58-28	2-MT 4.4% AC 10% SDA PG58-28
Gmm	2.510	2.529
Gmb	2.409	2.427
Gsb	2.671	2.671
Gse	2.688	2.688
Gb	1.028	1.028
Design Pb (%)	4.9	4.4
Pba (%)	0.2	0.2
Ps (%)	95.1	95.6
Pbe (%)	4.7	4.2
VMA (%) > 12	14.2	13.1
Va (%) = 4.0%	4.0	4.0
VFA (%) (65-75)	71.9	69.5
Dust-to-Binder Ratio (0.6-1.2)	0.8	1.0

Table 6.8: 4-MT HMA and WMA Mixture Volumetrics

Mixture	4-MT 5.6% AC 0% SDA PG58-28	4-MT 5.0% AC 10% SDA PG58-28	4-MT 5.0% AC 10% SDA PG52-34
Gmm	2.466	2.484	2.474
Gmb	2.368	2.385	2.375
Gsb	2.667	2.667	2.667
Gse	2.686	2.686	2.686
Gb	1.028	1.028	1.028
Design Pb (%)	5.6	5.0	5.0
Pba (%)	0.3	0.3	0.3
Ps (%)	94.4	95.0	95.0
Pbe (%)	5.3	4.7	4.7
VMA (%) > 14	16.2	15.0	15.4
Va (%) = 4.0%	4.0	4.0	4.0
VFA (%) (65-75)	75.3	73.4	74.0
Dust-to-Binder Ratio (0.6-1.2)	0.8	1.0	1.0

Table 6.9: 6-MT WMA Mixture Volumetrics

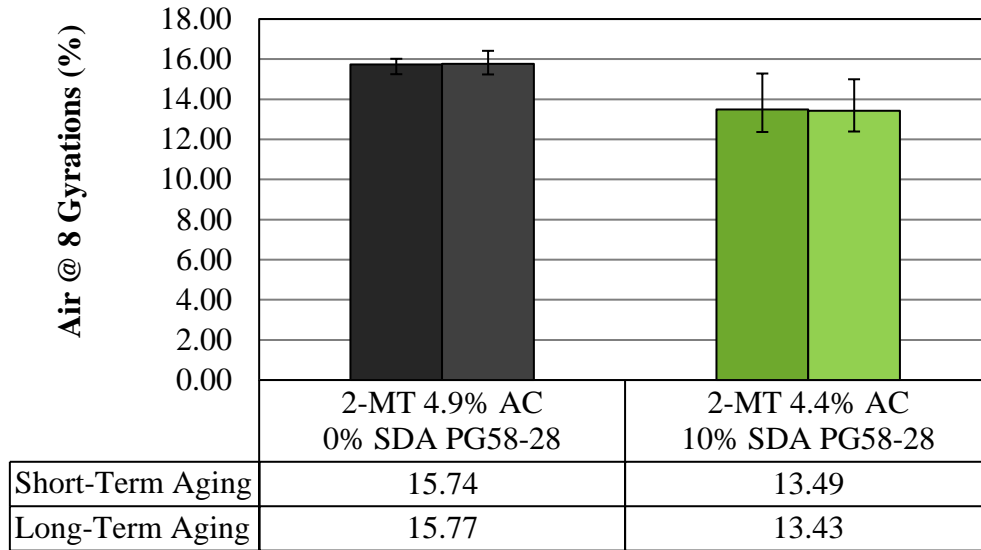
Mixture	4-MT 5.6% AC 0% SDA PG58-28 (W)	4-MT 5.0% AC 10% SDA PG58-28 (W)	4-MT 5.0% AC 10% SDA PG52-34 (W)
Gmm	2.458	2.469	2.468
Gmb	2.359	2.370	2.369
Gsb	2.667	2.667	2.667
Gse	2.686	2.686	2.686
Gb	1.028	1.028	1.028
Design Pb (%)	5.6	5.0	5.0
Pba (%)	0.3	0.3	0.3
Ps (%)	94.4	95.0	95.0
Pbe (%)	5.3	4.7	4.7
VMA (%) > 14	16.5	15.6	15.6
Va (%) = 4.0%	4.0	4.0	4.0
VFA (%) (65-75)	75.7	74.3	74.4
Dust-to-Binder Ratio (0.6-1.2)	0.8	1.0	1.0

6.1.6 Aging Resistance

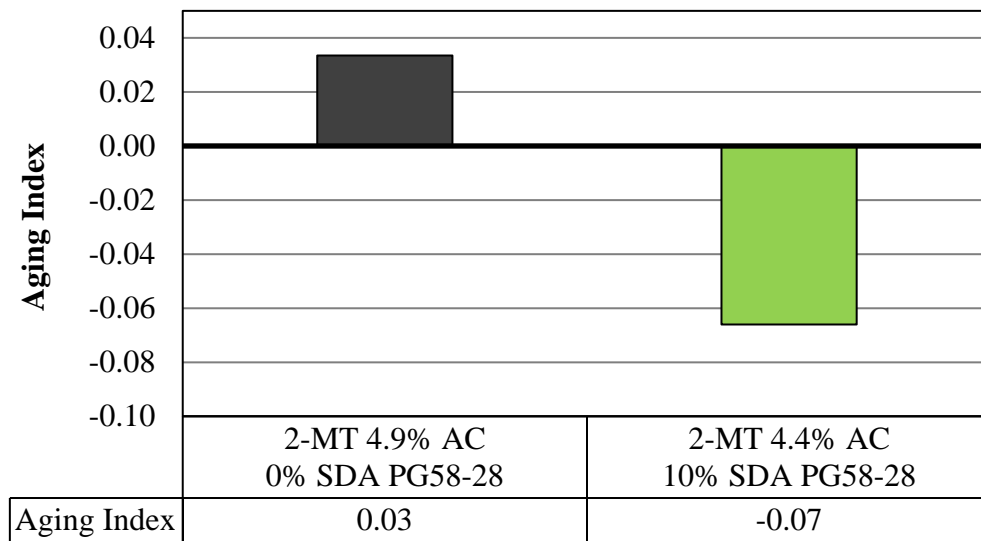
The aging resistance was evaluated by comparing the aging index of all the mixtures used in the field. The aging index is dependent on the air content for the short-term aged materials and the long-term aged materials. The aging index is defined as the difference in air content at 8 gyrations for long-term aged materials versus the air content at 8 gyrations for short-term aged materials. The short-term aging procedure used in this research mimics the aging due to mixing, placing, and compacting whereas the long-term aging procedure used in this research represents 8 to 10 years of aging in the field. Comparing the material in these different aging conditions was critical because resisting the effects of age-hardening could potentially increase the life expectancy of the material since it would stiffen at a slower rate.

Figure 6.6, Figure 6.7, and Figure 6.8 display the percentage of air for both the short-term and long-term compacted specimens at 8 gyrations (N_{ini}) and the aging index. Age-hardening increases the stiffness of the material which means the compaction effort typically increases. It is important to understand that mixtures with similar percentages of air at 8 gyrations resist the effects of aging. Materials with poor aging resistance reveal higher deviations in percentages of air at different aging conditions. The aging index is the difference in air content from the long-term aged samples compared to the short-term aged samples. Since there is typically more air in the long-term aged mixtures at 8 gyrations, these materials demonstrate age-hardening due to the increase in compaction effort. Materials with positive values for the aging index demonstrate age-hardening and materials with negative values for the aging index demonstrate age-softening.

Figure 6.7a reports the air contents for the 2-MT HMA mixtures at both the short-term aged and long-term aged condition. Figure 6.7b reports the aging index (difference in air contents between short-term and long-term aged samples). From Figure 6.6b it is evident that the 2-MT SDA mixture has a negative value of -0.07 for the aging index which means that this material experienced age-softening which is a very desirable response.



(a)

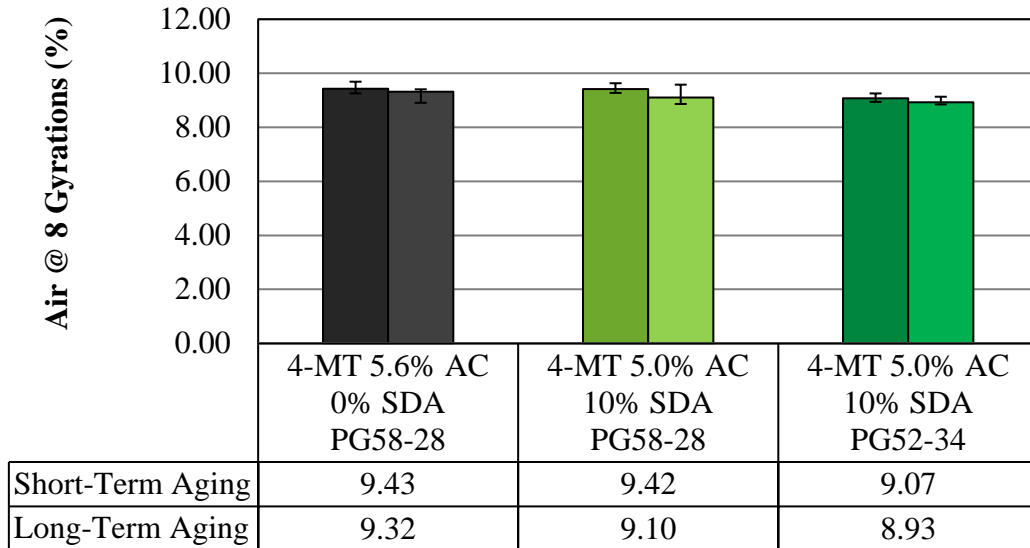


(b)

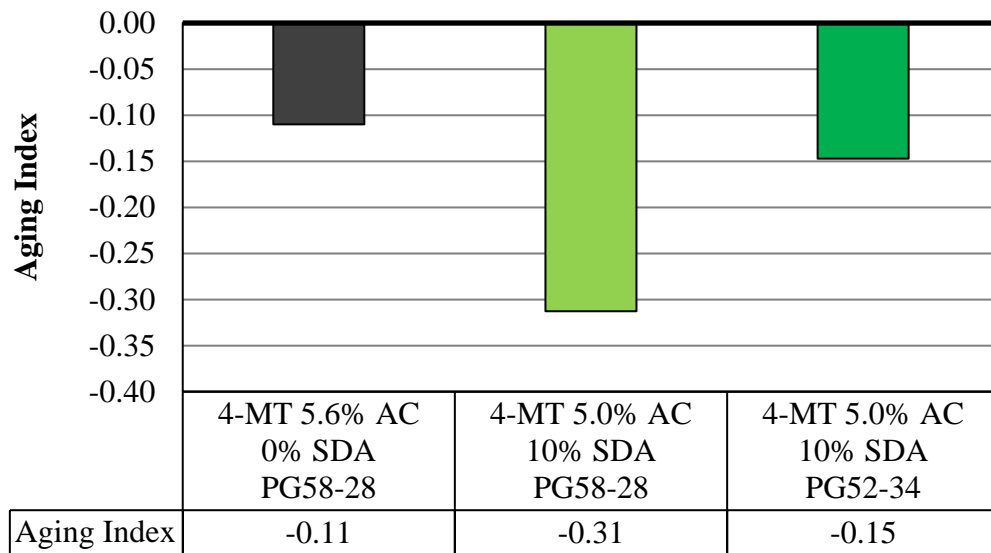
Figure 6.7: Aging of 2-MT HMA (a) %Air at 8 Gyration (b) Aging Index

Figure 6.8a displays the air contents for the 4-MT HMA mixtures at both the short-term aged and long-term aged condition. Figure 6.8b displays the aging index for these mixtures and it can be observed that these mixtures developed age-softening. More importantly, the 4-MT

SDA mixtures demonstrated the highest amount of age-softening since the material with PG58-28 had an aging index of -0.31 and the material with PG52-34 had an aging index of -0.15.



(a)

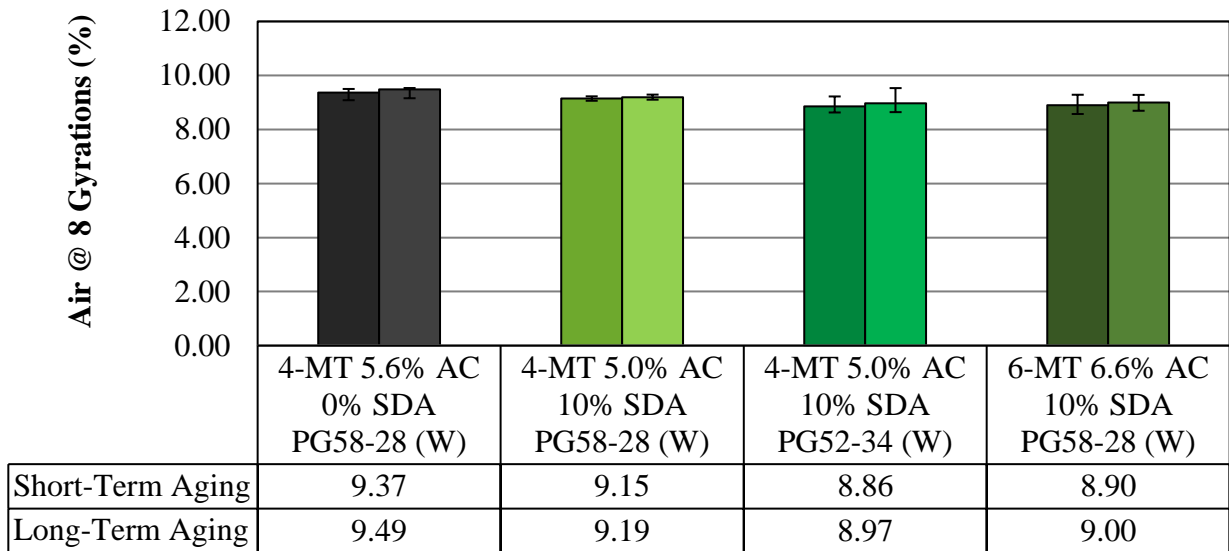


(b)

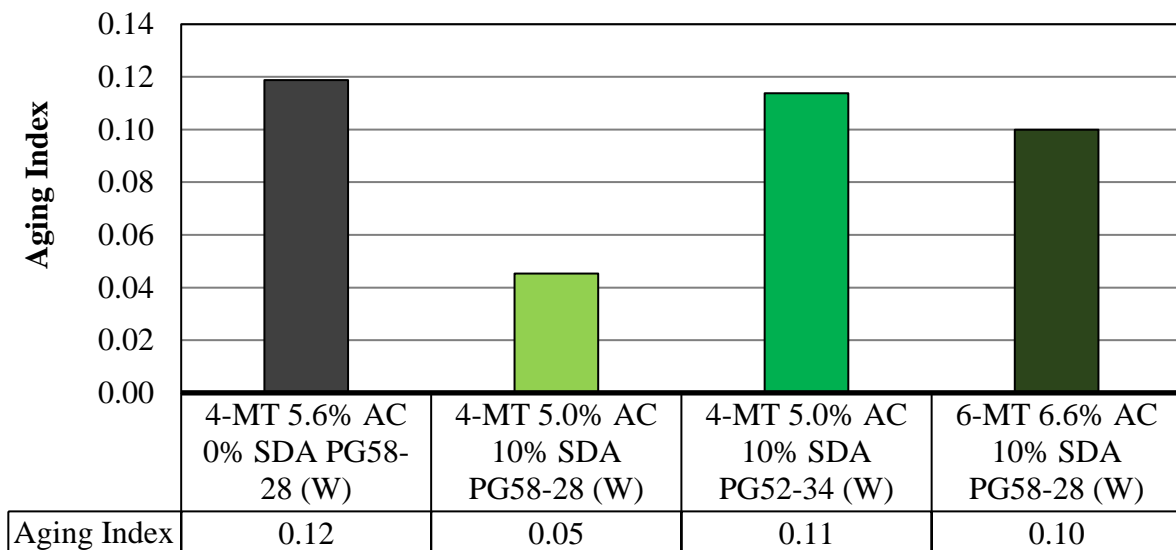
Figure 6.8: Aging of 4-MT HMA (a) %Air at 8 Gyration (b) Aging Index

Figure 6.9a reports on the air contents for the 4-MT WMA mixtures and the 6-MT WMA mixture at both the short-term aged and long-term aged conditions. Figure 6.8b provides

the aging index for these mixtures. From Figure 6.9b it can be seen that all of the mixtures developed age-hardening since the values of the aging index are all positive. Even though these mixtures experience age-hardening, the mixtures with the SDA material resisted the effects of age-hardening as compared to the control mixture since the aging index was lower.



(a)



(b)

Figure 6.9: Aging of 4-MT WMA and 6-MT WMA (a) %Air at 8 Gyration (b) Aging Index

It is important to note that this aging evaluation approach was damage independent and was used only as indication of potential differences in compaction due to aging. With the results being indiscriminate in some cases, it is difficult to assess whether the mixes had such low sensitivity to aging or that this approach was unable to truly test the aging effect. Since there is no standard or proposed test in the literature, the research relied more on damage dependent tests, namely moisture damage, fatigue resistance, and low-temperature resistance to evaluate the impact of the SDA material on aging. This is because the results of these tests are highly influenced by the extent of embrittlement in the binder due to oxidative aging.

Comparing the average air content for long-term aged materials at 8 gyrations against short-term aged materials, the results were still indiscriminate and unable to demonstrate significant difference between the mixes. As noted, all tests had comparable results with air content minimally varying. This could be due to the high temperature and high compaction stress applied by the gyratory loading where the effect of binder aging becomes masked.

6.1.7 Moisture Damage

Moisture damage was used as a parameter to predict the durability of asphalt pavements. Asphalt specimens were tested under different conditions to understand the effects of moisture damage. The saturated and conditioned specimens were both vacuum-saturated to a degree of saturation of 70 to 80%.

The results of the Indirect Tensile Test (IDT) for dry, saturated, and conditioned samples are reported in Table 6.10. These results demonstrate that all HMA SDA mixtures developed higher strength when compared to the appropriate control mixtures, however, in most cases the flow (displacement) was reduced. Load and displacement can be correlated as an inverse

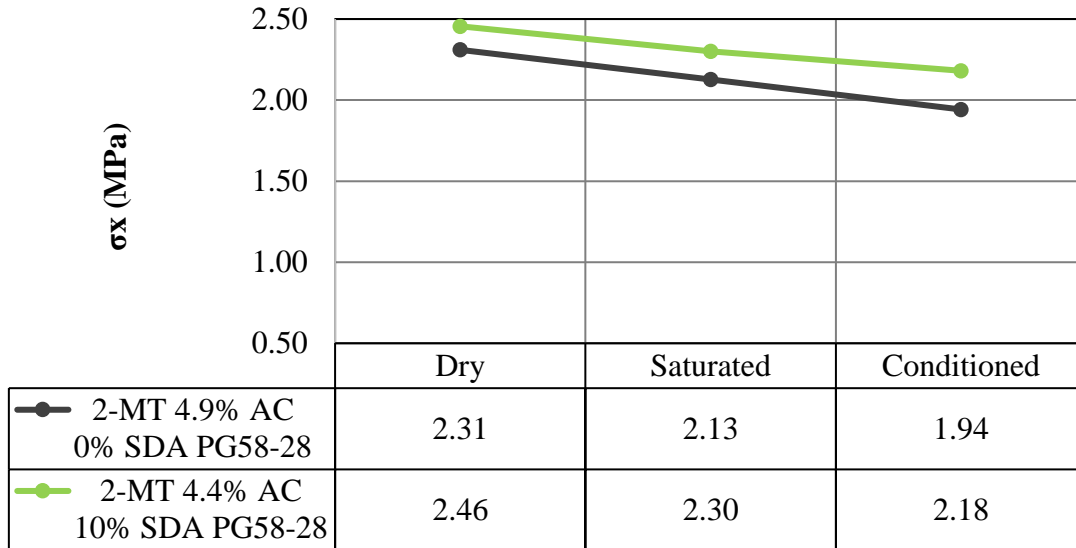
relationship in most cases. As the maximum load increased, the maximum flow of the sample decreased. The 2-MT HMA (due to large aggregates) dry SDA mixture with PG58-28 developed the highest ultimate strengths of 19.91 kN and the 4-MT WMA dry SDA mixture with PG52-34 developed the lowest ultimate strengths of 8.25 kN. The 4-MT WMA dry control mixture with PG58-28 developed the highest horizontal deformation at failure of 4.04 mm and the 4-MT HMA dry SDA mixture with PG58-28 developed the lowest horizontal deformation at failure of 2.41 mm.

For saturated samples it is interesting to observe that the maximum load increased in certain situations as compared to the dry samples even though the samples had a degree of saturation between 70 and 80%. The 4-MT HMA SDA mixture with PG58-28 binder experienced higher ultimate strengths when saturated. The 4-MT HMA control mixtures (PG58-28), 4-MT HMA SDA mixtures (both PG58-28 and PG52-34), and 6-MT WMA mixtures (PG58-28) all demonstrated higher horizontal deformations at failure when they were saturated and then tested. These results have to be investigated further to understand the contribution of fly ash.

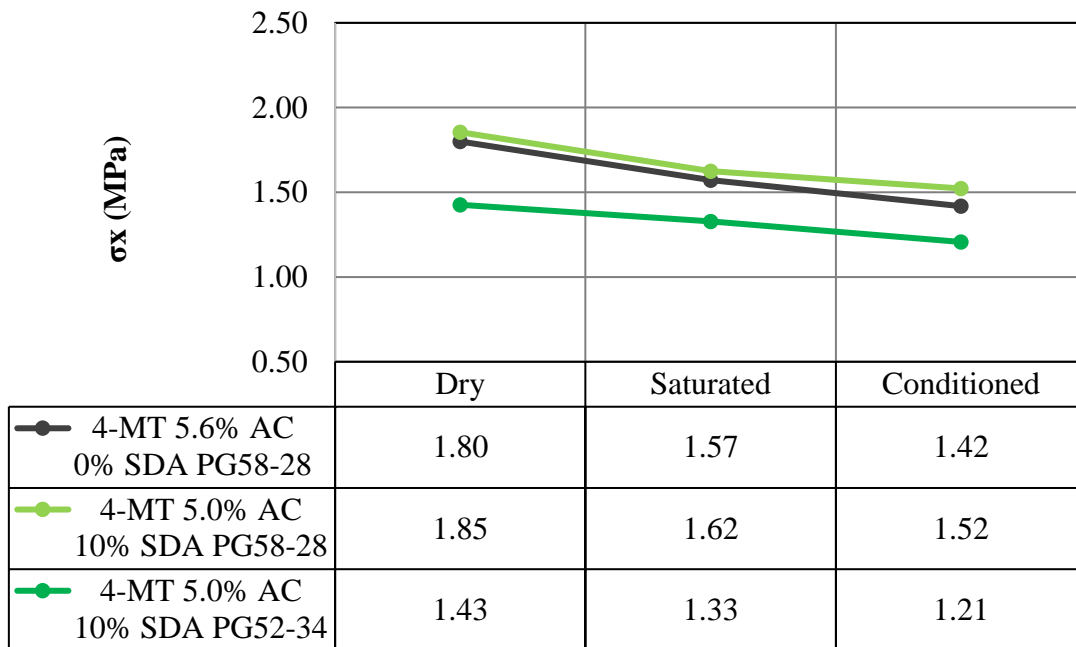
Table 6.10: The Ultimate Load (kN) and Horizontal Deformation at Failure (mm) of all Mixtures Tested for IDT

Sample	Ultimate Load (kN)			Horizontal Deformation at Failure (mm)		
	Dry	Saturated	Conditioned	Dry	Saturated	Conditioned
2-MT 4.9% AC 0% SDA PG58-28	18.73	17.24	15.75	2.72	2.59	2.57
2-MT 4.4% AC 10% SDA PG58-28	19.91	18.66	17.68	2.51	2.45	2.40
4-MT 5.6% AC 0% SDA PG58-28	14.59	12.74	11.50	3.06	3.10	2.98
4-MT 5.0% AC 10% SDA PG58-28	15.03	13.17	12.34	2.41	2.77	2.44
4-MT 5.0% AC 10% SDA PG52-34	11.57	10.76	9.79	2.88	3.23	2.83
4-MT 5.6% AC 0% SDA PG58-28 (W)	10.79	9.74	8.61	4.04	3.59	3.40
4-MT 5.0% AC 10% SDA PG58-28 (W)	10.68	11.05	10.25	3.45	3.39	3.33
4-MT 5.0% AC 10% SDA PG52-34 (W)	8.25	7.63	6.83	3.21	2.90	2.81
6-MT 6.6% AC 10% SDA PG58-28 (W)	10.99	9.52	8.79	3.63	3.87	3.42

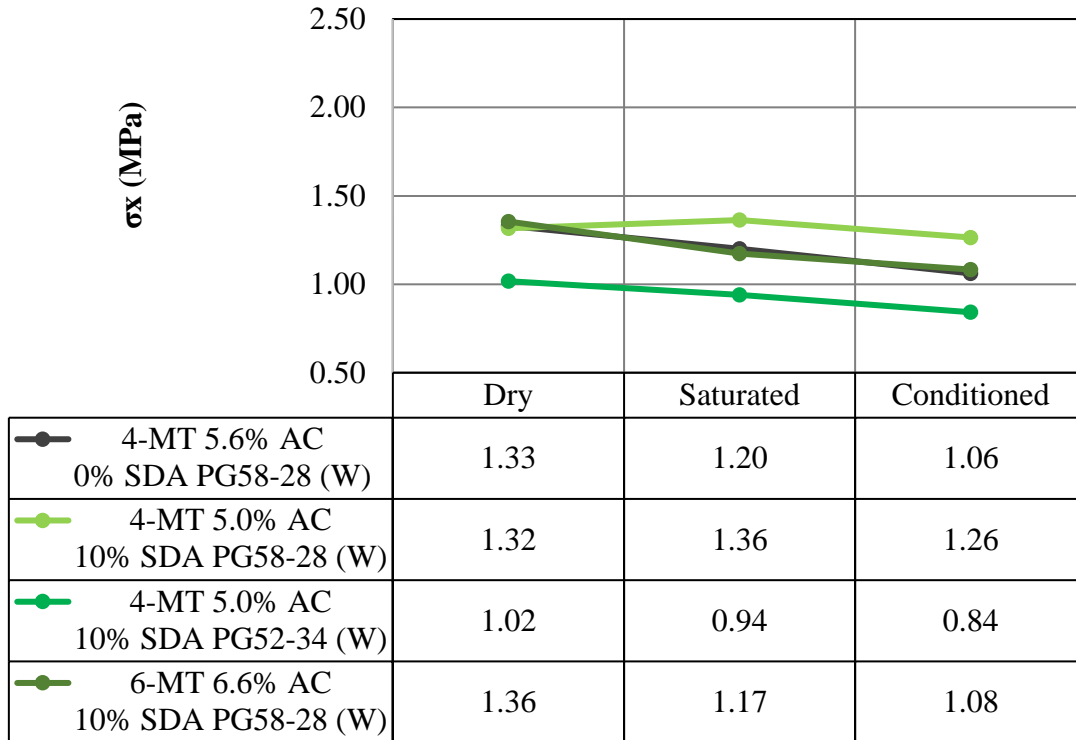
Figure 6.10 reports on the horizontal tensile stress and Figure 6.11 provides the vertical compressive stress of the SDA and control samples. These results give a visual correlation to the maximum load results represented in Table 6.10. These figures prove that the maximum vertical and horizontal stresses for SDA samples were higher than the control samples, when compared to the appropriate subset (2-MT HMA, 4-MT HMA, and 4-MT WMA and 6-MT WMA). For dry samples 2-MT HMA SDA mixtures had the highest maximum horizontal stress of 2.46 MPa and a maximum vertical stress of 7.37 MPa.



(a)

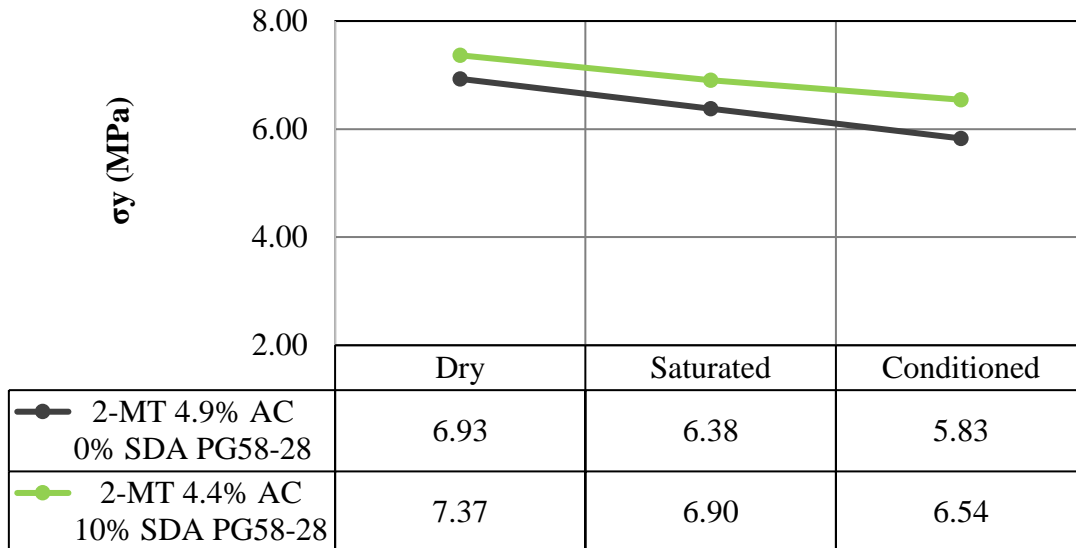


(b)

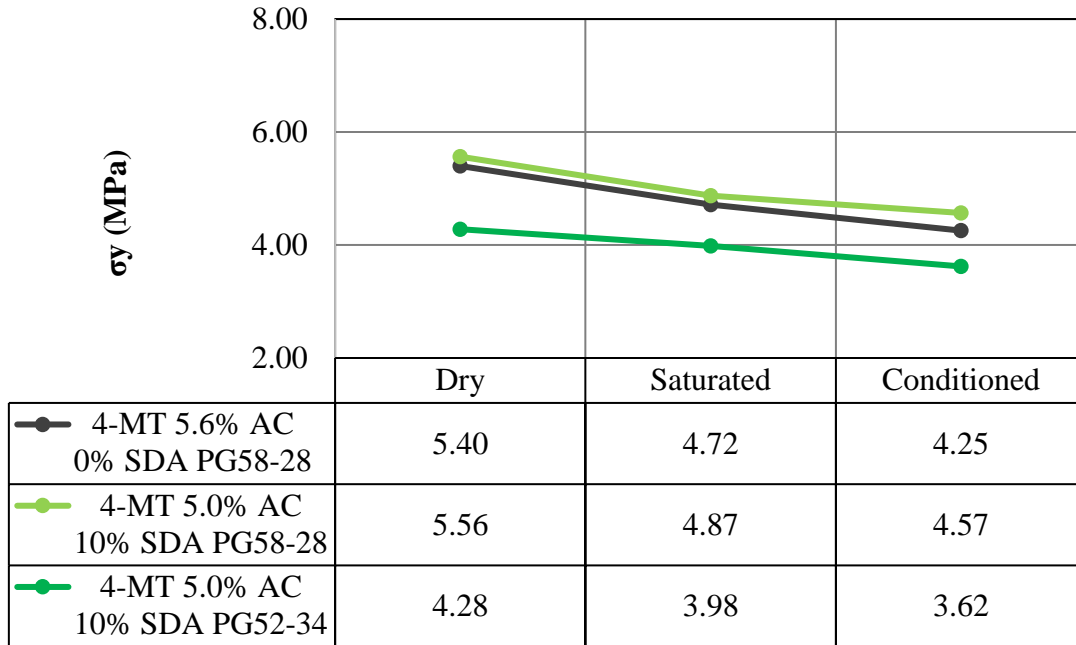


(c)

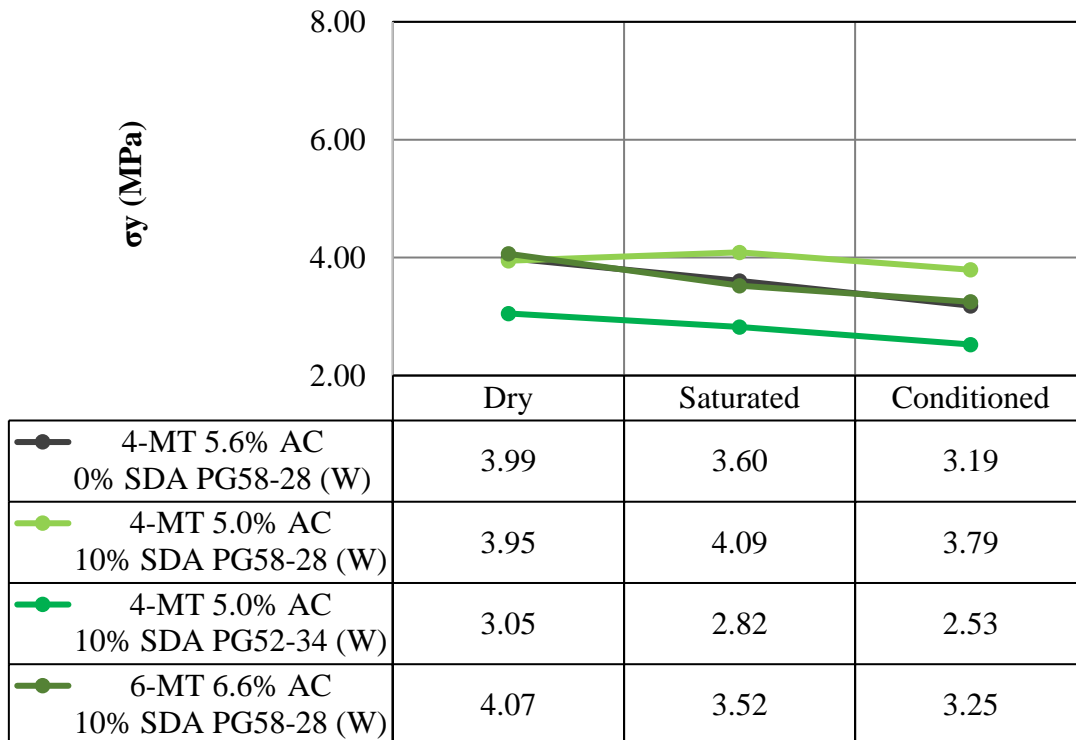
Figure 6.10: Horizontal Tensile Stress (MPa) at the Center of the Specimen (a) 2-MT HMA (b) 4-MT HMA (c) 4-MT WMA and 6-MT WMA



(a)



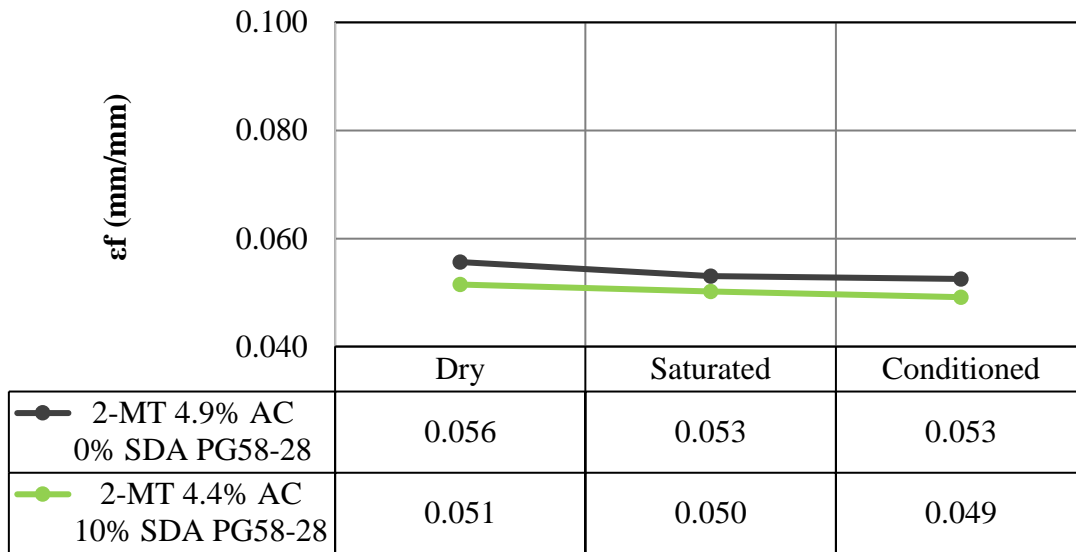
(b)



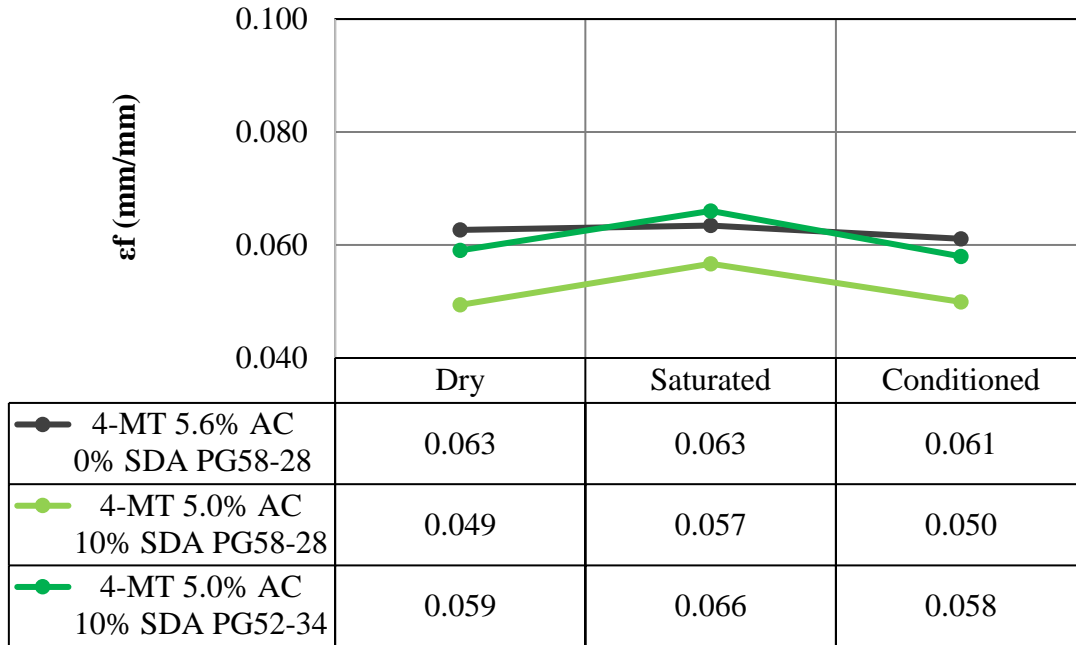
(c)

Figure 6.11: Vertical Tensile Stress (MPa) at the Center of the Specimen (a) 2-MT HMA (b) 4-MT HMA (c) 4-MT WMA and 6-MT WMA

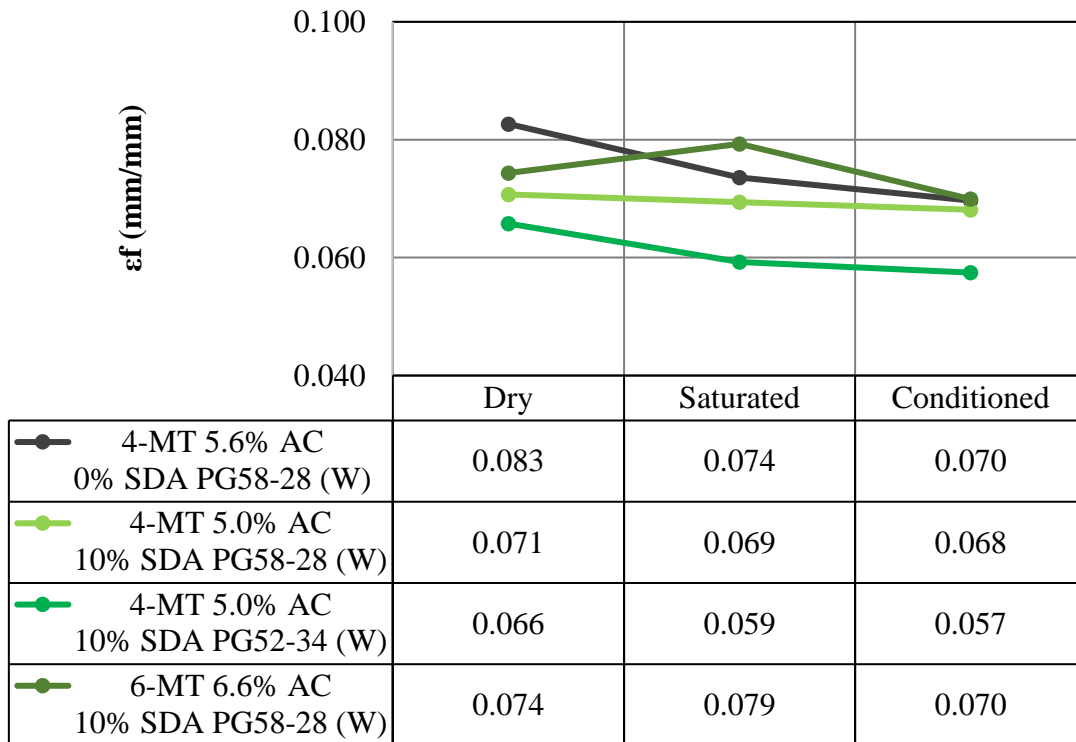
Figure 6.12 reports the tensile strain at failure for the control and SDA specimens. These results give a visual representation of the maximum flow (displacement) results represented in Table 6.10. This figure demonstrates the effects of moisture damage on the ability for asphalt pavements to deform. For conditioned specimens the strain at failure is reduced in most cases. It is interesting to observe that the ultimate strain (related to flow) increases for the saturated 4-MT HMA control mixtures (PG58-28), 4-MT HMA SDA mixtures (both PG58-28 and PG52-34), and 6-MT WMA mixtures (PG58-28). The 4-MT WMA dry control mixture with PG58-28 experienced the highest strain at failure of 0.083 mm/mm for the dry samples and 4-MT HMA dry SDA mixture with PG58-28 experienced the lowest strain at failure of 0.049 mm/mm.



(a)



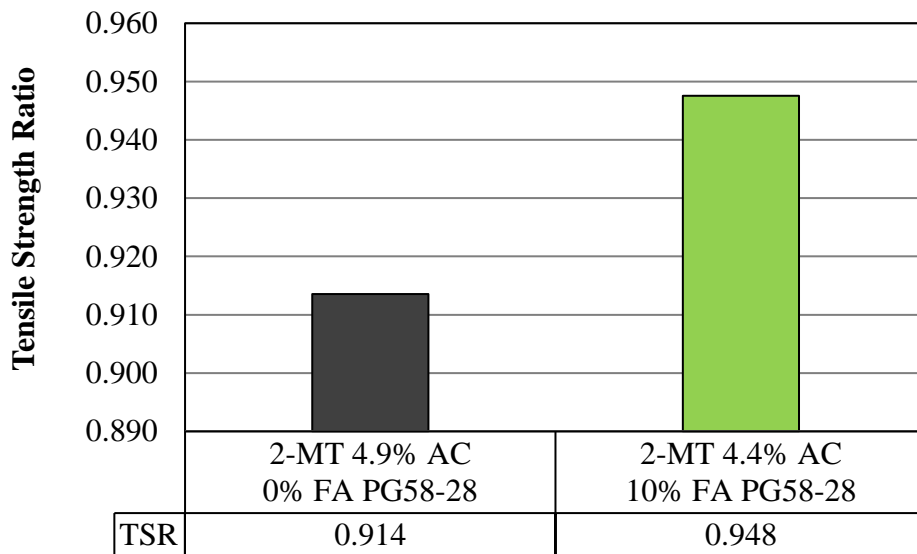
(b)



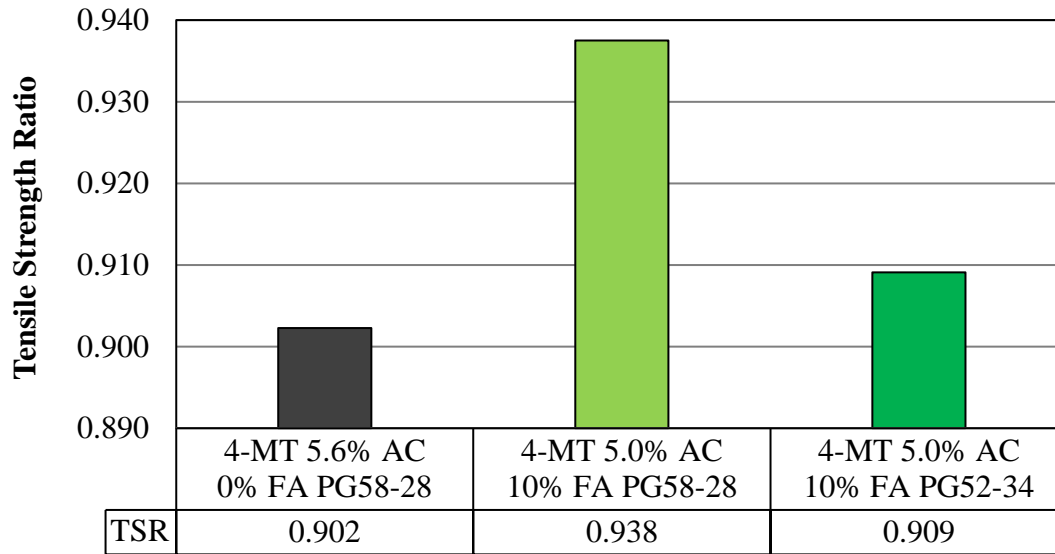
(c)

Figure 6.12: Horizontal Tensile Strain (mm/mm) at Failure (a) 2-MT HMA (b) 4-MT HMA (c) 4-MT WMA and 6-MT WMA

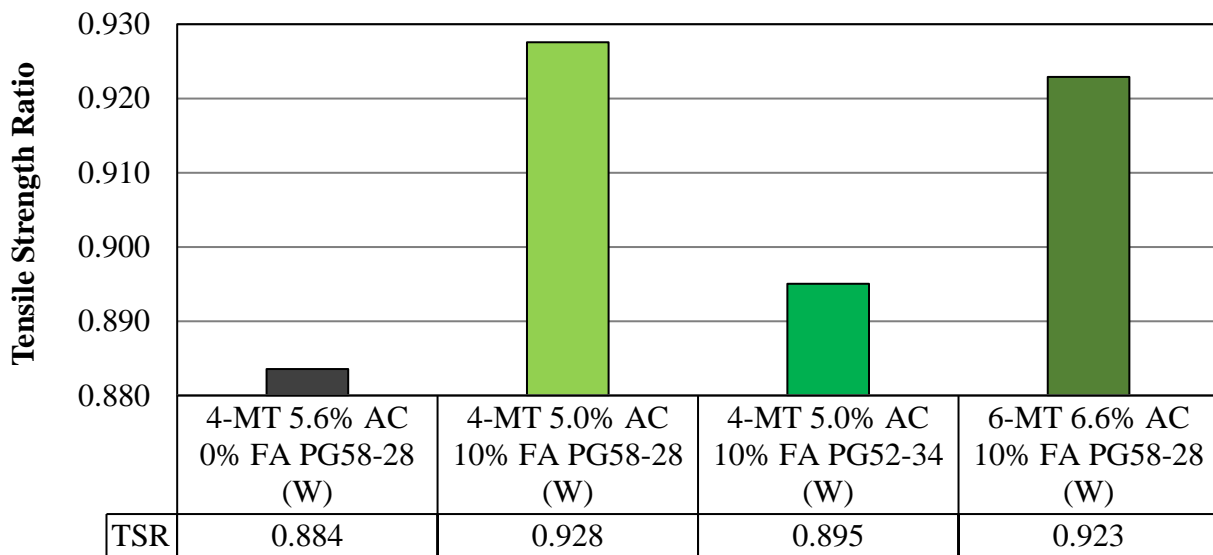
The Tensile Strength Ratio (TSR) was calculated and compared for conditioned and saturated samples (Figure 6.13). The TSR values are required to be at or above 80%; the results demonstrate that all mixtures fulfilled this requirement. Higher values of TSR are desired as this indicates a better performance in terms of moisture damage resistance. It can be observed that all SDA mixtures enhanced the moisture damage resistance when compared to the control mixture. The 2-MT SDA mixtures performed the best since the TSR was 0.948 and the 4-MT WMA control mixture performed the worst with a TSR of 0.884.



(a)



(b)



(c)

Figure 6.13: Tensile Strength Ratio (a) 2-MT HMA (b) 4-MT HMA (c) 4-MT WMA and 6-MT WMA

In terms of moisture damage it can be concluded that SDA mixtures resisted the effects of moisture damage better than the control mixtures. The results prove that adding the SDA powders to asphalt mixtures enhances the moisture damage resistance.

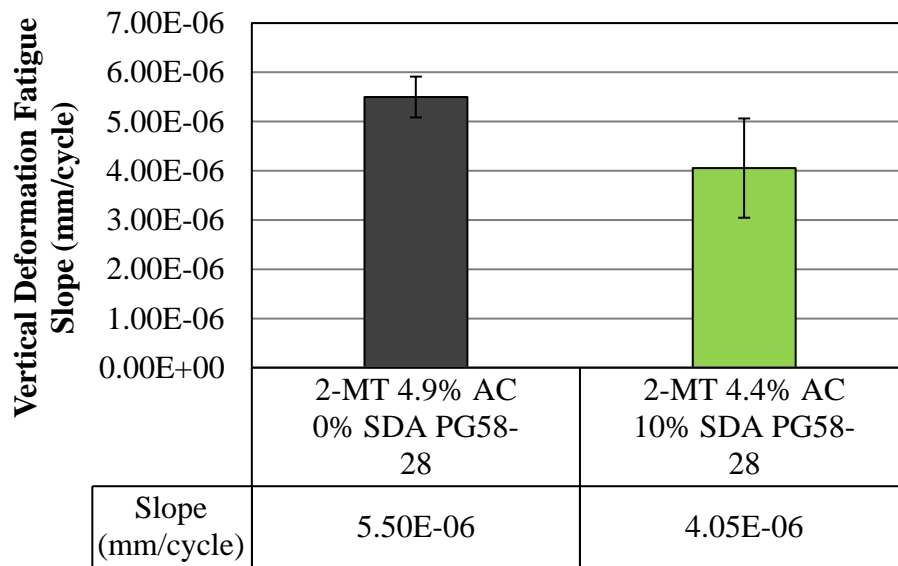
6.1.8 Fatigue Resistance

Fatigue cracking resistance was evaluated to understand the number of cycles each specimen could withstand till failure. The fatigue test that was used evaluated the slope of the secondary fatigue section as well as the failure point (N_f) which is where the tertiary fatigue section starts (Figure 3.16). It was determined that at this point, the complex modulus (E^*) started to decrease since the slope of the deformation (strain) line increased. For better performance, asphalt pavements must demonstrate smaller deformation rates and higher amounts of cycles till failure.

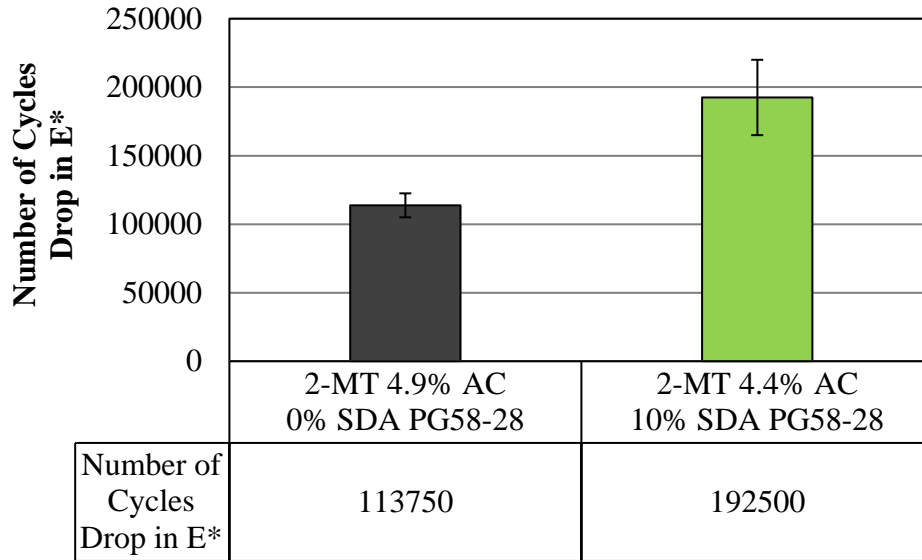
For this study, fatigue was assessed by using a sine wave loading condition, a test temperature of 20 to 25°C, a 2% pre-loading condition, a 25% ultimate loading condition, and a frequency of 10 Hz. After evaluating the IDT results for the dry samples, it was decided to use an ultimate load of 18.73 kN (2% pre-load = 0.38 kN, 25% of ultimate = 4.68 kN) for the 2-MT HMA mixtures, an ultimate load of 14.59 kN (2% pre-load = 0.29 kN, 25% of ultimate = 3.65 kN) for the 4-MT HMA mixtures, and an ultimate load of 10.79 kN (2% pre-load = 0.22 kN, 25% of ultimate = 2.70 kN) for the 4-MT WMA and 6-MT WMA mixtures. Here, the fatigue test was ran until the material failed.

The results of the fatigue testing are reported in Figures 6.14, 6.15, and 6.16. These results demonstrate the performance of duplicate samples that were tested in fatigue. These figures report the results for the secondary fatigue slopes as well as the number of cycles that the samples could withstand till there was a drop in E^* (complex modulus). This drop in E^* is directly correlated to N_f as this is the defined point of failure.

Figure 6.14a reports on the vertical deformation slope (mm/mm) for the 2-MT HMA mixtures and Figure 6.14b reports the number of cycles drop in E^* . Based on these figures, the 2-MT SDA samples performed better than the control mixtures because the samples were able to withstand 192,500 cycles whereas the control samples were only able to withstand 113,750 cycles. The slopes of the SDA samples in the secondary fatigue sections were also lower ($4.05\text{E-}06$ mm/cycle) than the control samples ($5.50\text{E-}06$ mm/cycle). This means that there was a slower rate of deformation due to loading. This decrease in deformation rate is critical because it is a characteristic of an elastic material that can recover from deformation and this parameter is directly related to fatigue cracking resistance.



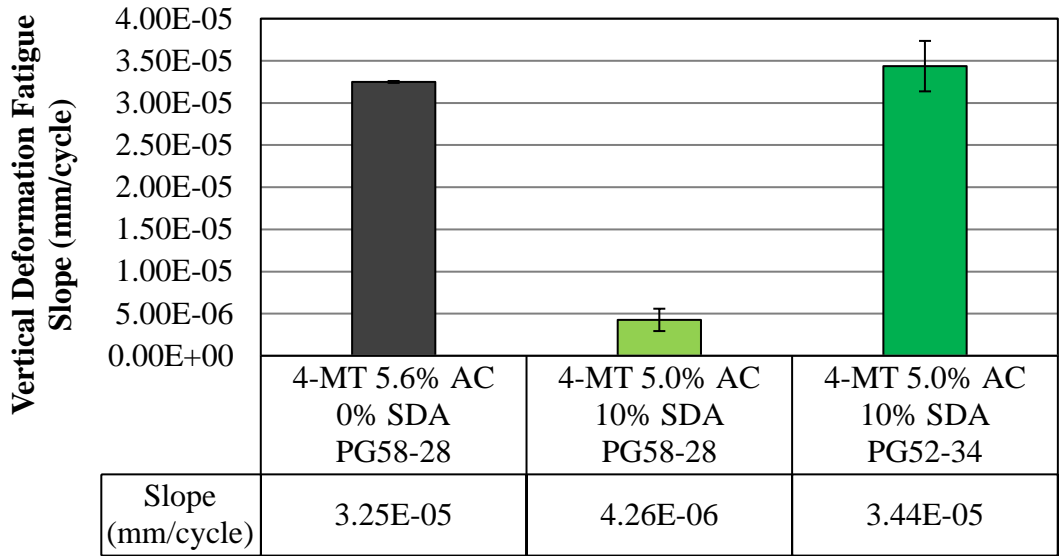
(a)



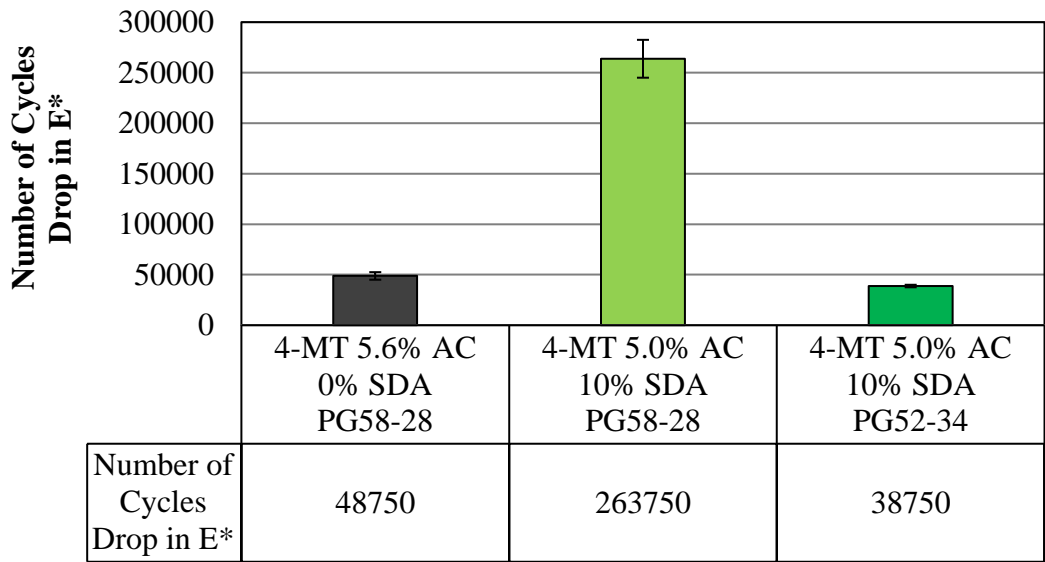
(b)

Figure 6.14: 2-MT HMA (a) Vertical Deformation Slope (b) Number of Cycles Drop in E*

Figure 6.15a reports on the vertical deformation slope (mm/mm) for the 4-MT HMA mixtures and Figure 6.15b reports the number of cycles drop in E*. The 4-MT HMA SDA samples with PG58-28 performed much better than the control mixtures since the samples were able to withstand 263,750 cycles till there was a drop in E* whereas the control samples were only able to withstand 48,750 cycles. The slopes of the 4-MT HMA samples with PG58-28 in the secondary fatigue sections were also lower (4.26E-06 mm/cycle) than the control samples (3.25E-05 mm/cycle). On the other hand, the 4-MT HMA samples with PG52-34 performed worse than the control samples based on PG58-28 since these samples were only able to withstand 38,750 cycles till there was a drop in E* and the vertical deformation slope was 3.44E-05 mm/cycle. However, this response is due to the use of PG52-34 binder.



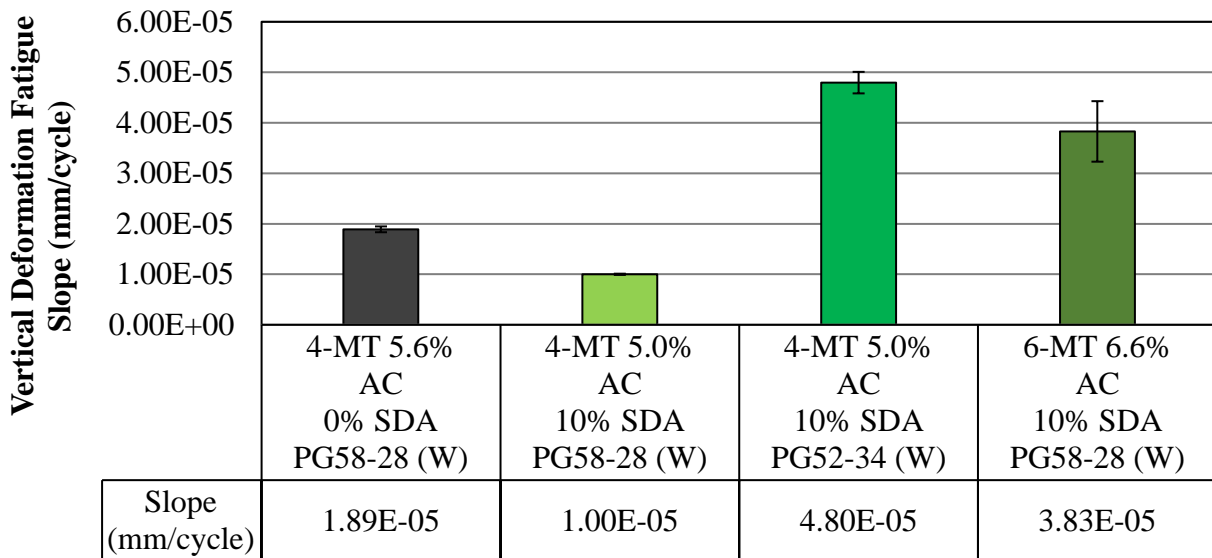
(a)



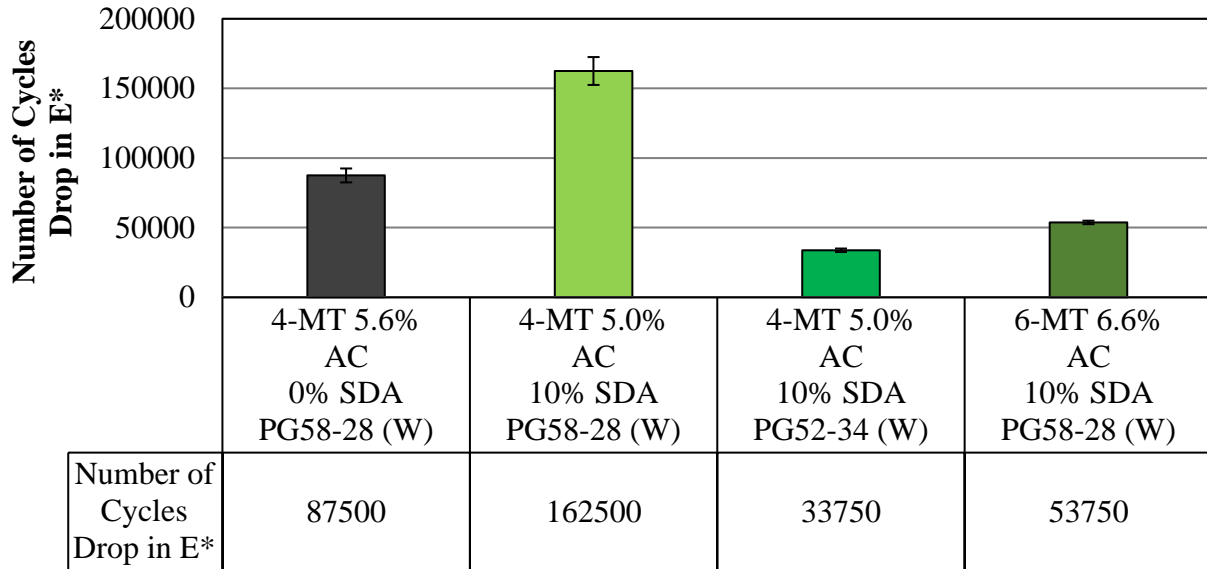
(b)

Figure 6.15: 4-MT HMA (a) Vertical Deformation Slope (b) Number of Cycles Drop in E*

Figure 6.16a reports on the vertical deformation slope (mm/mm) for the 4-MT WMA mixtures and the 6-MT WMA mixture and Figure 6.16b provides the number of cycles drop in E^* . The 4-MT WMA SDA samples with PG58-28 performed better than the control mixtures since the samples were able to withstand 162,500 cycles till there was a drop in E^* whereas the control samples were only able to withstand 87,500 cycles. The slopes of the 4-MT HMA samples with PG58-28 in the secondary fatigue sections were also lower ($1.00E-05$ mm/cycle) than the control samples ($1.89E-05$ mm/cycle). The 4-MT WMA samples with PG52-34 and the 6-MT WMA samples with PG58-28 performed worse than the control samples as these were only able to withstand 33,750 cycles and 53,750 cycles, respectively till there was a drop in E^* and the vertical deformation slopes were $4.8E-05$ mm/cycle and $3.83E-05$ mm/cycle, respectively. This behavior can be attributed to the use of low temperature binder PG52-34 in the 4-MT mixture as well as using higher volumes of binder in the 6-MT mixture.



(a)



(b)

Figure 6.16: 4-MT WMA and 6-MT WMA (a) Vertical Deformation Slope (b) Number of Cycles Drop in E*

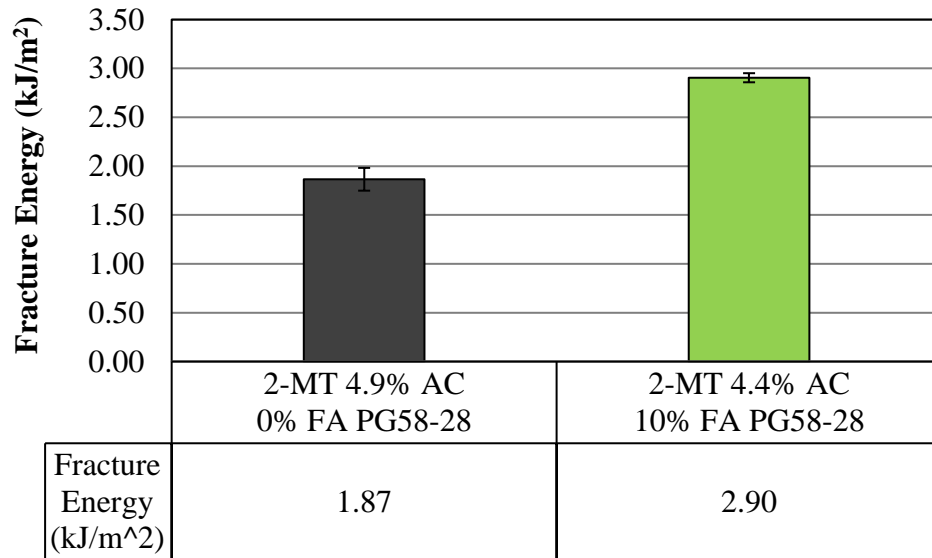
The results of this study prove that HMA and WMA SDA mixtures with PG58-28 binder perform better than control mixtures with respect to intermediate-temperature fatigue cracking resistance, except for the 6-MT SDA mixture. Every SDA mixture with PG58-28 binder demonstrated smaller deformation fatigue slopes, and these mixtures were also able to withstand more loading cycles till failure.

6.1.9 Thermal-Cracking Resistance

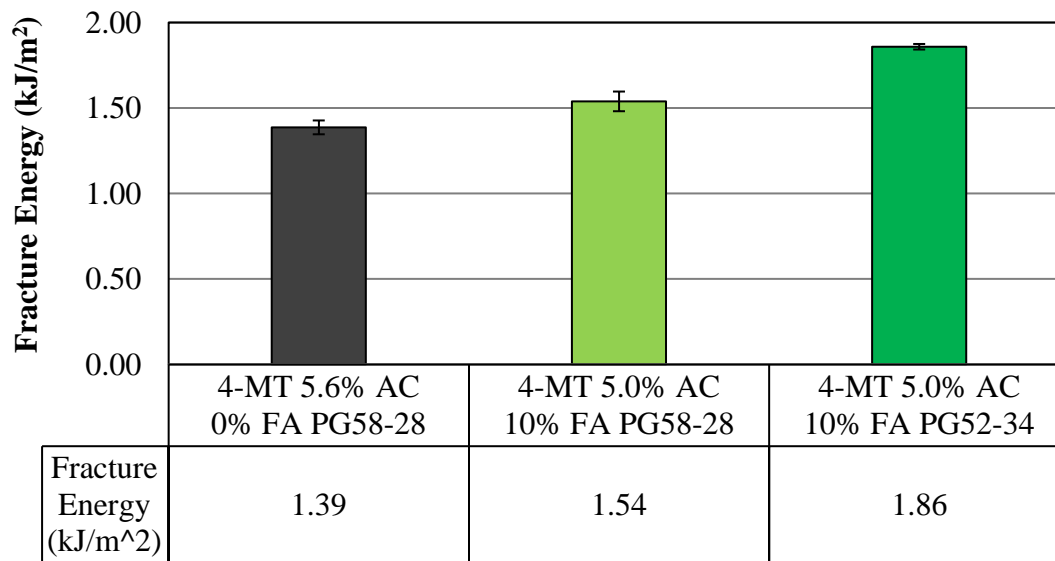
The Semi-Circular Bending (SCB) test was used to determine the low-temperature (-18°C) properties such as Fracture Energy (G_f) and Stiffness (S). Asphalt mixtures become brittle at low temperatures and when the developing thermal stresses become too large, the pavement cracks as a result. Therefore, asphalt materials that are too brittle at low temperature are undesirable whereas materials that are more elastic perform better since these are able to

recover from the emerging stresses. For this testing, higher values of G_f are desirable as this demonstrates larger amounts of energy that is necessary to crack the specimen. On the other hand, lower stiffness values are desirable as this demonstrates a more ductile material that can recover from the stresses that are developed due to traffic loads. The SCB test was performed at -18°C by applying a vertical load on the specimen at a rate of 0.03 mm/min and the test is done once the load decreases to 0.5 kN.

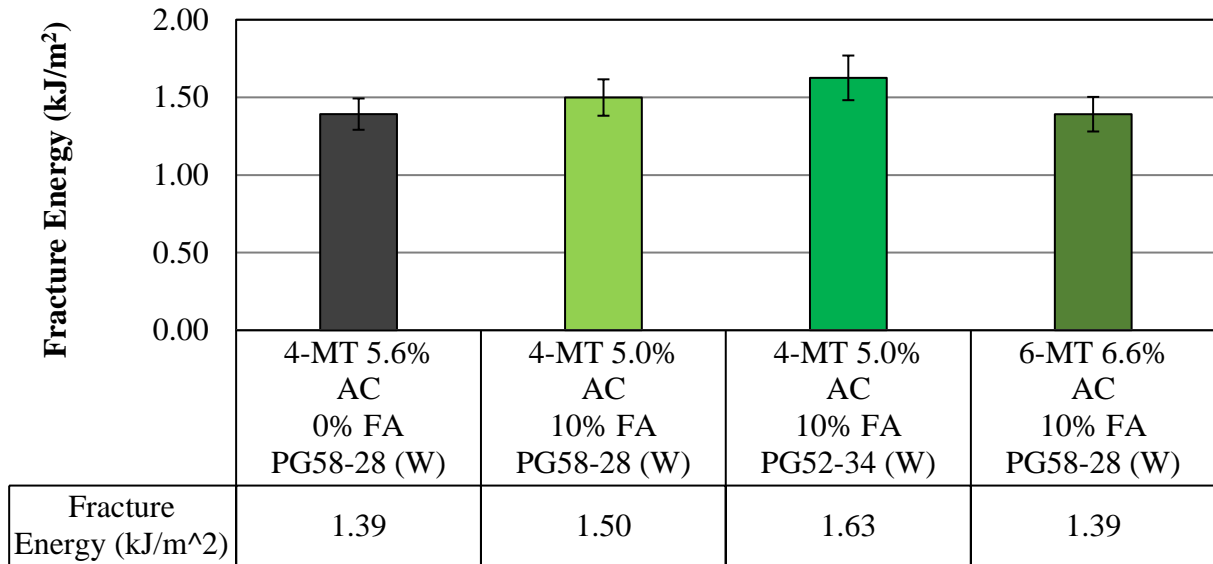
Figure 6.17 demonstrates the Fracture Energy (G_f) of investigated asphalt materials. As previously mentioned, larger values of G_f are desirable as this demonstrates a larger energy required to create a unit surface area of crack. This is obtained by dividing the work of fracture (area under the load vs. load line displacement curve) by the ligament area. The results show that the SDA mixtures performed better than the control mixture in terms of G_f . The 2-MT HMA SDA samples performed the best as this mixture was able to achieve a G_f value of 2.90 kJ/m^2 . An interesting trend is that the mixtures with PG52-34 binder demonstrate better performance when compared to the appropriate control mixture since the Fracture Energy (G_f) value is higher than the control mixture. These results are extremely significant since this demonstrates improved performance of SDA mixtures at low temperatures.



(a)



(b)

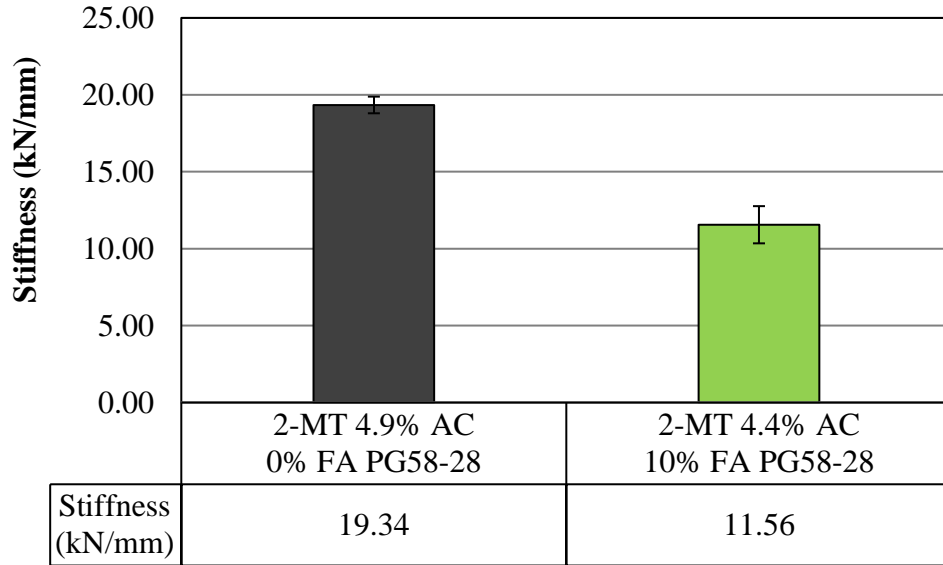


(c)

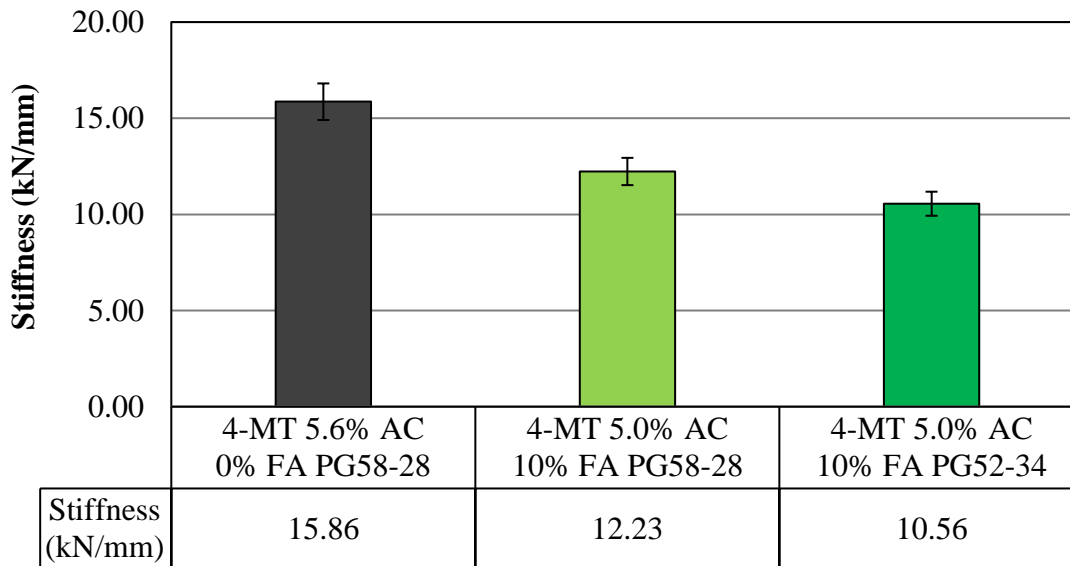
Figure 6.17: Fracture Energy (Gf) for (a) 2-MT HMA (b) 4-MT HMA (c) 4-MT WMA and 6-MT WMA

The stiffness $S(t)$ is represented as the slope of the linear portion of the load-line displacement curve. Lower stiffness values are desirable since this demonstrates a more elastic material that can recover from low-temperature stresses. Figure 6.18 demonstrates the stiffness results from the SCB testing. These results demonstrate that the SDA mixtures performed better than the corresponding control mixtures since the stiffness values were much lower (with the exception of the 6-MT WMA mixture). The 4-MT WMA SDA mixture with PG52-34 binder demonstrated the lowest stiffness of 9.13 kN/mm whereas the 2-MT HMA control mixture obtained the highest stiffness of 19.34 kN/mm. These results reveal that the control mixtures were much more brittle at the low temperature as compared to the SDA mixtures which acted in a more ductile manner. The mixtures with the PG52-34 binder demonstrated the best results when compared to the other mixtures and this makes sense because this lower binder grade acts

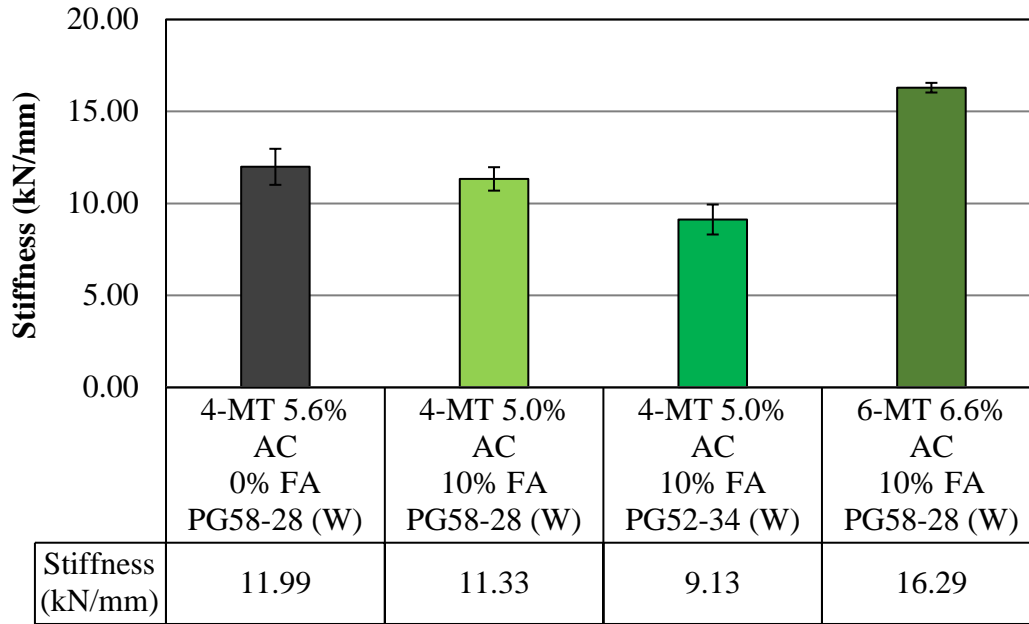
as a softer material at lower temperatures. This means that this soft binder behaves more elastically at lower temperatures and thus resists the thermal-cracking.



(a)



(b)



(c)

Figure 6.18: Stiffness $S(t)$ Values for (a) 2-MT HMA (b) 4-MT HMA (c) 4-MT WMA and 6-MT WMA

In terms of thermal cracking resistance, it can be concluded that SDA mixtures resisted the effects of low-temperature cracking better than the control mixtures for Fracture Energy (G_f) and Stiffness (S) evaluations. These results reveal that the control mixture is much more brittle at low temperatures as compared with the SDA mixtures. These results prove that the use of the SDA material in asphalt mixtures enhances low-temperature thermal cracking resistance.

6.2 COST ANALYSIS

The development of a new construction material should always be innovative and beneficial to the specific application. Specific physical or chemical properties can be altered in order to develop a more sustainable material with beneficial characteristics. However, when developing a new construction material, it is important to evaluate the cost associated with a

new material. If a material is beneficial in terms of performance, but at the same time elevates the production costs more than a reference material, there might be a need for comprehensive cost benefit analysis to validate the impact of innovation. Here, for effective application in the field, creating a new sustainable construction material that is cost effective is just as important as creating a new material with enhanced properties.

For the Wausau, WI Road Paving Project the innovation included the use of a 10% binder replacement by volume for the SDA mixtures. For these mixtures, there was approximately \$2.00/ton of asphalt savings on the base layer. There was a \$3.00/ton savings on the surface layer if the 4-MT PG58-28 binder was used. There was a \$3.50/ton increase for the 4-MT PG52-34 colder weather binder which was used for the surface layer to offset some increased stiffness in the SDA mixtures. Therefore, the total cost of the completed SDA pavement was reduced (the less expensive base layer is thicker thus offsetting the increased surface layer costs). The cost savings could also potentially increase when the prices of petroleum oil and asphalt binder increase. The total project cost for all materials used was \$400,643.90. The total pavement quantities per section of the roadway are reported in Table 6.11 for inbound traffic and in Table 6.12 for outbound traffic. Table 6.13 provides the direct costs associated with the specific pavement mixture that was used in the project. Table 6.14 and Table 6.15 summarize the overall total cost analysis for the Wausau, WI Road Paving Project for both traffic directions of the roadway.

Table 6.11: Pavement Quantities for Inbound Traffic Sections

Section	Length (km)	Width (m)	Base Layer	Thickness (mm)	Surface Layer	Thickness (mm)	Lower Layer Tons	Surface Layer Tons
1	0.52	3.96	2-MT HMA PG58-28	101.6	4-MT HMA PG58-28	50.8	513	280
2	0.52	3.96	2-MT HMA PG58-28	101.6	4-MT HMA PG58-28 SDA	50.8	513	280
3	0.52	3.96	2-MT HMA PG58-28 SDA	101.6	4-MT HMA PG52-34 SDA	50.8	513	280
4	0.52	3.96	2-MT HMA PG58-28 SDA	127	6-MT HMA PG52-34 SDA	25.4	640	140
5	0.07	6.10	2-MT HMA PG58-28 SDA	127	6-MT WMA PG58-28	25.4	112	61

Table 6.12: Pavement Quantities for Outbound Traffic Sections

Section	Length (km)	Width (m)	Base Layer	Thickness (mm)	Surface Layer	Thickness (mm)	Lower Layer Tons	Surface Layer Tons
4	0.52	3.96	2-MT HMA PG58-28 SDA	127	6-MT WMA PG52-34 SDA	25.4	640	140
3	0.52	3.96	2-MT HMA PG58-28 SDA	101.6	4-MT WMA PG52-34 SDA	50.8	513	280
2	0.52	3.96	2-MT HMA PG58-28 SDA	101.6	4-MT WMA PG58-28 SDA	50.8	513	280
1	0.52	3.96	2-MT HMA PG58-28 SDA	101.6	4-MT WMA PG58-28	50.8	513	280

Table 6.13: Material Cost Analysis for Different Asphalt Mixtures

Sample	Materials	Asphalt	Total
2-MT 4.9% AC 0% SDA PG58-28	\$ 42.60	\$ 19.60	\$ 62.20
2-MT 4.4% AC 10% SDA PG58-28	\$ 42.60	\$ 17.60	\$ 60.20
4-MT 5.6% AC 0% SDA PG58-28	\$ 41.10	\$ 22.40	\$ 63.50
4-MT 5.0% AC 10% SDA PG58-28	\$ 41.10	\$ 20.00	\$ 61.10
4-MT 5.0% AC 10% SDA PG52-34	\$ 41.10	\$ 23.50	\$ 64.60
6-MT 7.3% AC 0% SDA PG58-28	\$ 41.10	\$ 26.80	\$ 67.90
6-MT 7.3% AC 0% SDA PG52-34	\$ 41.10	\$ 31.49	\$ 72.59
6-MT 6.6% AC 10% SDA PG52-34	\$ 41.10	\$ 28.20	\$ 69.30

Table 6.14: Total Cost Analysis for Inbound Traffic Sections

Section	Lower Layer Price per Ton	Surface Layer Price per Ton	Total
1	\$ 62.20	\$ 63.50	\$ 49,688.60
2	\$ 62.20	\$ 61.10	\$ 49,016.60
3	\$ 60.20	\$ 64.60	\$ 48,970.60
4	\$ 60.20	\$ 69.30	\$ 48,230.00
5	\$ 60.20	\$ 67.90	\$ 10,884.30

Table 6.15: Total Cost Analysis for Outbound Traffic Sections

Section	Lower Layer Price per Ton	Surface Layer Price per Ton	Total
4	\$ 60.20	\$ 69.30	\$ 48,230.00
3	\$ 60.20	\$ 64.60	\$ 48,970.60
2	\$ 60.20	\$ 61.10	\$ 47,990.60
1	\$ 60.20	\$ 63.50	\$ 48,662.60

CHAPTER 7

CONCLUSIONS

The developments of this research produced promising results which is essential for implementation of portland cement reactive powders in asphalt pavements. The following sections summarize the research results.

7.1 MASTIC STUDY

- The addition of up to 25% by volume replacement of reactive powders and control limestone filler demonstrated a linear increase in complex modulus G^* . This research revealed that the SDA material was the most interactive in affecting G^* for both WMA PG58-28 and WMA PG52-34 binders and the increase in concentrations resulted in nonlinear relationships. The SDA material was also the stiffest at 15% and 25% concentrations for both binder types indicating that stiffening rate increases with a decrease in specific gravity (SDA has the lowest specific gravity) and an increase in Na_2O , P_2O_5 , and Rigden voids (SDA has the highest values for all of these), which was confirmed by the multiple linear regression method.
- Relative complex modulus G^*r was used to identify the interactions between the reactive powders and the binders. As demonstrated by the results of the complex modulus, the relative complex modulus also increased linearly (diluted region) with increase concentration of reactive powder. The CSA cement mastics demonstrated higher values of G^*r for both binder types at all concentrations as compared to the control limestone filler; this response was desirable as this indicates a better potential to rutting resistance. The SDA based mastics developed the highest G^*r values (became the stiffest) for both

binders, especially at higher concentrations, and this could be detrimental to mixing and compacting efforts. The results were important to determine that the increase in complex modulus was binder independent.

- Constructability (workability) was investigated by evaluating the viscosity of unaged mastics. These results had strong direct correlations to the non-performance indicator G^* . All mastics met Superpave® specifications as the viscosity was less than 3.0 Pa-s. As most reactive powder mastics demonstrated favorable results (in terms of rutting resistance) by increasing G^* values compared to the control limestone mastics, the reactive powder mastics also increased the viscosity at the same time. The SDA mastics were the most unfavorable in this sense as the viscosity was very dramatic past 5% concentrations. The SDA material yielded the highest viscosity at 15% and 25% concentrations for both binders which suggests the potential increase in mixing and compacting efforts. When compared to the original WMA PG58-28 unfilled asphalt binder the SDA mastic at 25% by volume concentration increased the viscosity by 210.71% which is significant.
- Rutting resistance was considered based on the rutting factor $G^*/\sin(\delta)$ for RTFO aged reactive powder mastics. For this testing, all mastics met Superpave specifications as $G^*/\sin(\delta)$ for RTFO aged mastics was greater than 2.20 kPa. The results proved that an increase in concentration of reactive powders increased $G^*/\sin(\delta)$ and this was due to the increase in stiffness. The CSA cement and SDA mastics again demonstrated enhanced rutting resistance potential as these materials performed better than the control limestone mastic since $G^*/\sin(\delta)$ was higher in most cases.

- Non-recoverable compliance J_{nr} and % Recovery were determined to characterize the deformation resistance of RTFO aged mastics from the Multiple Stress Creep and Recovery test. This test confirmed that the increase in concentration of powders increases rutting resistance as compared to the unfilled binder since J_{nr} values decrease with an increase in concentration. Most reactive powder mastics performed better than the control limestone mastics for both binder types. Specifically, HA cement mastics demonstrated a decrease in J_{nr} at all concentrations for both binders as compared to the control limestone mastics and this indicates the best rutting resistance potential for MSCR testing. The % Recovery indicated that the results for the unmodified asphalt binders were negligible and can't be considered significant. Even though there were increases in % Recovery, the increase is still insufficient to cause a meaningful change in performance.
- Fatigue resistance was examined for PAV aged mastics based on Superpave® specifications for the fatigue factor $G^* \sin(\delta)$. The results demonstrated that the increase in powder content decreased the fatigue resistance. For WMA PG58-28, only SM and CSA cements, as well as control limestone mastics, met the specifications up to 15% concentrations (by volume) as the results were below the 5,000 kPa limit. For WMA PG52-34, only OW cement mastics did not meet the specifications up to 15% concentrations. Beyond 15%, the mastics rapidly exceeded the Superpave® specifications for both binders which demonstrated an increase in stiffness.
- Aging index was used to evaluate aging resistance based on the increase in G^* of PAV aged mastics versus G^* of unaged mastics. The results proved that, for reactive powder mastics, the aging index was reduced at lower concentrations as compared to the control limestone mastics. This characteristic was desirable as this demonstrates a reduced rate at

which the reactive powder mastic ages and this can lead to a longer lasting material. The CSA mastics were the only mastic type that demonstrated a reduced aging index at elevated concentrations as compared to the control limestone mastic. However, based on the results, the aging index response need to be investigated further to fully understand the aging phenomena.

- Thermal cracking resistance was assessed by evaluating the creep stiffness $S(t)$ and m -value. The results discovered that $S(t)$ was within Superpave® specifications of 300 MPa for all mastics at 5% concentrations, however, this limit was exceeded for most mastics at 15% concentrations and beyond. The only reactive powder mastics that had consistent improvement were LF, SM, and CSA cements combined with WMA PG52-34 as these performed better than the control limestone mastics at both 5% and 15% concentrations. It is evident that most mastics with reactive fillers had a higher $S(t)$ than the control limestone mastics. However, the m -value results suggest a better potential for the reactive powder mastics to relax stresses at lower temperatures when compared to the control limestone mastics and this is important outcome of the study (all mastics also met Superpave® specifications at all concentrations of having an m -value greater than 0.300). In this regard, LF and CSA cement mastics demonstrated the most desirable results for both binder types, and this indicates great potential for resistance to thermal cracking.

7.2 MIXTURE STUDY

- Asphalt film thickness, which is related to asphalt binder coating, was used to understand the aggregate interaction with binder. The asphalt film thickness was higher for the control mixtures (8.24 μm) as compared to the reactive powder mixtures (5.90 μm). This result was apparent as the reactive powder mixtures had 25% binder replacement by volume as

compared to the control limestone mixtures. However, even with the reduction in binder quantity, there were no major differences observed for aggregate coating quality or mixing performance between the mixture types.

- Workability was used to evaluate the differences in compaction efforts for reactive powder WMA mixtures and control mixtures (both compacted at 115°C) by evaluating the differences in densification based on % G_{mm} . Since the reactive powder mixtures had a 25% (by volume) replacement of binder with portland cement, the workability was hindered for these mixtures as compared to the control limestone mixtures.
- The research results proved that the use of CSA cement in asphalt can drastically improve the aging resistance. For example, CSA cement mixtures performed the best in terms of aging resistance since this mixture had the lowest aging index of 0.07 with WMA PG58-28 binder when compared to the control mixture which had an aging index of 0.09. The CSA cement mixtures also performed the best for the WMA PG52-34 binder as these mixtures had an aging index of 0.06 as compared to the control mixtures which had an aging index of 0.10.
- It was demonstrated that all reactive powder WMA samples produced higher ultimate strengths in dry Indirect Tensile Testing (IDT) than the control samples. For the WMA PG58-28 binder, the CSA cement mixtures had the highest ultimate strength of 9.96 kN, however the control mixtures had the highest ultimate deformation at failure of 4.29 mm. For the WMA PG52-34 binder, the LF cement mixtures developed the highest ultimate strength of 6.29 kN, however, the CSA cement mixtures had the highest ultimate deformation at failure of 4.23 mm.
- The research results demonstrated that all reactive powder mixtures hindered the moisture-damage resistance based on the Tensile Strength Ratio (TSR) parameter as compared to

the control mixtures. The LF cement mixtures produced the lowest TSR of 0.945 for the WMA PG58-28 binder and the lowest TSR of 0.929 for the WMA PG52-34 binder.

- Intermediate-temperature fatigue cracking analysis was evaluated based on secondary fatigue slopes and complex modulus E^* . The results proved that all reactive powder mixtures performed considerably better than the control mixtures. The secondary fatigue deformation rate of the CSA cement mix was the lowest deformation rate of $1.69E-06$ mm/cycle in the vertical direction for the WMA PG58-28 binder and $1.20E-06$ mm/cycle for the WMA PG52-34 binder. The control samples performed the worst as these samples deformed at a rate of $7.28E-06$ mm/cycle in the vertical direction for the WMA PG58-28 binder and $6.34E-06$ mm/cycle for the WMA PG52-34 binder. All reactive powder mixtures also performed better than the control mixtures in terms of drop in Complex Modulus (E^*). The WMA PG58-28 CSA cement mix was able to withstand up to 184,750 loading cycles and the WMA PG52-34 CSA cement mix was able to withstand up to 158,750 loading cycles till there was a drop in E^* (i.e., point of failure) which was the most experienced by any mixture. The WMA PG58-28 control samples were only able to withstand 86,250 cycles and the WMA PG52-34 control samples were only able to withstand 98,750 cycles till there was a drop in E^* . Therefore, the addition of reactive powders in asphalt mixtures improves fatigue resistance.
- Low-temperature thermal cracking resistance demonstrated improved results for reactive powder mixtures. All reactive powder mixtures performed better in terms of Fracture Energy (G_f) than the control mixtures. For WMA PG58-28, CSA cement mixtures had the highest G_f value of 1.46 kJ/m^2 resulting in better performance, and the control mixture only had a G_f value of 1.23 J/m^2 . For WMA PG52-34, LF cement mixtures had the highest G_f value of 1.45 kJ/m^2 and the control mixture only had a G_f value of 1.29 J/m^2 . However, all

reactive powder mixtures performed worse than the control mixture in terms of stiffness $S(t)$. For WMA PG58-28, CSA cement mixtures had the highest $S(t)$ of 13.56 kN/mm whereas the control had the lowest $S(t)$ of 10.70 kN/mm. For the WMA PG52-34, LF cement mixtures had the highest $S(t)$ of 12.34 kN/mm whereas the control had the lowest $S(t)$ of 10.15 kN/mm. This increase in stiffness for the reactive powder mixtures is due to the high dosage of binder replacement.

7.3 DURABILITY STUDY

- Self-healing potential of portland cement was effectively discovered using SEM with mastics of 50% volume of binder replacement with reactive powder materials.
- Standard freeze-thaw testing proved that CSA cement increased the resistance to freeze-thaw damage when compared to the control limestone mixtures for 300 freezing and thawing cycles. This testing also demonstrated an increase in freeze-thaw damage resistance for LF cement but only for the mixtures with WMA PG52-34 binder. With WMA PG58-28 binder, the CSA cement mixtures performed considerably well with a mass change of only 0.17% compared to the control which had a mass change of 0.29%. With WMA PG52-34 binder, the CSA cement mixtures demonstrated a mass change of only 0.41% compared to the control which had a mass change of 0.55%.
- IDT freeze-thaw testing proved that both LF and CSA cement mixtures increased the resistance to freeze-thaw damage when compared to the control limestone mixtures. For WMA PG58-28, the CSA cement mixtures had an ultimate horizontal stress of 1.26 MPa and the control mixtures only had an ultimate horizontal stress of 0.82 MPa. For WMA PG52-34, the CSA cement compositions also had the highest ultimate horizontal stress of 0.75 MPa and the control mixtures only had an ultimate horizontal stress of 0.54 MPa.

- Salt-scaling testing demonstrated that there was no mass loss for all investigated specimens up to 45 cycles for both binder types. After 45 cycles (to 50 cycles) the results demonstrated inconsistent results between the binder types. For WMA PG58-28, the results revealed that LF cement samples had a mass loss of 0.0 g/m² after 50 cycles and the LS and CSA cement samples both had a total mass loss of 8.20 g/m². For the WMA PG52-34 mixtures, the results indicated that the reference LS samples had a total mass loss of 5.50 g/m² after 50 cycles and the LF cement samples had a total mass loss of 10.95 g/m² and the CSA cement samples had a total mass loss of 8.20 g/m². This testing needs to be extended beyond 50 cycles as the results were inconclusive.

7.4 STATISTICAL MODELING STUDY

- The complex modulus (G^*), viscosity, and rutting factor ($G^*/\sin(\delta)$) were used as output parameters to quantify the interaction of reactive powders and binders. This research classified all correlations to be at a confidence level of 85% or better. The goal of this research project was to maximize the effects of reactive powders and develop a statistical relationship for asphalt mastics at a 25% replacement (by volume) as higher cement loading demonstrates a better potential for self-healing. Based on the analysis, for all output parameters, the input factors that had strong correlations were specific gravity, D_{10} , D_{50} , D_{90} , Na_2O , P_2O_5 , SAF, and Rigden voids. Additionally, for $G^*/\sin(\delta)$, CaO and SO_3 contents demonstrated a good correlation. The results indicate that specific gravity, D_{10} , D_{50} , and CaO all decrease the stiffness of the mastic as the concentration increases whereas D_{90} , SO_3 , Na_2O , P_2O_5 , SAF, and Rigden voids all increase the stiffness as the concentration increases. These parameters also demonstrated multicollinearity.
- The primary indicators affecting mastic G^* were specific gravity, Na_2O , P_2O_5 , and Rigden voids. The primary indicators affecting viscosity were specific gravity, P_2O_5 ,

SAF, and Rigden voids. The primary indicators affecting $G^*/\sin(\delta)$ were specific gravity, Na_2O , P_2O_5 , and Rigden voids. These reactive powder physical and chemical properties are the input variables that can be used to estimate the performance of asphalt mastic with reactive powders.

- The developed multiple linear regression models for both binder types showed good correlations with the experimental data. For G^* at 25% concentrations, the Pearson's correlation coefficient was 0.999 for WMA PG58-28 and 0.945 for WMA PG52-34 binder. For viscosity at 25% concentrations, the Pearson's correlation coefficient was 1.000 for WMA PG58-28 and 0.962 for WMA PG52-34. For $G^*/\sin(\delta)$ at 25% concentrations, the Pearson's correlation coefficient was 0.966 for WMA PG58-28 and 1.000 for WMA PG52-34 binder.

CHAPTER 8

REFERENCES

1. **AASHTO R30-02. (2013).** “Mixture Conditioning of Hot Mix Asphalt (HMA)”. *American Association of State Highway and Transportation Officials*.
2. **AASHTO T2830-7. (2013).** “Resistance of Compacted Hot Mix Asphalt (HMA) to Moisture-Induced Damage”. *American Association of State Highway and Transportation Officials*.
3. **AASHTO T312-12. (2013).** “Preparing and Determining the Density of Hot Mix Asphalt (HMA) Specimens by Means of the Superpave Gyrotory Compactor”. *American Association of State Highway and Transportation Officials*.
4. **AASHTO T322-04. (2013).** “Determining the Creep Compliance and Strength of Hot-Mix Asphalt (HMA) Using the Indirect Tensile Test Device”. *American Association of State Highway and Transportation Officials*.
5. **AASHTO T342-11. (2013).** “Determining Dynamic Modulus of Hot Mix Asphalt (HMA)”. *American Association of State Highway and Transportation Officials*.
6. **AASHTO T240. (2013).** “Effect of Heat and Air on a Moving Film of Asphalt (Rolling Thin-Film Oven Test)”. *American Association of State Highway and Transportation Officials*.
7. **AASHTO R28 (2013).** “Standard Practice for Accelerated Aging of Asphalt Binder Using a Pressurized Aging Vessel (PAV)”. *American Association of State Highway and Transportation Officials*.
8. **AASHTO T315-12 (2013).** “Determining the Rheological Properties of Asphalt Binder Using a Dynamic Shear Rheometer (DSR)”. *American Association of State Highway and Transportation Officials*.
9. **AASHTO TP 70-13 (2013).** “Multiple Stress Creep Recovery (MSCR) Test of Asphalt Binder Using a Dynamic Shear Rheometer (DSR)”. *American Association of State Highway and Transportation Officials*.
10. **AASHTO T313-12 (2013).** “Determining the Flexural Creep Stiffness of Asphalt Binder Using the Bending Beam Rheometer (BBR)”. *American Association of State Highway and Transportation Officials*.
11. **Ali, N., Chan, J. S., Simms, S., Bushman, R., & Bergan, A. T. (1996).** “Mechanistic Evaluation of Fly Ashy Asphalt Concrete Mixtures”. *Journal of Materials in Civil Engineering*. 8 (1): 19-25.
12. **Al-Khateeb, G. G., Al-Akhras, N. M. (2011).** “Properties of Portland Cement-Modified Asphalt Binder using Superpave Tests”. *Construction and Building Materials*. Vol. 25.
13. **Al-Qadi, I. L., Gouru, H., Weyers, R. E. (1994).** “Asphalt Portland Cement Concrete Composite: Laboratory Evaluation”. *Journal of Transportation Engineering*. 120(1).
14. **American Coal Ash Association (ACAA). (2006).** “Fly Ash Facts for Engineers”. *Federal Highway Administration*. FHWA-IF-03-019.
15. **Anderson, D. A., Goetz, W. H. (1973).** “Mechanical Behavior and Reinforcement of Mineral Filler-Asphalt Mixtures”. *Proceedings of the Association of Asphalt Paving Technologists*. Vol. 42.
16. **Anderson, D. A., Brock, D., & Tarris, J. P. (1982).** “Dust Collector Fines and their Influence on Mixture Design”. *AAPT*. Proceeding No. 51, 363-374.

17. **Anderson, D. A., Tarris, J. P., and Brock, D. (1983).** “Dust Collector Fines and their Influence on Mixture Design”. *Journal of Association of Asphalt Paving Technology*. 51: 353-397.
18. **Anagnos, J. N., Kennedy, T. W. (1972).** “Practical Method of Conducting the Indirect Tensile Test”. *Center for Highway Research*. University of Texas, Research Report 98-10.
19. **Asphalt Institute. (2001).** “Superpave Mix Design. Superpave Series No. 2 (SP-02)”. *Asphalt Institute*. Lexington, KY.
20. **Asphalt Institute. (2003).** ”Performance Graded Asphalt Binder Specification and Testing”. Superpave Series No. 1 (SP-1). *Asphalt Institute*. Lexington, KY
21. **Asi, I., and Assa'ad, A. (2005).** “Effect of Jordanian Oil Shale Fly Ash on Asphalt Mixes”. *Journal of Materials in Civil Engineering*. 17 (5): 553-559.
22. **ASTM C136 / C136M-14. (2014).** “Standard Test Method for Sieve Analysis of Fine and Coarse Aggregates”. *ASTM International*. West Conshohocken, PA.
23. **ASTM D4123-82. (2003).** “Standard Test Method for Indirect Tension Test for Resilient Modulus of Bituminous Mixtures”. *ASTM International*. West Conshohocken, PA.
24. **ASTM D4464-15. (2015).** “Standard Test Method for Particle Size Distribution of Catalytic Materials by Laser Light Scattering”. *ASTM International*. West Conshohocken, PA.
25. **ASTM D5550-14. (2014).** “Standard Test Method for Specific Gravity of Soil Solids by Gas Pycnometer”. *ASTM International*. West Conshohocken, PA.
26. **ASTM D6752 / D6752M-11. (2011).** “Standard Test Method for Bulk Specific Gravity and Density of Compacted Bituminous Mixtures Using Automatic Vacuum Sealing Method”. *ASTM International*. West Conshohocken, PA.
27. **ASTM D6857 / D6857M-11. (2011).** “Standard Test Method for Maximum Specific Gravity and Density of Bituminous Paving Mixtures Using Automatic Vacuum Sealing Method”. *ASTM International*. West Conshohocken, PA.
28. **ASTM E986-04. (2010).** “Standard Practice for Scanning Electron Microscope Beam Size Characterization”. *ASTM International*. West Conshohocken, PA.
29. **ASTM C672-12 (2012).** “Standard Test Method for Scaling Resistance of Concrete Surfaces Exposed to Deicing Chemicals”. *ASTM International*. West Conshohocken, PA.
30. **ASTM E986-04 (2017).** “Standard Practice for Scanning Electron Microscope Beam Size Characterization”. *ASTM International*. West Conshohocken, PA.
31. **ASTM C114-18 (2010).** “Standard Test Methods for Chemical Analysis of Hydraulic Cement”. *ASTM International*. West Conshohocken, PA.
32. **ASTM C311-17 (2010).** “Standard Test Methods for Sampling and Testing Fly Ash or Natural Pozzolans for Use in Portland-Cement Concrete”. *ASTM International*. West Conshohocken, PA.
33. **ASTM D4402 (2012).** “Standard Test Method for Viscosity Determination of Asphalt at Elevated Temperatures Using a Rotation Viscometer”. *ASTM International*. West Conshohocken, PA.
34. **Bautista, E. G. et al. (2015).** "Experimental Evaluation of the Effect of Coal Combustion Products on Constructability, Damage, and Aging Resistance of Asphalt Mastics". *Theses and Dissertations*. Paper 858.
35. **Bentur, A., Gray, R., Mindess, S., & Young, J. F. (1998).** “The Science and Technology of Civil Engineering Materials”. *Prentice Hall*.

36. **Bianchetto, H., Martinez, A., Miro, R., & Perez, F. (2005).** “Proceedings of the Annual Meeting of the Transportation Research Board: Effect of Filler on the Aging Potential of Asphalt Mixtures”. *TRB*. Washington, DC. Asdf
37. **Brown, A. B., J. W. Sparks and O. Larsen (1957).** “Rate of Change of Softening Point, Penetration and Ductility of Asphalt in Bituminous Pavement”. *Proceedings AAPT*. Vol.26.
38. **Brown, E. R., McRae, J. L., & Crawley, A. (1989).** “Effect of Aggregates on Performance of Concrete”. *ASTM*. Special Technical Publication 1016.
39. **Cabrera, J. G., and Zoorob, S. (1994).** “Design of Low Energy Hot Rolled Asphalt”. *The Civil Engineering Materials Unit, Department of Civil Engineering, University of Leeds, United Kingdom*.
40. **Carpenter, C. A. (1952).** “A Comparative Study of Fillers in Asphaltic Concrete”. *Public Roads*. 27, 101-110. Asdf
41. **Churchill, E. V., & Amirhanian, S. N. (1999).** “Coal Ash Utilization in Asphalt Concrete Mixtures”. *Journal of Materials in Civil Engineering*. 11 (4): 295-301. 186
42. **DeFoe, J. H. (1983).** “Evaluation of Sulfur-Asphalt Binder for Bituminous Resurfacing Mixtures”. *Michigan Department of Transportation*. Research report R1-1220, Research Project 74-D-29. Asd
43. **Domone, P., & Illston, J. (2010).** “Construction Materials: Their Nature and Behavior (4th Edition)”. *Spon Press*, New York, New York. 2010.
44. **Doyle, P. C. (1958).** “Cracking Characteristics of Asphalt Cement”. *Proceedings AAPT*, Vol. 27.
45. **El-Maaty, A. E. A. (2013).** “Laboratory Evaluation of Resistance to Moisture Damage in Asphalt Mixtures”. *Ain Shams Engineering Journal*. Vol. 4, Issue 3.
46. **Elwardany, M. D., Rad, F. Y., Castorena, C., & Kim, Y. R. (2010).** “Evaluation of Asphalt Mixture Laboratory Long-Term Aging Methods for Performance Testing and Prediction”. *Cooperative Highway Research Program*. Project No. 9-39, National Research Council, Washington, D.C.
47. **Faheem, A. F., & Bahia, H. U. (2009).** “Conceptual Phenomenological Model for Interaction of Asphalt Binders with Mineral Fillers”. *Doctoral dissertation*. University of Wisconsin-Madison, Madison, WI.
48. **Faheem, A. F., & Bahia H. U. (2010).** “Modelling of Asphalt Mastic in Terms of Filler-Bitumen Interaction”.
49. **Faheem, A. F., Hintz, C., & Bahia, H. U. (2011).** “Test Methods and Specification Criteria for Mineral Filler Used in HMA”, NCHRP 9-45 Final Report.
50. **Finn, F. N. (1967).** “Factors Involved in the Design of Asphaltic Pavement Surfaces”. *HRB*, NCHRP Report 39.
51. **Finn, F. N., Nair, K., & Hilliard, J. M. (1978).** “Minimizing Premature Cracking in Asphaltic Concrete Pavement”. *TRB*, NCHRP Report 195.
52. **Fromm, H. J., & Phang, W. A. (1971).** “Temperature Susceptibility Control in Asphalt Cement Specifications”. *HRB*, Highway Research Record 350.
53. **Galloway, B. M. (1980).** “A Review of the Use of Mineral Filler in Asphalt-Aggregate Mixtures”. *Fly Ash Applications in 1980*.
54. **Gaw, W. J. (1977).** “Measurement and Prediction of Asphalt Stiffness and Their Use in Developing Specifications to Control Low-Temperature Pavement Transverse Cracking”. *ASTM*, Special Technical Publication 628.

55. **Goetz, W. H., & Wood, L. E. (1960).** “Bituminous Materials and Mixtures”. *Highway Engineering Handbook*. Ed. K. B. Woods, Section 18, McGraw-Hill, New York, NY.
56. **Goetz, R. O., Tons, E., & Razi, M. (1983).** “Fly Ash as Asphalt Reducer in Bituminous Base Courses”. *The Board of Water and Light, Consumer Power Co & Detroit Edison Co.* University of Michigan, Detroit, MI.
57. **Hadley, W. O., Hudson, W. R., & Kennedy, T. W. (1970).** “A Method of Estimating Tensile Properties of Materials Tested in Indirect Tension. *Center for Highway Research*. University of Texas, Research Report 98-7.
58. **Hadley, W. O., Hudson, W.R., & Kennedy, T. W. (1972).** “An Evaluation of Factors Affecting the Tensile Properties of Asphalt-Treated Materials”. *Center for Highway Research*. University of Texas, Research Report 98-2.
59. **Hartman, A. M., Gilchrist, M. D., Walsh, G. (2001).** “Effect of Mixture Compaction on Indirect Tensile Stiffness and Fatigue”. *Journal of Transportation Engineering*. Journal 127, 370-378.
60. **Henning, N. E. (1974).** “Evaluation of Lignite Fly Ash as a Mineral Filler in Asphaltic Concrete”. *Twin Cities Testing and Engineering Laboratory*. Report No. 2, St. Paul, MN.
61. **Heukelom, W., and Wija, P. W. O. (1971).** “Viscosity of Dispersions Governed by Concentration and Rate of Shear”. *Journal of Asphalt Paving Technologists*. Vol 40.
62. **Hmoud, H. R. (2011).** “Evaluation of VMA and Film Thickness Requirements in Hot-Mix Asphalt”. *Modern Applied Science*. Vol. 5, No. 4, Baghdad University, Baghdad, Iraq.
63. **Howell, H. C., Hudson, S. B., & Warden, W. B. (1952).** “Proceedings of the Association of Asphalt Paving Technologists: Evaluation of Mineral Filler in Terms of Practical Pavement Performance”. 27, 101-110.
64. **Kandhal, P. S., Sandvig, L.D., Koehler, W. C., & Wenger, M. E. (1973).** “Asphalt Viscosity-Related Properties of In-Service Pavements in Pennsylvania”. *ASTM*, Special Technical Publication No. 532, 1973.
65. **Kandhal, P. S., Sandvig, L. D., & Wenger, M. E. (1973).** “Shear Susceptibility of Asphalts in Relation to Pavement Performance”. *Proceedings AAPT*, Vol. 42.
66. **Kandhal, P. S., and M. E. Wenger (1975).** “Asphalt Properties in Relation to Pavement Performance”. *TRB*. Transportation Research Record 544.
67. **Kandhal, P. S. (1978).** “Low Temperature Shrinkage Cracking of Pavements in Pennsylvania”. *Proceedings of the AAPT*, Vol. 47.
68. **Kandhal, P. S. (1980).** “Evaluation of Low Temperature Pavement Cracking on Elk County Research Project”. *TRB*, Transportation Research Record 77.
69. **Kandhal, P. S. et al. (1988).** “Low-Temperature Properties of Paving Asphalt Cement”. *TRB*, State-of-the-Art Report 7.
70. **Krambeck, H. (2009).** “Draft GHG Emissions Calculator for Asphalt Production”. *The World Bank Group*. Washington D.C.
71. **Lakes, R. (2009).** “Viscoelastic Materials”. New York, NY. *Cambridge University Press*. 1st Edition.
72. **Lee, Dah-Yinn (1973).** “Asphalt Durability Correlation in Iowa”. *HRB*. Highway Research Record 468.
73. **Likitlersuang, S., Chompoorat, T. (2016).** “Laboratory Investigation of the Performances of Cement and Fly Ash Modified Asphalt Concrete Mixtures”. *International Journal of Pavement Research and Technology*. Vol. 9, Issue 5.

74. **Macosko, C. (1994).** "Rheology, Principles, Measurements, and Applications". *Wiley-VCH, Inc.*
75. **Mamlouk, M. S., & Zaniewski, J. P. (2017)** "Materials for Civil and Construction Engineering: 4th Edition. *Pearson Education, Inc.*, Upper Saddle River, NJ.
76. **McGennis, R. B. et al. (1994).** "Background of Superpave Asphalt Binder Test Methods". *Federal Highway Administration*. Publication no. FHWA-SA-94-069. Washington, DC.
77. **McGennis, R.B., et al. (1995).** "Background of Superpave Asphalt Mixture Design and Analysis". *Federal Highway Administration*. Publication no. FHWA-SA-95-003. Washington, DC.
78. **McLeod, N. A. (1975).** "The Case for Grading Asphalt Cements by Penetration at 77°F". *CTAA. Proceedings Canadian Technical Asphalt Association*, Vol. 20.
79. **Meininger, R. C., & Nichols, F. P. (1990).** "Highway Materials Engineering, Aggregates, and Unbound Bases". *Federal Highway Administration*. Publication no. FHWA-HI-90-007, NHI Course No. 13123. Washington, D.C.
80. **Meyers, M. A. and Chawla, K. K. (2008).** "Mechanical Behavior of Materials". *Cambridge University Press*. 2nd Edition.
81. **Perng, J. D. (1989).** "Analysis of Crack Propagation in Asphalt Concrete Using a Cohesive Crack Model". *Thesis*. Ohio State University, Columbus, OH.
82. **Petersen, J. C. (1984).** "Chemical Composition of Asphalt as Related to Asphalt Durability (State-of-the-Art)". *TRB, Transportation Research Record*. No. 999.
83. **Richardson, C. (1905).** "The Theory of the Perfect Sheet Asphalt Surface". *Journal of Industrial Engineering and Chemistry*. Pp 463-465.
84. **Rigden, P.J. (1947).** "The Use of Fillers in Bituminous Road Surfaces: A Study of Filler-Binder Systems in Relation to Filler Characteristics". *Journal of the Society of Chemical Industry*.
85. **RILEM TC176-IDC (2002).** "Capillary Suction, Internal Damage and Freeze Thaw Test: Reference Method and Alternative Methods A and B". *Materials and Structures*. Vol. 34.
86. **Roberts, F. L., Kandhal, P. S., Brown, E. R., Lee, D. Y., & Kennedy, T. W. (1996).** "Hot Mix Asphalt Materials, Mixture Design, and Construction: 2nd Edition". *NAPA Education Foundation*. Lanham, MD.
87. **Rosner, J. C., Chehovits, J.G., and Morris, G. R. (1982).** "Fly Ash as a Mineral Filler and Antistrip Agent for Asphalt Concrete". *Challenge of Change-6th International Ash Utilization Symposium Proceedings*. United States Department of Energy, Morgantown.
88. **Sankaran, K. S., and Rao, D. R. (1973).** "The Influence of the Quality of Filler in Asphaltic Paving Mixtures". *Indian Roads Congress*. 35: 141-151.
89. **Shell Bitumen. (2003).** "The Shell Bitumen Handbook", *Shell Bitumen*, UK.
90. **Shu, X., Huang, B., & Vukosavljevic, D. (2007).** "Laboratory Evaluation of Fatigue Characteristics of Recycled Asphalt Mixtures". *Department of Civil and Environmental Engineering*. University of Tennessee, Knoxville, TN.
91. **Siddique, R., & Iqbal Khan, M. (2011).** "Supplementary Cementing Materials". Springer-Verlag Berlin Heidelberg.
92. **Sobolev, K., Flores, I. V., & Wasiuddin, N. M. (2013).** "The Use of Fly Ash as Filler in Asphalt Cement: Phase 1". Final Report, *UWM-We Energies*, 17 p.
93. **Suheibani, A. R. S. (1986).** "The Use of Fly as an Asphalt Extender". *Doctoral dissertation*. University of Michigan, Ann Arbor, MI.

94. **Tadros, T. F. (2010).** “Rheology of Dispersions: Principles and Applications”. *WILEY-VCH Verlag GmbH & Co. KGaA*. Weinheim.
95. **Tapkin, S. (2008).** “Improved Asphalt Aggregate Mix Properties by Portland Cement Modification”. *Can. J. Civ. Eng.* 35: 27-40.
96. **Termkhajornkit, P., Nawa, T., Yamashiro, Y., Saito, T. (2009).** “Self-Healing Ability of Fly Ash-Cement Systems”. *Cement and Concrete Composites*. Vol. 31, Issue 3.
97. **Tons, E. et al. (1983).** “Fly Ash as an Asphalt Reducer in Bituminous Base Courses”. Report prepared by the University of Michigan, *The Board of Water and Light*. Consumer Power Co. and Detroit Edison Co. Detroit, Michigan.
98. **Wang, H. et al (2011).** “Effect of Filler Characteristics on Asphalt Mastic and Mixture Rutting Potential”. *TRB*. Transportation Research Board, 2208: 33-39.
99. **Warden, W. B., Hudson, S. B., and Howell H. C. (1952).** “Evaluation of Mineral Filler in Terms of Practical Pavement Performance”. *Proceedings of the Association of Asphalt Paving Technologists*. 27(52): 101-110
100. **Wen, H. (2001).** “Fatigue performance Evaluation of WesTrack Asphalt Mixtures Based on Viscoelastic Analysis of Indirect Tensile Test”. *Doctoral dissertation*. North Carolina State University, Raleigh, North Carolina.
101. **Wu, S. P. (2009).** “Effect of Organo-Montmorillonite on Aging Properties of Asphalt”. *Elsevier*. Construction and Building Materials Vol. 23, Issue 7, 2636-2640.
102. **Zimmer, F. V. (1970).** “Proceedings of the 2nd Ash Utilization Symposium: Fly Ash as Bituminous Filler”. Pittsburgh, PA.

Clayton J. Cloutier

Education	<u>University of Wisconsin – Milwaukee</u>	9/2010 – 5/2019
	Milwaukee, WI 53211 <i>College of Engineering and Applied Sciences</i>	
	Ph.D. in Civil Engineering	5/2019
	<ul style="list-style-type: none">• Emphasis in Structural Engineering• Minor: Materials Science and Engineering• Major GPA: 4.0 / 4.0• Cumulative GPA: 3.898 / 4.0	
	Master of Science in Civil Engineering	5/2016
	<ul style="list-style-type: none">• Emphasis in Structural Engineering• Cumulative GPA: 4.0 / 4.0	
	Bachelor of Science in Civil Engineering	12/2014
	<ul style="list-style-type: none">• Cumulative GPA: 3.957 / 4.0• Passed the FE Exam: 7/2014	

Ph.D. Dissertation	<u>The Effective Use of Portland Cement in Reactive Powder Hybrid Asphalt Concrete</u>	5/2019
	<i>Advisor: Dr. Konstantin Sobolev</i> Conducted an extensive research study on Warm Mix Asphalt (WMA) mastics and mixtures modified with different types of portland cement reactive powders. This study evaluated constructability, rutting resistance, fatigue resistance, and thermal cracking resistance based on Superpave methodology. Significant developments were made to understand the influence of self-healing properties on crack characteristics under freeze-thaw conditions.	

Master's Thesis	<u>The Effective Use of Coal Combustion Products (CCPs) in ASHphalt Pavements</u>	5/2016
	<i>Advisor: Dr. Konstantin Sobolev</i> Used Superpave methodology to evaluate mixtures with different fly ashes in Hot Mix Asphalt (HMA) pavements. Parameters such as workability, fatigue resistance, and thermal cracking resistance were evaluated.	

Computer Skills	Revit 2018, AutoCAD 2018, SAP2000 19, ANSYS Workbench 14.5
------------------------	--

Work Experience	<u>Structural Engineer</u> – Milwaukee, WI 53211	6/2016 – Present
	<i>Computerized Structural Design (CSD)</i>	
	Designed steel beams, columns, stepped laced columns, roof joist girders, anchor rods, and diagonal and moment connection components relating mostly to steel mill construction using ASD and LRFD methodology. Analyzed large steel mill frames using SAP2000 and designed concrete foundations. Reviewed shop drawings and developed Revit project models and project plan sets.	
	<u>Teaching Assistant</u> – Milwaukee, WI 53211	9/2015 – 5/2019
	<i>University of Wisconsin - Milwaukee</i>	
	Responsible for teaching lab/discussion sections in the following courses: Material of Construction, Mechanics of Materials, Engineering Surveying, and Sustainable Construction Materials and Technologies	
	<u>Research Assistant</u> – Milwaukee, WI 53211	9/2012 – 5/2015
	<i>University of Wisconsin - Milwaukee</i>	
	Tested and evaluated different mixtures of Hot Mix Asphalt (HMA) and fly ashes. Tested cement pastes, mortars, and concrete samples to optimize pavements for PCA, WisDOT, WE Energies, and EPRI.	
	<u>Civil Engineering Internship</u> – St. Paul, MN 55107	6/13 – 8/15
	<i>MSA Professional Services, Inc.</i>	
	Involved in a variety of duties related primarily to municipal engineering and field surveying.	
	<u>Painter</u> – North St. Paul, MN 55109	6/2009 – 8/2012
	<i>Hurd Maintenance Painting, Inc.</i>	
	Painted commercial and residential buildings with a team of construction workers.	
	<u>Concrete Laborer</u> – New Richmond, WI 54017	6/2008 – 8/2008
	<i>Paulus Excavating</i>	
	Poured concrete driveways, sidewalks, patios, etc. and was able to gain direct experience working with concrete.	
<hr/>		
Organizations	(AISC) American Institute of Steel Construction	5/2018 – Present
	Participated in the Mortar Workability Competition.	
	(ACI) American Concrete Institute	1/2013 – Present
	Participated in the Mortar Workability Competition.	
	(ASCE) American Society of Civil Engineers	9/2012 – 12/2013
	Concrete canoe competition for ASCE conference.	

Organization Project	<u>ACI Mortar Workability Competition</u> <i>ACI Spring 2013 Convention: Minneapolis, MN</i> Competition focused on workability and rheological properties of concrete. Teams were challenged to create a mortar mixture with optimum flowability and stability.	4/2013
Honors	<ul style="list-style-type: none"> - Advanced Opportunity Program Fellowship Award - Chancellor's Award - UW-Milwaukee Student Excellence Award - Dean's List (Every Semester) - WCPA (Wisconsin Concrete Pavement Association) Scholarship - Graef, Anhalt, Schloemer Foundation Scholarship - Associated General Contractors of Greater Milwaukee Scholarship 	<p>9/2017 – 5/2018 9/2018 – 5/2019 9/2015, 9/2016 5/2016 9/2010 – 5/2016 12/2012, 12/2014 9/2014 9/2014</p>
Publications & Presentations	<u>Effect of Spray Dryer Absorbers as Mix Enhancer on HMA Performance</u> <i>Cloutier, C. J., Bautista, E. G., Faheem, A. F., Sobolev, K.</i> International Congress and Exhibition “Sustainable Civil Infrastructures: Innovative Infrastructure Geotechnology”	7/2018
	<u>Influence of Coal Combustion By-Products Physiochemical Properties on Aging Related Performance of Asphalt Mastics and HMA</u> <i>Bautista, E. G., Faheem, A. F., Cloutier, C. J., Sobolev, K.</i> International Conference on Highway Pavement and Airfield Technology	8/2017
	<u>Impact of Coal Combustion Products Incorporation on Asphalt Mixtures Performance</u> <i>Faheem, A. F., Cloutier, C. J., Bautista, E. G., Sobolev, K.</i> Transportation Research Board (TRB)	8/2017
	<u>Effect of Spray Dryer Absorber (SDA) Ash on the Performance of Warm Mix Asphalt (WMA)</u> <i>Cloutier, C. J., Jansen, T., Meidl, R., Sobolev, K., Faheem, A. F., Dukatz, E.</i> World of Coal Ash (WOCA)	5/2017